An Engineering Approach to Cancer Therapy Using

Systemically Delivered siRNA

Thesis by

Derek William Bartlett

In Partial Fulfillment of the Requirements

for the Degree of

Doctor of Philosophy

California Institute of Technology

Pasadena, California

2007

(Defended May 15, 2007)

Acknowledgments

It has been a distinct pleasure working with my advisor, Mark Davis. I am inspired by the excitement and tenacity he brings to every research project. He has shaped, guided, and challenged me as a researcher. I am also grateful for the helpful advice and critique provided by my committee members, Anand Asthagiri, Christina Smolke, and John Rossi. It has been an honor to interact with them over the past few years.

Thanks to the past and present members of the Davis lab. I am especially obliged to Jeremy Heidel and Swaroop Mishra for taking me under their wing and giving me a running start in the early stages of my graduate career. They are both highly talented researchers whose work was characterized by a meticulousness and intellectual curiosity that I have attempted to model in my own research.

I have enjoyed working with several immensely talented collaborators for whom I have profound respect as individuals and as scientific researchers. I learned many of the in vivo techniques by observing the highly skilled postdoctoral fellow, Siwen Hu-Lieskovan, from Timothy Triche's lab at Children's Hospital Los Angeles. I will also never forget the late nights spent working at the Crump Institute at UCLA with Helen Su and Isabel Hildebrandt from Wolfgang Weber's lab. Their patience and always pleasant demeanor were crucial to keeping our wits about us in the early morning hours at times when nothing seemed to be going right.

This research would not be possible without an army of other collaborators and support staff, and I am thankful for everyone who has made contributions along the way. Much of my time was spent in the Broad animal facility at Caltech, and I am indebted to

Abstract

The next generation of cancer therapeutics will specifically target processes responsible for the growth and survival of cancer cells. Among the most promising of these molecularly targeted therapeutics are small interfering RNAs (siRNAs). These siRNAs serve as the effectors of RNA interference, a naturally occurring and highly specific mechanism for regulating gene expression through sequence-specific degradation of messenger RNA. While these siRNAs have shown potential in vitro and in preclinical animal models, safe and effective systemic delivery remains one of the greatest challenges hindering their clinical application. This thesis describes an engineering approach to address the challenge of systemic delivery of siRNAs for cancer therapy.

Analysis of the kinetics of siRNA-mediated gene silencing reveals that gene inhibition by unmodified siRNAs can last for one week in rapidly dividing cells and up to one month in cells with minimal division. Additionally, chemical modifications to enhance siRNA nuclease stability do not prolong intracellular siRNA activity. These data, when used in combination with results from a mathematical model of siRNA function, demonstrate that dilution from cell division, and not intracellular nuclease stability, is the dominant factor governing the duration of gene inhibition by siRNAs.

Cyclodextrin-containing polycations (CDP) can self-assemble with siRNAs to form nanoparticles with desirable properties for systemic application. Characterization of these nanoparticles demonstrates that they can contain several thousand siRNAs, protect the siRNA payload from nuclease degradation, and be modified with transferrin targeting ligands that show multivalent binding to cell surface receptors.

Multimodality in vivo imaging with positron emission tomography (PET) and bioluminescent imaging (BLI) is used to monitor the biodistribution and function of the siRNA nanoparticles after intravenous administration in live mice. Attachment of targeting ligands to the surface of the nanoparticles enhances gene inhibition within the tumor, although the biodistribution and tumor localization are not dependent on the amount of targeting ligand. The targeting ligand likely serves to augment nanoparticle uptake by the tumor cells. When the siRNA nanoparticles are used to deliver therapeutic siRNAs to achieve tumor growth inhibition in disseminated and subcutaneous murine cancer models, schedule-dependent anti-tumor effects are observed.

Table of Contents

Figures

Tables

1 Introduction: Big potential for small interfering RNA in cancer therapy

1.1 Small interfering RNAs: A new class of cancer therapeutics

Significant progress has been made in the war on cancer, evidenced by the decline in cancer-related deaths in the US. According to the National Cancer Institute, approximately 65% of patients diagnosed with cancer will live longer than 5 years (1). These numbers are expected to improve even more with the advent of novel molecularly targeted cancer therapies. The traditional approach to cancer chemotherapy involves injecting highly toxic drugs to interfere with cell division, thereby killing the rapidly dividing cancer cells. However, this non-specific killing of rapidly dividing cells also destroys non-cancerous cells such as those in the bone marrow, leading to potentially serious side effects and providing a very narrow therapeutic index. As a result of an increased understanding of the molecular mechanisms underlying cancer development and progression, a new generation of cancer therapeutics are being developed to specifically interfere with molecules that are responsible for driving the growth and survival of the cancer cells (2). These molecularly targeted therapies have the potential to exert much more selective killing of cancer cells and may substantially reduce the often serious complications associated with current cancer treatments.

Small interfering RNA (siRNA) molecules are a promising new class of therapeutic agents that are perfectly suited for molecularly targeted cancer therapy. The siRNA molecules are double-stranded nucleic acids approximately 19-21 bp in length that act as the effectors of RNA interference (RNAi), a naturally occurring mechanism for post-transcriptional gene silencing (3). siRNAs interact with their cognate mRNAs through

Watson-Crick base pairing and subsequently trigger degradation of the target mRNAs in a sequence-specific fashion. The consequence of the mRNA degradation is a reduction in protein expression. This mechanism can be exploited therapeutically to inhibit the expression of a wide variety of disease-associated targets (4,5). Furthermore, because the RNAi mechanism results in sequence-specific mRNA degradation, it has the potential to help realize the goal of developing novel cancer therapies that specifically attack cancer cells while minimizing the effect on normal healthy cells.

1.2 Opportunities for siRNA in cancer therapy

Cancer is the number one cause of death for people under age 65 in the United States, accounting for nearly 25% of all deaths in 2001 (6). It is predicted that half of all men and a third of all women in the United States will develop cancer at some point in their lifetimes. According to the World Health Organization, death rates from cancer are expected to increase by 104% worldwide by 2020 (7). Needless to say, the war on cancer is still raging and the development of more-effective and less-toxic cancer therapeutics is urgently needed. siRNA molecules have the potential to revolutionize cancer therapy by providing highly potent and specific cancer cell killing with drastically reduced side effects. Some of the most promising targets for siRNA-based cancer therapy involve oncogenic fusion proteins resulting from chromosomal translocations, overexpressed or mutated oncogenes, or molecules controlling cell survival or division (8).

1.2.1 Targeting chromosomal translocations

In human cells, genetic information is stored in DNA molecules that are assembled into 23 pairs of protein:nucleic acid complexes called chromosomes. Typically, these chromosomal structures act to compact the DNA (which is nearly 3

meters long end to end), protect it from degradation or damage, help to control when particular genes are transcribed, and ensure proper replication and distribution of the genetic code during cell division. Sometimes, however, these chromosomal structures can be disrupted by rearrangements that cause part of one chromosome to break off and attach to a different chromosome, a process called translocation. Transcription factors and kinases involved in cell signaling, cycling, and death are common targets of the chromosomal translocations that can lead to cancer. This chromosomal rearrangement can result in the production of an oncogenic fusion protein or it can place a gene under the control of a new promoter; in either case, the product can cause a cell to become cancerous through processes such as overexpression of certain proteins and/or constitutive activation of cellular processes.

Several translocation breakpoints have been implicated in specific cancers including leukemias and lymphomas. One of the most notable cases of chromosomal translocation is the t(9:22) that leads to the altered Philadelphia chromosome 22 in chronic myelogenous leukemia (CML). This leads to production of the Bcr-Abl fusion protein that acts as an unregulated protein tyrosine kinase and is involved in neoplastic transformation. In 2001, Novartis received FDA approval for Gleevec (imatinib mesylate, STI 571), a small-molecular inhibitor of this Bcr-Abl fusion protein. Gleevec blocks the ATP-binding pocket of the tyrosine kinase domain of the fusion protein, thereby blocking its kinase activity. This method of specifically targeting the fusion product represents a powerful new technique for the treatment of cancers caused by chromosomal translocations.

RNA interference is a promising therapy for these cancers because it can specifically target and degrade the mRNA transcript corresponding to these aberrant fusion genes. Instead of blocking the action of the fusion protein itself, as performed by Gleevec, RNAi would degrade the transcript before translation could occur. Additionally, because RNAi is highly specific (even a few mismatches can abrogate function), it can target degradation of these unwanted fusion transcripts while leaving the normal versions untouched. This means that degradation will only occur in cancer cells where this fusion transcript is produced.

Another type of cancer characterized by a chromosomal translocation, t(11:22), is the Ewing's family of tumors (EFT), a poorly differentiated mesenchymal malignancy that arises in bone or soft tissue. It is the second most common primary osseous malignancy in childhood and adolescence (9). The translocation t(11;22) is commonly detected in EFT and produces the chimeric EWS-FLI1 fusion gene found in 85% of EFT patients(10). The EWS domain replaces the normal transcriptional activator domain in the 5' region of the FLI1 DNA-binding protein, leading to altered transcriptional activation that contributes to the tumorigenic phenotype (9). Reduction of the EWS-FLI1 protein in EFT cells in vitro or in subcutaneous xenograft tumors by antisense oligonucleotides complementary to EWS-FLI1 mRNA results in decreased proliferation (11-13), suggesting a potential therapeutic intervention directed at this tumor-specific chimeric gene. Small interfering RNAs (siRNAs) have recently been shown to silence the EWS-FLI1 gene and suppress proliferation of an EFT cell line in vitro (14-16).

1.2.2   Reducing the expression of overexpressed or mutated oncogenes

While fusion genes such as EWS-FLI1 represent ideal targets for RNAi because the sequence-specific degradation will only occur in cells expressing the fusion transcript, RNAi can also be used to treat cancers characterized by gene amplification and overexpression. Gene amplification can result when chromosomal replication goes awry, leading to the production of multiple copies of certain regions in the chromosomes. This can lead to the cancerous state if an oncogene such as K-ras, myc, or HER2/neu is included in this amplified region. Cancer cells may also have amplification of the multiple drug resistance (mdr) genes, causing them to develop resistance to many chemotherapeutic drugs. In 1998, Genentech received FDA approval for its drug Herceptin, a monoclonal antibody against the human epidermal growth factor receptor 2 (HER2), for the treatment of advanced-stage breast cancer. While antibodies represent a promising therapy for targeting cancer-specific molecules like the HER2 protein, RNA interference also holds promise as an effective therapy because of its ability to specifically degrade the transcripts of these amplified oncogenes before the proteins are produced. A recent in vitro study by Faltos et al. demonstrated the use of RNAi for sequence-specific decrease in HER2/neu mRNA and protein levels, leading to antiproliferative and apoptotic responses in cells overexpressing HER2/neu (17). This indicates that RNAi therapy may be a feasible treatment for cancers that are characterized by overexpression of certain genes.

Another promising target for siRNA-based cancer therapy is the mutated K-ras gene found in over 85% of pancreatic cancers. Currently, the five-year survival rate of pancreatic cancer patients is only 4.4% (1). One of the reasons that this type of cancer is so deadly is that it has the ability to infiltrate nearby tissue and metastasize at an early

stage. New treatment modalities are required to treat the advanced stages of this disease. On a positive note, much progress has been made with respect to the molecular basis of pancreatic cancers, revealing the prevalence of the mutated K-ras gene. Ras proteins are GTPases that participate in signal transduction from growth factor receptors on the cell surface; a point mutation in this gene can lead to its constitutive activation that causes the cell to continuously receive a signal for proliferation. Recent studies have shown that reduction of K-ras levels in pancreatic cancer tumors leads to loss of anchorage-dependent growth and tumorigenesis (18,19).

1.2.3   Controlling cell survival and death

One of the hallmarks of cancer cells is their ability to avoid the normal regulatory signals that control cell growth and death (20). Although normal cell growth and division is characterized by a finely tuned balance between cell division and apoptotic cell death, the ability of cancer cells to perturb this steady-state allows them to accumulate and develop into invasive tumors. Anti-apoptotic proteins such as bcl-2 and survivin are overexpressed in many cancer cells. The Bcl-2 protein helps govern mitochondrial death signaling, a key step in the apoptotic mechanism. Inhibition of bcl-2 expression using siRNA can lead to apoptosis in vitro and slow the growth of tumor xenografts (21,22). Likewise, survivin has been show to help regulate cell death mechanisms by interacting with caspases and also helping control mitotic spindle formation. Survivin represents a promising target for molecularly targeted therapies since it is upregulated in many cancers but minimally expressed in normal tissues (8). Survivin inhibition by siRNAs can lead to cell arrest in the G2/M phase and inhibition of clonogenic survival of cancer

cells (23). In other cancer types, siRNA directed against survivin can induce apoptosis and significantly inhibit the growth of xenograft tumors in vivo (24).

Other possible targets are proteins that are necessary for processes involved in cell division. Although these molecular targets are not necessarily unique to cancer cells, they are often overexpressed in rapidly dividing cancerous cells with minimal expression in non-mitotic cells. Ribonucleotide reductase is an attractive target for cancer therapies since it catalyzes the reduction of ribonucleotides into deoxyribonucleotides necessary for DNA replication and repair. Several potent siRNA inhibitors of the M2 subunit of RNR (RRM2) have been identified, and these siRNAs have demonstrated the ability to inhibit the growth of tumor cell lines after transfection in vitro and transplantation into mice (25). A recent study by Avolio et al. also demonstrated the in vitro and in vivo efficacy of an siRNA targeting ribonucleotide reductase (26).

1.3   The challenge of systemic siRNA delivery

Despite the promises and hype surrounding siRNA therapeutics for cancer, the clinical realization of siRNA therapeutics faces several significant hurdles, foremost of which may be a safe and effective delivery method (27). Naked siRNA molecules are rapidly degraded by nucleases present in the bloodstream, and their small size leads to first-pass renal clearance (4). Chemically modified siRNAs can be designed to maintain functional efficacy while increasing their stability against nuclease degradation. Furthermore, attachment of specific targeting ligands can induce binding to protein carriers or uptake by the desired population of cells to be treated. For example, siRNA conjugated to targeting ligands such as cholesterol and antibodies have shown efficacy both in vitro and in vivo (28,29). While these methods for nuclease stabilization and

covalent attachment of targeting ligands are promising, nanoparticle-mediated delivery methods may provide functions not achievable with naked nucleic acids or direct attachment to targeting moieties.

The design of nanoparticle carriers for systemic siRNA delivery aptly highlights the challenges and intricacies associated with attempts to manipulate biological systems. Many times, therapeutic interventions thought to act through a certain mechanism may turn out to achieve the effect through an entirely different mechanism. Additionally, modifications designed to overcome a certain problem may only reveal a still more challenging barrier to success.

Surface decoration with hydrophilic polymers such as polyethylene glycol (PEG) has been used to minimize uptake by the reticuloendothelial system (RES) and stabilize nanoparticles against aggregation in physiological environments (30,31). Moreover, addition of targeting ligands to the surface helps to increase uptake of the injected nanoparticles by a specific cell type such as tumor cells (32). However, recent studies have demonstrated that these modifications do not necessarily achieve the expected results after systemic delivery. For example, polycationic nucleic acid carriers, even when coated with PEG for stabilization, exhibit extremely rapid clearance from the bloodstream after intravenous administration (33). Studies have also indicated that addition of tumor-specific targeting ligands to the surface of the nanoparticles does not increase the amount of the injected dose that reaches the tumor compared to non-targeted nanoparticles. Nevertheless, the targeted nanoparticles show significantly greater efficacy in terms of gene expression (plasmid DNA delivery) or target gene knockdown leading to tumor growth inhibition (siRNA delivery) (34,35). It is hypothesized that the

targeting ligands do not necessarily enhance the tumor localization of the injected nanoparticles, but instead act to enhance the internalization by the tumor cells once the nanoparticles achieve tumor localization.

There exists the potential that the short circulation times of these nanoparticle carriers could limit the potential differences that might arise between targeted and non-targeted forms if circulation times were extended. Longer circulation times have been achieved for nanoparticles that are cross-linked after formation, but irreversible cross-linking will inhibit the release of the payload after cell internalization. The use of reversible cross-linking systems that can respond to the reducing environment inside a cell represents a clever approach to the design of nanoparticle carriers that can be stable for prolonged circulation in the blood yet willingly release the payload when inside the cell (36).

Even if the nanoparticles do navigate the complex milieu of the bloodstream and begin to be internalized by the target cells of interest, a completely new set of barriers exist to potentially block therapeutic efficacy. Upon internalization, the nanoparticles must escape the vesicular compartment in which they were internalized. Smart polymer systems help address the barrier of endosomal escape by responding to changes in pH in the endosomes, leading to nucleic acid release and endosomal disruption (37,38). If the delivered therapeutic molecule exerts its effect in the cytosol (e.g., siRNA), then it has reached its site of action. However, many therapeutic molecules (e.g., plasmid DNA) must reach the nucleus to have their effect. This requires intracellular trafficking to the nuclear compartment, a process that can be severely diffusion-limited but may be aided

by the use of nuclear localization signals or peptides designed to harness the dynein motor complex (39,40).

1.4   An engineering approach for the design of siRNA therapeutics

An engineer desires to not only learn how a given system works but also how it can be manipulated to achieve a desired goal. Oftentimes, this is accomplished by dismantling the system and analyzing the component systems individually in a methodical and quantitative fashion. Once the nature and function of these component systems is sufficiently understood, they can be assembled into systems with higher levels of complexity that possess properties suitable for their intended application. In this way an engineer does not act as a passive observer, but instead actively seeks ways to apply new knowledge and improve existing technologies. This thesis describes an engineering approach to address the challenge of systemic delivery of small interfering RNA (siRNA) molecules for cancer therapy.

The analysis begins at the molecular level with an attempt to understand the properties and function of individual siRNA molecules. Chapters 2 and 3 focus on the behavior of siRNA molecules in vitro and in vivo, with a specific emphasis on understanding factors governing the magnitude and persistence of the inhibition after siRNA treatment. The results demonstrate that the rate of cell division is one of the most important factors governing the activity of siRNAs, and therapies targeting rapidly dividing cells will require different dosing schedules than therapies targeting non-mitotic cell populations.

Chapter 4 addresses the next level of complexity when these siRNA molecules are assembled into nanoparticles using cyclodextrin-containing polycations (CDP). The

siRNA and CDP self-assemble to yield macromolecular nanoparticles with distinct properties that emerge from the interactions between the individual components within the assembled system. Extensive physicochemical and biological characterization of these siRNA nanoparticles reveals how their properties can be tuned to make them suitable for systemic delivery of siRNA in vivo.

Chapters 5 through 7 examine the in vivo behavior and function of the siRNA nanoparticles. In Chapter 5, noninvasive live-animal imaging with positron emission tomography (PET) and bioluminescent imaging (BLI) is used to monitor the in vivo biodistribution and function of the siRNA nanoparticles in mice, providing important insights into the behavior of these nanoparticles inside a living organism. In Chapters 6 and 7, the nanoparticles are used to deliver therapeutic siRNAs to achieve tumor growth inhibition in disseminated and subcutaneous murine cancer models.

Finally, recommendations for future work in the area of systemic siRNA delivery for cancer therapy are offered in Chapter 8.

1.5 References

1.   Ries, L., Harkins, D., Krapcho, M., Mariotto, A., Miller, B., Feuer, E., Clegg, L., Eisner, M., Horner, M., Howlader, N. et al. (2005) SEER Cancer Statistics Review, 1975-2003.

2.   Sawyers, C. (2004) Targeted cancer therapy. *Nature*, **432,** 294-297.

3.   Elbashir, S.M., Harborth, J., Lendeckel, W., Yalcin, A., Weber, K. and Tuschl, T. (2001) Duplexes of 21-nucleotide RNAs mediate RNA interference in cultured mammalian cells. *Nature*, **411,** 494-498.

4.   Dykxhoorn, D.M., Palliser, D. and Lieberman, J. (2006) The silent treatment: siRNAs as small molecule drugs. *Gene Ther*, **13,** 541-552.

5.   Dykxhoorn, D.M. and Lieberman, J. (2006) Running interference: prospects and obstacles to using small interfering RNAs as small molecule drugs. *Annu Rev Biomed Eng*, **8,** 377-402.

6.   Jemal, A., Tiwari, R.C., Murray, T., Ghafoor, A., Samuels, A., Ward, E., Feuer, E.J. and Thun, M.J. (2004) Cancer Statistics, 2004. *CA: A Cancer Journal for Clinicians*, **54,** 8-29.

7.   Rastogi, T., Hildesheim, A. and Sinha, R. (2004) Opportunities for cancer epidemiology in developing countries. *Nature Reviews: Cancer*, **4,** 909-917.

8.   Gartel, A.L. and Kandel, E.S. (2006) RNA interference in cancer. *Biomol Eng*, **23,** 17-34.

9.   Ginsberg, J.P., Woo, S.Y., Johnson, M.E., Hicks, M.J. and Horowitz, M.E. (2002) In Pizzo, P. A. and Poplack, D. G. (eds.), *Principles and Practice of Pediatric Oncology*. Lippincott Williams & Wilkins, Philadelphia, pp. 973-1016.

10.   Rodriguez-Galindo, C., Spunt, S.L. and Pappo, A.S. (2003) Treatment of Ewing sarcoma family of tumors: current status and outlook for the future. *Med Pediatr Oncol*, **40,** 276-287.

11.   Tanaka, K., Iwakuma, T., Harimaya, K., Sato, H. and Iwamoto, Y. (1997) EWS-Fli1 antisense oligodeoxynucleotide inhibits proliferation of human Ewing's sarcoma and primitive neuroectodermal tumor cells. *J Clin Invest*, **99,** 239-247.

12.   Maksimenko, A., Malvy, C., Lambert, G., Bertrand, J.R., Fattal, E., Maccario, J. and Couvreur, P. (2003) Oligonucleotides targeted against a junction oncogene are made efficient by nanotechnologies. *Pharm Res*, **20,** 1565-1567.

13.   Maksimenko, A., Lambert, G., Bertrand, J.R., Fattal, E., Couvreur, P. and Malvy, C. (2003) Therapeutic potentialities of EWS-Fli-1 mRNA-targeted vectorized antisense oligonucleotides. *Ann N Y Acad Sci*, **1002,** 72-77.

14.   Dohjima, T., Lee, N.S., Li, H., Ohno, T. and Rossi, J.J. (2003) Small interfering RNAs expressed from a Pol III promoter suppress the EWS/Fli-1 transcript in an Ewing sarcoma cell line. *Mol Ther*, **7,** 811-816.

15.   Kovar, H., Ban, J. and Pospisilova, S. (2003) Potentials for RNAi in sarcoma research and therapy: Ewing's sarcoma as a model. *Semin Cancer Biol*, **13,** 275-281.

16.   Chansky, H.A., Barahmand-Pour, F., Mei, Q., Kahn-Farooqi, W., Zielinska-Kwiatkowska, A., Blackburn, M., Chansky, K., Conrad, E.U., 3rd, Bruckner, J.D., Greenlee, T.K. et al. (2004) Targeting of EWS/FLI-1 by RNA interference

attenuates the tumor phenotype of Ewing's sarcoma cells in vitro. *J Orthop Res*, **22,** 910-917.

17. Faltus, T., Yuan, J., Zimmer, B., Kramer, A., Loibl, S., Kaufmann, M. and Strebhardt, K. (2004) Silencing of the HER2/neu gene by siRNA inhibits proliferation and induces apoptosis in HER2/neu-overexpressing breast cancer cells. *Neoplasia*, **6,** 786-795.

18. Brummelkamp, T.R., Bernards, R. and Agami, R. (2002) Stable suppression of tumorigenicity by virus-mediated RNA interference. *Cancer Cell*, **2,** 243-247.

19. Hatanaka, K., Suzuki, K., Miura, Y., Yoshida, K., Ohnami, S., Kitade, Y., Yoshida, T. and Aoki, K. (2004) Interferon-alpha and antisense K-ras RNA combination gene therapy against pancreatic cancer. *J Gene Med*, **6,** 1139-1148.

20. Hanahan, D. and Weinberg, R.A. (2000) The Hallmarks of Cancer. *Cell*, **100,** 57-70.

21. Fu, G.-F., Lin, X.-H., Han, Q.-W., Fan, Y.-R., Xu, Y.-F., Guo, D., Xu, G.-X. and Hou, Y.-Y. (2005) RNA interference remarkably suppresses bcl-2 gene expression in cancer cells in vitro and in vivo. *Cancer Biol Ther*, **4,** 822-829.

22. Benimetskaya, L., Ayyanar, K., Kornblum, N., Castanotto, D., Rossi, J., Wu, S., Lai, J., Brown, B.D., Popova, N., Miller, P. et al. (2006) Bcl-2 protein in 518A2 melanoma cells in vivo and in vitro. *Clin Cancer Res*, **12,** 4940-4948.

23. Kappler, M., Bache, M., Bartel, F., Kotzsch, M., Panian, M., Wurl, P., Blumke, K., Schmidt, H., Meye, A. and Taubert, H. (2004) Knockdown of survivin expression by small interfering RNA reduces the clonogenic survival of human sarcoma cell lines independently of p53. *Cancer Gene Ther*, **11,** 186-193.

24. Uchida, H., Tanaka, T., Sasaki, K., Kato, K., Dehari, H., Ito, Y., Kobune, M., Miyagishi, M., Taira, K., Tahara, H. et al. (2004) Adenovirus-mediated transfer of siRNA against survivin induced apoptosis and attenuated tumor cell growth in vitro and in vivo. *Mol Ther*, **10,** 162-171.

25. Heidel, J.D., Liu, J.Y.-C., Yen, Y., Zhou, B., Heale, B.S.E., Rossi, J.J., Bartlett, D.W. and Davis, M.E. (2007) Potent siRNA inhibitors of ribonucleotide reductase subunit RRM2 reduce cell proliferation in vitro and in vivo. *Clin Cancer Res*, **13,** 2207-2215.

26. Avolio, T.M., Yoon, L., Feng, N., Xiong, K., Jin, H., Wang, M., Vassilakos, A., Wright, J. and Young, A. (2007) RNA interference targeting the R2 subunit of ribonucleotide reductase inhibits growth of tumor cells in vitro and in vivo. *Anti-Cancer Drug*, **18,** 377-388.

27. Behlke, M.A. (2006) Progress towards in vivo use of siRNAs. *Mol Ther*, **13,** 644-670.

28. Soutschek, J., Akinc, A., Bramiage, B., Charisse, K., Constien, R., Donoghue, M., Elbashir, S., Geick, A., Hadwiger, P., Harborth, J. et al. (2004) Therapeutic silencing of an endogenous gene by systemic administration of modified siRNAs. *Nature*, **432,** 173-178.

29. Song, E., Zhu, P., Lee, S.-K., Chowdhury, D., Kussman, S., Dykxhoorn, D.M., Feng, Y., Palliser, D., Weiner, D.B., Shankar, P. et al. (2005) Antibody mediated in vivo delivery of small interfering RNAs via cell-surface receptors. *Nat Biotechnol*, **23,** 709-717.

30. Ogris, M., Brunner, S., Schuller, S., Kircheis, R. and Wagner, E. (1999) PEGylated DNA/transferrin-PEI complexes: reduced interaction with blood components, extended circulation in blood and potential for systemic gene delivery. *Gene Ther.*, **6,** 595-605.

31. Mishra, S., Webster, P. and Davis, M.E. (2004) PEGylation significantly affects cellular uptake and intracellular trafficking of non-viral gene delivery particles. *Eur J Cell Biol*, **83,** 97-111.

32. Schatzlein, A.G. (2003) Targeting of synthetic gene delivery systems. *J Biomed Biotechnol*, **2,** 149-158.

33. de Wolf, H.K., Snel, C.J., Verbaan, F.J., Schiffelers, R.M., Hennink, W.E. and Storm, G. (2007) Effect of cationic carriers on the pharmacokinetics and tumor localization of nucleic acids after intravenous administration. *Int J Pharm*, **331,** 167-175.

34. Kirpotin, D.B., Drummond, D.C., Shao, Y., Shalaby, M.R., Hong, K., Nielsen, U.B., Marks, J.D., Benz, C.C. and Park, J.W. (2006) Antibody targeting of long-circulating lipidic nanoparticles does not increase tumor localization but does increase internalization in animal models. *Cancer Res*, **66,** 6732-6740.

35. Maeda, N., Miyazawa, S., Shimizu, K., Asai, T., Yonezawa, S., Kitazawa, S., Namba, Y., Tsukada, H. and Oku, N. (2006) Enhancement of anticancer activity in antineovascular therapy is based on the intratumoral distribution of the active targeting carrier for anticancer drugs. *Biol Pharm Bull*, **29,** 1936-1940.

36. Oupicky, D., Carlisle, R. and Seymour, L. (2001) Triggered intracellular activation of disulfide crosslinked polyelectrolyte gene delivery complexes with extended systemic circulation in vivo. *Gene Ther*, **8,** 713-724.

37. Piskin, E., Dincer, S. and Turk, M. (2004) Gene delivery: intelligent but just at the beginning. *Journal of Biomaterial Sciences Polymer Edition*, **15,** 1181-1202.

38. Oishi, M., Nagatsugi, F., Sasaki, S., Nagasaki, Y. and Kataoka, K. (2005) Smart polyion complex micelles for targeted intracellular delivery of PEGylated antisense oligonucleotides containing acid-labile linkages. *Chem Bio Chem*, **6,** 718-725.

39. Bergen, J.M. and Pun, S.H. (2007) Evaluation of an LC8-binding peptide for the attachment of artificial cargo to dynein. *Mol. Pharmaceutics*, **4,** 119-128.

40. Tkachenko, A.G., Xie, H., Coleman, D., Glomm, W., Ryan, J., Anderson, M.F., Franzen, S. and Feldheim, D.L. (2003) Multifunctional gold nanoparticle-peptide complexes for nuclear targeting. *J Am Chem Soc*, **125,** 4700-4701.

2   Insights into the kinetics of siRNA-mediated gene silencing from live-cell and live-animal bioluminescent imaging[†]

2.1   Abstract

Small interfering RNA (siRNA) molecules are potent effectors of post-transcriptional gene silencing. Using noninvasive bioluminescent imaging and a mathematical model of siRNA delivery and function, the effects of target-specific and treatment-specific parameters on siRNA-mediated gene silencing are monitored in cells stably expressing the firefly luciferase protein. In vitro, luciferase protein levels recover to pre-treatment values within <1 week in rapidly dividing cell lines, but take longer than 3 weeks to return to steady-state levels in nondividing fibroblasts. Similar results are observed in vivo, with knockdown lasting ~10 days in subcutaneous tumors in A/J mice and 3-4 weeks in the nondividing hepatocytes of BALB/c mice. These data indicate that dilution due to cell division, and not intracellular siRNA half-life, governs the duration of gene silencing under these conditions. To demonstrate the practical use of the model in treatment design, model calculations are used to predict the dosing schedule required to maintain persistent silencing of target proteins with different half-lives in rapidly dividing or nondividing cells. The approach of bioluminescent imaging combined with mathematical modeling provides useful insights into siRNA function and may help expedite the translation of siRNA into clinically relevant therapeutics for disease treatment and management.

2.2   Introduction

RNA interference (RNAi) refers to the ability of double-stranded RNA (dsRNA) to cause sequence-specific degradation of complementary mRNA molecules. Since its discovery in *C. elegans* in 1998 (1), it has rapidly attracted attention from researchers in fields ranging from genetics to clinical medicine. A natural intracellular process likely involved in cell-based defense against mobile genetic elements such as viruses and transposons (2), RNAi promises to be an invaluable tool for gene function analysis as well as a powerful therapeutic agent that can be used to silence pathogenic gene products associated with diseases including cancer, viral infections, and autoimmune disorders (3-8).

A central component of RNAi is a double-stranded siRNA molecule that is 21-23 nucleotides in length with 2-nt long 3' overhangs (9). These siRNA effector molecules can be introduced into cells directly as synthetic siRNAs or indirectly as precursor long dsRNAs or short hairpin RNAs (shRNA). RNA polymerase II- or III-driven expression cassettes can be used for constitutive expression of shRNA molecules (10). Both the long dsRNAs and shRNAs are cleaved by Dicer (RNase III family of endonucleases) into the appropriately sized siRNA effectors. Although the presence of dsRNA >30 nucleotides can elicit an interferon response in mammalian cells (11), Elbashir and colleagues demonstrated that synthetic 21-mer siRNAs evaded the interferon response and yet were still effective mediators of sequence-specific gene silencing in mammalian cells (9). Here, we have chosen to focus on the use of synthetic 21-mer siRNA duplex molecules in mammalian cells for transient gene silencing.

Because synthetic siRNA molecules must be transported into the cells before they can function in RNAi, successful delivery of siRNA is of central importance. Delivery vehicles must protect the siRNA from nucleases in the serum or extracellular media, enhance siRNA transport across the cell membrane, and guide the siRNA to its proper location through interactions with the intracellular trafficking machinery. While naked siRNA molecules have been shown to enter cells, significantly more siRNA can be delivered using carrier vehicles (12,13). Both viral and nonviral vectors deliver siRNA into cells, although viral vectors are limited to delivering siRNA-expressing constructs such as shRNA. Commercially available cationic lipids such as Oligofectamine can effectively deliver siRNA molecules into cells in vitro with transfection efficiencies approaching 90% (9). However, the high toxicity of cationic lipids limits their use for systemic delivery in vivo. Recent studies from our laboratory have shown that cyclodextrin-containing polycations (CDP) can achieve safe and effective systemic delivery of siRNA in mice (14). Here, we consider the nonviral delivery of siRNA using cationic lipids or polymers.

A challenge for the successful application of siRNA will be to determine the dosing schedule required for efficacy, making insights into the kinetics of siRNA-mediated gene silencing foundational for the future clinical use of siRNA. Without a proper understanding of the kinetics of the process and the parameters that can affect the resulting gene silencing, application of RNAi will be governed largely by trial and error. The ability to specifically tailor and optimize the treatment for each particular system would save significant time and resources, especially given the high cost of synthetic siRNA molecules and the amount of material required for in vivo studies. Mathematical

modeling using simple kinetic equations for each step in the RNAi process can shed light on many of these questions regarding the kinetic aspects of RNAi. To our knowledge, there are only a few published examples of such studies looking at the kinetics of the intracellular RNAi process (15-18). Of these studies, none has combined the delivery process and the interaction with the RNAi machinery in mammalian cells. Bergstrom and colleagues proposed a unidirectional amplification method in their mathematical model of RNAi-mediated gene silencing (15). Because no RNA-dependent RNA polymerase has yet been found in mammalian cells, they acknowledged that their model did not address the silencing mechanisms observed in mammals. Groenenboom and colleagues recently proposed a mathematical model for RNAi that contained several extensions to the core RNAi pathway, providing for siRNA degradation by RNase as well as primed amplification (16). Their model aimed to explain transgene- or virus-induced gene silencing and avoidance of self-reactivity, but did not consider any steps in the delivery process. Similarly, Raab and Stephanopoulos looked at the dynamics of gene silencing by siRNA given at different doses and at various times relative to plasmid transfection, but did not incorporate siRNA delivery (17). Arciero and colleagues created a mathematical model to investigate tumor-immune evasion and siRNA treatment (18). Although this model provided insights into how siRNA can be used in cancer treatment, it did not examine the delivery process and there were no experimental data from in vitro or in vivo studies. Here, we use bioluminescent imaging and mathematical modeling to investigate the steps of RNAi from siRNA delivery to intracellular function with the aim of enabling the practical application and design of siRNA-based treatment strategies both in vitro and in vivo. Because the imaging is noninvasive and nondestructive, the same set

of cells or animals can be followed for the entire study. These results will complement investigations using more traditional analytical methods to monitor mRNA or protein knockdown and hopefully serve to encourage the rational design of experimental and clinical siRNA-based treatments.

2.3 Materials and methods

2.3.1 *Production of luciferase-expressing cell lines by lentiviral transduction*

Cell lines were incubated with viral supernatant containing SMPU-R-MNCU3-LUC, a lentiviral vector based on HIV-1 that transduces the firefly luciferase gene. The backbone vector SMPU-R has deletions of the enhancers and promoters of the HIV-1 long terminal repeat (SIN), has minimal HIV-1 gag sequences, contains the cPPT/CTS sequence from HIV-1, has three copies of the UES polyadenylation enhancement element from SV40, and has a minimal HIV-1 RRE (gift of Paula Cannon, Children's Hospital Los Angeles, Los Angeles, CA; (19)). The vector has the U3 region from the MND retroviral vector as an internal promoter driving expression of the firefly luciferase gene from SP-LUC+ (Promega, Madison, WI; (20)).

2.3.2 *siRNA duplexes*

All siRNA molecules were ordered purified and pre-annealed ("Option C") from Dharmacon Research, Inc. (Lafayette, CO). siGL3 (sense, 5'-CUUACGCUGAGUACUUCGAdTdT-3'; antisense, 5'-UCGAAGUACUCAGCGUAAGdTdT-3') is an unmodified siRNA duplex that targets the luciferase gene, while siCONTROL non-targeted siRNA #1 (siCON1; sense, 5'-UAGCGACUAAACACAUCAAUU-3'; antisense, 5'-UUGAUGUGUUUAGUCGCUAUU-3') is an unmodified siRNA duplex

bioinformatically designed to minimize the potential for targeting any known human or mouse genes.

2.3.3 In vitro transfections

Cells were seeded in 24-well plates 2-3 days prior to transfection at 2×10^4-1×10^5 cells per well and grown in media supplemented with 10% fetal bovine serum (FBS) and antibiotics (penicillin/streptomycin). siRNA was complexed with Oligofectamine (Invitrogen, Carlsbad, CA) according to manufacturer's instructions and applied to each well in a total volume of 200 μL Opti-MEM I (Invitrogen). Transfection media was removed and replaced with complete media after 5 hours.

2.3.4 Formation of subcutaneous tumors in mice

Luciferase-expressing Neuro2A (Neuro2A-Luc) cells were grown to confluence in media supplemented with 10% FBS and antibiotics (penicillin/streptomycin). Immediately prior to injection, cells were washed with phosphate-buffered saline (PBS), trypsinized, and resuspended in serum-free media at 2×10^6 cells/mL. Each mouse received 0.5 mL of the resulting cell suspension by subcutaneous injection.

2.3.5 Low-pressure tail-vein (LPTV) injection of formulated siRNA nanoparticles

All nanoparticles were made with siRNA and an imidazole-modified CDP (CDP-Im) synthesized as described previously (21,22). Before addition to siRNA, CDP-Im was mixed with an adamantane-PEG$_{5000}$ (AD-PEG) conjugate and an AD-PEG-transferrin (Tf) conjugate such that the total moles of AD-PEG or AD-PEG-Tf equaled the number of moles of β-CD. Tf-targeted nanoparticles contained 1% AD-PEG-Tf relative to AD-PEG. This mixture was added to an equal volume of siRNA at a charge ratio (positive

charges from CDP-Im to negative charges from siRNA backbone) of 3:1 (+:-). An equal volume of 10% (w/v) glucose in water was added to the resulting nanoparticles to yield a 5% (w/v) glucose (D5W) solution suitable for injection. Each mouse was injected with 200 μL of this nanoparticle solution containing 50 μg siRNA per 20-g mouse (2.5 mg/kg siRNA).

2.3.6 High-pressure tail-vein (HPTV) co-injection of plasmid and siRNA

Hydrodynamic, or HPTV, injection of nucleic acids can achieve significant levels of nucleic acid in the hepatocytes of mice (23,24). A. McCaffrey and M. Kay kindly donated a plasmid (pApoEHCRLuc) containing the firefly luciferase gene under the control of the human α_1-antitrypsin promoter and the apolipoprotein E locus control region. For HPTV co-injection studies in BALB/c mice, each 20-g mouse received a 10% w/v injection of a D5W solution containing 0.25 mg/kg of the luciferase-containing plasmid and 2.5 mg/kg siRNA.

2.3.7 Bioluminescent imaging

Cell culture plates or mice containing the luciferase-expressing cells were imaged using the Xenogen IVIS 100 Imaging System (Xenogen, Alameda, CA). D-luciferin (Xenogen) was dissolved in PBS at 15 g/L. For in vitro assays in 24-well plates, 50 μL of the 15 g/L luciferin solution was added to each well containing 1 mL of media. Light emission was measured 2-3 minutes after addition of the luciferin. For in vivo experiments, 0.2 mL of the 15 g/L luciferin solution was injected intraperitoneally 10 minutes before measuring the light emission. Mice were anesthetized with an initial dose of 5% isoflurane followed by a maintenance dose of 2.5% isoflurane. Bioluminescent signal intensities were quantified using Living Image software (Xenogen).

2.3.8   Mathematical model

The model presented here was designed to allow the user to specifically study the

impact of parameter values on gene silencing by RNAi. When designing an siRNA-

based treatment, the main controllable parameters are the delivery method (naked siRNA,

formulated with vector, chemically modified) and dosing schedule. These choices must

be governed by parameters such as the target mRNA half-life, target protein half-life,

threshold for reduction (in either target mRNA or protein), number of target cells, and

desired knockdown duration. The model's design criteria therefore included the ability to

enable user-defined values for these parameters that characterize each experimental

system.

A simplified schematic of the major processes included in the model is shown in

Figure 2.1. Model variables (Table 1) and parameters (Table 2) were used to develop a

set of ordinary differential equations for the steps involved in siRNA delivery to and

function within mammalian cells in vitro and in vivo. The differential equations

governing each major process from the delivery of siRNA to its intracellular interaction

with the RNAi machinery are grouped into modules that can be changed independently to

modify the model complexity as desired.
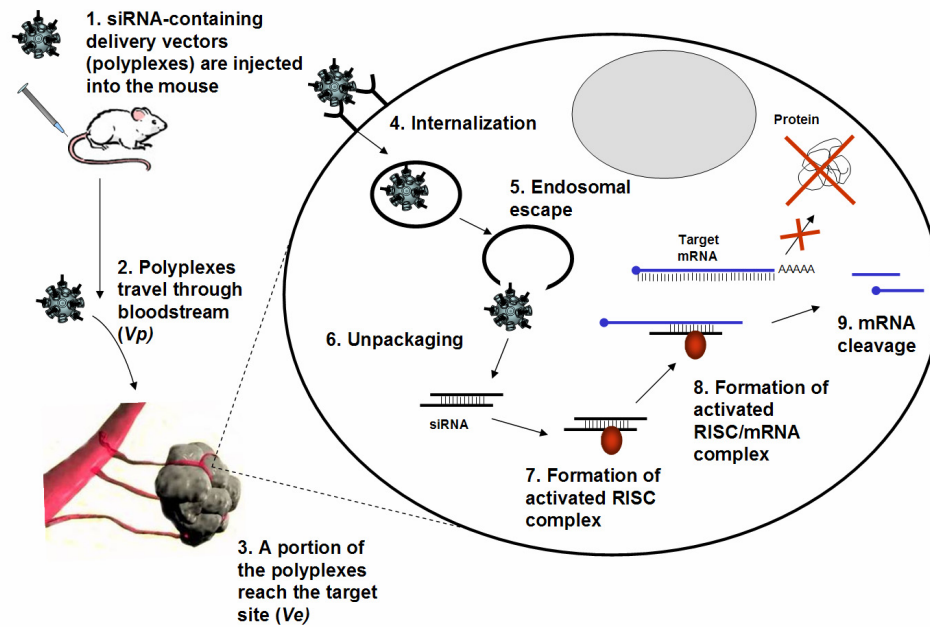
Figure 2.1. Simplified schematic of the key steps required for siRNA delivery to and function within mammalian cells. Steps 1-3 are unique to in vivo application of siRNA, whereas steps 4-9 represent the general processes on the level of an individual cell and are therefore common to both in vivo and in vitro application of siRNA.

Table 2.1. Model variables.

Model Variables		
Name	Model Compartment	Description (units)
Bcf	Plasma	Free complex in circulation (# vol^{-1})
Bcb	Plasma	Bound complex in circulation (# vol^{-1})
Ec	Extracellular	Extracellular complex in local vicinity (# vol^{-1})
Enc	Intracellular	Endosomal complex (# vol^{-1})
$Enna$	Intracellular	Endosomal free siRNA (# vol^{-1})
Cc	Intracellular	Cytoplasmic complex (# vol^{-1})
Cna	Intracellular	Cytoplasmic free siRNA (# vol^{-1})
R	Intracellular	Activated RISC complex (# vol^{-1})
C	Intracellular	Activated RISC complex bound to mRNA (# vol^{-1})
M	Intracellular	Target mRNA (# vol^{-1})
P	Intracellular	Target protein (# vol^{-1})
Z	Intracellular	Number of cells (#)

Table 2.2. Model parameters. For parameters common to both in vitro and in vivo applications, the in vivo parameter values are shown in *italics* below the in vitro parameter values.

Name	Description (units)	Determination	Value
Model Parameters			
max	Maximum # of cells (#)	Determined experimentally	*Fit to each system*
partition	Effective fraction of dose available to target cells	Estimated from experimental data	1×10^{-3}
rtot	Total available amount of RISC protein complexes (# L^{-1})	Literature (25-27)	1.9×10^{15}
Ve	Extracellular volume (L)	Specified experimentally in vitro, Estimated from experimental data and literature (28,29)	2×10^{-4} *1×10^{-5}*
Vi	Intracellular volume (L)	Literature (30)	4×10^{-12}
Vp	Plasma volume, mouse (L)	Literature (31)	1.5×10^{-3}
kbloodbind	Complex binding to blood components (hr^{-1})	Estimated from experimental data	1×10^{-4}
kblooddis	Complex dissociation from blood components (hr^{-1})	Estimated from experimental data	1×10^{-2}
kcleavage	Cleavage of target mRNA by activated RISC complex (hr^{-1})	Literature (27)	7.2
kdegendna	Endosomal siRNA degradation (hr^{-1})	Literature (32-35)	5×10^{-1}
kdeginna	Intracellular siRNA degradation (hr^{-1})	Estimated from experimental data and literature (34)	2.9×10^{-2}
kdegmRNA	Target mRNA degradation (hr^{-1})	Literature (36-39)	2
kdegprot	Target protein degradation, Luciferase (hr^{-1})	Literature (40)	3.5×10^{-1}
kdegRISC	Activated RISC complex degradation (hr^{-1})	Estimated from experimental data	7.7×10^{-2}
kdisRISC	Dissociation of activated RISC complex (hr^{-1})	Chosen to be negligible once activated RISC is formed	1×10^{-9}
kdisRISCm	Dissociation of activated RISC complex and target mRNA (hr^{-1})	Literature (25-27)	1
kelimec	Extracellular complex degradation (hr^{-1})	Estimated from experimental data	8.7×10^{-2} *2.9×10^{-2}*
kelimpl	Plasma complex degradation (hr^{-1})	Estimated from experimental data	5.8×10^{-2}
kescendna	Endosomal escape for siRNA (hr^{-1})	Estimated from experimental data and literature (41)	6×10^{-2}
kescendvec	Endosomal escape for complex (hr^{-1})	Estimated from experimental data and literature (41)	1×10^{-2}
kformmRNA	Formation of target mRNA (# L^{-1} hr^{-1})	Literature (36,37)	5.2×10^{13}
kformprot	Formation of target protein (hr^{-1})	Literature (36,37)	5.2×10^{2}
kformRISC	Formation of activated RISC complex (L $\#^{-1}$ hr^{-1})	Estimated from experimental data	2×10^{-19}
kformRISCm	Formation of activated RISC/mRNA complex (L $\#^{-1}$ hr^{-1})	Literature (25-27)	1.1×10^{-14}
kgrowth	Cell growth rate (hr^{-1})	Determined experimentally	*Fit to each system*
kint	Internalization (hr^{-1})	Literature (12,13,42)	1×10^{-5} *5×10^{-7}*
ktransblood	Transport from plasma to extracellular fluid (hr^{-1})	Estimated from experimental data	1×10^{-2}
kunpackcyt	Cytosolic complex unpackaging (hr^{-1})	Estimated from experimental data	5×10^{-1} *6×10^{-2}*
kunpackend	Endosomal complex unpackaging (hr^{-1})	Estimated from experimental data	1×10^{-4} *1×10^{-3}*

Circulation/Extracellular Transport

$$\frac{dBcf}{dt} = kblooddis \cdot Bcb - kbloodbind \cdot Bcf - ktransblood \cdot partition \cdot Bcf - kelimpl \cdot Bcf$$

$$\frac{dBcb}{dt} = kbloodbind \cdot Bcf - kblooddis \cdot Bcb$$

$$\frac{dEc}{dt} = ktransblood \cdot partition \cdot \frac{Vp}{Ve} \cdot Bcf - kint \cdot Ec \cdot Z - kelimec \cdot Ec$$

Cellular Uptake and Intracellular Trafficking

$$\frac{dEnc}{dt} = kint \cdot \frac{Ve}{Vi} \cdot Ec \cdot - kescendvec \cdot Enc - kunpackend \cdot Enc - dilution \cdot Enc$$

$$\frac{dEnna}{dt} = kunpackend \cdot Enc - kescendna \cdot Enna - kdegendna \cdot Enna - dilution \cdot Enna$$

$$\frac{dCc}{dt} = kescendvec \cdot Enc - kunpackcyt \cdot Cc - dilution \cdot Cc$$

$$\frac{dCna}{dt} = kescendna \cdot Enna + kunpackcyt \cdot Cc + kdisRISC \cdot R - kformRISC \cdot (rtot - R - C) \cdot Cna$$
$$- kdeginna \cdot Cna - dilution \cdot Cna$$

RNAi

$$\frac{dR}{dt} = kformRISC \cdot (rtot - R - C) \cdot Cna + kdisRISCm \cdot C + kcleavage \cdot C - kdisRISC \cdot R$$
$$- kdegRISC \cdot (R + C) - kformRISCm \cdot R \cdot M - dilution \cdot R$$

$$\frac{dC}{dt} = kformRISCm \cdot R \cdot M - kdisRISCm \cdot C - kdegRISC \cdot (R + C) - kcleavage \cdot C - dilution \cdot C$$

$$\frac{dM}{dt} = kformmRNA + kdisRISCm \cdot C - kdegmRNA \cdot M - kformRISCm \cdot R \cdot M$$

Cell Growth and Target Protein Production

$$\frac{dP}{dt} = kformprot \cdot M - kdegprot \cdot P$$

$$\frac{dZ}{dt} = kgrowth \cdot Z \cdot \left(1 - \frac{Z}{max}\right)$$

All of the equations for intracellular siRNA-associated species contain a term to account for dilution due to cell division, where *dilution* is equal to the ratio of new cells divided by the total number of cells. For example, if the number of cells doubles in one

day, then *dilution* would equal 0.5 and the concentration of the intracellular species would likewise be reduced by 50%. For the sake of calculation simplicity, only species involving the delivered siRNA molecules are diluted by this factor; all other intracellular species (i.e., target mRNA and target protein) are assumed to not change after cell division because they are produced intracellularly by both of the daughter cells. The net effect of this is that the siRNA-associated species are diluted equally between the two daughter cells after each cell division.

The set of ODEs was solved with MATLAB (The MathWorks, Inc., Natick, MA) using the stiff ODE15s solver. The ODE15s solver is a variable-order solver based on the numerical differentiation formulas. Parametric sensitivity analysis was performed using SENS_SYS written by V. M. Garcia Molla. This MATLAB routine is an extension to the ODE15s solver that calculates the derivatives of the solution with respect to the parameters.

2.4   Results

In vitro and in vivo experiments were conducted to gain insights into the general kinetics of siRNA-mediated gene silencing in cell lines that constitutively express the luciferase gene. Constitutively expressed genes, in contrast to genes expressed transiently by plasmids, provide a more realistic model for clinical application in which an endogenous gene, such as an oncogene, is the target for a therapeutic siRNA. The Xenogen IVIS 100 Imaging System allowed us to monitor luciferase activity in luciferase-expressing cells growing in 24-well plates or present in subcutaneous tumors or livers in live mice; because the imaging was noninvasive, luciferase activity was measured in the same plate of cells or the same animals over the entire duration of the

study. Monitoring the kinetics of siRNA-mediated gene silencing in the same population of cells helps to avoid variability introduced when using different cell populations for each time point as required in luminometer-based luciferase detection or flow cytometry (for fluorescent reporters). Additionally, firefly luciferase has a short half-life of approximately 2 hours, so that its level should change concomitantly with the level of mRNA (40,43). This enables the use of bioluminescent imaging of luciferase protein activity as an indicator of mRNA transcript degradation by the delivered siRNA molecules.

2.4.1 *Effect of siRNA dose on luciferase knockdown in vitro*

The amount of siRNA applied to the extracellular media has a significant impact on the magnitude of the gene silencing but a minimal impact on the overall duration (Figure 2.2A). Using the baseline parameters given in Table 2, the mathematical model predicts the trends observed experimentally (Figure 2.2B). Similar trends are observed with these siRNA doses in other luciferase-expressing cell lines (data not shown).
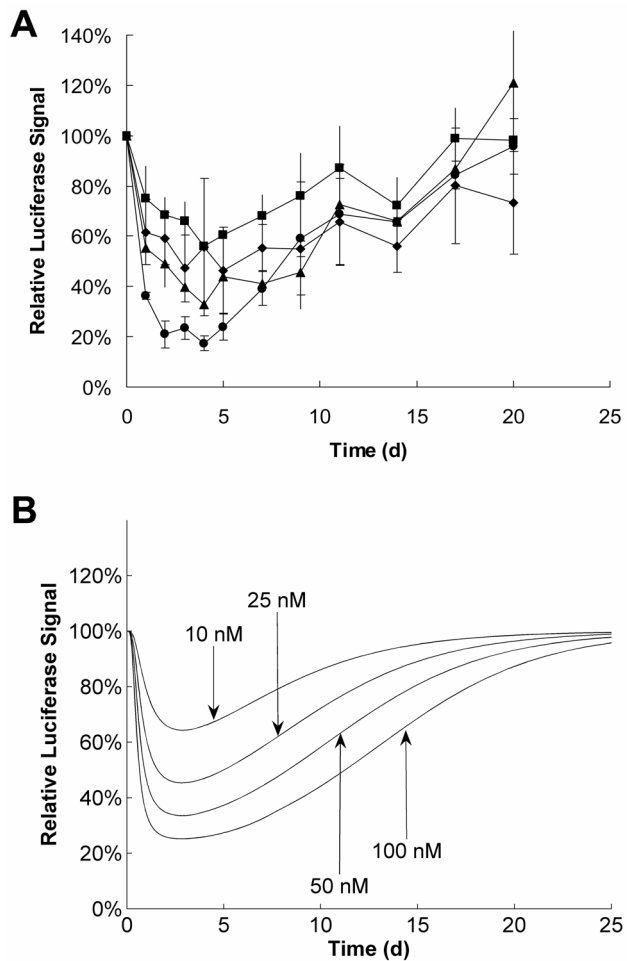
Figure 2.2. Effect of siRNA dose on the duration and magnitude of luciferase knockdown by siRNA in nondividing cells. (A) Experimental results using Oligofectamine to deliver siRNA to luciferase-expressing, nondividing fibroblasts with 1.5×10^5 cells per well in a 24-well plate. Data points represent the ratio of the average luciferase signal intensity from triplicate wells receiving siGL3 and siCON1 on day 0. Squares = 10 nM, Diamonds = 25 nM, Triangles = 50 nM, Circles = 100 nM. (B) Luciferase knockdown after siRNA transfection predicted by the mathematical model using the baseline in vitro parameters given in Table 2.2 with the number of cells held constant at 1.5×10^5, a transfection time of 5 hours, and a transfection efficiency of 90%.

2.4.2 *Effect of cell doubling time on luciferase knockdown in vitro*

The majority of studies examining the kinetics of siRNA-mediated gene silencing

in vitro have used rapidly dividing cell lines that typically have doubling times of ~1 day.

Using these cell lines, the silencing effect generally lasts for ~1 week (44,45). To

investigate whether this duration of silencing is intrinsic to siRNA or a result of dilution

due to cell division, siRNA-mediated gene silencing was monitored in four luciferase-

expressing cell lines with different observed doubling times: Neuro2A-Luc (0.8 days), LNCaP-Luc (1.4 days), HeLa-Luc (1.6 days), and CCD-1074Sk-Luc (nondividing). The cells were plated in 24-well plates and transfected under identical conditions to enable direct observation of the effect of cell doubling time alone. The experimental results in Figure 2.3A reveal that the dilution effect from cell division can alter the duration of gene silencing. Consistent with previous observations, the duration of gene silencing in rapidly growing cell lines is ~1 week; however, cell lines with slower doubling times show a corresponding increase in the duration of silencing. Figure 2.3B shows the predicted effect of cell doubling time when the experimental transfection parameters are input into the mathematical model. The model predictions confirm that the dilution effect due to cell doubling time alone can account for the decreased duration of gene silencing in dividing cells. It is interesting to note that the duration of gene silencing in nondividing cells is ~3 weeks. This duration is consistent with the kinetics observed in two previous reports looking at siRNA-mediated gene silencing in nondividing mammalian neurons and primary macrophages (46,47). In nondividing cells, the duration of gene silencing is not controlled by dilution from cell division but by the intrinsic stability of siRNA within the cell.
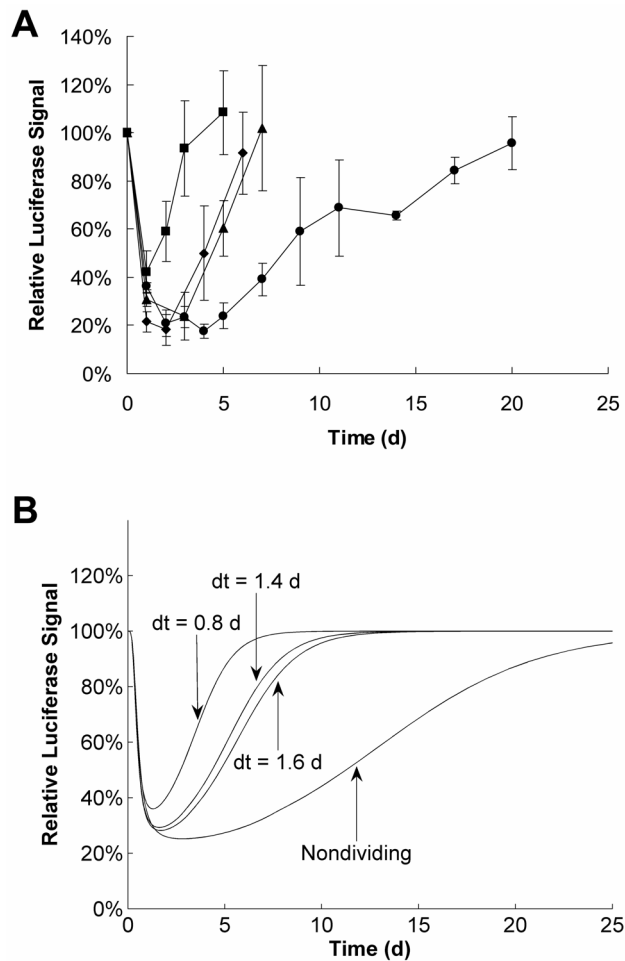
Figure 2.3. Effect of cell doubling time on the duration of luciferase knockdown by siRNA in vitro. (A) Experimental results using Oligofectamine to deliver 100 nM siRNA to luciferase-expressing cells with a range of doubling times (dt). Data points represent the ratio of the average luciferase signal intensity from triplicate wells receiving siGL3 and siCON1 on day 0. Squares = Neuro2A-Luc (dt = 0.8 d), Diamonds = LNCaP-Luc (dt = 1.4 d), Triangles = HeLa-Luc (dt = 1.6 d), Circles = CCD-1074Sk-Luc (nondividing). (B) Luciferase knockdown after siRNA transfection predicted by the mathematical model using the baseline in vitro parameters given in Table 2.2 with the initial number of dividing and nondividing cells equal to 5×10^4 and 1.5×10^5, respectively, a transfection time of 5 hours, and a transfection efficiency of 90%.

2.4.3 Kinetics of luciferase knockdown by siRNA in subcutaneous tumors

Many tumors exhibit rapid growth with doubling times on the order of only a few days, and the duration of gene silencing should be limited by this rapid cell division. To test this hypothesis, subcutaneous tumors were created in A/J mice using luciferase-expressing Neuro2A-Luc cells. Since the goal was to observe the kinetics of gene silencing and not an actual therapeutic effect on the growth rate of the cells, siRNA

against the luciferase gene (siGL3) and a control siRNA (siCON1) were used to show the

sequence-specificity of the luciferase knockdown. Each mouse received three

consecutive daily LPTV injections of transferrin-targeted nanoparticles containing 2.5

mg/kg siRNA. After quantifying the luciferase activity in each tumor using the Xenogen

camera, data were used to create a predicted logistic growth curve (Figure 2.4A).

Because the siRNA targets only the luciferase gene, the growth rate of the cells should be

unaffected; as a result, a decrease in luciferase signal intensity indicates a change in the

luciferase protein level. Normalization to predicted growth curves allowed estimation of

the knockdown resulting from siRNA treatment (Figure 2.4B). By adjusting only the

parameters for the circulation/extracellular transport of the siRNA nanoparticles, very

good agreement was obtained between the model's predictions and the experimental data.

The observed knockdown duration after three consecutive injections was around 10 days,

consistent with the in vitro data for cell lines with similar observed growth rates.
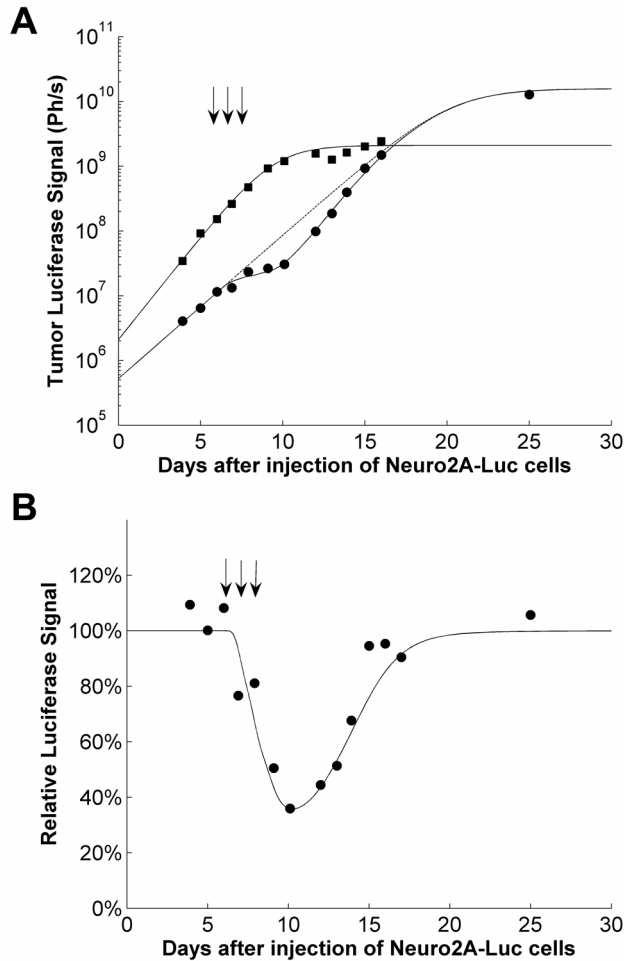
Figure 2.4. Kinetics of luciferase knockdown by siRNA in Neuro2A-Luc subcutaneous tumors in A/J mice. **(A)** Experimental and predicted results for luciferase knockdown after three consecutive LPTV injections on days 6, 7, and 8 of transferrin-targeted CDP-Im nanoparticles containing 50 μg siRNA per 20-g mouse. Experimental data points are shown for a mouse receiving siCON1 (squares) and a mouse receiving siGL3 (circles). Solid lines represent the predicted luciferase signal with siRNA treatment and dashed lines represent the predicted luciferase signal in the absence of siRNA treatment. (B) Normalization of the observed luciferase signal in the siGL3-treated mouse to the predicted luciferase signal in the absence of treatment. Circles indicate the normalized experimental data points, while the solid line represents the response predicted by the mathematical model using the baseline in vivo parameters given in Table 2.2 and assuming that 50% of the total cells are reached with each dose.

2.4.4   Kinetics of luciferase knockdown by siRNA in hepatocytes

While cells in subcutaneous tumors are dividing rapidly (e.g., once per day), most

of the hepatocytes in a normal mouse liver are in a state of growth arrest (48). Therefore,

it was hypothesized that gene silencing by siRNA would exhibit different kinetics in

hepatocytes versus tumors. Each BALB/c mouse received a single HPTV injection of

0.25 mg/kg plasmid and 2.5 mg/kg siGL3 on day 0, and the Xenogen camera was used to

follow the luciferase signal in each mouse liver. Normalization to the signal intensity in

mice that received plasmid only (no siRNA) allowed quantification of the percent

knockdown by siRNA. Figure 2.5 shows the experimental data together with the model

predictions. Similar to the in vitro results for gene silencing in nondividing cells, the

duration of gene silencing lasts for ~3-4 weeks in the hepatocytes after a single dose of

siRNA.
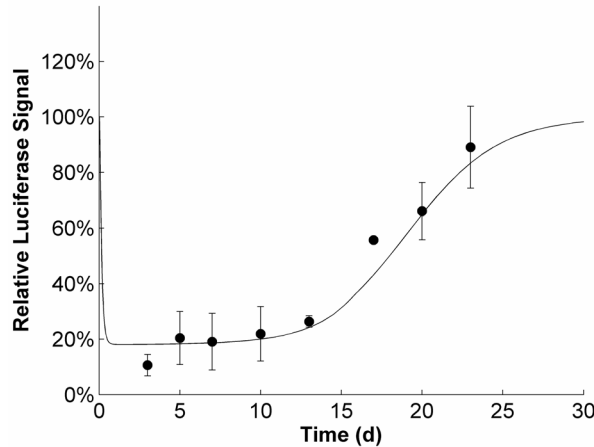
Figure 2.5. Kinetics of luciferase knockdown by siRNA in nondividing hepatocytes in BALB/c mice. Experimental and predicted results are shown for luciferase knockdown after hydrodynamic tail-vein co-injection of 5 μg pApoEHCRLuc and 50 μg siRNA per 20-g mouse on day 0. Circles represent the ratio of the average luciferase signal intensity from three mice receiving plasmid + siRNA to the luciferase signal intensity from three mice receiving plasmid alone. The predicted luciferase knockdown, given by the solid line, was calculated using the baseline in vivo parameters given in Table 2.2 with the following modifications to account for hydrodynamic injection of naked siRNA without a delivery vehicle: eliminate steps involving the nanoparticles (*kescendvec*, *kunpackend*, *kunpackcyt*), modify uptake and intracellular trafficking to match observed kinetics (*partition* = 1×10^{-2}, *ktransblood* = 1, *kint* = 1×10^{-3} hr^{-1}, *kescendna* = 1×10^{-2} hr^{-1}, *kdegendna* = 5×10^{-3} hr^{-1}), and modify extracellular volume (*Ve* = 1.5×10^{-5} L). The *kescendna* and *kdegendna* may no longer represent endosomal processes as hydrodynamically injected naked siRNA may be internalized through different vesicles or partitioned into a separate intracellular compartment (e.g., nucleus) that exhibits different degradation and release kinetics than in standard or receptor-mediated endocytosis of siRNA-containing nanoparticles. The total number of hepatocytes was chosen to be 5×10^7, on the same order of magnitude as the number of hepatocytes in a mouse liver (49,50).

2.4.5   *Effect of siRNA stability on luciferase knockdown by siRNA*

Because both double-stranded and single-stranded nucleic acids are rapidly

degraded in serum, current efforts in the field of nucleic-acid based therapeutics seek to

enhance the stability of the nucleic acids with the goal of increasing the duration of gene

silencing by boosting their bioavailability and possibly prolonging their persistence

intracellularly (32-34). Layzer and colleagues studied the kinetics of gene silencing in

HeLa cells using 2'-F-modified siRNA and unmodified 2'-OH siRNA. Although the 2'-

F-modified siRNA led to a significant increase in serum stability, it appeared to have no

effect on the duration of gene silencing after transfection. This suggests that the

intracellular stability of siRNA molecules is not the limiting factor controlling the

duration of gene silencing in rapidly dividing cells; instead, dilution due to cell division

limits how long gene silencing can occur under these conditions. If the intracellular half-

life of siRNA molecules is already around 24 hours, then even modifications to increase

the half-life to >72 hours have an insignificant effect on the duration of gene silencing

(Figure 2.6). These model predictions corroborate the experimental results obtained by

Layzer and colleagues (34). On the other hand, the outcome of using modified siRNA

may be different in slowly dividing or nondividing cells since the intracellular siRNA

half-life will be shorter than the cell doubling time, meaning dilution due to cell division

will no longer be the dominant factor. Increasing the persistence of siRNA within the

cell might prolong the duration of gene silencing. Results from such studies in

nondividing cells should be interpreted carefully since the apparent intracellular stability

of siRNA molecules may be caused by association with other intracellular components or

localization to specific compartments, both of which could lead to degradation kinetics

independent of the properties of the siRNA molecules alone. In that case, modified

siRNA would not necessarily increase the duration of gene silencing relative to unmodified siRNA even in nondividing cells.
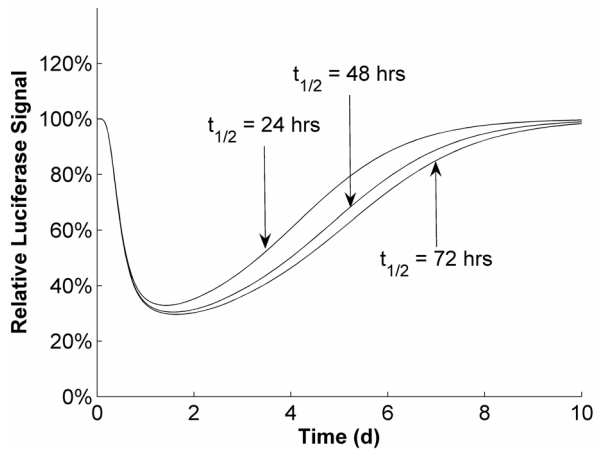
Figure 2.6. Effect of intracellular siRNA half-life on the duration of siRNA-mediated gene silencing in vitro. Curves represent model predictions for luciferase knockdown after transfection with 100 nM siRNA against luciferase on day 0 with a cell doubling time of 1 day (*kgrowth* = 0.0.029 hr^{-1}) and intracellular siRNA half-lives of 24, 48, and 72 hours (*kdeginna* = 0.029, 0.014, and 0.01 hr^{-1}). The initial number of cells was 5x10^4, transfection time was 5 hours, transfection efficiency was 90%, and all other parameters were kept at their baseline in vitro values given in Table 2.2.

2.4.6   Multiple doses to prolong luciferase knockdown by siRNA in nondividing cells

The previous studies have looked at the transient knockdown of the luciferase reporter gene by 1-3 injections of siRNA over a short-term period; even in nondividing cells, the maximum duration of silencing using typical siRNA doses is ~3-4 weeks. However, a clinically relevant treatment regimen using siRNA may require that a gene be silenced for a prolonged period of time. Some have attempted to solve this problem by using lentiviral delivery of expressed short-hairpin siRNAs (shRNA) to achieve sustained gene silencing in vitro and in vivo (51,52). Precise control of the intracellular level of siRNA and having a means to turn off its production when treatment is no longer necessary represent two major challenges to this use of shRNA. On the other hand, the intrinsically transient nature of siRNAs makes them more amenable to disease treatments

in which the treatment is given over a period of time and then stopped once the desired

therapeutic outcome (e.g., regression of a tumor or inhibition of viral growth) is achieved.

To illustrate how properly timed doses of siRNA can prolong gene silencing by siRNA,

nondividing CCD-1074Sk-Luc cells were transfected with a second dose of siRNA four

days after the initial dose (Figure 2.7A). With a second dose of 100 nM siRNA, the

luciferase protein levels remained at <40% of the steady-state value for an additional four

days. If the trends continue in such a fashion, a 100-nM dose every four days could lead

to persistent gene silencing as shown by model calculations in Figure 2.7B.
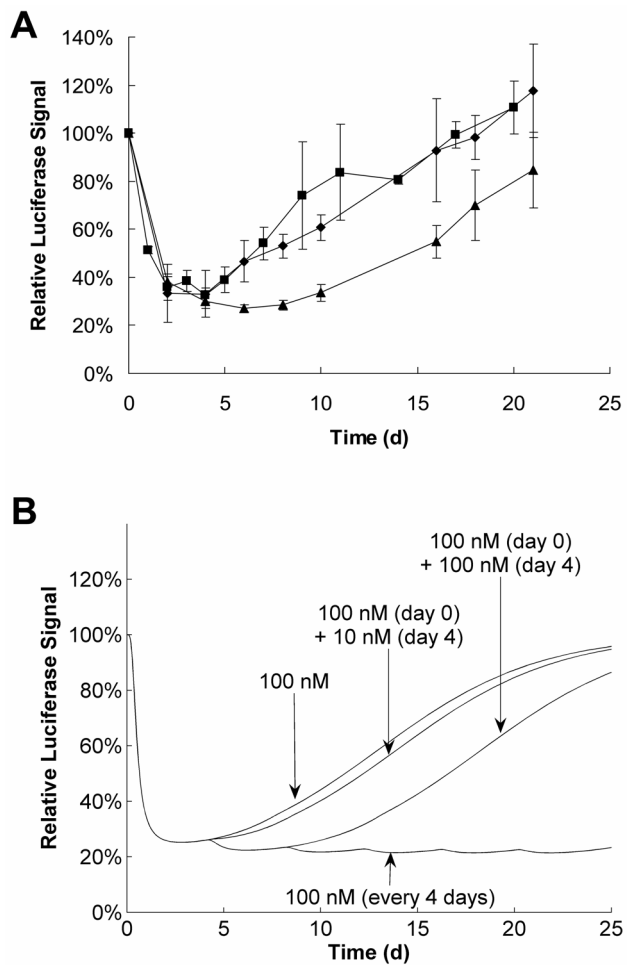
Figure 2.7. Effect of siRNA dose frequency on the duration of luciferase knockdown by siRNA in
nondividing cells. (A) Experimental results using Oligofectamine to deliver siRNA to luciferase-
expressing nondividing fibroblasts in vitro. Data points represent the ratio of the average luciferase signal
intensity from triplicate wells receiving siGL3 and siCON1. To facilitate comparison of the knockdown

kinetics, the data points are normalized such that all three curves exhibit the same magnitude of knockdown for the first four days since all three received the same treatment over this period. This normalization permits comparison of the kinetics of gene silencing observed with different treatments even though the absolute magnitude of the knockdown varied slightly in each experiment. Squares = 100 nM (day 0), Diamonds = 100 nM (day 0) + 10 nM (day 4), Triangles = 100 nM (day 0) + 100 nM (day 4). (B) Luciferase knockdown after siRNA transfection predicted by the mathematical model using the baseline in vitro parameters given in Table 2.2 with the number of cells equal to 1.5×10^5, a transfection time of 5 hours, and a transfection efficiency of 90%.

2.4.7   *Considerations for siRNA-based treatments that require a threshold knockdown for efficacy*

Because siRNA treatment of rapidly dividing cells requires treating more cells over time while also having to deal with dilution effects, the amount of target gene or protein knockdown will be less than that observed in slowly dividing or nondividing cells. More frequent dosing is required to overcome these barriers. Cancer is one example of a disease often characterized by rapid cell division that may require target gene knockdown lasting longer than that which can be achieved with a single dose of siRNA. To address this situation, the mathematical model was used to estimate siRNA dosing schedules needed to maintain a given gene below a threshold value for an extended period of time in dividing cells. While the magnitude of target gene (or protein) reduction or the duration of knockdown relative to the steady-state value in the absence of treatment can be relatively good indicators of the success of an siRNA treatment, the therapeutic efficacy of an siRNA treatment regimen should perhaps be judged by the length of time it is able to maintain the target gene or protein level below a given threshold. Although a short, substantial knockdown of certain targets may be sufficient to trigger a cascade of downstream effects, other situations may require considerably longer knockdown to achieve the desired therapeutic effect. Additionally, this

therapeutic effect may only be seen when the target protein is reduced below a threshold, or some fraction of its pre-treatment value.

The data in Figure 2.8 show how the mathematical model can be used to simulate the effects of cell doubling time and target protein half-life during treatment with siRNA. To avoid unnecessary complications, the calculations ignore the circulation/extracellular transport and consider each siRNA dose already in the local extracellular environment of the cells (analogous to the in vitro situation). Figures 2.8A-D give results that demonstrate how target protein half-life can impact the observed dynamics of protein knockdown with once- or twice-weekly dosing in rapidly dividing or nondividing cells. For a target protein with a short half-life in rapidly dividing cells, even twice-weekly dosing still can result in significant oscillations which may hinder the ability to cause a phenotypic change in the target cells (Figure 2.8A). If the target protein has a long half-life, then twice-weekly dosing is able to maintain steady knockdown at ~50% of the steady-state level, but this magnitude of protein knockdown is not achieved until about a week after the first dose of siRNA (Figure 2.8B). In nondividing cells, once-weekly dosing is adequate to maintain persistent silencing at ~20% of the steady-state value (Figures 2.8C-D). Again, this protein knockdown can only be achieved after more than a week from the initial siRNA dose if the target protein half-life is very long (Figure 2.8D). The fraction of the total treatment time during which a target protein is below a threshold (e.g., 50% steady-state value) can be used as a metric to compare the efficacy of different treatment regimens. The data illustrated in Figure 2.8E reveal how cell growth rate and target protein half-life can affect protein knockdown when siRNA is administered once on day 0, once-weekly, or twice-weekly over the 25-day treatment. As expected, cell

growth rate has a large impact on the duration of knockdown, directly affecting the fraction of the total time that the target protein level can be reduced below the threshold of 50%.
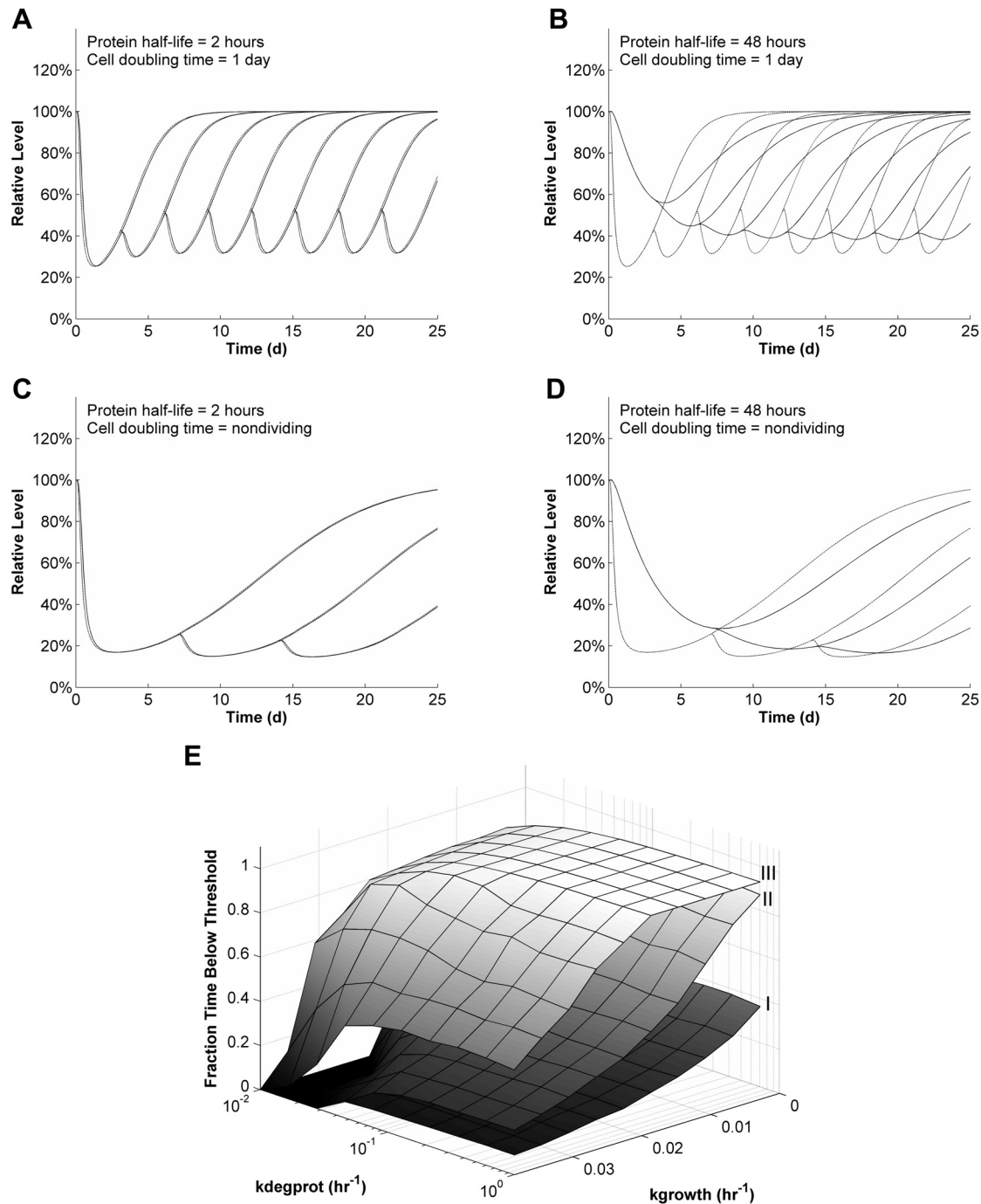
Figure 2.8. Effect of cell doubling time and target protein half-life on the ability to maintain persistent gene silencing. All plots represent predicted mRNA (dashed lines) and protein (solid lines) knockdown in

transfected cells using the baseline in vitro parameters given in Table 2.2, a transfection time of 5 hours, and an initial number of dividing and nondividing cells equal to 5×10^4 and 1.5×10^5, respectively. (A) Dose of 100 nM siRNA every 3 days with a target protein half-life of 2 hours (*kdegprot* = 0.35 hr^{-1}) in cells with a doubling time of 1 day (*kgrowth* = 0.029 hr^{-1}). (B) Dose of 100 nM siRNA every 3 days with a target protein half-life of 48 hours (*kdegprot* = 0.014 hr^{-1}) in cells with a doubling time of 1 day (*kgrowth* = 0.029 hr^{-1}). (C) Dose of 100 nM siRNA every 7 days with a target protein half-life of 2 hours (*kdegprot* = 0.35 hr^{-1}) in nondividing cells. (D) Dose of 100 nM siRNA every 7 days with a target protein half-life of 48 hours (*kdegprot* = 0.014 hr^{-1}) in nondividing cells. (E) Effect of variations in cell doubling time and target protein half-life on the ability to maintain a target protein level below a threshold of 50% its pre-treatment value over the 25-day period. I = 100 nM (day 0), II = 100 nM (days 0, 7, 14), III = 100 nM (days 0, 3, 7, 10, 14, 17, 21, 24).   Surface vertices represent the fraction of the total time during which the relative protein level is below the 50% threshold.

2.5   Discussion

A more thorough understanding of the factors affecting the kinetics of siRNA-mediated gene silencing should prove to be invaluable for experimental and clinical applications of siRNA.   Given the relatively recent discovery of RNAi, details of its action are still being elucidated, and many of the current siRNA dosing schedules used in literature are based on precedence rather than being optimized for each system. The high cost of siRNA molecules, especially for in vivo studies, limits systematic exploration of the parameter space needed to achieve the most effective siRNA dosing schedule for each model system. This situation can be partially rectified by using mathematical modeling to give insights that help direct experimental studies. Here, we employed bioluminescent imaging and mathematical modeling to investigate the effects of target-specific and treatment-specific parameters on siRNA-mediated gene silencing in vitro and in vivo.

The experimental data presented here show the effects of cell doubling time, siRNA dosing schedule, and siRNA delivery method on luciferase reporter-protein knockdown and aid in developing mathematical models of siRNA delivery to and function within mammalian cells. Luciferase knockdown in cell lines engineered to constitutively express luciferase was used to mimic the knockdown of an endogenously

expressed gene, analogous to an oncogene whose presence in a cell can lead to tumorigenicity. The luciferase-expressing cell lines were used in cell culture experiments or injected into mice and then monitored for luciferase expression using noninvasive bioluminescent imaging with the Xenogen Imaging System. The duration of gene silencing lasted for ~1 week in rapidly dividing cells but longer than three weeks in nondividing cells both in vitro and in vivo, supporting the hypothesis that dilution due to cell division is the major factor controlling the duration of luciferase knockdown in rapidly dividing cells.

The duration of gene silencing by siRNA can be longer than that achieved with other nucleic-acid based gene inhibition strategies, such as antisense, whose knockdown typically lasts only on the order of 1-2 days. Bertrand and colleagues studied antisense- and siRNA-mediated inhibition of GFP in HeLa cells and showed that while antisense-mediated inhibition diminished after only 1 day, the siRNA-mediated inhibition was still increasing (32). This significant difference in the duration of gene silencing could become important when trying to use either antisense or siRNA molecules as therapeutic agents. In fact, the short duration of gene silencing by certain nucleic-acid based gene inhibition strategies could preclude their ability to alter cellular behavior if the target gene is not silenced for an adequate amount of time. This would be particularly apparent if the target protein has a long intracellular half-life; then, knockdown of the target mRNA may not result in target protein knockdown if the mRNA levels can be restored before a significant amount of protein has degraded.

The findings presented here highlight several key considerations for experimental design when evaluating the efficacy of siRNA against certain genes that produce proteins

with long half-lives. If the knockdown phenotype does not become apparent until the protein is below a certain threshold, then observation at early time points may not reveal any effect. This is crucial for in vitro studies aimed at testing the ability of a therapeutic siRNA to induce apoptosis or growth arrest in certain cell lines. Common practice is to look at time points within 48 to 72 hours; here, model predictions suggest that these time points may be too early if the target protein half-life is any longer than a couple of days. Similar considerations should be made when deciding dosing schedules for in vivo studies using siRNA for protein knockdown in tumors (e.g., an oncogenic fusion protein), since proteins with longer half-lives will show a slower initial response to the therapy but will require less frequent dosing for persistent silencing. An important area for future research will be to determine to what extent a gene or protein needs to be knocked down before the intended therapeutic effect is realized. Such information can be combined with mathematical models like the one presented here to more accurately determine the required treatment regimen needed to achieve efficacy. Although the model in its current form does not allow for treatment effects other than target gene knockdown, the simple addition of a death parameter to the cell growth equation could provide a target cell death rate that depends on the reduction of the target protein level below a certain threshold. Other slightly more complicated modifications to the current set of equations could incorporate recruitment of immune effector cells, effects on angiogenesis, or even sensitization to other treatments including chemotherapy.

While the mathematical model can predict many of the trends observed experimentally for the systems used here, confidence in the actual magnitude and duration of the predicted gene silencing in hypothetical situations can still be greatly

increased as more accurate parameter values become available. Parametric sensitivity

analysis was performed using the SENS_SYS modification of the ODE15s solver in

MATLAB. Parameters governing RISC formation (*kformRISC*) and binding to target

mRNA (*kformRISCm*) have a significant impact on target mRNA or protein levels.

Although studies of the RISC complex are rapidly elucidating details of its mechanism

and kinetics, these parameters will need to be refined as more data become available.

Additional equations will be needed to model a multi-step RISC formation process, or the

lumped rate constants currently used can be modified to provide reasonable estimates of

the overall kinetics. As expected, target mRNA and protein levels are also sensitive to

parameters governing the siRNA delivery process, such as cellular uptake, endosomal

escape, and vector unpackaging. It will be important to determine these parameters for

each individual delivery vehicle since such rates will vary from system to system. With

knowledge of these different parameters, the model can be used to mimic delivery by a

variety of methods including naked siRNA (by high-pressure or low-pressure tail-vein

injection) or formulation into liposomes, lipoplexes, or polyplexes. Such comparisons

may reveal how the characteristics of each delivery method specifically affect the kinetics

of gene silencing. This information may help to focus design improvements for delivery

vehicles or improve the efficacy of treatment regimens employing them, as suggested in

general for gene delivery by Varga and colleagues (53). Of the parameters intrinsic to the

target cells, the most important are the cell growth rate (dilution effect), compartment

volumes (that control the concentration of siRNA available to drive uptake or association

processes), and the stability of the target mRNA and protein molecules. The current set

of model equations predicts that the stability of the mRNA transcript has a greater effect

on the magnitude and duration of gene silencing than the absolute transcript number. This is because the relative knockdown is controlled largely by the relative sizes of the two mRNA degradation terms: natural turnover within the cell and degradation by RNAi. Therefore, the contribution from RNAi leads to greater deviation from the steady-state mRNA level for more stable mRNA molecules. Similar reasoning can be applied to other gene inhibition strategies, such as antisense, that act at the mRNA level (54).

Based on these findings and the literature to date, siRNA appears to be the most potent and effective nucleic acid-based therapeutic aimed at post-transcriptional gene silencing. The siRNA molecules can achieve >80% target protein inhibition at nanomolar concentrations, and their enhanced intracellular stability enables knockdown that can last for weeks in nondividing cells. It is shown here that an optimized siRNA-based treatment schedule can be designed to achieve prolonged gene silencing by properly timed injections of siRNA. Mathematical modeling can help to realize these optimized treatments at a fraction of the time and cost that would be required by experimentation alone. Although there is no substitute for experimental data, especially for highly variable and not completely definable biological systems, model calculations can help to guide effective experimental design and aid in data interpretation. With the burgeoning interest in nucleic acid-based therapeutics such as siRNA, development of mathematical models such as the one presented here may expedite their translation into clinically relevant therapeutics for disease treatment and management.

2.6 Acknowledgments

2.7 References

1.	Fire, A., Xu, S., Montgomery, M.K., Kostas, S.A., Driver, S.E. and Mello, C.C. (1998) Potent and specific genetic interference by double-stranded RNA in Caenorhabditis elegans. *Nature*, **391,** 806-811.

2.	Medema, R.H. (2004) Optimizing RNA interference for application in mammalian cells. *Biochem J*, **380,** 593-603.

3.	Mittal, V. (2004) Improving the efficiency of RNA interference in mammals. *Nat Rev Genet*, **5,** 355-365.

4.	Sioud, M. (2005) On the delivery of small interfering RNAs into mammalian cells. *Expert Opin Drug Deliv*, **2,** 639-651.

5.	Ryther, R., Flynt, A., Phillips III, J. and Patton, J. (2005) siRNA therapeutics: big potential from small RNAs. *Gene Ther*, **12,** 5-11.

6.	Hannon, G.J. and Rossi, J.J. (2004) Unlocking the potential of the human genome with RNA interference. *Nature*, **431,** 371-378.

7.	Dorsett, Y. and Tuschl, T. (2004) siRNAs: applications in functional genomics and potential as therapeutics. *Nat Rev Drug Discov*, **3,** 318-329.

8.	Caplen, N.J. and Mousses, S. (2003) Short interfering RNA (siRNA)-mediated RNA interference (RNAi) in human cells. *Ann N Y Acad Sci*, **1002,** 56-62.

9.	Elbashir, S.M., Harborth, J., Lendeckel, W., Yalcin, A., Weber, K. and Tuschl, T. (2001) Duplexes of 21-nucleotide RNAs mediate RNA interference in cultured mammalian cells. *Nature*, **411,** 494-498.

10.	Scherer, L.J. and Rossi, J.J. (2003) Approaches for the sequence-specific knockdown of mRNA. *Nature Biotechnology*, **21,** 1457-1465.

11.	Stark, G.R., Kerr, I.M., Williams, B.R.G., Silverman, R.H. and Schreiber, R.D. (1998) How cells respond to interferons. *Annu Rev Biochem*, **67,** 227-264.

12.	Overhoff, M., Wunsche, W. and Sczakiel, G. (2004) Quantitative detection of siRNA and single-stranded oligonucleotides: relationship between uptake and biological activity of siRNA. *Nucleic Acids Res*, **32,** e170.

13.	Lingor, P., Michel, U., Scholl, U., Bahr, M. and Kugler, S. (2004) Transfection of "naked" siRNA results in endosomal uptake and metabolic impairment in cultured neurons. *Biochem Biophys Res Commun*, **315,** 1126-1133.

14.	Hu-Lieskovan, S., Heidel, J.D., Bartlett, D.W., Davis, M.E. and Triche, T.J. (2005) Sequence-specific knockdown of EWS-FLI1 by targeted, nonviral delivery of small interfering RNA inhibits tumor growth in a murine model of Ewing's sarcoma. *Cancer Res*, **65,** 8984-8992.

15.	Bergstrom, C.T., McKittrick, E. and Antia, R. (2003) Mathematical models of RNA silencing: Unidirectional amplification limits accidental self-directed reactions. *Proc Natl Acad Sci U S A*, **100,** 11511-11516.

16.	Groenenboom, M.A.C., Maree, A.F.M. and Hogeweg, P. (2005) The RNA silencing pathway: the bits and pieces that matter. *PLoS Comput Biol*, **1,** 155-165.

17.	Raab, R.M. and Stephanopoulos, G. (2004) Dynamics of gene silencing by RNA interference. *Biotechnol Bioeng*, **88,** 121-132.

18.	Arciero, J.C., Jackson, T.L. and Kirschner, D.E. (2004) A mathematical model of tumor-immune evasion and siRNA treatment. *Discret Contin Dyn S*, **4,** 39-58.

19. Bahner, I., Kearns, K., Hao, Q., Smogorzewska, E. and Kohn, D. (1996) Transduction of human CD34+ hematopoietic progenitor cells by a retroviral vector expressing an RRE decoy inhibits human immunodeficiency virus type 1 replication in myelomonocytic cells produced in long-term culture. *J Virol*, **70,** 4352-4360.

20. Challita, P.-M., Skelton, D., El-Khoueiry, A., Yu, X.-J., Weinberg, K. and Kohn, D.B. (1995) Multiple modifications in cis elements of the long terminal repeat of retroviral vectors lead to increased expression and decreased DNA methylation in embryonic carcinoma cells. *J Virol*, **69,** 748-755.

21. Davis, M.E., Pun, S.H., Bellocq, N.C., Reineke, T.M., Popielarski, S.R., Mishra, S. and Heidel, J.D. (2004) Self-assembling nucleic acid delivery vehicles via linear, water-soluble cyclodextrin-containing polymers. *Curr Med Chem*, **11,** 1241-1253.

22. Pun, S.H. and Davis, M.E. (2002) Development of a nonviral gene delivery vehicle for systemic application. *Bioconjug Chem*, **13,** 630-639.

23. Kobayashi, N., Nishikawa, M., Hirata, K. and Takakura, Y. (2004) Hydrodynamics-based procedure involves transient hyperpermeability in the hepatic cellular membrane: implication of a nonspecific process in efficient intracellular gene delivery. *J Gene Med*, **6,** 584-592.

24. Andrianaivo, F., Lecocq, M., Wattiaux-De Coninck, S., Wattiaux, R. and Jadot, M. (2004) Hydrodynamics-based transfection of the liver: entrance into hepatocytes of DNA that causes expression takes place very early after injection. *J Gene Med*, **6,** 877-883.

25. Martinez, J. and Tuschl, T. (2004) RISC is a 5' phosphomonoester-producing RNA endonuclease. *Genes Dev*, **18,** 975-980.

26. Haley, B. and Zamore, P.D. (2004) Kinetic analysis of the RNAi enzyme complex. *Nat Struct Mol Biol*, **11,** 599-606.

27. Brown, K.M., Chu, C.-y. and Rana, T.M. (2005) Target accessibility dictates the potency of human RISC. *Nat Struct Mol Biol*, **12,** 469-470.

28. Krol, A., Maresca, J., Dewhirst, M.W. and Yuan, F. (1999) Available volume fraction of macromolecules in the extravascular space of a fibrosarcoma: implications for drug delivery. *Cancer Res*, **59,** 4136-4141.

29. Pathak, A.P., Artemov, D., Ward, B.D., Jackson, D.G., Neeman, M. and Bhujwalla, Z.M. (2005) Characterizing extravascular fluid transport of macromolecules in the tumor interstitium by magnetic resonance imaging. *Cancer Res*, **65,** 1425-1432.

30. Chiu, D.T. and Zare, R.N. (1998) Assaying for peptides in individual *Aplysia* neurons with mass spectrometry. *Proc Natl Acad Sci U S A*, **95,** 3338-3340.

31. Hoff, J. (2000) Methods of Blood Collection in the Mouse. *Lab Animal*, **29,** 47-53.

32. Bertrand, J.-R., Pottier, M., Vekris, A., Opolon, P., Maksimenko, A. and Malvy, C. (2002) Comparison of antisense oligonucleotides and siRNAs in cell culture and in vivo. *Biochem Biophys Res Commun*, **296,** 1000-1004.

33. Elmén, J., Thonberg, H., Ljungberg, K., Frieden, M., Westergaard, M., Xu, Y., Wahren, B., Liang, Z., Ørum, H., Koch, T. et al. (2005) Locked nucleic acid

(LNA) mediated improvements in siRNA stability and functionality. *Nucleic Acids Res*, **33,** 439-447.

34. Layzer, J.M., McCaffrey, A.P., Tanner, A.K., Huang, Z., Kay, M.A. and Sullenger, B.A. (2004) In vivo activity of nuclease-resistant siRNAs. *RNA*, **10,** 766-771.

35. Chiu, Y.-L. and Rana, T.M. (2003) siRNA function in RNAi: a chemical modification analysis. *RNA*, **9,** 1034-1048.

36. Alberts, B., Johnson, A., Lewis, J., Raff, M., Roberts, K. and Walter, P. (2002) Molecular Biology of the Cell. 4 ed. Garland Science, New York.

37. Stryer, L. (1995) Biochemistry. 4 ed. W. H. Freeman and Company, New York.

38. Velculescu, V.E., Madden, S.L., Zhang, L., Lash, A.E., Yu, J., Rago, C., Lal, A., Wang, C.J., Beaudry, G.A., Ciriello, K.M. et al. (1999) Analysis of human transcriptomes. *Nat Genet*, **23,** 387-388.

39. Godfrey, T.E., Kim, S.-H., Chavira, M., Ruff, D.W., Warren, R.S., Gray, J.W. and Jensen, R.H. (2000) Quantitative mRNA expression analysis from formalin-fixed, paraffin-embedded tissues using 5' nuclease quantitative reverse transcription-polymerase chain reaction. *J Mol Diagn*, **2,** 84-91.

40. Ignowski, J.M. and Schaffer, D.V. (2004) Kinetic analysis and modeling of firefly luciferase as a quantitative reporter gene in live mammalian cells. *Biotechnol Bioeng*, **86,** 827-834.

41. Varga, C.M., Hong, K. and Lauffenburger, D.A. (2001) Quantitative analysis of synthetic gene delivery vector design properties. *Mol Ther*, **4,** 438-446.

42. Banks, G.A., Roselli, R.J., Chen, R. and Giorgio, T.D. (2003) A model for the analysis of nonviral gene therapy. *Gene Ther*, **10,** 1766-1775.

43. Sweeney, T.J., Mailander, V., Tucker, A.A., Olomu, A.B., Zhang, W., Cao, Y.-a., Negrin, R.S. and Contag, C.H. (1999) Visualizing the kinetics of tumor-cell clearance in living animals. *Proc Natl Acad Sci U S A*, **96,** 12044-12049.

44. Novina, C.D., Murray, M.F., Dykxhoorn, D.M., Beresford, P.J., Riess, J., Lee, S.-K., Collman, R.G., Lieberman, J., Shankar, P. and Sharp, P.A. (2002) siRNA-directed inhibition of HIV-1 infection. *Nat Med*, **8,** 681-686.

45. Tuschl, T. (2002) Expanding small RNA interference. *Nat Biotechnol*, **20,** 446-448.

46. Song, E., Lee, S.-K., Dykxhoorn, D.M., Novina, C., Zhang, D., Crawford, K., Cerny, J., Sharp, P.A., Lieberman, J., Manjunath, N. et al. (2003) Sustained small interfering RNA-mediated human immunodeficiency virus type I inhibition in primary macrophages. *J Virol*, **77,** 7174-7181.

47. Omi, K., Tokunaga, K. and Hohjoh, H. (2004) Long-lasting RNAi activity in mammalian neurons. *FEBS Lett*, **558,** 89-95.

48. Schibler, U. (2003) Circadian rhythms: liver regeneration clocks on. *Science*, **302,** 234-235.

49. Kumaran, V., Benten, D., Follenzi, A., Joseph, B., Sarkar, R. and Gupta, S. (2005) Transplantation of endothelial cells corrects the phenotype in hemophilia A mice. *J Thromb Haemost*, **3,** 2022-2031.

50. Rajvanshi, P., Kerr, A., Bhargava, K., Burk, R.D. and Gupta, S. (1996) Studies of liver repopulation using the dipeptidyl peptidase IV-deficient rat and other rodent

recipients: Cell size and structure relationships regulate capacity for increased transplanted hepatocyte mass in the liver lobule. *Hepatology*, **23,** 482-496.

51. Tiscornia, G., Singer, O., Ikawa, M. and Verma, I.M. (2003) A general method for gene knockdown in mice by using lentiviral vectors expressing small interfering RNA. *Proc Natl Acad Sci U S A*, **100,** 1844-1848.

52. Rubinson, D.A., Dillon, C.P., Kwiatkowski, A.V., Sievers, C., Yang, L., Kopinja, J., Zhang, M., McManus, M.T., Gertler, F.B., Scott, M.L. et al. (2003) A lentivirus-based system to functionally silence genes in primary mammalian cells, stem cells and transgenic mice by RNA interference. *Nat Genet*, **33,** 401-406.

53. Varga, C., Tedford, N., Thomas, M., Klibanov, A., Griffith, L. and Lauffenburger, D. (2005) Quantitative comparison of polyethylenimine formulations and adenoviral vectors in terms of intracellular gene delivery processes. *Gene Ther*, **12,** 1023-1032.

54. Roth, C.M. (2005) Molecular and cellular barriers limiting the effectiveness of antisense oligonucleotides. *Biophys J*, **89,** 2286-2295.

3 Effect of siRNA nuclease stability on the in vitro and in vivo kinetics of siRNA-mediated gene silencing[†]

3.1 Abstract

Small interfering RNA (siRNA) molecules achieve sequence-specific gene silencing through the RNA interference (RNAi) mechanism. Here, live-cell and live-animal bioluminescent imaging (BLI) is used to directly compare luciferase knockdown by unmodified and nuclease-stabilized siRNAs in rapidly (HeLa) and slowly (CCD-1074Sk) dividing cells to reveal the impact of cell division and siRNA nuclease stability on the kinetics of siRNA-mediated gene silencing. Luciferase knockdown using unmodified siRNAs lasts approximately 1 week in HeLa cells and up to 1 month in CCD-1074Sk cells. There is a slight increase in the duration of luciferase knockdown by nuclease-stabilized siRNAs relative to unmodified siRNAs after cationic lipid transfection, but this difference is not observed after electroporation. In BALB/cJ mice, a four-fold increase in maximum luciferase knockdown is observed after hydrodynamic injection (HDI) of nuclease-stabilized siRNAs relative to unmodified siRNAs, yet the overall kinetics of the recovery after knockdown are nearly identical. By using a mathematical model of siRNA-mediated gene silencing, the trends observed in the experimental data can be duplicated by changing model parameters that affect the stability of the siRNAs before they reach the cytosolic compartment. Based on these findings, we hypothesize that the stabilization advantages of nuclease-stabilized siRNAs

---

originate primarily from effects prior to and during internalization before the siRNAs can interact with the intracellular RNAi machinery.

3.2 Introduction

Small interfering RNA (siRNA) molecules are potent triggers of sequence-specific gene silencing through RNA interference (RNAi) (1,2). Because the duration of gene inhibition by siRNA is a primary factor in determining the dosing schedules required to achieve therapeutic effects, insights into the kinetics of siRNA-mediated gene silencing are crucial to the design of effective siRNA-based treatment strategies.

We have previously reported on the kinetics of unmodified siRNAs in cultured cells and in mice, observing that unmodified siRNA molecules can achieve luciferase knockdown that lasts for around 1 week in rapidly dividing cell lines and as long as 1 month in slowly dividing fibroblasts (3). This prolonged duration of gene silencing by siRNA in vitro has also been observed with primary macrophages and mammalian neurons, both of which exhibit minimal cell proliferation (4,5). Additionally, we showed that the in vivo kinetics of gene silencing in mice were comparable to those observed in vitro (3). Recently, Zimmermann et al. reported that siRNAs can achieve long-lasting target inhibition in the livers of mice and non-human primates, suggesting that the trends in gene silencing are not species-specific (6). These results support the claim that dilution of intracellular siRNAs by cell division is a major factor limiting the duration of siRNA-mediated gene silencing in dividing cells. Furthermore, the prolonged duration of gene inhibition by unmodified siRNAs in slowly or nondividing cells suggests an enhanced intracellular stability of these molecules and is consistent with previous reports showing the extended intracellular persistence of double-stranded siRNAs in living cells

(5,7). The ability of unmodified siRNAs to produce such lengthy gene inhibition implies

that they are somehow protected against intracellular nucleases. One possibility is that

capture by the RNA-induced silencing complex (RISC) sequesters siRNA and blocks

nuclease attack. If unmodified siRNAs have high intracellular stability, then nuclease

stability may not be a limiting factor once siRNAs enter the cell. This would be in

contrast to the situation observed with antisense oligonucleotides, where it has been

demonstrated that the nuclease resistance of the oligonucleotide correlates with the

magnitude and duration of the gene silencing effect in vitro after cationic lipid

transfection (8).

For siRNAs to retain their functional activity, they must also resist degradation

prior to cellular internalization. The half-life reported for unmodified siRNAs in serum

ranges from several minutes to around an hour (2,6,9,10). The susceptibility to

degradation by nucleases present in serum appears to preclude the systemic application of

naked, unmodified siRNAs through clinically feasible administration routes. Chemical

modifications to the nucleotides (e.g., 2'-F, 2'-OMe, LNA) or the backbone (e.g.,

phosphorothioate linkages) have been used successfully to enhance nuclease stability and

prolong siRNA half-life in serum while still enabling siRNA function (9-14). The effects

of nuclease stabilization should be most dramatic in situations where the siRNAs can

directly interact with nucleases present in the extracellular environment such as the

bloodstream. However, transfection of cultured cells is accomplished most effectively

using carrier-mediated delivery, often through cationic lipid encapsulation of the siRNAs

to enhance cellular uptake. Because the siRNAs are protected by the carrier prior to

cellular uptake, in vitro studies most aptly highlight the effects of intracellular processes

on the activity of transfected siRNAs. A similar situation should be expected in vivo when delivery vehicles are used to transport the siRNAs to the target cells. However, hydrodynamic injection (HDI) provides a unique situation in which naked siRNAs can be successfully delivered systemically in vivo (15). The duration of the exposure to the bloodstream prior to cellular uptake by cells such as hepatocytes is not precisely known, although the rapid degradation of unmodified siRNAs in serum indicates that even a short exposure can be sufficient to degrade a portion of the injected unmodified siRNAs, while nuclease-stabilized siRNAs should be affected to a much lesser extent by this serum exposure.

The studies by Chiu and Rana and Layzer et al. both examined the kinetics of reporter gene inhibition in vitro after cationic lipid transfection of HeLa cells with unmodified and nuclease-stabilized siRNAs (10,11). Chiu and Rana asserted that a nuclease-stabilized, 2'-F modified siRNA against EGFP slightly prolonged EGFP knockdown relative to an unmodified siRNA. Layzer et al. used unmodified and 2'-F-modified siRNAs against luciferase and observed no significant difference in the magnitude or duration of luciferase knockdown in cultured HeLa cells. The slight differences in the observed kinetics by these two studies could be attributed to variations in the methods used, such as the transfection agent, or the effects of transient versus constitutive reporter gene expression.

As mentioned previously, an additional complexity of direct serum exposure is introduced during systemic delivery of naked siRNAs in vivo. Two previously published reports comparing unmodified and nuclease-stabilized siRNAs in vivo utilized HDI to deliver naked siRNAs to liver cells (9,10). Layzer et al. observed no substantial

difference in either the magnitude or duration of luciferase knockdown after injection of unmodified or nuclease-stabilized siRNAs (10). On the other hand, Morrissey et al. saw considerably greater knockdown of HBV DNA or surface antigen levels after 72 hours by nuclease-stabilized siRNAs compared to unmodified siRNAs (9).

To further examine these questions regarding the efficacy of unmodified versus nuclease-stabilized siRNAs, we employed live-cell and live-animal bioluminescent imaging (BLI) and mathematical modeling to directly compare the kinetics of siRNA-mediated gene silencing using unmodified and nuclease-stabilized siRNAs. The primary objective of our study is to determine how siRNA nuclease stability affects gene inhibition kinetics both in vitro and in vivo. We explore whether siRNA-mediated gene silencing kinetics are affected by chemical modifications to enhance nuclease resistance and whether the kinetics strongly depend on cell doubling times like we observed with unmodified siRNAs (3). To our knowledge, this is the first study to directly compare unmodified and nuclease-stabilized siRNAs delivered under identical conditions in both rapidly and slowly dividing cells, allowing us to concurrently address the impact of cell division and siRNA nuclease stability on the kinetics of siRNA-mediated gene silencing. Our findings indicate that while nuclease stability is important to prevent siRNA degradation in the extracellular environment, such as the bloodstream after systemic administration, it is not a dominant factor controlling the persistence of siRNAs that have already been internalized into the cytosolic compartment of cells.

3.3 Materials and methods

3.3.1 Luciferase-expressing cell lines

Cell lines were incubated with viral supernatant containing SMPU-R-MNDU3-LUC, a lentiviral vector based on HIV-1 that transduces the firefly luciferase gene (16,17). The backbone vector SMPU-R has deletions of the enhancers and promoters of the HIV-1 long terminal repeat (SIN), has minimal HIV-1 gag sequences, contains the cPPT/CTS sequence from HIV-1, has three copies of the USE polyadenylation enhancement element from SV40, and has a minimal HIV-1 RRE (gift of Paula Cannon, Children's Hospital Los Angeles). The vector has the U3 region from the MND retroviral vector as an internal promoter driving expression of the firefly luciferase gene from SP-LUC+ (Promega).

3.3.2 siRNA duplexes

siGL3, siLuc1, and siLuc2 target the firefly luciferase gene, siEGFP targets the enhanced green fluorescent protein (EGFP) gene, and siCON1 is a control sequence that is bioinformatically designed to minimize the potential for targeting any known human or mouse genes:

siGL3:
```
    sense:      5'- CUUACGCUGAGUACUUCGAdTdT -3'
    antisense:  5'- UCGAAGUACUCAGCGUAAGdTdT -3'
```

siLuc1:
```
    sense:      5'- GGUUCCUGGAACAAUUGCUUUUAdCdA -3'
    antisense:  5'- UGUAAAAGCAAUUGUUCCAGGAACCAG -3'
```

siLuc2:
```
    sense:      5'- GUGCCAGAGUCCUUCGAUAGG -3'
    antisense:  5'- UAUCGAAGGACUCUGGCACAA -3'
```

siEGFP:
```
    sense:      5'- GACGUAAACGGCCACAAGUUC -3'
    antisense:  5'- ACUUGUGGCCGUUUACGUCGC -3'
```

siCON1:
```
    sense:      5'- UAGCGACUAAACACAUCAAUU -3'
    antisense:  5'- UUGAUGUGUUUAGUCGCUAUU -3'
```

Unmodified siLuc1 and siLuc2 were synthesized by Integrated DNA Technologies, unmodified siEGFP was synthesized by Dharmacon, and unmodified and siSTABLEv2 versions of siGL3 and siCON1 were synthesized by Dharmacon. The siSTABLEv2 siRNAs contain Dharmacon's proprietary chemical modifications that provide enhanced nuclease resistance.

3.3.3   siRNA serum stability

1.5 µL of a 20 µM solution of unmodified or nuclease-stabilized siGL3 in water were added to 13.5 µL of active mouse serum (Sigma) and incubated at 37°C and 5% CO_2. After incubation for the desired amount of time, 3 µL loading buffer was added and 15 µL of each sample was loaded into a 2% agarose gel. Bands were visualized by ethidium bromide staining and quantified using ImageJ image analysis software.

3.3.4   In vitro transfection

Oligofectamine Transfection

Cells were seeded at $2x10^4$ cells per well in 24-well plates 2 days prior to transfection and grown in media supplemented with 10% fetal bovine serum (FBS) and antibiotics (penicillin/streptomycin). siRNA was complexed with Oligofectamine (Invitrogen) according to manufacturer's instructions and applied to each well in a total

volume of 200 µL Opti-MEM I (Invitrogen). Transfection media was removed and replaced with complete media after 5 h.

Electroporation

Cells growing in a 25 cm^2 flask were trypsinized, counted, and resuspended in Opti-MEM I at $2x10^6$ cells mL^{-1}. 100 µL of this suspension were added to an electroporation cuvette (Bio-Rad) with a 0.2-cm gap width and incubated on ice for 15 minutes. 5 µL of each 20 µM siRNA stock solution were added to the individual cuvettes to give a final siRNA concentration of 952 nM. Each cuvette was then placed in the ShockPod of a Gene Pulser Xcell with a CE module (Bio-Rad), and the protocol for HeLa cells was used to apply an exponential decay pulse (160 V, 500 µF). After electroporation, the cells in the cuvette were allowed to recover for 15 minutes at room temperature and then plated in 1 mL pre-warmed complete media at $6x10^4$ cells per well in a 24-well plate.

3.3.5 *Hydrodynamic co-injection of plasmid DNA and siRNA*

The plasmid, pApoEHCRLuc, contains the firefly luciferase gene under a hepatocyte-specific promoter. For kinetic studies in BALB/cJ mice, a 5% glucose solution containing 0.25 mg kg^{-1} of the luciferase-containing plasmid and 2.5 mg kg^{-1} siRNA was injected by hydrodynamic tail-vein injection (2 mL per 20-g mouse). Mice were restrained in a holding device while the entire volume (~2 mL) was injected into a lateral tail vein over a 5-second period. At the time of injection, the BALB/cJ mice were 7 weeks old and had an average body weight of 18 g.

3.3.6 Bioluminescent imaging (BLI)

Cell culture plates or mice were imaged using the Xenogen IVIS 100 imaging system (Xenogen). D-luciferin (Xenogen) was dissolved in PBS at 15 g L^{-1}. For in vitro assays in 24-well plates, 50 μL of the 15 g L^{-1} luciferin solution was added to each well containing 1 mL of media. Light emission was measured 2-3 minutes after addition of the luciferin. For in vivo experiments, 0.2 mL of the 15 g L^{-1} luciferin solution was injected i.p. 10 minutes before measuring the light emission. Mice were anesthetized with an initial dose of 5% isoflurane followed by a maintenance dose of 2.5% isoflurane. Bioluminescent signals were quantified using Living Image software (Xenogen).

The relative luciferase knockdown for in vitro and in vivo experiments was calculated by taking the ratio of the change in luciferase expression resulting from an siRNA against luciferase to the change in luciferase expression resulting from a non-targeting control siRNA. This normalization to an identically transfected control siRNA should help to minimize artifacts from nonspecific effects that have been observed with siRNA transfection (18,19).

3.3.7 Mathematical modeling

We employed the mathematical model of siRNA-mediated gene silencing described previously to determine which parameters may be responsible for the differences in gene silencing using unmodified and nuclease-stabilized siRNAs (3). The majority of the parameters were left unchanged from those described previously, and an explanation of which parameters were changed and why is provided in more detail in the Results section.

3.4   Results

3.4.1   Verification of luciferase knockdown by multiple siRNA sequences

siRNA sequences can be designed to cleave at different regions within a given

mRNA transcript with the same end result of mRNA cleavage and a concomitant

reduction in protein levels. Therefore, three different siRNAs were designed that target

three separate regions on the luciferase mRNA transcript. Both siGL3 and siLuc2 have a

standard 19-bp duplex region, while the siLuc1 sequence is designed to have a 25-bp

duplex region that may aid in processing by the Dicer component of the RNAi pathway

(20). Luciferase-expressing HeLa and CCD-1074Sk fibroblast cells were transfected

under identical conditions with these three different siRNA sequences against luciferase

(siGL3, siLuc1, and siLuc2) and two control siRNA sequences (siCON1 and siEGFP).

The results shown in Figure 3.1 represent the luciferase knockdown by each sequence

relative to siCON1 at doses of 25 nM and 100 nM. The lack of knockdown by 100 nM

siEGFP in Figure 3.1B indicates that cells transfected with siEGFP show nearly identical

luciferase expression to cells transfected with siCON1, validating the use of siCON1 as a

nonspecific control. On the other hand, all three siRNA sequences targeting luciferase

gave nearly identical luciferase knockdown kinetics, with negligible variations in both the

magnitude and duration of knockdown at all concentrations tested. The knockdown

lasted slightly over 1 week in HeLa cells, which exhibited average cell doubling times of

1-2 days. On the other hand, the luciferase levels did not recover to control levels for up

to 1 month in the fibroblasts, which exhibited average cell doubling times of 15-20 days.

These results corroborate our previous findings and provide further evidence supporting

the claim that cell division directly impacts the duration of siRNA-mediated gene

silencing (3). The slightly longer duration of gene silencing for the fibroblasts in this study compared to our previous study may be attributed to the averaging of a greater number of data points that are now available or variations in the initial lipoplex formulation and cell passage number. Given the variability inherent to these systems, the consistency of the observed knockdown between multiple independent experiments is encouraging. The nearly identical results with multiple sequences targeting independent sites on the luciferase mRNA indicate that the observed kinetics of the luciferase knockdown are not specific to only a certain sequence.
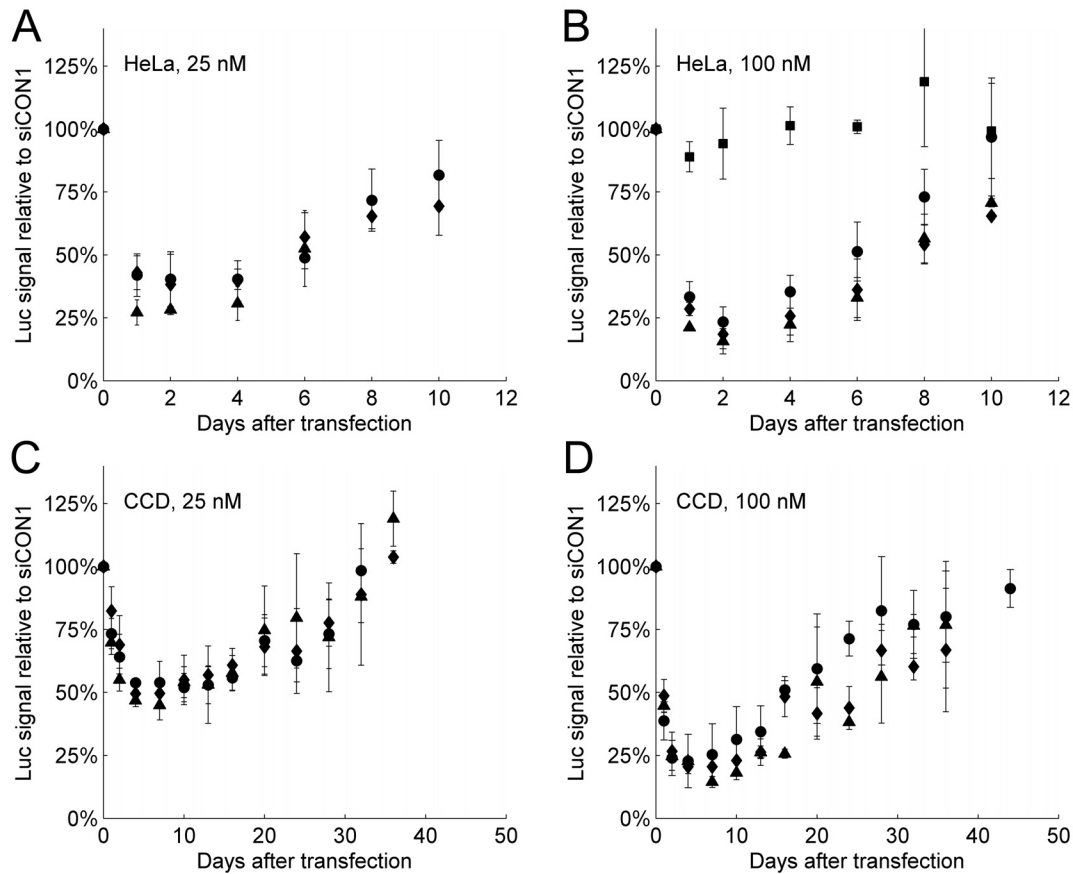
Figure 3.1. Validation of luciferase-targeting and control siRNA sequences in rapidly dividing (HeLa) and slowly dividing (CCD) luciferase-expressing cells after Oligofectamine transfection. (A) HeLa, 25 nM siRNA, (B) HeLa, 100 nM siRNA, (C) CCD-1074Sk, 25 nM siRNA, (D) CCD-1074Sk, 100 nM siRNA. Luciferase knockdown is reported relative to the luciferase activity from cells transfected with equal doses of the siCON1 control sequence. Squares = siEGFP, circles = siGL3, diamonds = siLuc1, triangles = siLuc2.

3.4.2   Serum stability of unmodified and nuclease-stabilized siRNAs

The siGL3 and siCON1 sequences were used as the luciferase-targeting and non-targeting siRNAs, respectively, for the remainder of the in vitro and in vivo studies. Previously, we examined the kinetics of luciferase downregulation by unmodified siRNAs; here, we expand this investigation to include nuclease-stabilized siRNAs. There are several commercially available modified siRNAs that are purported to have increased nuclease stability. Dharmacon's siSTABLEv2 modified siRNAs were used in these studies because their reported half-life in human serum exceeds several days and because the unmodified siGL3 and siCON1 were also purchased from Dharmacon. A serum stability assay was conducted to verify that the siSTABLEv2 siRNAs from Dharmacon exhibited enhanced nuclease stability. 2 μM of unmodified and nuclease-stabilized siGL3 were incubated in 90% active mouse serum for 1 to 24 hours at 37°C and 5% CO_2 and subsequently visualized by ethidium bromide staining after gel electrophoresis. Nuclease stability can be judged from the relative intensity of the bands at each time point, with degradation indicated by the disappearance of the bands over time. As shown by the data given in Figure 3.2, unmodified siGL3 degrades rapidly in the presence of serum, with the bands becoming undetectable by 6 hours. On the other hand, there is little detectable degradation of the nuclease-stabilized siGL3 after 6 hours, and a band is still clearly visible after 24 hours. The relative changes in the band intensities for both unmodified and nuclease-stabilized siGL3 are also plotted in Figure 3.2. By fitting an exponential curve to these data, an estimated half-life for each siRNA species under these conditions can be calculated. Whereas the unmodified siGL3 had a half-life of around 1 hour, the nuclease-stabilized siGL3 had an observed half-life of almost 1 day. The

observed half-life for the nuclease-stabilized siGL3 is shorter than the half-life of several days reported by Dharmacon, but this discrepancy could be the result of different serum preparations (e.g., mouse vs. human) and/or the result of the quantification method used. Regardless, these results confirm that the modified siRNAs display enhanced nuclease resistance relative to unmodified siRNAs.
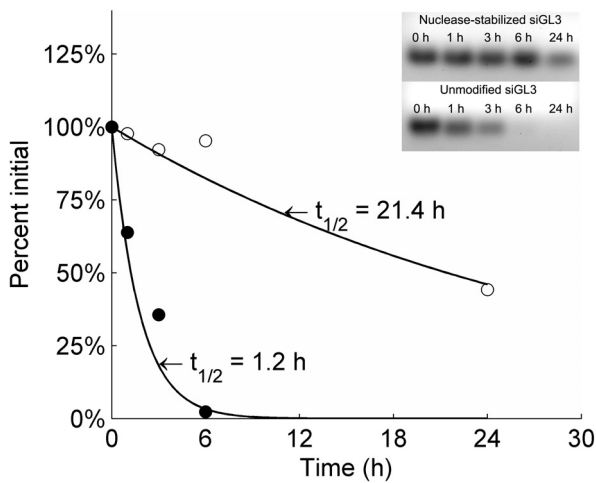
Figure 3.2. Nuclease stability of unmodified and nuclease-stabilized siRNAs after incubation at 37°C and 5% CO_2 in 90% mouse serum. After gel electrophoresis, band intensities were quantified with ImageJ software and plotted versus time to estimate the half-life of the unmodified (solid circles) and nuclease-stabilized (open circles) siGL3.

3.4.3   In vitro activity of unmodified and nuclease-stabilized siRNAs in rapidly and slowly dividing cells

The cationic lipid transfection reagent, Oligofectamine, can deliver siRNA to luciferase-expressing HeLa and CCD-1074Sk cells (3). Luciferase knockdown by unmodified and nuclease-stabilized siRNAs was first studied in rapidly dividing HeLa cells. The cells were transfected with 25 nM or 100 nM of each siRNA species and then the luciferase activity was monitored through live-cell BLI. Since the exact modifications of the nuclease-stabilized siRNAs may also introduce some nonspecific effects, a nuclease-stabilized version of the siCON1 control siRNA was used for

normalization of the cells receiving nuclease-stabilized siGL3. This should minimize any

artifacts from nonspecific effects that may arise from sequence-independent mechanisms.

The results shown in Figure 3.3A-B represent the average of duplicate or triplicate wells

per transfection condition, and the data from at least four independent experiments are

represented at the 100 nM dose. There was a slight increase in the duration of luciferase

knockdown for the nuclease-stabilized siGL3 as seen by the shift in the knockdown

curve, indicating that the inhibition lasts approximately 1-2 days longer under these

conditions.
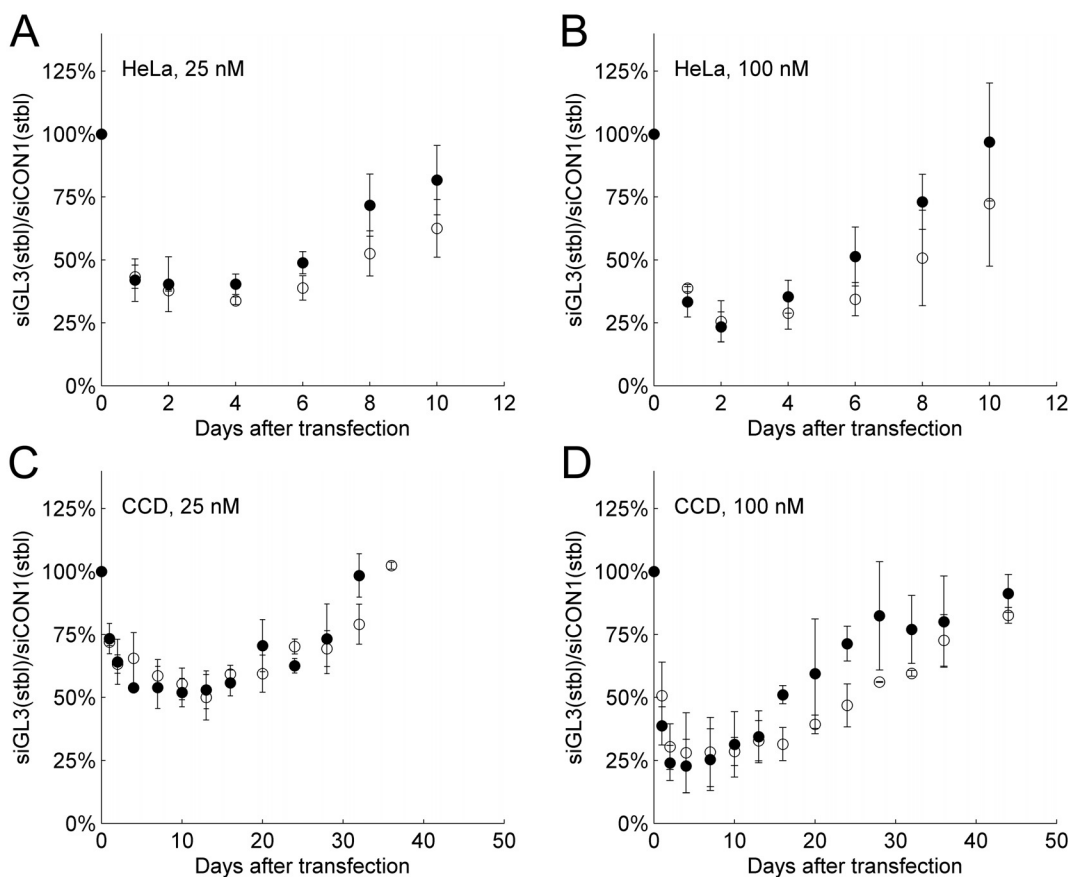
Figure 3.3. In vitro luciferase knockdown by unmodified and nuclease-stabilized siGL3 in rapidly dividing (HeLa) and slowly dividing (CCD) luciferase-expressing cells after Oligofectamine transfection. (A) HeLa, 25 nM siRNA, (B) HeLa, 100 nM siRNA, (C) CCD-1074Sk, 25 nM siRNA, (D) CCD-1074Sk, 100 nM siRNA. Luciferase knockdown is reported relative to the luciferase activity from cells transfected with equal doses of the unmodified or nuclease-stabilized siCON1 control sequence. Solid circles = unmodified siGL3, open circles = nuclease-stabilized siGL3.

The CCD-1074Sk fibroblast cell line has constitutive luciferase expression and divides very slowly, providing a system for examining the effects of enhanced siRNA nuclease stability in the absence of significant cell division. The observed average cell doubling time during these experiments was 15-20 days, meaning the cells essentially were nondividing relative to the rapidly dividing HeLa cells that divide once every 1-2 days. Under these conditions, the amount of siRNA dilution that occurs in the fibroblast cell line should be low, allowing other processes, such as nuclease degradation, to possibly become limiting. The cells were transfected with 25 nM or 100 nM of the unmodified and nuclease-stabilized siRNAs and the luciferase activity of the cells was monitored over time with live-cell BLI. The data shown in Figure 3.3C-D represent the average of duplicate or triplicate wells per transfection condition, and the data from at least two independent experiments are represented at the 100 nM dose. While the magnitude of the knockdown remained nearly the same for the unmodified and nuclease-stabilized siRNAs, there was again a slight increase in the duration of the knockdown for the nuclease-stabilized siGL3, this time shifting the curve by 5-10 days at its maximum point of difference. Since similar trends are again observed at both 25 nM and 100 nM even though the magnitude of the knockdown is lower for the 25 nM dose, it appears that the trends are not caused by saturation of the RNAi machinery.

To explore whether the use of a transfection reagent affects the observed kinetics, we used electroporation to achieve intracellular localization of the unmodified and modified siRNAs in HeLa cells. The results shown in Figure 3.4 represent the average of triplicate wells per transfection condition. The kinetics of the luciferase knockdown after electroporation were similar to those observed after Oligofectamine transfection, with the

knockdown again lasting slightly over a week in the rapidly dividing HeLa cells. However, there was no noticeable increase in the duration of the knockdown when using nuclease-stabilized siGL3.
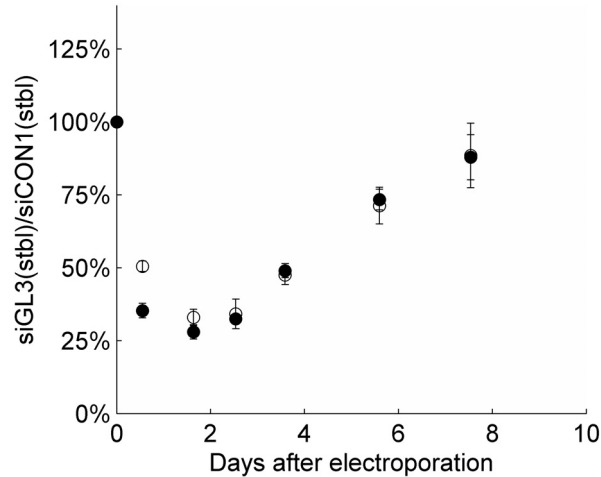
Figure 3.4. In vitro luciferase knockdown by unmodified and nuclease-stabilized siGL3 in HeLa cells after electroporation. Luciferase knockdown is reported relative to the luciferase activity from cells that received equal doses of the unmodified or nuclease-stabilized siCON1 control sequence. Solid circles = unmodified siGL3, open circles = nuclease-stabilized siGL3.

Although the nuclease-stabilized siRNAs did not appear to provide significant advantages in terms of the magnitude or the duration of gene silencing in vitro, the situation may be vastly different in vivo. Specifically, the enhanced resistance of nuclease-stabilized siRNAs to degradation in the extracellular environment can increase the amount of the injected dose that remains intact for uptake and ultimately intracellular function.

3.4.4   *In vivo activity of unmodified and nuclease-stabilized siRNAs after hydrodynamic injection (HDI)*

Systemic delivery of naked nucleic acid molecules such as siRNAs can be achieved using HDI through the tail vein in mice. Because HDI leads to substantial uptake by cells in the liver, it was used to compare the function of unmodified and

nuclease-stabilized siRNAs in vivo. A plasmid containing the firefly luciferase gene driven by a hepatocyte-specific promoter was co-injected with siRNAs through HDI. Uptake of the plasmid by liver hepatocytes leads to a strong luciferase signal in the liver that can be followed using BLI. When an siRNA sequence that targets luciferase is co-injected with the plasmid, the total liver luciferase signal is decreased relative to the signal in mice that receive the plasmid and a non-targeting control siRNA sequence. As in the in vitro experiments, a nuclease-stabilized version of the control siCON1 was used for determining the relative luciferase knockdown in the group of mice receiving nuclease-stabilized siGL3. The luciferase signals of the mice were followed by BLI for 7 weeks. Bioluminescent images of representative mice from each treatment group after 2, 12, and 30 days are shown in Figure 3.5, and the average integrated luciferase signals over the entire experiment are shown in Figure 3.6A. The rapid decline in luciferase signals over the first several weeks followed by a non-zero steady-state value that persists for months is reproducibly observed after HDI of this plasmid. The inherent variability from mouse to mouse leads to inevitable deviations in the final steady-state values reached by the mice in each group; therefore, normalization of these final values facilitates comparison between groups (Figure 3.6B). Since the final normalized steady-state values in Figure 3.6B are the same for all treatment groups, division of the signal for the siGL3-treated mice by the signal for the siCON1-treated mice gives a relative luciferase knockdown at each time point.
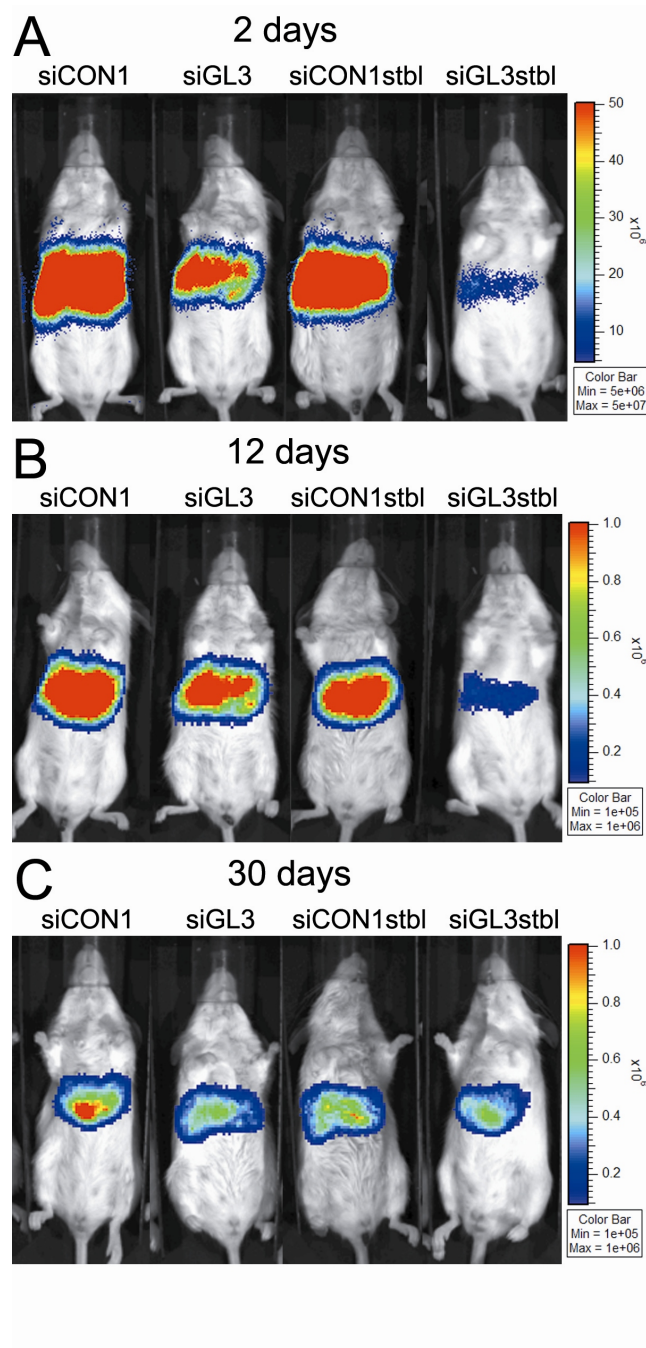
Figure 3.5. Bioluminescent images of BALB/cJ mice after hydrodynamic co-injection of a plasmid containing the firefly luciferase gene under a hepatocyte-specific promoter and unmodified (siCON1, siGL3) or nuclease-stabilized (siCON1stbl, siGL3stbl) siRNAs. One representative mouse was chosen from each of the four treatment groups and images are shown of each mouse after (A) 2 days, (B) 12 days, and (C) 30 days.
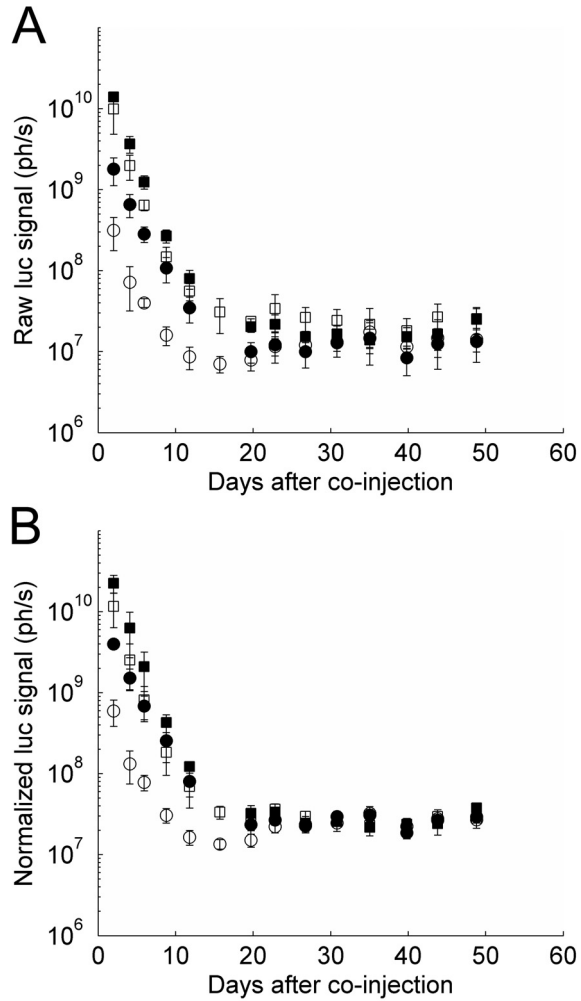
Figure 3.6. Luciferase activity in BALB/cJ mice after hydrodynamic co-injection of a plasmid containing the firefly luciferase gene under a hepatocyte-specific promoter and unmodified or nuclease-stabilized siRNAs. (A) Average raw luciferase signals and (B) average normalized luciferase signals are shown for mice co-injected with the plasmid and either unmodified siCON1 (solid squares, n = 3), unmodified siGL3 (solid circles, n = 4), nuclease-stabilized siCON1 (open squares, n = 4), or nuclease-stabilized siGL3 (open circles, n = 5). Normalization was performed by multiplying all data points of the raw luciferase signals for each group by an adjustment factor such that the final steady-state luciferase signals are equal for all four groups.

The curves in Figure 3.7A represent the relative luciferase knockdown for the unmodified and nuclease-stabilized siGL3-treated mice relative to their respective controls. The maximum magnitude of knockdown by each treatment can be assessed directly from Figure 3.7A. The nuclease-stabilized siGL3 achieved a four-fold greater reduction in luciferase activity than the unmodified siGL3, reaching 5% of control

luciferase activity after 2 days compared to 20% of control luciferase activity for unmodified siGL3. Determination of the duration of luciferase knockdown is more complicated because the nuclease-stabilized siGL3 gave a greater degree of knockdown. For example, if the luciferase signals for each treatment group recover at the same rate, the one that exhibits greater knockdown will take longer to return to the steady-state value. Therefore, even though the results in Figure 3.7A indicate that the relative luciferase knockdown by nuclease-stabilized siGL3 lasts longer than the knockdown by unmodified siGL3, this may not necessarily imply different overall kinetics. One approach to answering this question is shown in Figure 3.7B. The curve for unmodified siGL3 is identical to the one shown in Figure 3.7A; however, the curve for nuclease-stabilized siGL3 is shifted so that the knockdown after 2 days is equivalent for both. Such data analysis allows direct comparison of the kinetics at points of equivalent knockdown. It is remarkable that the curves for both the unmodified and nuclease-stabilized siRNAs nearly coincide over the duration of the knockdown, revealing that the overall kinetics are essentially identical in both cases.
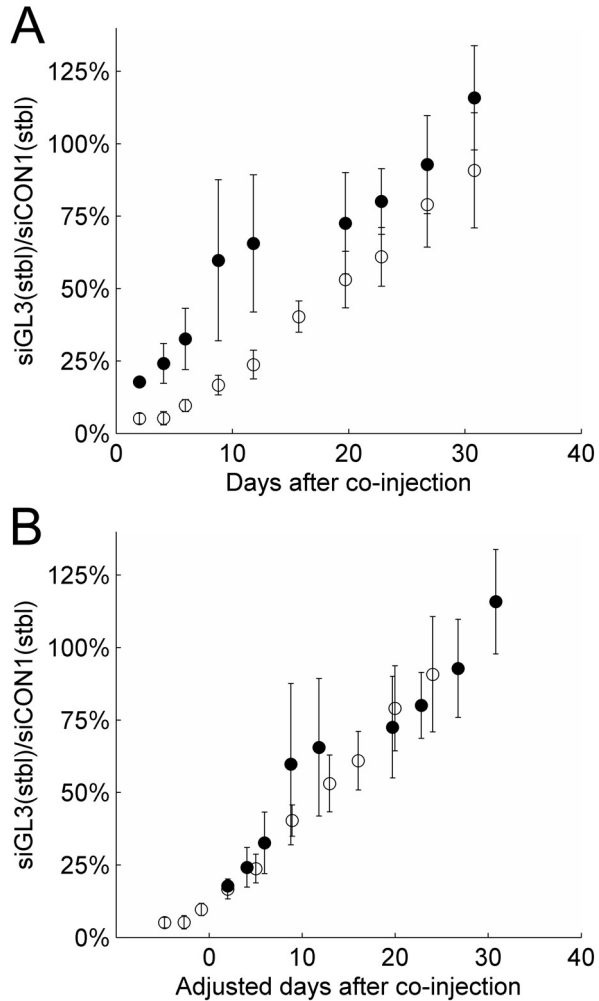
Figure 3.7. In vivo luciferase knockdown by unmodified and nuclease-stabilized siGL3 in BALB/cJ mice after hydrodynamic co-injection with a plasmid containing the firefly luciferase gene under a hepatocyte-specific promoter. (A) Relative luciferase knockdown for mice treated with unmodified siGL3 (solid circles, n = 4) or nuclease-stabilized siGL3 (open circles, n = 5). Relative knockdown is calculated by dividing the normalized luciferase signals for the siGL3-treated mice by the normalized luciferase signals for the siCON1-treated mice. (B) Comparison of the kinetics of luciferase knockdown by unmodified siGL3 (solid circles, n = 4) and nuclease-stabilized siGL3 (open circles, n = 5) at points of equivalent knockdown.

3.4.5   *Model predictions for the effect of siRNA nuclease stability*

Further analysis of these data using a mathematical model of siRNA-mediated

gene silencing supports the notion that siRNA nuclease stabilization has its primary effect

prior to cellular internalization and cytosolic localization. The mathematical model

enabled us to calculate how changes in certain parameters, such as intracellular or

extracellular siRNA half-life, could affect the kinetics of gene silencing. The goal was to

find which set of parameters must be varied to match the experimental results in Figures

3.3 and 3.7. If we assume that the differences between the curves for the unmodified and

nuclease-stabilized siGL3 in Figure 3.3 are not just due to inherent variability, then the

model must predict that the nuclease-stabilized siRNAs will slightly increase the duration

of gene silencing without significantly impacting its magnitude when applied in vitro

using Oligofectamine. The model must also predict that HDI of nuclease-stabilized

siRNAs will increase the magnitude of gene silencing, but not the kinetics of the

recovery, relative to that achieved by unmodified siRNAs. These goals can be achieved

by changing relatively few parameters in the mathematical model described previously

(3). The rate of intracellular siRNA degradation, *kdeginna*, was kept constant for both

unmodified and nuclease-stabilized siRNAs, although the rate of degradation was

decreased to 7.2×10^{-3} h^{-1} to more closely match the experimental data now available.

Additionally, the rate for the target mRNA degradation, *kdegmRNA*, was fixed at 0.69 h^{-1}

for both in vitro and in vivo models to provide the best approximation of the observed

magnitude of luciferase knockdown. For the in vitro version of the model, the value for

vector endosomal unpackaging, *kunpackend*, was increased to 5×10^{-2} h^{-1} after

Oligofectamine transfection and the value for siRNA endosomal degradation

(*kdegendna*) was adjusted to reflect the nuclease stability of the unmodified (0.58 h^{-1}) and

nuclease-stabilized (0.03 h^{-1}) siRNAs. These changes result in a greater amount of naked

(unpackaged) siRNA that has the potential to be degraded before it can enter the cytosolic

compartment and interact with the intracellular machinery, such as the RISC components,

that might contribute to its enhanced stability. For the in vivo version of the model, the

rate of naked siRNA internalization, *kint*, after HDI was reduced to 1×10^{-8} h^{-1} to reflect a situation where some of the injected siRNA is not internalized immediately by the hepatocytes but remains in the extracellular environment where it is still susceptible to nuclease degradation (21). The volume of this extracellular environment, such as the sinusoidal space in the liver, can be estimated to be around 300 µL for a mouse liver with 50 million hepatocytes (22). The *partition* parameter, controlling the effective amount of the injected dose that reaches this extracellular space, was adjusted to 5×10^{-3} from 1×10^{-2} to match the magnitude of the knockdown by both unmodified and nuclease-stabilized siRNAs. Unlike siRNAs internalized after Oligofectamine transfection, siRNAs internalized after HDI were assumed to not undergo any degradation in internalizing vesicles such as endosomes. This enabled us to focus specifically on the differences in extracellular stability after HDI since all intracellular parameters were kept identical for unmodified and nuclease-stabilized siRNAs. Finally, the rates for siRNA plasma elimination (*kelimpl*) and siRNA extracellular degradation (*kelimec*) were adjusted to reflect the nuclease stability of the unmodified and nuclease-stabilized siRNAs. We assumed a relatively rapid plasma siRNA elimination with *kelimpl* = 0.1 h^{-1} for all siRNAs since renal clearance and nuclease degradation will both lead to plasma elimination. The siRNA extracellular degradation and endosomal degradation rates were chosen to match the results from Figure 3.2, with values of 0.58 h^{-1} and 0.03 h^{-1} for unmodified and nuclease-stabilized siRNAs, respectively.

Model simulations for luciferase knockdown by unmodified and nuclease-stabilized siRNAs are shown in Figures 3.8 and 3.9. The curves in Figure 3.8 represent the model predictions for luciferase knockdown in HeLa and CCD-1074Sk cells by

unmodified and nuclease-stabilized siRNAs, analogous to the experimental results shown

in Figures 3.3B and 3.3D. The differences between the two curves result only from the

different degradation rates of the unmodified and nuclease-stabilized siRNAs prior to

endosomal escape and interaction with the RNAi machinery; all other parameters are the

same. The intracellular siRNA degradation rate, reflecting the stability of the siRNAs in

the cytosolic compartment, remains constant for both types of siRNA.
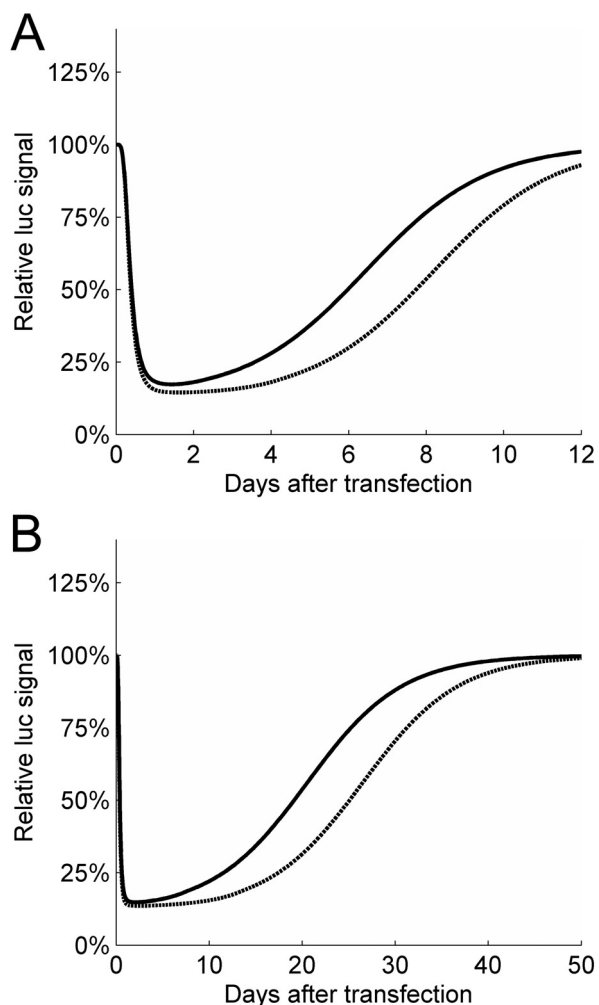
Figure 3.8. Model predictions for luciferase knockdown in luciferase-expressing (A) HeLa cells and (B) CCD-1074Sk cells after Oligofectamine transfection with 100 nM of unmodified siGL3 (solid line) or nuclease-stabilized siGL3 (dashed line). In these simulations, the intracellular siRNA degradation rate remains constant while the parameters governing the stability of the siRNAs before cytosolic localization are changed as described in the Results.

The curves in Figure 3.9, corresponding to the experimental data shown in Figure 3.7, represent the luciferase knockdown predicted after HDI using unmodified and nuclease-stabilized siRNAs. The magnitude of the luciferase knockdown by the nuclease-stabilized siRNAs is predicted to be greater than that by unmodified siRNAs, yet the kinetics of the overall knockdown are very similar as shown in Figure 3.9B. Again, the intracellular siRNA degradation rate was kept constant, and this time only the extracellular siRNA degradation rate was altered to reflect the enhanced nuclease stability of the stabilized siRNAs.
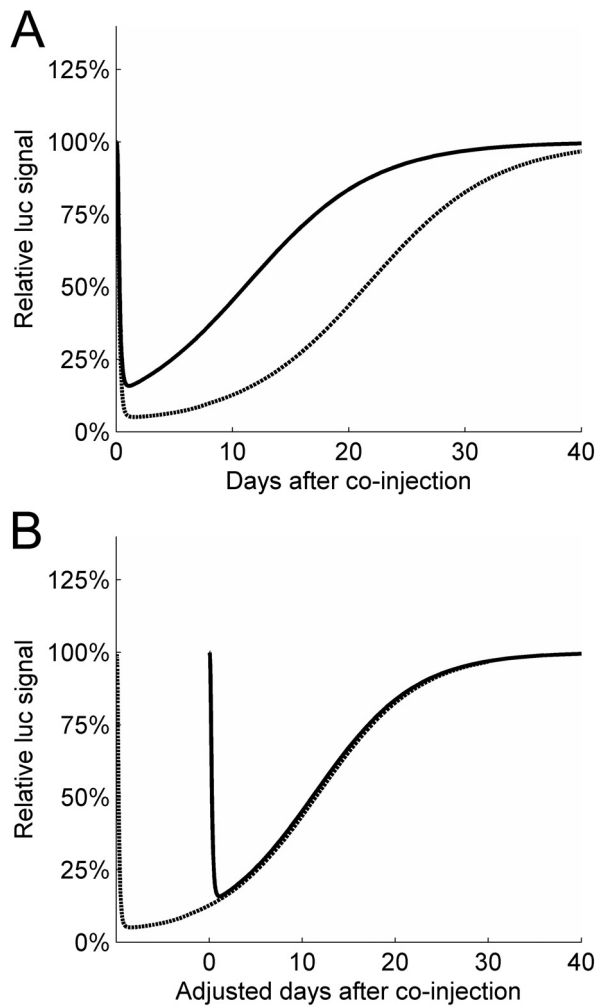
Figure 3.9. Model predictions for luciferase knockdown in BALB/cJ mice after HDI. (A) Relative luciferase knockdown after injection of unmodified siGL3 (solid line) or nuclease-stabilized siGL3 (dashed

line). (B) Comparison of the kinetics of luciferase knockdown by unmodified siGL3 (solid line) and nuclease-stabilized siGL3 (dashed line) at points of equivalent knockdown. In these simulations, the intracellular siRNA degradation rate remains constant while the parameters governing the stability of the siRNAs before cytosolic localization are changed as described in the Results.

The model simulations shown in Figure 3.10 provide further justification for our decision to maintain a constant intracellular siRNA degradation rate. The rate of intracellular siRNA degradation, *kdeginna*, was varied from 1.4×10^{-2} h^{-1} to 3.6×10^{-3} h^{-1} to reflect a situation in which nuclease stabilization prolongs the intracellular siRNA half-life. However, the parameters governing the stability of the siRNAs prior to cytosolic localization were kept constant. The model predictions for luciferase knockdown in rapidly dividing HeLa cells (Figure 3.10A) appear reasonably close to what was observed experimentally (Figure 3.3B), yet the predictions for luciferase knockdown in the slowly dividing CCD-1074Sk cells (Figure 3.10B) or mouse liver hepatocytes after HDI (Figure 3.10C) do not provide reasonable approximations to the experimental trends.
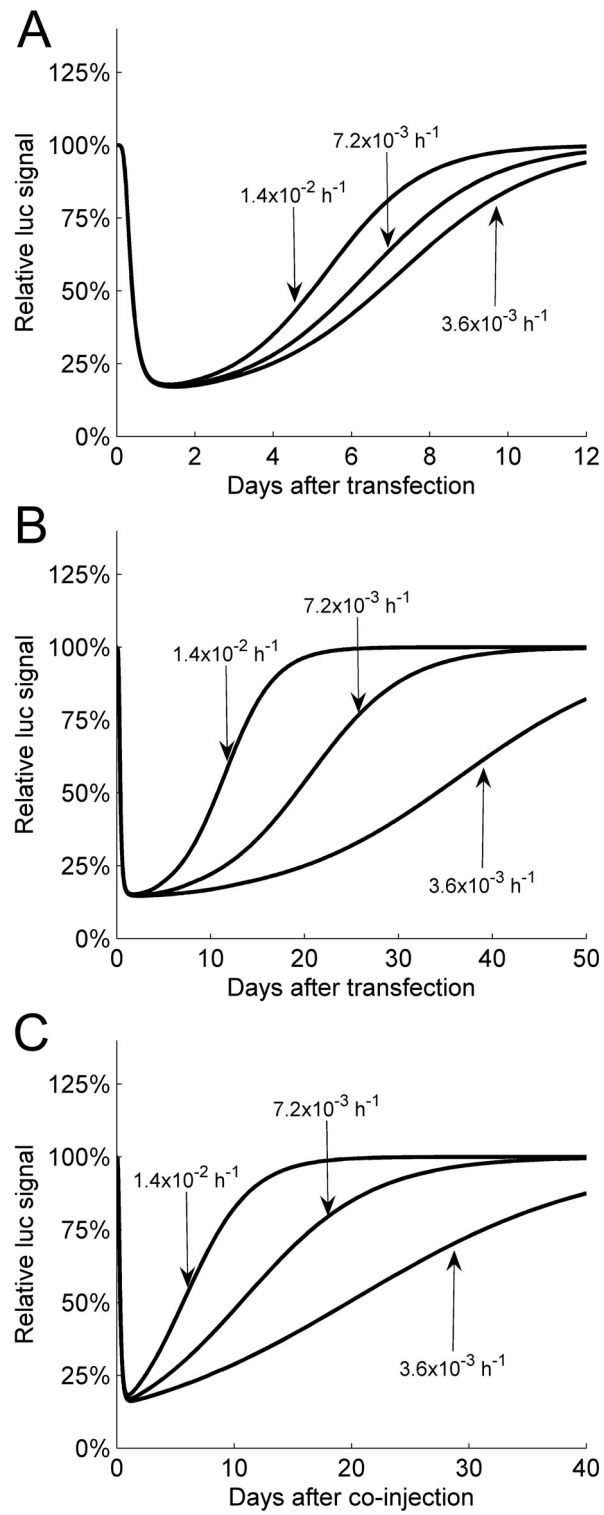
Figure 3.10. Model predictions for the effect of intracellular siRNA degradation rate (*kdeginna*) on luciferase knockdown in (A) HeLa cells after transfection with 100 nM siGL3, (B) CCD-1074Sk cells after transfection with 100 nM siGL3, and (C) mouse liver hepatocytes after HDI of a luciferase-expressing plasmid and siGL3.

3.5   Discussion

Although numerous studies have been conducted in a variety of animal models to investigate the efficacy of siRNAs as therapeutic agents, there has been less attention devoted to dosing schedule considerations that will depend upon how long knockdown lasts after a given dose of siRNA. We previously showed that unmodified siRNAs can achieve luciferase downregulation for extended periods of time, lasting approximately 1 week in rapidly dividing cells and 1 month in cells with minimal cell division (3). These results help to guide the design of more effective dosing schedules by highlighting the importance of cell division. Here, we extend the analysis of the kinetics of siRNA-mediated gene silencing to include nuclease-stabilized siRNAs.

Because of the rapid degradation of naked siRNAs in serum, it is clear that some form of protection will be required for systemic delivery. This can be achieved either by the use of a delivery vehicle or by chemical modification of the siRNA itself. Several studies have shown that chemically modified siRNAs can be highly resistant to nuclease degradation yet still function as effectors of RNA interference (9-14). As a result, nuclease-stabilized siRNAs have been touted as holding great promise for in vivo applications where exposure to serum in the extracellular environment would rapidly degrade unmodified siRNAs. A question that remains is whether or not nuclease stabilization also affects the kinetics of siRNA-mediated gene silencing. If enhanced nuclease stability allows the siRNAs to remain intact longer inside the cell, it might lead to an increase in the duration of gene inhibition. For example, Monia et al. observed a correlation between the nuclease resistance of antisense oligonucleotides and the magnitude and duration of the antisense effect (8). Even though the 2'-methoxy modified

oligonucleotides with phosphodiester backbones had higher affinity for the target mRNA, the more nuclease-resistant 2'-pentoxy modified oligonucleotides displayed the greatest antisense activity, with a significant increase in both the magnitude and duration of Ha-*ras* mRNA silencing. On the other hand, Layzer et al. observed no significant difference in the magnitude or duration of gene silencing by unmodified or nuclease-stabilized siRNAs after cationic lipid transfection in cultured HeLa cells or in mice after HDI of naked siRNAs (10). It is important to note that the studies with antisense oligonucleotides were also performed using a cationic lipid transfection reagent, indicating that the lack of apparent differences between the unmodified and nuclease-stabilized siRNAs is not likely an artifact of the use of a transfection reagent. Because cell division is a dominant factor that could govern the intracellular persistence of siRNA species in rapidly dividing cells, it is possible that nuclease-stabilized siRNAs are still diluted rapidly enough by cell division to limit prolonged gene silencing. However, cell division cannot explain the lack of differences observed after HDI since liver hepatocytes divide very slowly. The simplest explanation of these results is that the intrinsic nuclease stability of the individual siRNAs, unlike with antisense oligonucleotides, does not control their intracellular persistence. To test this hypothesis, we compared the activities of unmodified and nuclease-stabilized siRNAs in both rapidly and slowly dividing cells in vitro to determine if the nuclease-stabilized siRNAs would affect the magnitude or duration of gene silencing. Then, we used HDI to co-deliver a luciferase-expressing plasmid and either unmodified or nuclease-stabilized siRNAs in BALB/cJ mice, and we compared the kinetics of luciferase knockdown by the respective siRNAs using BLI.

The data presented here directly address the impact of nuclease stabilization on siRNA activity in vitro in rapidly and slowly dividing cells and in vivo after HDI in mice. There was a slight increase in the duration of luciferase knockdown by nuclease-stabilized siRNAs relative to unmodified siRNAs after cationic lipid transfection, but this difference was not observed after electroporation. In BALB/cJ mice, a four-fold increase in maximum luciferase knockdown was observed after hydrodynamic injection (HDI) of nuclease-stabilized siRNAs relative to unmodified siRNAs, yet the overall kinetics of the recovery after knockdown were nearly identical.

These experimental results, combined with the mathematical model predictions, imply that the differences in the knockdown observed with nuclease-stabilized siRNAs result chiefly from processes that occur during internalization before the siRNAs have the chance to interact with the intracellular RNAi machinery. For example, the predicted curves shown in Figure 3.8 can be made to closely match the experimental trends if the nuclease-stabilized siRNAs are more stable than unmodified siRNAs during internalization yet have similar degradation kinetics as unmodified siRNAs once localized to the cytosol. It should be noted that for these conditions the model also predicts a slight change in the magnitude of knockdown that was not observed experimentally, but this difference is likely caused by intricacies of the RNAi process that are not captured by our simplified model. Furthermore, there were no observed differences after electroporation of unmodified and nuclease-stabilized siRNAs, where the rapid entry of the siRNAs directly into the cytosol of the cells would allow both types of siRNAs to quickly associate with the intracellular machinery. This is exactly the result

predicted by the model if the intracellular siRNA degradation rate is constant and there is no opportunity for degradation in internalizing vesicles before escape into the cytosol.

Additionally, the in vivo results presented here are consistent with those reported by Morrissey et al. who observed much stronger knockdown after HDI by nuclease-stabilized siRNAs relative to unmodified siRNAs after 72 hours (9). Exposure to serum prior to uptake by the hepatocytes can lead to an appreciable degradation of the injected unmodified siRNAs, especially given the rapid degradation kinetics observed in the serum stability assay shown in Figure 3.2. Lecocq et al. reported that a significant portion of hydrodynamically injected plasmid DNA remained bound to the outer surface of hepatocytes for at least 1 hour after injection (21). If similar distribution patterns occur with siRNAs, then nuclease degradation of this portion of the injected dose that is not internalized rapidly could also lead to the greater magnitude of knockdown by nuclease-stabilized siRNAs relative to unmodified siRNAs after HDI of equivalent doses. Changes only in this extracellular siRNA degradation rate for the unmodified and nuclease-stabilized siRNAs can account for the observed experimental trends, as revealed by the model predictions shown in Figure 3.9. Although the overall kinetics of the luciferase knockdown are similar for unmodified and nuclease-stabilized siRNAs, the nuclease-stabilized siRNAs are predicted to increase the absolute magnitude of the knockdown. However, the degree to which this difference in effective dose that ultimately is internalized by the hepatocytes will affect the magnitude of knockdown will depend on the initial dose applied. If the magnitude of knockdown is already at its maximum using the unmodified siRNAs, then even a higher effective dose resulting from using nuclease-stabilized siRNAs cannot further reduce gene expression since the RNAi

machinery is saturated. This maximum administered dose will vary from one system to another since it can be affected by parameters such as the target mRNA degradation rate and the percent of the injected dose that reaches the target cells.

Further support for the idea that the intracellular nuclease stability of siRNAs is not a dominant factor controlling the kinetics of siRNA-mediated gene silencing comes from the model simulations shown in Figure 3.10. Although changes in the intracellular degradation rate can reasonably approximate the experimental results obtained using HeLa cells, this cannot account for the observed luciferase knockdown by unmodified and nuclease-stabilized siRNAs in slowly dividing fibroblasts or liver hepatocytes. Without cell division, the intracellular siRNA degradation rate plays a more dominant role in the duration of the inhibition. A mere two-fold reduction in the rate of intracellular siRNA degradation leads to a larger change in the duration of the knockdown (Figure 3.10B) than we observed experimentally between the unmodified and nuclease-stabilized siRNAs (Figure 3.3D), even though there was an approximately 20-fold difference in the observed serum stability of the unmodified and nuclease-stabilized siRNAs (Figure 3.2). Therefore, the intracellular siRNA degradation rate does not appear to be the parameter that is responsible for the observed differences. Moreover, the model predictions for luciferase knockdown after HDI in mice (Figure 3.10C) reveal that changes in the intracellular siRNA degradation rate alone cannot account for our observations showing that nuclease-stabilized siRNAs led to a greater magnitude of luciferase knockdown without affecting the overall kinetics (Figure 3.7). In fact, changes in the intracellular siRNA degradation rate alone do the exact opposite, leaving the

magnitude of the luciferase knockdown essentially unchanged while instead affecting the kinetics of the recovery back to the steady-state value.

Of practical importance, this comparison of the kinetics of gene silencing by unmodified and nuclease-stabilized siRNAs may serve as an additional method to confirm whether an observed knockdown phenotype is a result of an RNAi or an antisense mechanism. While nuclease-stabilized antisense oligonucleotides have been shown to enhance both the magnitude and duration of gene silencing, unmodified and nuclease-stabilized siRNAs do not exhibit significantly different functional behavior once inside cells. If the observed kinetics of gene silencing are nearly identical using both unmodified and modified siRNAs, then this would support the notion that the siRNAs are acting through an RNAi mechanism.

It is also important to consider under what circumstances nuclease-stabilized siRNAs can provide a significant benefit relative to unmodified siRNAs. Our observations indicate that nuclease-stabilized siRNAs do not provide considerable advantages in vitro with regard to either the magnitude or duration of gene silencing. In fact, nuclease-stabilized siRNAs are more costly to produce and frequently show decreased activity relative to unmodified siRNAs of the same sequence. However, the added costs and the potential for decreased activity of nuclease-stabilized siRNAs may be outweighed by other factors for in vivo applications. Recent reports have indicated that chemical modifications can modulate the immunostimulatory properties of siRNAs (23). Moreover, chemical modifications to confer added nuclease stability can increase the bioavailability of an injected siRNA species by protecting it from the rapid nuclease degradation that occurs with unmodified siRNAs. If siRNAs are injected locally, as in

intratumoral or intramuscular injection, the added nuclease stability may increase the time during which siRNAs can be internalized by the target cells. Systemic administration of siRNAs through hydrodynamic tail-vein injection, as employed in this study, or standard intravenous injection can also benefit from siRNA nuclease stabilization. Standard intravenous injection of relatively high doses (up to 30 mg kg^{-1}) of nuclease-stabilized siRNAs reduced hepatitis B virus (HBV) DNA levels in a mouse model of HBV (9). However, since the rapid renal clearance of naked siRNAs is a result of their small size, nuclease-stabilized siRNAs are still cleared rapidly from the bloodstream after systemic administration (2). To address both limitations of renal clearance and nuclease stability, Soutschek et al. showed that nuclease-stabilized, cholesterol-targeted siRNAs had a lower plasma clearance than unconjugated siRNAs after intravenous injection, presumably due to enhanced binding to serum proteins that slowed renal filtration (24). These nuclease-stabilized, cholesterol-targeted siRNAs were able to silence endogenous apolipoprotein B levels after standard intravenous injection, albeit at a high dose of 50 mg kg^{-1}. Development of nucleic acid delivery vehicles that encapsulate and protect siRNAs until internalization by the target cells represents another promising approach to avoid rapid removal of systemically administered siRNAs by renal filtration and nuclease degradation. Not only can carrier-mediated siRNA delivery considerably lower the required siRNA dose for efficacy, but it also permits the use of unmodified siRNAs even for systemic administration, as indicated by the multitude of published studies showing efficacy after intravenous injection of delivery vehicles containing unmodified siRNAs (25,26).

3.6   Conclusions

The results presented here indicate that the most significant impact of siRNA nuclease stability on gene silencing involves processes that occur prior to cellular internalization. The magnitude and duration of luciferase knockdown in vitro were not affected by the siRNA nuclease stability after electroporation, and only a slight increase in the duration of knockdown was observed after Oligofectamine transfection in both rapidly and slowly dividing cells. Moreover, use of nuclease-stabilized siRNAs led to a greater observed magnitude of luciferase knockdown after HDI in mice, but the kinetics of the knockdown were unaffected. By employing a mathematical model of siRNA-mediated gene silencing, we showed that only changes in the siRNA stability before cytosolic entry would lead to predicted luciferase knockdown curves consistent with all of the available experimental data. These findings suggest that nuclease-stabilized siRNAs do not offer any significant advantages over unmodified siRNAs with respect to either the magnitude or the duration of gene silencing once they achieve cytosolic localization in cells.

3.7 Acknowledgments

3.8 References

1.   Bertrand, J.-R., Pottier, M., Vekris, A., Opolon, P., Maksimenko, A. and Malvy, C. (2002) Comparison of antisense oligonucleotides and siRNAs in cell culture and in vivo. *Biochem Biophys Res Commun*, **296,** 1000-1004.

2.   Dykxhoorn, D.M., Palliser, D. and Lieberman, J. (2006) The silent treatment: siRNAs as small molecule drugs. *Gene Ther*, **13,** 541-552.

3.   Bartlett, D.W. and Davis, M.E. (2006) Insights into the kinetics of siRNA-mediated gene silencing from live-cell and live-animal bioluminescent imaging. *Nucleic Acids Res*, **34,** 322-333.

4.   Omi, K., Tokunaga, K. and Hohjoh, H. (2004) Long-lasting RNAi activity in mammalian neurons. *FEBS Lett*, **558,** 89-95.

5.   Song, E., Lee, S.-K., Dykxhoorn, D.M., Novina, C., Zhang, D., Crawford, K., Cerny, J., Sharp, P.A., Lieberman, J., Manjunath, N. et al. (2003) Sustained small interfering RNA-mediated human immunodeficiency virus type I inhibition in primary macrophages. *J Virol*, **77,** 7174-7181.

6.   Zimmermann, T.S., Lee, A.C.H., Akinc, A., Bramlage, B., Bumcrot, D., Fedoruk, M.N., Harborth, J., Heyes, J.A., Jeffs, L.B., John, M. et al. (2006) RNAi-mediated gene silencing in non-human primates. *Nature*, **441,** 111-114.

7.   Raemdonck, K., Remaut, K., Lucas, B., Sanders, N.N., Demeester, J. and De Smedt, S.C. (2006) In situ analysis of single-stranded and duplex siRNA integrity in living cells. *Biochemistry*, **45,** 10614-10623.

8.   Monia, B.P., Johnston, J.F., Sasmor, H. and Cummins, L.L. (1996) Nuclease resistance and antisense activity of modified oligonucleotides targeted to Ha-ras. *J Biol Chem*, **271,** 14533-14540.

9.   Morrissey, D.V., Blanchard, K., Shaw, L., Jensen, K., Lockridge, J.A., Dickinson, B., McSwiggen, J.A., Vargeese, C., Bowman, K., Shaffer, C.S. et al. (2005) Activity of stabilized short interfering RNA in a mouse model of hepatitis B virus replication. *Hepatology*, **41,** 1349-1356.

10.   Layzer, J.M., McCaffrey, A.P., Tanner, A.K., Huang, Z., Kay, M.A. and Sullenger, B.A. (2004) In vivo activity of nuclease-resistant siRNAs. *RNA*, **10,** 766-771.

11.   Chiu, Y.-L. and Rana, T.M. (2003) siRNA function in RNAi: a chemical modification analysis. *RNA*, **9,** 1034-1048.

12.   Choung, S., Kim, Y.J., Kim, S., Park, H.O. and Choi, Y.C. (2006) Chemical modification of siRNAs to improve serum stability without loss of efficacy. *Biochem Biophys Res Commun*, **342,** 919-927.

13.   Elmén, J., Thonberg, H., Ljungberg, K., Frieden, M., Westergaard, M., Xu, Y., Wahren, B., Liang, Z., Ørum, H., Koch, T. et al. (2005) Locked nucleic acid (LNA) mediated improvements in siRNA stability and functionality. *Nucleic Acids Res*, **33,** 439-447.

14.   Czauderna, F., Fechtner, M., Dames, S., Aygun, H., Klippel, A., Pronk, G.J., Giese, K. and Kaufmann, J. (2003) Structural variations and stabilising modifications of synthetic siRNAs in mammalian cells. *Nucleic Acids Res*, **31,** 2705-2716.

15. McCaffrey, A.P., Meuse, L., Pham, T.-T.T., Conklin, D.S., Hannon, G.J. and Kay, M.A. (2002) RNA interference in adult mice. *Nature*, **418,** 38-39.

16. Challita, P.-M., Skelton, D., El-Khoueiry, A., Yu, X.-J., Weinberg, K. and Kohn, D.B. (1995) Multiple modifications in cis elements of the long terminal repeat of retroviral vectors lead to increased expression and decreased DNA methylation in embryonic carcinoma cells. *J Virol*, **69,** 748-755.

17. Bahner, I., Kearns, K., Hao, Q., Smogorzewska, E. and Kohn, D. (1996) Transduction of human CD34+ hematopoietic progenitor cells by a retroviral vector expressing an RRE decoy inhibits human immunodeficiency virus type 1 replication in myelomonocytic cells produced in long-term culture. *J Virol*, **70,** 4352-4360.

18. Persengiev, S.P., Zhu, X. and Green, M.R. (2004) Nonspecific, concentration-dependent stimulation and repression of mammalian gene expression by small interfering RNAs (siRNAs). *RNA*, **10,** 12-18.

19. Huppi, K., Martin, S.E. and Caplen, N.J. (2005) Defining and assaying RNAi in mammalian cells. *Mol Cell*, **17,** 1-10.

20. Rose, S.D., Kim, D.-H., Amarzguioui, M., Heidel, J.D., Collingwood, M.A., Davis, M.E., Rossi, J.J. and Behlke, M.A. (2005) Functional polarity is introduced by Dicer processing of short substrate RNAs. *Nucleic Acids Res*, **33,** 4140-4156.

21. Lecocq, M., Andrianaivo, F., Warnier, M., Wattiaux-De Coninck, S., Wattiaux, R. and Jadot, M. (2003) Uptake by mouse liver and intracellular fate of plasmid DNA after a rapid tail vein injection of a small or a large volume. *J Gene Med*, **5,** 142-156.

22. Reinoso, R.F., Telfer, B.A., Brennan, B.S. and Rowland, M. (2001) Uptake of teicoplanin by isolated rat hepatocytes: comparison with in vivo hepatic distribution. *Drug Metab Dispos*, **29,** 453-349.

23. Judge, A.D., Bola, G., Lee, A.C.H. and MacLachlan, I. (2006) Design of noninflammatory synthetic siRNA mediating potent gene silencing in vivo. *Mol Ther*, **13,** 494-505.

24. Soutschek, J., Akinc, A., Bramiage, B., Charisse, K., Constien, R., Donoghue, M., Elbashir, S., Geick, A., Hadwiger, P., Harborth, J. et al. (2004) Therapeutic silencing of an endogenous gene by systemic administration of modified siRNAs. *Nature*, **432,** 173-178.

25. Behlke, M.A. (2006) Progress towards in vivo use of siRNAs. *Mol Ther*, **13,** 644-670.

26. Hu-Lieskovan, S., Heidel, J.D., Bartlett, D.W., Davis, M.E. and Triche, T.J. (2005) Sequence-specific knockdown of EWS-FLI1 by targeted, nonviral delivery of small interfering RNA inhibits tumor growth in a murine model of Ewing's sarcoma. *Cancer Res*, **65,** 8984-8992.

4 Physicochemical and biological characterization of targeted, nucleic acid-containing nanoparticles[†]

4.1 Abstract

Nucleic acid-based therapeutics have the potential to provide potent and highly specific treatments for a variety of human ailments. However, systemic delivery continues to be a significant hurdle to success. Multifunctional nanoparticles are being investigated as systemic, nonviral delivery systems, and here we describe the physicochemical and biological characterization of cyclodextrin-containing polycations (CDP) and their nanoparticles formed with nucleic acids including plasmid DNA (pDNA) and small interfering RNA (siRNA). These polycation/nucleic acid complexes can be tuned by formulation conditions to yield nanoparticles with sizes ranging from 60-150 nm, zeta potentials from 10-30 mV, and molecular weights from $\sim 7 \times 10^7$-1×10^9 g mol^{-1} as determined by light scattering techniques. Inclusion complexes formed between adamantane (AD)-containing molecules and the β-cyclodextrin molecules enable the modular attachment of polyethylene glycol (AD-PEG) conjugates for steric stabilization and targeting ligands (AD-PEG-transferrin) for cell-specific targeting. A 70-nm nanoparticle can contain $\sim$10,000 CDP polymer chains, $\sim$2,000 siRNA molecules, $\sim$4,000 AD-PEG$_{5000}$ molecules, and $\sim$100 AD-PEG$_{5000}$-Tf molecules; this represents a significant payload of siRNA and a large ratio of siRNA to targeting ligand (20:1). The nanoparticles protect the nucleic acid payload from nuclease degradation, do not

aggregate at physiological salt concentrations, and cause minimal erythrocyte aggregation and complement fixation at the concentrations typically used for in vivo application. Uptake of the nucleic acid-containing nanoparticles by HeLa cells is measured by flow cytometry and visualized by confocal microscopy. Competitive uptake experiments show that the transferrin-targeted nanoparticles display enhanced affinity for the transferrin receptor through avidity effects (multi-ligand binding). Functional efficacy of the delivered pDNA and siRNA is demonstrated through luciferase reporter protein expression and knockdown, respectively. The analysis of the CDP delivery vehicle provides insights that can be applied to the design of targeted nucleic acid delivery vehicles in general.

4.2   Introduction

Nucleic acid-based therapeutics are envisioned to play a significant role in the next generation of treatments for a variety of diseases such as cancer. In addition to the classic gene therapy approach of delivering DNA to replace mutated or absent genes, nucleic acid molecules can also be used to regulate the production of disease-associated proteins at both the transcriptional and translational levels. These nucleic acid-based drugs have received significant attention as promising new therapeutics, yet their application in vivo has been largely limited by the challenge of delivery; this has been particularly true for systemic delivery.

Naked nucleic acid molecules are rapidly degraded by ubiquitous nucleases present in the bloodstream. Double-stranded nucleic acid molecules ranging in size from small-interfering RNAs (siRNAs) to plasmids (pDNA) have a half-life of less than one hour in serum (1-3). Selective chemical modification of nucleic acids can increase

nuclease resistance and enable systemic delivery of naked siRNA molecules with functional efficacy in vivo (1,4). However, even nuclease-stabilized nucleic acids must still overcome other elimination barriers such as renal clearance that severely limit the efficacy of systemically delivered, small nucleic acid therapeutics (5). Attachment of specific targeting ligands can induce binding to protein carriers or uptake by the desired population of cells to be treated. Bioconjugates of the nucleic acid therapeutics covalently attached directly to targeting ligands such as cholesterol and antibodies have shown efficacy both in vitro and in vivo (4,6). While these methods for nuclease stabilization and covalent attachment of targeting ligands are promising for small nucleic acid therapeutics, the use of lipid- or polymer-based delivery vehicles is an approach for systemic delivery that can provide functions not achievable with naked nucleic acids or their covalent attachment to targeting moieties.

Carrier-mediated delivery has several advantages over the delivery of individual nucleic acid molecules. Encapsulation of the payload within a lipid bilayer or through electrostatic interactions is nonspecific, so these delivery vehicles can be used for generalized nucleic acid delivery. The use of a carrier enables delivery of many nucleic acid molecules per uptake event (this is especially important if the uptake involves highly specific cell-surface receptors since they are typically low in number), and isolation from exposure to the systemic environment can permit the use of unmodified nucleic acids (7). Modularly designed delivery vehicles can also take advantage of covalent or non-covalent attachment of hydrophilic polymers for steric stabilization and/or targeting ligands for cell-specific delivery, two critical features for systemic delivery (7,8). Such

modifications can affect the resulting biodistribution of delivery vehicles through passive and/or active targeting (7-10).

Passive targeting occurs as a result of the intrinsic physicochemical properties of the delivery vehicle. For example, the charge and size of the delivery vehicle alone can bias its biodistribution. The charge of the delivery vehicle significantly impacts its interaction with components of the bloodstream; highly charged particles can lead to complement activation, while near-neutral particles exhibit reduced phagocytic uptake (11,12). Specifically, cationic polymers such as polylysine and polyethylenimine have been shown to activate the complement system, and increasing polycation length and surface charge density lead to higher complement activation (11). Rapid binding of charged molecules by complement proteins or other opsonins can lead to immune stimulation and rapid clearance of the delivery vehicles from the bloodstream. The size of the delivery vehicle also matters for systemic delivery. Based on measured sieving coefficients for the glomerular capillary wall, it is estimated that the threshold for first-pass elimination by the kidneys is approximately 10 nm (diameter) (13), placing a lower size limit on the assembled delivery vehicles. On the other end of the size spectrum, macromolecular complexes preferentially accumulate in tumors through the enhanced permeability and retention (EPR) effect. However, large macromolecules or delivery vehicles exhibit limited diffusion in the extracellular space, such as the tumor interstitium, and in the complex intracellular environment (14); in both situations, restricted movement will severely limit efficacy by preventing uptake by a sufficient number of cells or hindering the ability of the delivered nanoparticles to localize to intracellular compartments such as the nucleus. Other restrictions limiting the maximum

size of delivery vehicles can also be imposed by the selectivity of receptors on certain cell types. For example, a study by Rensen et al. demonstrated that nanoparticles larger than 70 nm in diameter were not recognized by the asialoglycoprotein receptor (ASGPR) (15), placing an upper size limit on the nanoparticles that can be delivered to hepatocytes through this receptor.

Recent efforts toward targeted delivery have focused on decorating the surface of delivery vehicles with cell surface receptor-specific targeting ligands as a means of active targeting. Hydrophilic polymers, such as polyethylene glycol (PEG), can be attached to the surface of the delivery vehicles to mask surface charge and prevent nonspecific interactions, helping to prevent unwanted binding to components of the bloodstream, slow uptake by the reticuloendothelial system (RES), and alter the cellular uptake patterns (8,16). Further addition of entities that can interact with cell surface receptors, such as the receptors' natural ligands, antibodies, or antibody fragments, allows the delivery vehicle to target particular cell types and undergo receptor-mediated endocytosis upon binding to the surface receptor (7,8,15).

In light of these considerations, a successful delivery vehicle must be engineered to have the following characteristics: (i) be small enough to extravasate and exhibit adequate tissue penetration, yet avoid rapid renal clearance; (ii) minimize nonspecific interactions and opsonization while providing specific targeting to a given cell; and (iii) protect the nucleic acid from degradation, but willingly release it upon arrival at the proper site. Over the past few years, we have been developing a synthetic delivery system based on a cyclodextrin-containing polycation (CDP) that has demonstrated some success in delivering nucleic acid payloads that include pDNA, siRNA, and DNAzymes

(7,17-20). This delivery system is the first to be *de novo* designed for systemic delivery

of nucleic acids and completely formulated by self-assembly (17). Here, we describe the

physicochemical and biological characterization of the cyclodextrin-containing

polycation delivery system and its formulation with nucleic acids. We illustrate issues of

importance when designing any polycation composite with nucleic acids through the use

of the CDP and point out when the conclusions are specific to this system only.

4.3 Materials and methods

4.3.1 *Formulation of nucleic acid nanoparticles*

The chemical structure of the cyclodextrin-containing polycation is shown in

Figure 4.1A. This short, linear polycation can be synthesized with (CDP-Im) or without

(CDP) the imidazole groups on the terminal amines (17,18). A schematic showing

nanoparticle formation using CDP-Im and nucleic acid is shown in Figure 4.1B;

nanoparticles are formed by mixing equal volumes of CDP-Im and nucleic acid. The

ratio of positive (+) charges (2 moles of positive charge per CDP-Im monomer; denoted

β-CD) to negative (-) charges (1 mole of negative charge per nucleotide) is defined as the

formulation charge ratio (+/-). Polyethylene glycol (PEG) molecules containing

adamantane (AD) on the proximal end and either methoxy (AD-PEG) or a targeting

ligand such as transferrin (AD-PEG-Tf) on the distal end can be attached to the surface of

the nanoparticles via inclusion complex formation between adamantane and the β-CD

molecules on the polycation backbone (16,17). The molecular weight of the PEG chain

is typically 5,000 daltons (PEG_{5000}).
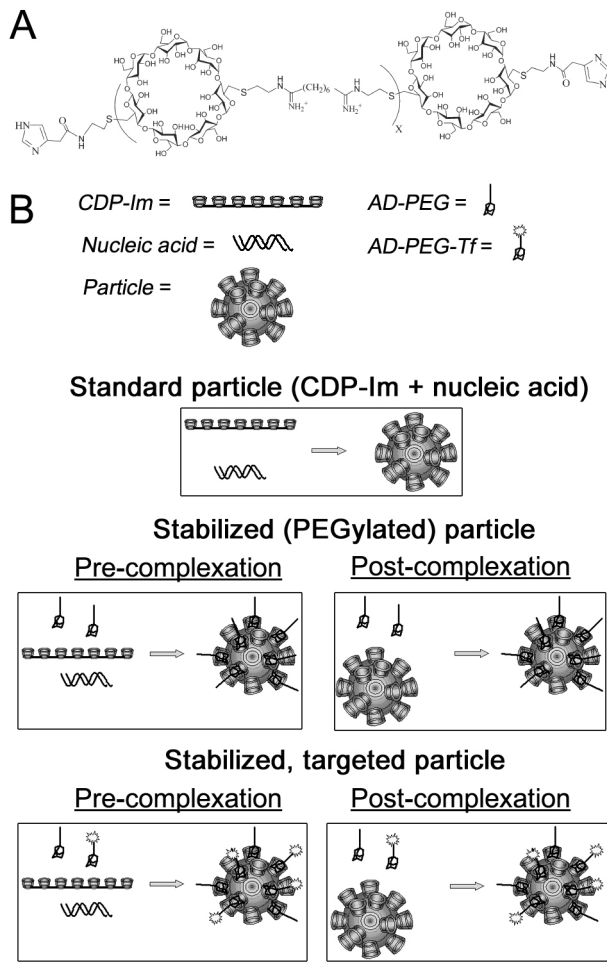
Figure 4.1. Formation of nucleic acid-containing nanoparticles using CDP-Im. (A) Schematic of the chemical structure of CDP-Im. (B) Schematic of nanoparticle assembly.

4.3.2   Formulation of PEGylated/targeted nucleic acid nanoparticles

Pre-complexation (self-assembly)

Before addition to the nucleic acid, the CDP or CDP-Im was mixed with an AD-PEG conjugate at a 1:1 AD-PEG:β-CD (mol:mol) ratio in water. Targeted nanoparticles also require the addition of ligand-modified AD-PEG-X (e.g., AD-PEG-Tf (7,19,20)) as a percentage of the total AD-PEG in the mixture. For example, 1 mol% AD-PEG-Tf nanoparticles contain 0.01 moles AD-PEG-Tf for every 0.99 moles AD-PEG. The mixture of CDP (or CDP-Im), AD-PEG, and AD-PEG-Ligand in water was then added to

an equal volume of nucleic acid in water such that the ratio of positive charges from CDP or CDP-Im to negative charges from the nucleic acid was equal to the desired charge ratio. A schematic of this assembly process is shown in Figure 4.1B. Unless specified otherwise, all PEGylated or targeted nucleic acid nanoparticles used in these studies were prepared through the pre-complexation method.

Post-complexation

Particles were initially formulated in water by mixing equal volumes of nucleic acid and the cyclodextrin-containing polycation. After nanoparticles had formed, the AD-PEG and AD-PEG-Tf conjugates were added directly to the formulation mixture at the desired ratio of AD-PEG:β-CD (mol:mol). A schematic of this assembly process is shown in Figure 4.1B.

4.3.3   Electrophoretic mobility shift assay

siRNA-containing nanoparticles were formulated at different charge ratios by changing the amount of CDP added to 1 μg of siRNA. CDP was first dissolved in 10 μL water and then added to an equal volume of water containing 1 μg of nucleic acid. After a 30-min incubation at room temperature, 10 μL of each formulation was run on a 1% agarose gel and visualized by ethidium bromide staining.

4.3.4   Individual nanoparticle charge ratio

siRNA nanoparticles were formulated in 40 μL water at charge ratios from 5 to 30 (+/-). After formulation, the nanoparticles were separated from the free components by addition of 400 μL PBS, to cause nanoparticle aggregation, followed by centrifugation to pellet the aggregated nanoparticles. Since the CDP is terminated by primary amines, quantitation of polycation content was accomplished by measuring the amount of primary

amines as follows. 400 µL of the supernatant was removed and combined with 200 µL

of 0.01% w/v 2,4,6-trinitrobenzenesulfonic acid (Sigma). After incubating these samples

for 2 h at 37°C, 200 µL 10% SDS and 100 µL of 1 N HCl were added to each sample

before measuring the absorbance at 335 nm with a spectrophotometer. The amount of

CDP in each sample was determined by comparison to a standard curve of CDP. The

total positive charge present in each sample was calculated from the mass of CDP present

using the fixed charge density of 0.0014 moles "+" per gram. This gave the number of

unbound "+" charges present, so the number of bound "+" charges in the nanoparticles

could be determined by subtracting the number unbound from the total "+" charges added

during formulation. Assuming 100% incorporation of the nucleic acid into the

nanoparticles at a formulation charge ratio of 3 (+/-) (based on the electrophoretic

mobility shift assays; see Results), the ratio of CDP to nucleic acid within each

nanoparticle is equal to the number of bound "+" charges divided by the total number of

"-" charges from the nucleic acid.

4.3.5 *Serum stability*

Particles were formulated in water at a charge ratio of 3 (+/-) with an siRNA

concentration of 0.05 g L^{-1}. 10 µL of 100% mouse serum (Sigma) were added to 10 µL

of the nanoparticle formulation and subsequently incubated for 4 h at 37°C and 5% CO_2.

0.25 µg naked siRNA in 5 µL water were added to 5 µL of 100% mouse serum and also

incubated for 4 h at 37°C and 5% CO_2. For comparison to the t = 4 h samples, identical

amounts of naked siRNA or siRNA nanoparticles were exposed to 50% mouse serum

immediately before gel loading (t = 0 h). 10 µL of each sample (containing 0.25 µg

siRNA) were loaded per well of a 1% agarose gel. Displacement of the nucleic acid from

the nanoparticles was achieved by adding 1% sodium dodecyl sulfate (SDS) to the sample immediately prior to gel loading. Gel electrophoresis was performed by applying 100 V for 30 min, and the bands were visualized by ethidium bromide staining.

4.3.6   Dynamic light scattering (DLS)

Particle formulations were diluted to a volume of 1.4 mL, placed in a cuvette, and inserted into a ZetaPALS (Brookhaven Instruments Corporation) instrument to measure both the size and zeta potential. Reported effective hydrodynamic diameters represent the average values from a total of 5-10 runs of 30 seconds each, while zeta potentials represent the average of 10 runs each.

4.3.7   Transmission electron microscopy (TEM)

Particles containing CDP-Im and siRNA (0.1 g L^{-1}) and PEGylated nanoparticles containing CDP-Im, AD-PEG (1:1 AD-PEG:β-CD mole ratio), and siRNA (0.5 g L^{-1}) were formulated in water at a charge ratio of 3 (+/-). Samples were stained with 2% uranyl acetate and then examined with an EM201C electron microscope (Philips).

4.3.8   Atomic force microscopy (AFM)

Particles containing CDP-Im and siRNA (0.1 g L^{-1}) and PEGylated nanoparticles containing CDP-Im, AD-PEG (1:1 AD-PEG:β-CD mole ratio), and siRNA (0.5 g L^{-1}) were formulated in water at a charge ratio of 3 (+/-). 20 μL of each formulation solution were dropped on a freshly cleaved mica disc (Ted Pella, Inc.) and dried with pressurized air. Images were acquired with a Digital Instruments MultiMode AFM with a Nanoscope IV controller in tapping mode at a scan rate of 1 Hz using a BS Multi75 probe (BudgetSensors) with a resonant frequency of 75 kHz and a force constant of 3 N m^{-1}. Height images were flattened and processed for visualization with the derivative matrix

convolution filter using WSxM scanning probe microscopy software (Nanotec Electronica).

4.3.9 Isothermal titration calorimetry (ITC)

A MicroCal MCS titration calorimeter was used to investigate the thermodynamic properties of the interaction between AD-PEG conjugates and the β-cyclodextrin molecules on the CDP-Im backbone. CDP-Im (free or in nanoparticles) at 0.22 mM total β-CD in water was placed in the sample cell of the instrument. The reference cell contained water alone without CDP-Im. Small amounts of an AD-PEG stock solution at a concentration of 2.2 mM in water were titrated into the sample cell in 25 separate 10-µL increments. Titrations were performed at 30°C. The measured parameters were δn, the number of moles of ligand (AD-PEG) added to the sample cell, and q, the amount of heat released or absorbed. The Simplex algorithm in the Origin data analysis software was used to determine the following parameters: K, the equilibrium binding constant; n, the number of available binding sites; and ΔH, the change in enthalpy. A more in-depth description of the thermodynamic analysis applied to ITC is provided by Blandamer et al. (21).

4.3.10 Percentage of AD-PEG$_{5000}$ bound after formulation

The small molecule, lactose (Lac), was attached to the end of AD-PEG$_{5000}$ to enable quantification using the Amplex Red Galactose Oxidase Assay Kit (Molecular Probes). Nanoparticles were formulated in a total volume of 100 µL water by adding a 50 µL solution containing CDP-Im and AD-PEG$_{5000}$-Lac (1:1 mole ratio of AD-PEG$_{5000}$-Lac: β-CD) in water to a 50 µL solution of siRNA in water. Control formulations were

created by mixing CDP-Im and AD-PEG$_{5000}$-Lac without siRNA in 100 µL water. Nanoparticles and control formulations were filtered with Biomax (Millipore) centrifugal filtration devices with a 50 kDa MWCO to separate free and bound components. The Amplex Red Galactose Oxidase Assay Kit (Molecular Probes) was used to quantify the amount of AD-PEG$_{5000}$-Lac in the filtrate and retentate of all samples. Concentrations were determined by comparison to a standard curve of AD-PEG$_{5000}$-Lac. The percentage of AD-PEG$_{5000}$-Lac bound to the nanoparticles was determined by subtracting the fraction of recovered AD-PEG$_{5000}$-Lac in the filtrate of the nanoparticle samples from the fraction of recovered AD-PEG$_{5000}$-Lac in the filtrate of the control samples.

4.3.11 Percentage of AD-PEG$_{5000}$-Tf bound after formulation

Tf-targeted nanoparticles were formulated in a total volume of 100 µL water by adding a 50 µL solution of CDP-Im, AD-PEG$_{5000}$, and AD-PEG$_{5000}$-Tf (1:1 mole ratio of AD-PEG$_{5000}$-X:β-CD where AD-PEG$_{5000}$-X was composed of either 1 mol% or 5 mol% AD-PEG$_{5000}$-Tf and the remainder AD-PEG$_{5000}$) in water to a 50 µL solution of siRNA in water. Control formulations were created by mixing CDP-Im, AD-PEG$_{5000}$, and AD-PEG$_{5000}$-Tf without siRNA in 100 µL water. Nanoparticles and control formulations were filtered with Nanosep (Millipore) centrifugal filtration devices with a 300 kDa MWCO to separate free and bound components. Total protein content in the filtrate (unbound AD-PEG$_{5000}$-Tf) and retentate (bound AD-PEG$_{5000}$-Tf) was determined using the BioRad DC protein assay. The percentage of AD-PEG$_{5000}$-Tf bound to the nanoparticles was determined by subtracting the fraction of recovered AD-PEG$_{5000}$-Tf in the filtrate of the nanoparticle samples from the fraction of recovered AD-PEG$_{5000}$-Tf in the filtrate of the control samples.

4.3.12 Multi-angle light scattering (MALS)

Particle formulations were loaded into a 10-mL syringe connected to a syringe pump to control the flow rate into a Dawn EOS (Wyatt Technology) multi-angle light scattering instrument. The typical flow rate used was 1 mL min^{-1}. Data were fit by the Astra software to the Debye model with a detector fit degree of 2. The *dn/dc* value for the nanoparticles was determined to be 0.14 mL g^{-1}, and the mass concentration used in the calculations was determined from the total amount of CDP-Im and nucleic acid incorporated into the nanoparticles assuming an individual nanoparticle charge ratio of 1.1 (+/-) and complete incorporation of the nucleic acid added during formulation.

4.3.13 Individual nanoparticle stoichiometry

An estimate for the stoichiometry of each nanoparticle (i.e., number of CDP, nucleic acid, AD-PEG, and AD-PEG-Tf molecules) can be calculated from the following equations.

$$MW_{part} = \#NA \times \#bp \times MW_{bp} + \#CDP \times MW_{CDP} + \#PEG \times MW_{PEG} + \#Tf \times MW_{Tf} \qquad (4.1)$$

$$CR = \frac{\#CDP}{\#NA \times \#bp} \qquad (4.2)$$

$$\#PEG = f_{PEG} \times (100\% - \%Tf) \times \#CDP \times PR \times \frac{FR}{CR} \qquad (4.3)$$

$$\#Tf = f_{Tf} \times \%Tf \times \#CDP \times PR \times \frac{FR}{CR} \qquad (4.4)$$

where *#NA* is the number of nucleic acid molecules in the nanoparticle, *#CDP* is the number of CDP monomers (β-CD) in the nanoparticle, *#PEG* is the number of AD-PEG molecules in the nanoparticle, *#Tf* is the number of AD-PEG-Tf molecules in the nanoparticle, *MW$_{part}$* is the molecular weight of an individual nanoparticle (determined by

MALS), *#bp* is the number of base pairs per nucleic acid molecule (e.g., 21 for siRNA),

MW_{bp} is the average molecular weight of each nucleic acid base pair (~650 Da as an

approximation), MW_{CDP} is the molecular weight of each CDP monomer (~1,460 Da),

MW_{PEG} is the molecular weight of each AD-PEG molecule (~5,200 Da for AD-PEG$_{5000}$),

MW_{Tf} is the molecular weight of each AD-PEG-Tf molecule (~85,000 Da for AD-

PEG$_{5000}$-Tf), f_{PEG} is the fraction of the AD-PEG molecules that bind to nanoparticles

during formulation, *PR* is the mole ratio of AD-PEG to β-CD during formulation, *FR* is

the formulation charge ratio (+/-), *CR* is the charge ratio (+/- = 1.1) of each individual

nanoparticle, f_{Tf} is the fraction of the AD-PEG-Tf molecules that bind to nanoparticles

during formulation, and *%Tf* is the mole percent AD-PEG-Tf during formulation.

4.3.14 Salt stability

Particle formulations were diluted to a volume of 1260 μL, placed in a cuvette,

and inserted into a ZetaPALS (Brookhaven Instruments Corporation) instrument. Kinetic

studies of aggregation were performed by recording the effective diameters at 1 minute

intervals after the addition of 1/10 volume 10X PBS to achieve a final concentration of

1X PBS, corresponding to physiological salt concentration.

4.3.15 Erythrocyte aggregation

Erythrocytes were obtained from whole bovine calf blood (Rockland

Immunochemicals, Inc.) by multiple rounds of centrifugation at 700x*g* and 4°C for 10

min followed by removal of the supernatant and resuspension of the pellet of erythrocytes

in cold PBS (Cellgro) until the supernatant became clear. Finally, the erythrocytes were

resuspended at a concentration of 1% (v/v). The free polycations or formulated

nanoparticles were added to a 24-well plate and diluted with PBS to a volume of 100 μL.

Subsequently, 100 μL of the erythrocyte suspension were added to each well and the plate was incubated for 1 h at 37°C. Images were taken of each well using a CCD-IRIS/RGB (Sony) video camera attached to an Eclipse TE-300 (Nikon) inverted microscope to visually determine the degree of aggregation.

4.3.16 Complement fixation

To test the complement fixation by polycations or CDP-based nanoparticles, antibody-sensitized sheep erythrocytes were used in a CH50 assay modified from Plank et al. (11). 25 μL human complement sera (Sigma) in gelatin veronal buffer (Sigma) were added in a 1:1.5 dilution series across a row of wells in a 96-well plate. To this same row of wells were added 25 μL of the desired concentration of polycation in its free form or complexed with calf thymus DNA (CT-DNA). A different concentration of the polycations or nanoparticles was added to each row of wells. After a 30-min incubation at 37°C, 1.25×10^7 antibody-sensitized sheep erythrocytes (Sigma) were added to each well and the plate was incubated with shaking for 1 h at 37°C. Finally, the plate was centrifuged at 2,000 RPM for 10 min, 100 μL of the supernatant from each well was transferred to a new 96-well plate, and the absorbance at 410 nm was determined using a SpectraMax 190 (Molecular Devices) microplate reader. This wavelength corresponds to an absorbance peak for the hemoglobin that is released after lysis of the erythrocytes. The CH50 unit is used to define the serum dilution required to achieve 50% lysis of the antibody-sensitized sheep erythrocytes. If the substance being tested binds complement proteins to an appreciable degree, it will sequester these complement proteins and prevent them from binding to and lysing the erythrocytes. As a result, a lower serum dilution (CH50) will be required to achieve 50% erythrocyte lysis under these conditions. The

reported *%CH50max* represents the ratio of the CH50 for the substance being tested to the CH50 determined for the complement sera alone (CH50max).

4.3.17 Cellular uptake

Method 1: Flow cytometry

A FACSCalibur (BD Biosciences) flow cytometer was used to detect the uptake of FL-siRNA (fluorescein attached to the 5' end of the sense strand) delivered with or without the CDP-Im delivery vehicle. HeLa cells were seeded at $2x10^4$ cells per well in 24-well plates 2-3 days prior to transfection and grown in medium supplemented with 10% fetal bovine serum (FBS) and antibiotics (penicillin/streptomycin). The growth medium was removed from each well and replaced with 200 µL Opti-MEM I (Invitrogen), 200 µL Opti-MEM I with 100 nM FL-siRNA, or 200 µL Opti-MEM I with 100 nM FL-siRNA formulated into CDP-Im nanoparticles at a charge ratio of 3 (+/-). After incubation for 2 h at 37°C and 5% CO_2, the transfection medium was removed and the cells were trypsinized and resuspended in Hanks Balanced Salt Solution (HBSS) with 1% bovine serum albumin (BSA) and 10 µg mL^{-1} propidium iodide to detect cell viability.

Method 2: Confocal microscopy

HeLa cells were seeded at $2x10^4$ cells per well in a LabTek II Chamber Slide 2 days prior to transfection and grown in medium supplemented with 10% FBS and antibiotics (penicillin/streptomycin). The growth medium was removed from each well and replaced with 200 µL Opti-MEM I containing 100 nM FL-siRNA formulated into CDP-Im nanoparticles at a charge ratio of 3 (+/-). After incubation for 2 h at 37°C and 5% CO_2, cells were fixed for 15 min at room temperature using 4% paraformaldehyde in

PBS. F-actin was stained with rhodamine phalloidin (Invitrogen) according to manufacturer's instructions. Cells were mounted with Biomeda Gel/Mount according to manufacturer's instructions and the coverslips were subsequently sealed using nail polish. Fluorescent images were acquired using a Zeiss LSM 510 Meta laser scanning confocal microscope with a 40X water-immersion objective.

4.3.18 Competitive uptake

Competitive uptake studies were conducted to determine the impact of free holo-transferrin (holo-Tf) on the relative uptake of transferrin-targeted (containing 1 mol% AD-PEG$_{5000}$-Tf) or non-targeted nanoparticles. By formulating the nanoparticles with Cy3-siRNA (Cy3 attached to the 5' end of the sense strand), a Tecan SPECTRAFluorPlus plate reader could be used to measure the total cell-associated fluorescence after transfection. Cells were seeded at $2x10^4$ cells per well in 24-well plates 2-3 days prior to transfection and grown in medium supplemented with 10% FBS and antibiotics (penicillin/streptomycin). The growth medium was removed from each well and replaced with 200 μL Opti-MEM I containing 100 nM Cy3-siRNA formulated in nanoparticles. After incubation for 30 min at 37°C and 5% CO_2, the transfection medium was removed and the cells were lysed in 100 μL cell lysate buffer (Promega). Total fluorescence in the 100 μL lysate per well was measured with the SPECTRAFluorPlus plate reader and the number of siRNA molecules was estimated from a standard curve of Cy3-siRNA. Cells in two wells that were not transfected were trypsinized and counted to provide an estimate for the average number of cells per well.

4.3.19 Avidity effects

Method 1: Competitive cell-surface transferrin receptor (TfR) binding assay

Competitive uptake experiments were performed using flow cytometry to detect the uptake of fluorescently labeled holo-Tf. Unlabeled holo-Tf, Tf conjugates (AD-PEG_{5000}-Tf), or Tf-targeted siRNA nanoparticles (1 mol% AD-PEG_{5000}-Tf) were used to compete for uptake by the transferrin receptors on the surface of HeLa cells. Cells were seeded at $2x10^4$ cells per well in 24-well plates 2-3 days prior to transfection and grown in medium supplemented with 10% FBS and antibiotics (penicillin/streptomycin). The growth medium was removed from each well and replaced with 200 μL Opti-MEM I containing 1% BSA, 20 nM AlexaFluor488-labeled holo-Tf (AF488-Tf), and the desired unlabeled Tf competitor. After incubation for 1 h at 37°C and 5% CO_2, the transfection medium was removed and the cells were trypsinized and resuspended in Hanks Balanced Salt Solution (HBSS) with 1% bovine serum albumin (BSA) and 10 μg mL^{-1} propidium iodide to detect cell viability. To enable direct comparison of the effects of avidity, the total amount of Tf was kept constant whether it was in its free form, as AD-PEG_{5000}-Tf, or as AD-PEG_{5000}-Tf on the siRNA nanoparticles. The relative uptake under each condition is reported as the ratio of the mean fluorescence of the wells with unlabeled competitor to the mean fluorescence of the wells with AF488-Tf alone.

Method 2: Live-cell binding assay

A live-cell binding assay was used to measure the relative binding of transferrin-targeted siRNA nanoparticles. $3x10^5$ HeLa cells were resuspended in 100 μL PBS in individual microcentrifuge tubes and cooled on ice. To each microcentrifuge tube were added 100 μL PBS containing PEGylated or Tf-targeted nanoparticles formulated with Cy3-labeled siRNA such that the final Cy3-siRNA concentration was 100 nM. After incubating for 30 minutes on ice, the microcentrifuge tubes were centrifuged for 5

minutes at 200x*g* to pellet the cells. 100 µL of the supernatant from each microcentrifuge tube were added to a well in a black 96-well plate, and the Cy3 fluorescence was measured using a Tecan Safire plate reader. Comparison to a standard curve of Cy3-siRNA nanoparticles allowed quantification of the amount of Cy3-siRNA in each well, and the percent bound (fraction associated with the cell pellet) was determined by subtracting the fluorescence remaining in the supernatant from the initial amount added.

4.3.20 Luciferase knockdown after siRNA transfection

Functional efficacy of pDNA and siRNA delivered by CDP-Im nanoparticles was demonstrated in HeLa cells by co-transfecting the pGL3-CV vector (Promega) containing the firefly luciferase gene and a non-targeting control siRNA (siCON1) synthesized by Dharmacon or a luciferase-targeting siRNA (siLuc) synthesized by Integrated DNA Technologies. The sequence of the siCON1 siRNA is UAGCGACUAAACACAUCAAUU (sense) and UUGAUGUGUUUAGUCGCUAUU (antisense). The sequence of the siLuc siRNA is GUGCCAGAGUCCUUCGAUAdTdT (sense) and UAUCGAAGGACUCUGGCACdTdT (antisense). The Promega Luciferase Assay System was then used to quantify the relative luciferase expression in cells that had been transfected with 1 µg pGL3-CV alone, 1 µg pGL3-CV and 100 nM siCON1, or 1 µg pGL3-CV and 100 nM siLuc. HeLa cells were seeded at $2x10^4$ cells per well in 24-well plates 2-3 days prior to transfection and grown in medium supplemented with 10% FBS and antibiotics (penicillin/streptomycin). CDP-Im nanoparticles were formulated to contain 1 µg pGL3-CV vector and 100 nM siRNA in 200 µL Opti-MEM I. The growth medium was removed from each well and replaced with 200 µL Opti-MEM I containing the formulated nanoparticles. After incubation for 5 h at 37°C and 5% CO_2, 800 µL

complete growth medium was added to each well. 48 h later, the cells were lysed in

100 μL 1X Luciferase Cell Culture Lysis Reagent (Promega). 10 μL of the cell lysate

were added to 90 μL of the luciferase substrate, and bioluminescence was measured

using a MonoLight (Pharmingen) luminometer. 5 μL of the cell lysate were used in a

BioRad DC protein assay to determine the protein concentration in each lysate sample.

Luciferase activities are reported as relative light units per mg protein.

4.4   Results and discussion

4.4.1   *Particle formation requires a slight excess of positive charge and protects siRNA from degradation in serum*

Results from an electrophoretic mobility shift assay (EMSA) demonstrate that

siRNA nanoparticles completely form at charge ratios (+/-) greater than ~1 to 1.5 (Figure

4.2A). At sufficiently high charge ratios, the band corresponding to the free nucleic acid

becomes undetectable since the nucleic acid remains associated with the nanoparticles

that have greatly reduced electrophoretic mobility. To determine what portion of the

polycations (CDP) added during formulation actually are incorporated into the

nanoparticles, the free polycations were separated from the nanoparticles after

formulation. Regardless of the formulation charge ratio up to 30 (+/-), the charge ratio of

individual nanoparticles remains ~1 (+/-) (Figure 4.2B). This is consistent with the

results shown in Figure 4.2A where charge ratios slightly greater than 1 were required to

achieve complete nanoparticle formation. A nuclease stability assay was conducted to

determine if the formation of nanoparticles could protect the nucleic acid payload from

degradation by nucleases present in serum. While naked siRNA degrades rapidly in

serum, siRNA within nanoparticles is protected from significant degradation even after 4

hours in 50% mouse serum (Figure 4.3). Additionally, the data given in Figure 4.3 show

(i) there is essentially complete encapsulation of the siRNA by the nanoparticles, and (ii)

when the nanoparticles exposed to serum are disrupted with SDS, the nucleic acids

released are still intact siRNA duplexes.
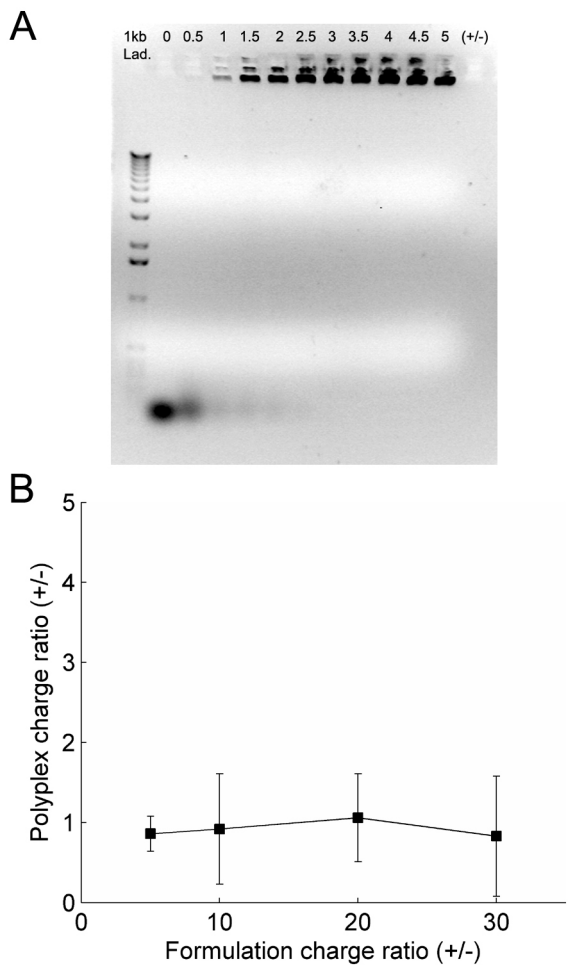
Figure 4.2. Effect of formulation charge ratio (+/-). (A) Electrophoretic gel mobility shift assay demonstrating the effect of formulation charge ratio on siRNA nanoparticle formation. (B) Individual nanoparticle charge ratio as a function of formulation charge ratio.

Time(h)	0	0	4	0	0	4	4
CDPIm	-	-	-	+	+	+	+
siRNA	-	+	+	+	+	+	+
SDS	+	+	+	-	+	-	+
Serum	+	+	+	+	+	+	+
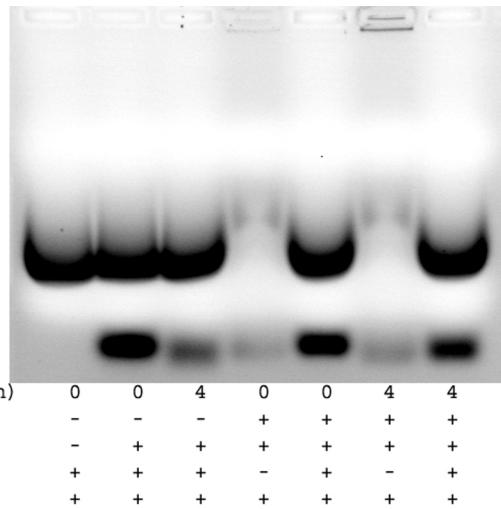
Figure 4.3. Nuclease stability of siRNA encapsulated within nanoparticles. For the t = 4 lanes, naked siRNA or siRNA within CDP-Im nanoparticles (3 (+/-)) was incubated in 50% mouse serum for 4 h at 37°C and 5% CO_2. For the t = 0 lanes, serum was added to an equivalent amount of naked siRNA or siRNA within CDP-Im nanoparticles immediately before loading into the gel. Addition of 1% SDS was used to displace the siRNA from the nanoparticles to visualize the amount of intact siRNA remaining. The first lane demonstrates that the upper bands are nonspecific bands resulting from the interaction between SDS, serum, and the ethidium bromide stain, while the lower bands correspond to the free siRNA.

4.4.2   Formulation conditions affect nanoparticle size and zeta potential

Transmission electron microscopy (TEM) and atomic force microscopy (AFM) were used to visualize the siRNA nanoparticles formulated at a charge ratio of 3 (+/-). The images in Figure 4.4 demonstrate that the siRNA nanoparticles assume a roughly spherical shape, but the unPEGylated nanoparticles display more variability in size and adopt a slightly oblong shape relative to the PEGylated nanoparticles when they are visualized by AFM on the mica surface. While a large fraction of the unPEGylated nanoparticles (0.1 g L^{-1} siRNA) have diameters that exceed 100 nm, PEGylated nanoparticles (0.5 g L^{-1} siRNA) formulated with a 1:1 mole ratio of AD-PEG$_{5000}$:β-CD consistently have diameters <100 nm and are approximately 60-80 nm.
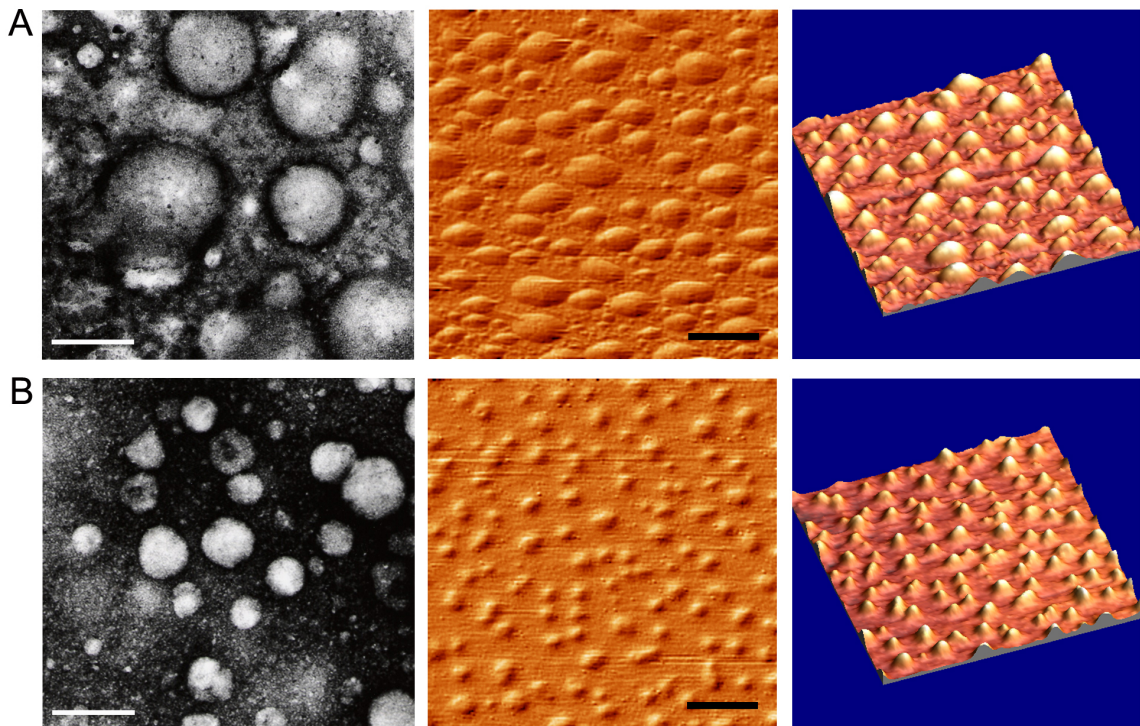
Figure 4.4. Transmission electron microscopy (left panels) and atomic force microscopy (center and right panels) images of (A) unPEGylated and (B) PEGylated siRNA nanoparticles formulated at a charge ratio of 3 (+/-). Scale bar = 100 nm (left panels) and 200 nm (center and right panels).

To further investigate the effects of formulation conditions, dynamic light scattering was used to measure the effective hydrodynamic diameter and zeta potential of the nanoparticles. Consistent with the TEM and AFM images, the results shown in Figure 4.5A reveal that the nucleic acid concentration during formulation affects the size of the nanoparticles. Nanoparticles formulated with siRNA, pDNA, and calf thymus (CT-DNA) show nearly identical trends of increased size with higher nucleic acid concentration. However, nanoparticles that are formulated in the presence of AD-PEG$_{5000}$ (PEGylated nanoparticles formed by the pre-complexation method) do not exhibit such a dependence on formulation conditions (Figure 4.5B).
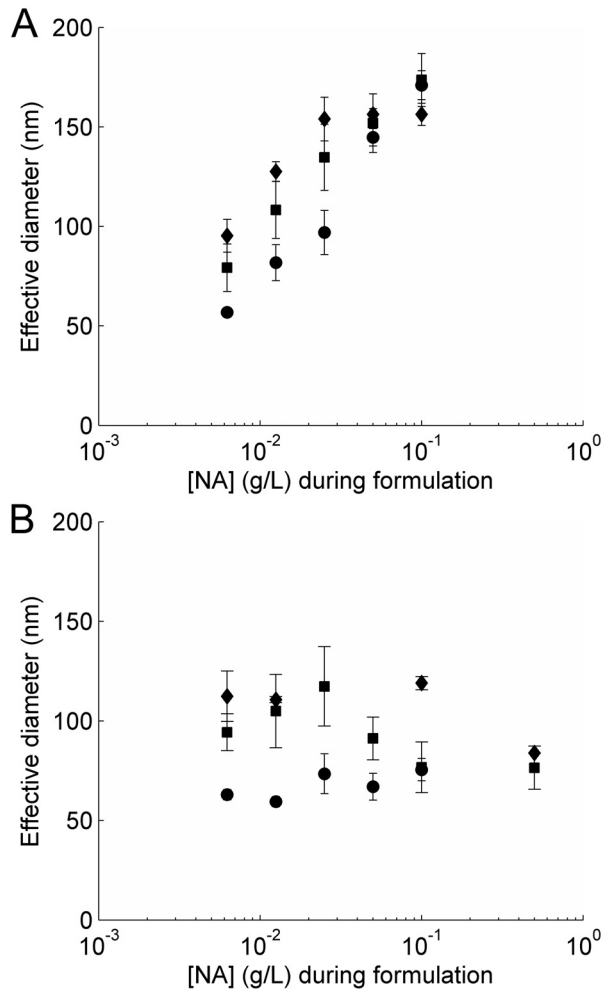
Figure 4.5. Effect of nucleic acid concentration ([NA]) during formulation on the size of (A) unPEGylated or (B) PEGylated nanoparticles. Nanoparticles were formulated at a charge ratio of 3 (+/-) using CDP-Im and either siRNA, pDNA, or CT-DNA (calf thymus DNA). PEGylated nanoparticles were formulated by adding a 1:1 mole ratio of AD-PEG$_{5000}$:β-CD. Nanoparticle effective diameter was determined using dynamic light scattering. Squares = CDP-Im/siRNA nanoparticles, circles = CDP-Im/pDNA nanoparticles, diamonds = CDP-Im/CT-DNA nanoparticles.

These properties allow the delivery vehicles to be fine-tuned with respect to size by altering the formulation conditions accordingly (i.e., PEGylation through the pre- or post-complexation method). The zeta potential of unPEGylated nanoparticles ranges from 10 (particles ~60 nm in diameter) to 30 mV (particles ~150 nm in diameter), while that of PEGylated nanoparticles ranges from 10 to 20 mV for similarly sized nanoparticles. This positive zeta potential implies that the charge ratio of the individual

nanoparticles is slightly greater than 1 (+/-). The AD-PEG$_{5000}$ conjugates can be further modified to contain targeting ligands on the distal end of the PEG chain. For example, transferrin can be conjugated to the AD-PEG$_{5000}$ molecules to yield AD-PEG$_{5000}$-Tf (19). Because the transferrin protein is negatively charged, inclusion of AD-PEG$_{5000}$-Tf molecules during nanoparticle formulation reduces the zeta potential of siRNA nanoparticles in a concentration-dependent manner (Figure 4.6). Bellocq et al. reported a similar trend using nanoparticles made with pDNA (19).
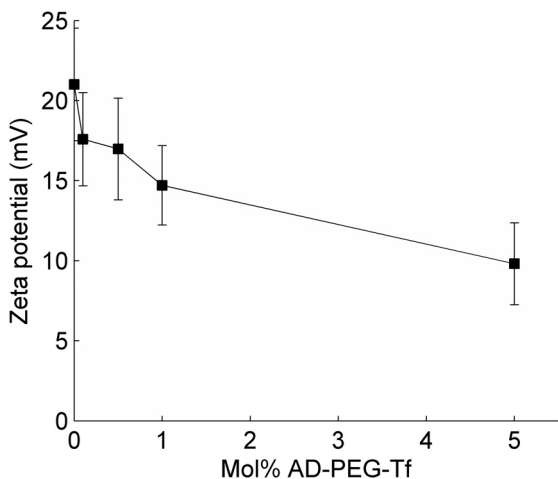
Figure 4.6. Nanoparticle zeta potential as a function of AD-PEG$_{5000}$-Tf ligand concentration during formulation. Nanoparticles were formulated at a charge ratio of 3 (+/-) using CDP-Im and siRNA, and the AD-PEG$_{5000}$ or AD-PEG$_{5000}$-Tf molecules were added after nanoparticle formation (post-complexation). The total number of moles of AD-PEG$_{5000}$-X (AD-PEG$_{5000}$ and AD-PEG$_{5000}$-Tf) was equal to the number of moles of β-CD, and the mixture of AD-PEG$_{5000}$ and AD-PEG$_{5000}$-Tf is defined by the % AD-PEG$_{5000}$-Tf.

4.4.3   *AD-PEG conjugates bind to the surface of nanoparticles through inclusion complex formation*

An important property of the cyclodextrin-containing polycations is their ability to form inclusion complexes with hydrophobic molecules. This provides the opportunity for modular attachment of different stabilizing molecules or targeting ligands through coupling to an adamantane (AD) molecule that forms inclusion complexes with the β-

cyclodextrin molecules. Isothermal titration calorimetry was used to investigate the

thermodynamics of the interaction between AD-PEG molecules and CDP-Im either in its

free form or within siRNA-containing nanoparticles (Table 4.1).

Table 4.1. Measured ITC parameters for the binding between AD-PEG$_{5000}$ and β-CD alone, polycation alone (CDP-Im), or CDP-Im/siRNA nanoparticles formulated at charge ratios from 3 to 15 (+/-). For comparison, literature values are provided for the binding between β-CD alone and adamantane carboxylate (22).

	n	$K\ (M^{-1})$	$\Delta H\ (cal\ M^{-1})$
β-CD + adamantane carboxylate			
β-CD	1	42000	-4440
β-CD + AD-PEG$_{5000}$			
β-CD	1.1	30600	-7358
siRNA nanoparticle + AD-PEG$_{5000}$			
3 (+/-)	0.34 ± 0.09	5110 ± 730	-15200 ± 4090
5 (+/-)	0.38 ± 0.04	6320 ± 330	-12600 ± 570
10 (+/-)	0.48 ± 0.02	8090 ± 620	-10100 ± 520
15 (+/-)	0.49 ± 0.01	8050 ± 800	-10600 ± 450
CDP-Im	0.54 ± 0.04	8380 ± 940	-9460 ± 1490

Figure 4.7 shows representative ITC data plots for binding between AD-PEG$_{5000}$

and CDP-Im formulated with siRNA at a charge ratio of 3 (+/-), CDP-Im formulated with

siRNA at a charge ratio of 10 (+/-), and CDP-Im alone. As the charge ratio increases, the

measured binding parameters approach those of free CDP-Im. Given the previous results

showing the actual nanoparticle charge ratio is slightly greater than 1 (+/-), this is

consistent with the presence of excess free CDP-Im at charge ratios >1.
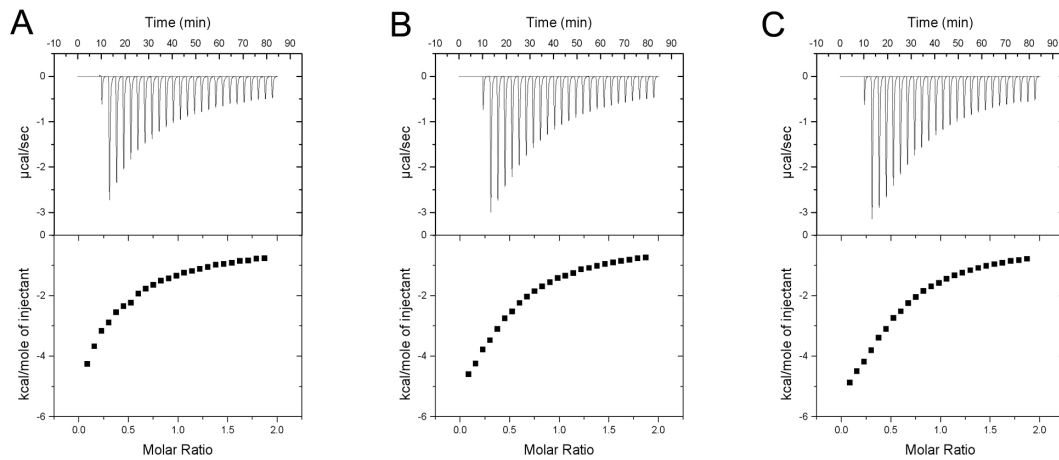
Figure 4.7. Isothermal titration calorimetry (ITC) plots characterizing the binding between AD-PEG$_{5000}$ molecules and free CDP-Im or siRNA nanoparticles. (A) CDP-Im/siRNA nanoparticle (3 (+/-)) and AD-PEG$_{5000}$, (B) CDP-Im/siRNA nanoparticle (10 (+/-)) and AD-PEG$_{5000}$, (C) CDP-Im and AD-PEG$_{5000}$.

The value of n represents the fraction of the β-CD molecules available for inclusion complex formation with the AD-PEG molecules. Each β-CD cup can interact with a single adamantane molecule, as previous reports have shown a 1:1 binding stoichiometry between adamantane molecules and β-CD (*22*). While binding between individual β-cyclodextrins and AD-PEG$_{5000}$ conjugates gives the expected n value of ~1, binding between CDP-Im and AD-PEG$_{5000}$ exhibits an n value of ~0.5. When the AD-PEG$_{5000}$ molecule containing a 5000-Da PEG chain binds to a β-CD cup on the CDP-Im polymer, it likely provides steric hindrance that impedes binding between other AD-PEG$_{5000}$ molecules and nearby β-CD molecules. Support for this hypothesis comes from the observation that the n value for binding between CDP-Im and AD-PEG$_{500}$ molecules containing short 500-Da PEG chains is 0.92 ± 0.05, likely indicating that the shorter PEG chains do not interfere to as great an extent with the binding of AD-PEG$_{500}$ to neighboring β-CD molecules.

Another interesting pattern is observed with the ΔH values, representing the

change in enthalpy that results from binding between an AD-PEG molecule and a β-CD

cup. These values are all negative, indicating that energy is released upon binding due to

the favorable interaction between the hydrophobic adamantane and the β-CD cup.

Notably, ΔH is more negative for AD-PEG$_{5000}$ binding to the siRNA nanoparticles than it

is for AD-PEG$_{5000}$ binding to free CDP-Im. We hypothesize that this increased

stabilization energy, in addition to the inclusion complex formation, is a result of

favorable interactions between the PEG chains themselves when they are grouped

together on the surface of an siRNA nanoparticle.

4.4.4 *Particle molecular weight can be used to estimate individual nanoparticle stoichiometry*

Determining the individual component stoichiometry of the nanoparticles

provides important insights into their functional properties. Centrifugal filtration was

used to separate unbound components from those bound to the nanoparticles. As

discussed previously, it was determined that the individual nanoparticle charge ratio (i.e.,

the ratio of positive charges from the CDP-Im to negative charges from the nucleic acid)

is slightly greater than 1; we used 1.1 (+/-) for the calculations. The percent of the total

AD-PEG$_{5000}$ or AD-PEG$_{5000}$-Tf added to the formulation mixture that remains free was

determined by quantifying the AD-PEG$_{5000}$ (experiment actually used AD-PEG$_{5000}$-Lac

and we assumed that the value for AD-PEG$_{5000}$ would be approximately the same) or AD-

PEG$_{5000}$-Tf recovered in the filtrate versus the retentate after centrifugal filtration. The

results of these measurements indicated that approximately 3% of the total AD-PEG$_{5000}$

and 10% of the total AD-PEG$_{5000}$-Tf added during formulation remained associated with

the nanoparticles. The greater degree of binding measured for the AD-PEG$_{5000}$-Tf

conjugates may be partly due to charge interactions between the negatively charged

transferrin proteins and the positively charged nanoparticles. The final piece of data

needed to estimate the individual nanoparticle stoichiometry is the molecular weight of

the nanoparticles. This was determined using multi-angle light scattering. The results in

Figure 4.8 show that the molecular weight of nanoparticles formulated with siRNA,

pDNA, or calf thymus (CT-DNA) scales approximately as r^3, where r is the radius of the

nanoparticle determined by DLS.
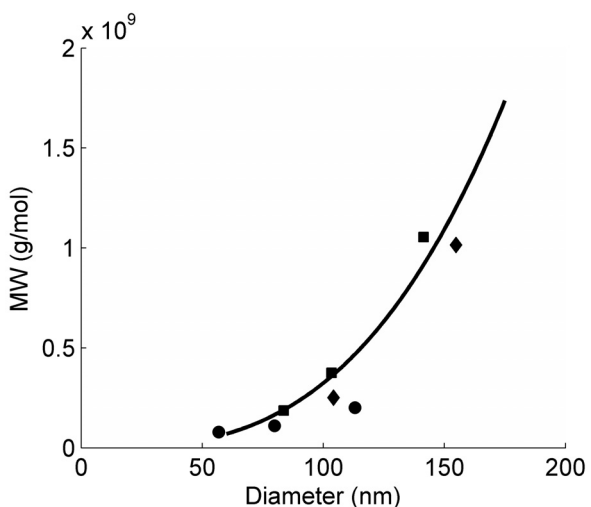
Figure 4.8. Relationship between nanoparticle size and molecular weight (MW) as determined by dynamic and multi-angle light scattering. Nanoparticles were formulated at a charge ratio of 3 (+/-) using CDP-Im and either siRNA, pDNA, or CT-DNA. Effective diameters were measured using dynamic light scattering, and molecular weights were determined using multi-angle light scattering. Squares = CDP-Im/siRNA nanoparticles, circles = CDP-Im/pDNA nanoparticles, diamonds = CDP-Im/CT-DNA nanoparticles, solid line = r^3 scaling dependence of the MW of nanoparticles starting with a MW of 7×10^7 g mol^{-1} for a 60-nm nanoparticle.

This similarity between all three types of nanoparticles is consistent with the

trends observed in Figure 4.5, further supporting the interesting result that formulation

with a variety of nucleic acids leads to nanoparticles with similar physical properties. An

unPEGylated nanoparticle with a diameter of 70 nm is expected to have a molecular

weight around 1×10^8 g mol^{-1} from data given in Figure 4.8. Inserting this molecular

weight and an individual nanoparticle charge ratio of 1.1 (+/-) into Equations 1 and 2

yields 48,800 CDP monomers (or 9,750 CDP chains with a degree of polymerization of

5) and 2,110 siRNA molecules (with 21 bp per siRNA) per nanoparticle. For the sake of

calculation, we can then use this value for *#CDP* to estimate the number of AD-PEG$_{5000}$

and AD-PEG$_{5000}$-Tf molecules per nanoparticle using Equations 3 and 4. For example, a

70-nm siRNA nanoparticle with a molecular weight of 1.3×10^8 g mol^{-1} (accounting for

the added mass from the PEG conjugates) formulated at a charge ratio of 3 (+/-) with 1

mol% AD-PEG$_{5000}$-Tf is calculated to contain 9,750 CDP chains, 2,110 siRNA

molecules, 3,950 AD-PEG$_{5000}$ molecules, and 133 AD-PEG$_{5000}$-Tf molecules.

By approximating each siRNA molecule as a cylinder with a diameter of 2.37 nm

and a length of 7.14 nm (approximated based on the dimensions of a double-stranded

DNA helix), each siRNA molecule can be estimated to occupy a volume of 3.15×10^{-25}

m^3. Therefore, 2,110 siRNA molecules would occupy a minimum volume of 6.7×10^{-23}

m^3; this represents approximately 37% of the total nanoparticle volume of 1.8×10^{-22} m^3

for a 70-nm sphere. Therefore, this number of siRNA molecules appears to be reasonable

given the size constraints of the nanoparticles. Furthermore, the corresponding surface

density for the estimated number of AD-PEG$_{5000}$ chains on a 70-nm nanoparticle is ~43

pmol cm^{-2} or 0.26 chains nm^{-2}. The calculated average distance between PEG$_{5000}$

molecules at this surface density is ~2.0 nm, while the Flory radius is ~6 nm. Since the

distance between PEG$_{5000}$ molecules is much less than the Flory radius, the PEG$_{5000}$

chains are expected to interact laterally and extend out from the surface in a dense brush

layer with an estimated thickness of ~12.5 nm. Hansen et al. further examined the brush

scaling laws for polyethylene glycols and predicted that PEG_{5000} solutions must have

monomer volume fractions, ϕ, greater than 0.07-0.09 to be in the brush regime (23). This

is satisfied when the PEG_{5000} surface density exceeds ~26-28 pmol cm^{-2}, again indicating

that the PEG_{5000} chains on the nanoparticles are in the brush regime.

4.4.5 *PEGylation provides steric stabilization to the nanoparticles and reduces nonspecific interactions*

DLS-based kinetic studies of aggregation were performed to determine whether

the inclusion of AD-PEG conjugates could help to stabilize the nanoparticles against

aggregation at physiological salt concentrations. First, the ratio of AD-PEG_{5000}:β-CD

(mol:mol) was varied from 0 to 2 to investigate how the surface density of AD-PEG_{5000}

affects the steric stability of siRNA nanoparticles formulated through the post-

complexation method (Figure 4.9A). Nanoparticles formulated with AD-PEG_{5000}:β-CD

(mol:mol) ratios >1 do not exhibit observable aggregation after 15 minutes in 1X PBS.

At ratios <1, aggregation increases as the ratio of AD-PEG_{5000}:β-CD (mol:mol)

decreases. These results with siRNA-containing nanoparticles are consistent with those

observed by Pun et al. using nanoparticles made with pDNA (24). The length of the PEG

molecule in the AD-PEG conjugate also impacts its ability to confer steric stabilization to

the nanoparticles. As shown in Figure 4.9B, the stabilization effects increase with the

length of the PEG chain, with AD-PEG_{500} (AD-PEG_{500}:β-CD = 1) only slightly slowing

the aggregation while AD-PEG_{5000} (AD-PEG_{5000}:β-CD = 1) prevents detectable

aggregation up to 15 minutes after salt addition. If the AD-PEG_{500} chains, like the AD-

PEG_{5000} chains, also achieve a surface density of ~43 pmol cm^{-2} (AD-PEG_{500}:β-CD = 1),

then the average distance between PEG_{500} chains remains ~2.0 nm. However, since this

is not less than the Flory radius for a PEG$_{500}$ molecule (~1.5 nm), the PEG$_{500}$ molecules

are not expected to form the brush-like layer on the nanoparticle surface that is needed

for steric stabilization. Furthermore, modification of up to 1 mol% of the AD-PEG$_{5000}$

chains with Tf (AD-PEG$_{5000}$-Tf) leads to minimal perturbations in the salt stability of the

nanoparticles. However, at 5 mol% AD-PEG$_{5000}$-Tf, gradual nanoparticle aggregation

becomes apparent during the 15-minute incubation in 1X PBS.
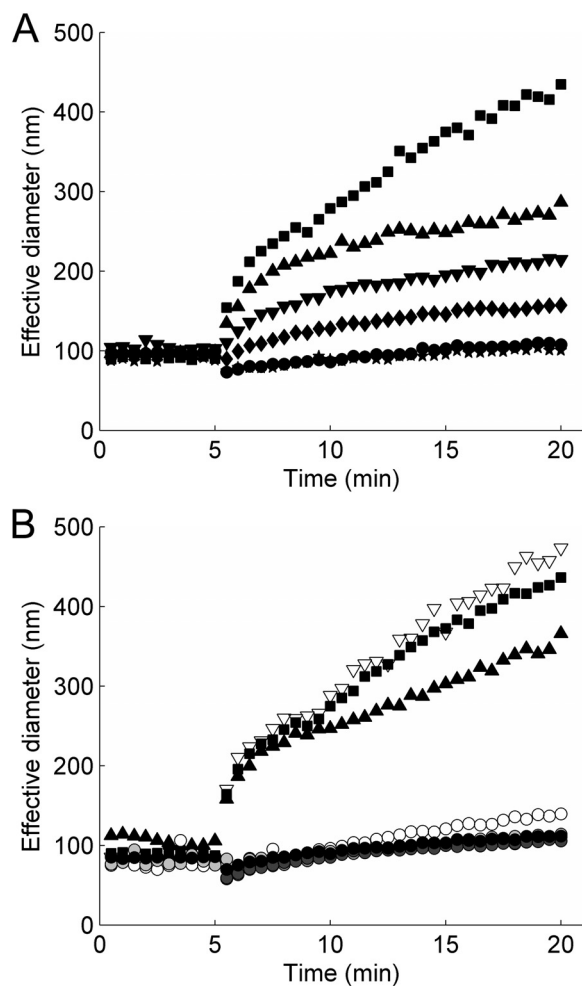
Figure 4.9. Aggregation of siRNA nanoparticles in physiological salt solutions. 140 µL of a 10X PBS solution were added to 1260 µL of the nanoparticles in water after 5 minutes, and dynamic light scattering was used to follow the formation of aggregates with time. (A) Effect of the ratio of AD-PEG$_{5000}$:β-CD on nanoparticle stability. CDP-Im/siRNA (3 (+/-)) nanoparticles were formulated without AD-PEG$_{5000}$ (black squares) or through the post-complexation method with an AD-PEG$_{5000}$:β-CD mole ratio of 0.25:1 (black triangles), 0.5:1 (inverted black triangles), 0.75:1 (black diamonds), 1:1 (black circles), or 2:1 (black stars). (B) Effect of PEG chain length, adamantane conjugation, and Tf targeting ligand density on nanoparticle

stability. CDP-Im/siRNA (3 (+/-)) nanoparticles were formulated without AD-PEG$_{5000}$ (black squares), with a PEG$_{5000}$ (no adamantane):β-CD mole ratio of 1:1 (open inverted triangles), with an AD-PEG$_{500}$:β-CD mole ratio of 1:1 (black triangles), with an AD-PEG$_{5000}$:β-CD mole ratio of 1:1 (black circles), or with a 1:1 mole ratio of AD-PEG$_{5000}$-X:β-CD where AD-PEG$_{5000}$-X was composed of 0.1 wt% AD-PEG$_{5000}$-Tf (dark gray circles), 0.1 mol% AD-PEG$_{5000}$-Tf (gray circles), 1 mol% AD-PEG$_{5000}$-Tf (light gray circles), or 5 mol% AD-PEG$_{5000}$-Tf (open circles) and the remainder AD-PEG$_{5000}$.

Besides providing steric stabilization to the nanoparticles, PEGylation can help to reduce nonspecific interactions. Specifically, experiments were performed to study the interaction between the polycations (or nanoparticles) and erythrocytes (Figure 4.10). Significant erythrocyte binding will lead to aggregation that can be observed by visual inspection using a light microscope. While the free CDP or CDP-Im showed negligible aggregation at 0.2 g L^{-1}, some aggregation was observed as the concentration increased to 2 g L^{-1} (Figure 4.10A-D). Erythrocyte aggregation was also measured after incubation with siRNA nanoparticles that were formulated with CDP-Im and a 1:1 mole ratio of AD-PEG$_{5000}$:CDP-Im (Figure 4.10E). The results demonstrate that PEGylated nanoparticles do not lead to any observable aggregation at a total CDP-Im concentration of 0.2 g L^{-1}, corresponding to the expected concentration after systemic delivery in vivo (7).
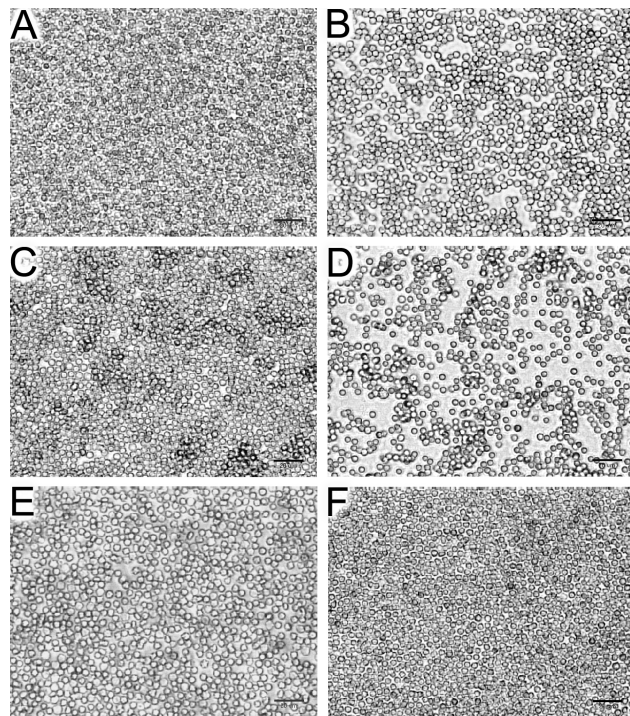
Figure 4.10. Erythrocyte aggregation. (A) 0.2 g L^{-1} CDP, (B) 2 g L^{-1} CDP, (C) 0.2 g L^{-1} CDP-Im, (D) 2 g L^{-1} CDP-Im, (E) CDP-Im/siRNA (3 (+/-)) nanoparticles at 0.2 g L^{-1} CDP-Im formulated with a 1:1 mole ratio of AD-PEG$_{5000}$:β-CD, (F) PBS alone. Scale bar = 20 μm.

4.4.6 PEGylated nanoparticles show minimal complement fixation

Complement fixation by polyethylenimine and polylysine was compared to that of CDP or CDP-Im. The CDP and CDP-Im molecules do not show as much complement fixation as PEI (branched or linear) or a 36-mer of polylysine, but they do exhibit higher complement fixation than a 5-mer of polylysine (Figure 4.11A). This is consistent with the notion that polycation length and charge density can augment complement activation (11).

Because complement fixation was observed at the physiologically relevant concentration of 0.2 g L^{-1}, corresponding to the typical concentration of polycations in the bloodstream after delivery of nucleic acids at a dose of 2.5 mg kg^{-1} (a typical dose used for in vivo siRNA delivery (7)), experiments were performed to test nanoparticles

formulated with calf thymus DNA and stabilized by PEGylation (Figure 4.11B).

Notably, these formulations showed minimal complement fixation at polymer

concentrations of 0.2 g L^{-1}.
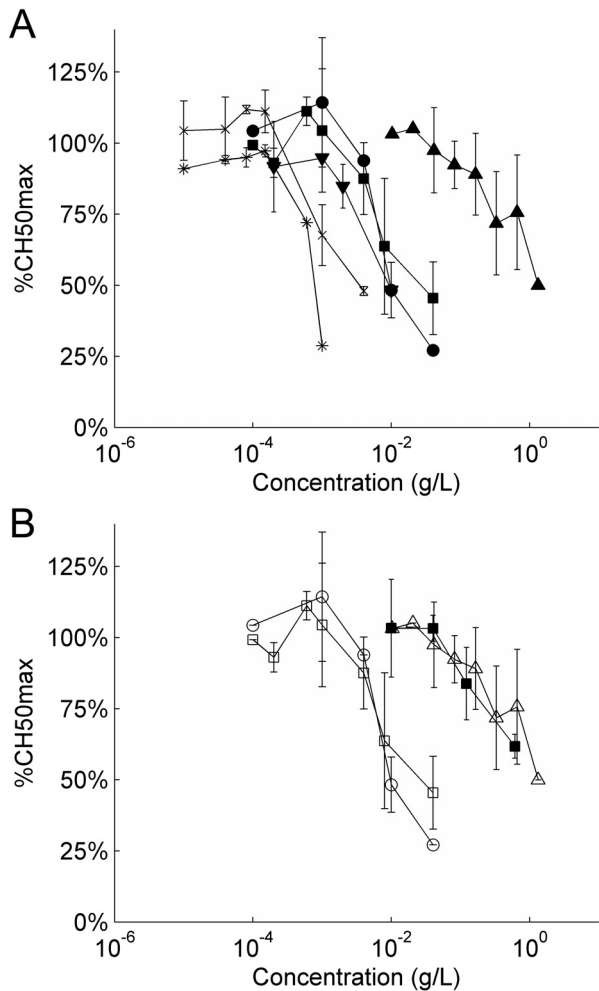
Figure 4.11. Complement fixation. (A) Complement fixation by free polycations. Asterisks = branched PEI, x = linear PEI, black triangles = pentalysine, inverted black triangles = polylysine (36-mer), black squares = CDP, black circles = CDP-Im. (B) Complement fixation by CDP/CT-DNA (3 (+/-)) nanoparticles formulated with a 1:1 mole ratio of AD-PEG$_{5000}$:β-CD (black squares). The curves for CDP (open squares), CDP-Im (open circles), and pentalysine (open triangles) are shown again for comparison.

4.4.7 Particles achieve intracellular delivery of siRNA in vitro

The uptake of nanoparticles containing fluorescently labeled siRNA was assessed

using flow cytometry and confocal fluorescence microscopy. While naked siRNAs do

not achieve measurable levels of cellular uptake, formulation into nanoparticles with CDP-Im dramatically increases the amount of cell-associated siRNA as measured by flow cytometry (Figure 4.12A). To confirm that the siRNA was being delivered to the interior of cells, confocal fluorescence microscopy was used to visualize cells transfected with nanoparticles containing fluorescently labeled siRNA (Figure 4.12B). The internalized nanoparticles exhibited a punctate staining and were eventually observed to accumulate in the perinuclear region.
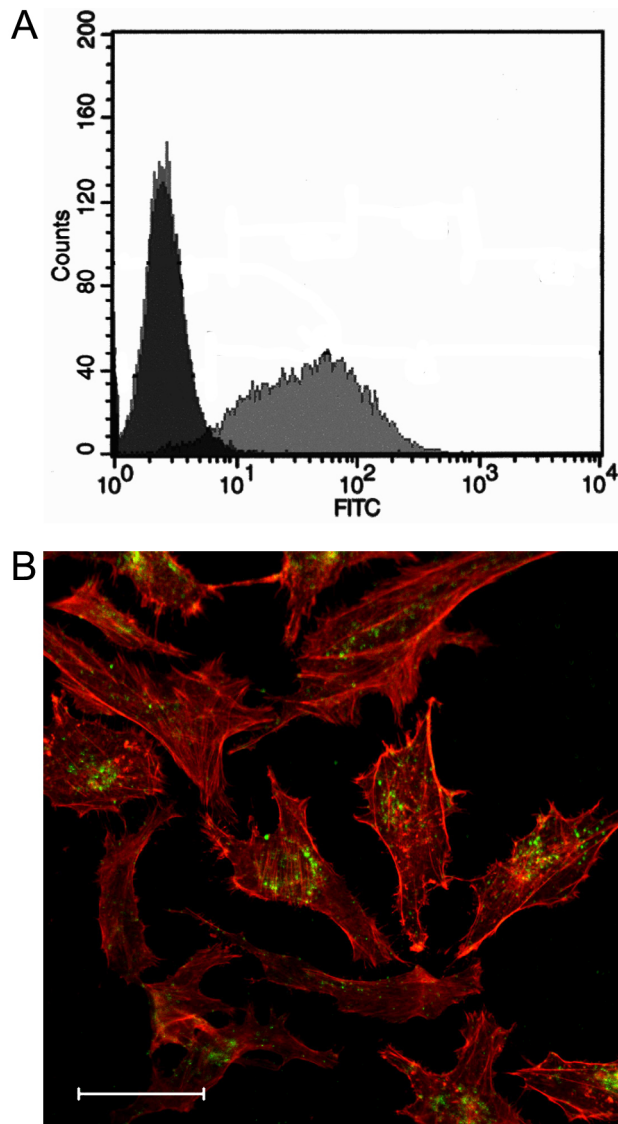
Figure 4.12. Uptake of CDP-Im nanoparticles containing fluorescein (FL)-labeled siRNA by HeLa cells. (A) Histogram of cell-associated fluorescence measured by flow cytometry. The left-most peaks correspond to the overlapping peaks for HeLa cells incubated with either Opti-MEM I alone or 100 nM naked FL-siRNA, while the right-most peak represents the cell-associated fluorescence after transfection with CDP-Im/FL-siRNA nanoparticles. (B) Confocal fluorescence microscopy image of HeLa cells after transfection with CDP-Im/FL-siRNA nanoparticles (green) and rhodamine phalloidin staining of F-actin (red). Scale bar = 50 μm.

4.4.8 Targeting ligands enhance cellular uptake of PEGylated nanoparticles

To verify that attachment of AD-PEG$_{5000}$-Tf can lead to uptake through

transferrin receptor (TfR)-mediated endocytosis, the uptake of stabilized (PEGylated)

nanoparticles was measured in the presence or absence of free holo-Tf. While the uptake of PEGylated nanoparticles without AD-PEG$_{5000}$-Tf was not affected by the presence of free holo-Tf, the uptake of Tf-targeted nanoparticles was reduced as a result of competition with free holo-Tf (Figure 4.13). Because the nanoparticles can be internalized simultaneously by numerous mechanisms including simple pinocytosis, there is still significant uptake even without TfR-mediated internalization under these conditions.
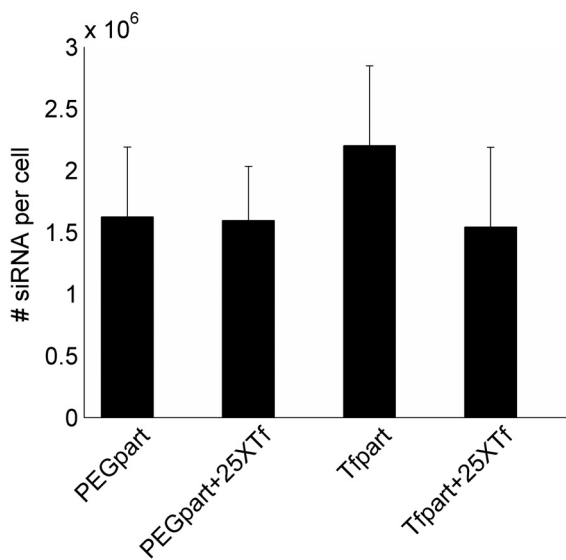
Figure 4.13. Uptake of PEGylated and Tf-targeted nanoparticles in the presence of holo-Tf competitor. Nanoparticles were formulated at a charge ratio of 3 (+/-) using CDP-Im and siRNA. PEGylated nanoparticles (PEGpart) were formulated with a 1:1 mole ratio of AD-PEG$_{5000}$:β-CD and Tf-targeted nanoparticles (Tfpart) were formulated with a 1:1 mole ratio of AD-PEG$_{5000}$-X:β-CD where AD-PEG$_{5000}$-X was composed of 99 mol% AD-PEG$_{5000}$ and 1 mol% AD-PEG$_{5000}$-Tf. Nanoparticles containing 100 nM siRNA were added to HeLa cells in 200 μL Opti-MEM I in the absence or presence of a 25X (moles holo-Tf: moles AD-PEG$_{5000}$-Tf) excess of holo-Tf competitor.

4.4.9   Targeted nanoparticles exhibit avidity effects

If multiple receptor/ligand interactions can occur simultaneously, then the effective affinity of the binding interaction can be enhanced through avidity effects. Antibodies or divalent antibody fragments are excellent examples of molecules whose

binding affinities are enhanced through avidity effects. Their divalent interactions allow

single antibodies to bind two separate receptors, leading to a stronger apparent affinity

than exhibited by the monovalent antibody fragment (25). Targeted delivery vehicles

that contain multiple targeting ligands on the surface should also display these avidity

effects if multiple targeting ligands can simultaneously interact with the receptors. A

typical cancer cell may contain thousands of receptors on its surface (26,27), and the Tf-

targeted delivery vehicles can contain tens or even hundreds of Tf ligands (depending on

the percent of the AD-PEG$_{5000}$ molecules with Tf molecules attached to the distal end of

the flexible PEG$_{5000}$ chains) decorating each nanoparticle surface. This arrangement

should enable multiple Tf molecules to bind to TfR on the surface of the cells. To test

whether these avidity effects increase the apparent affinity of the Tf-targeted

nanoparticles for the TfR on the cell surface, a competitive uptake assay was performed

using flow cytometry. The results shown in Figure 4.14A demonstrate that the Tf-

targeted nanoparticles possess enhanced affinity for the TfR relative to individual AD-

PEG$_{5000}$-Tf molecules. Additionally, nanoparticles without the Tf targeting ligand had a

minimal impact on the uptake of the fluorescently labeled holo-Tf. To determine how

targeting ligand density affects nanoparticle binding to cell-surface TfR, nanoparticles

were incubated with HeLa cells in PBS at 4°C to measure the amount of binding in the

absence of internalization. The results shown in Figure 4.14B show that Tf targeting

increases the amount of cell-associated nanoparticles under these conditions, and the

amount of binding increases with the targeting ligand density.
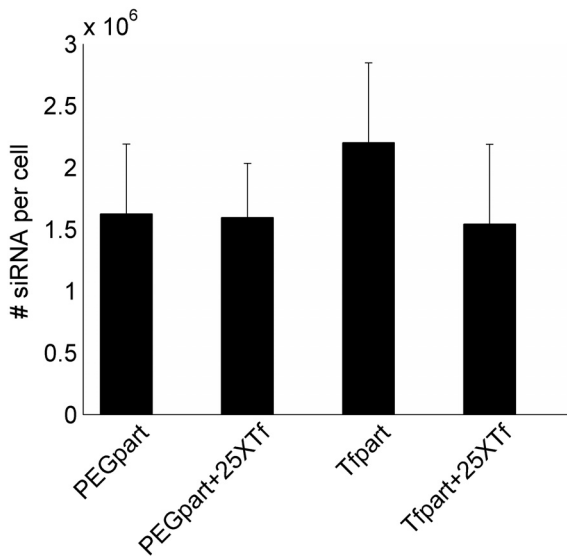
Figure 4.14. Effect of transferrin targeting ligand density on relative binding affinity. (A) Competitive TfR binding by free holo-Tf (circles), free AD-PEG$_{5000}$-Tf (triangles), Tf-targeted CDP-Im/siRNA (3 (+/-), 1 mol% AD-PEG$_{5000}$-Tf) nanoparticles (squares), and PEGylated CDP-Im/siRNA (3 (+/-)) nanoparticles (diamonds) in the presence of 20 nM AlexaFluor488-labeled holo-Tf. As a control, the PEGylated nanoparticles were formulated identically to the Tf-targeted nanoparticles at each concentration except without the addition of AD-PEG$_{5000}$-Tf during formulation. (B) Live-cell binding assay. Nanoparticles were formulated at a charge ratio of 3 (+/-) using CDP-Im and Cy3-labeled siRNA. PEGylated nanoparticles (PEGpart) were formulated with a 1:1 mole ratio of AD-PEG$_{5000}$:β-CD and Tf-targeted nanoparticles (Tfpart) were formulated with a 1:1 mole ratio of AD-PEG$_{5000}$-X:β-CD where AD-PEG$_{5000}$-X was composed of the stated % AD-PEG$_{5000}$-Tf and the remainder AD-PEG$_{5000}$. Nanoparticles containing 100 nM Cy3-siRNA were added to HeLa cells in 200 μL PBS and incubated on ice for 30 minutes. The "percent bound" represents the fraction of nanoparticles associated with the cell pellet after centrifugation.

4.4.10 Particles deliver functional pDNA and siRNA to cells in vitro

In addition to achieving intracellular delivery of the nucleic acid-containing nanoparticles, the nanoparticles need to release their nucleic acid payload intracellularly to allow it to function. Co-delivery of a luciferase-expressing plasmid and either a control or luciferase-targeting siRNA was used to demonstrate the ability of the nanoparticles to deliver functional pDNA and siRNA. The luciferase activity in cell lysates was quantified using a luminometer, and relative light units (RLU) were normalized to total cellular protein levels. As shown in Figure 4.15, cells that received

CDP-Im nanoparticles containing the plasmid and siRNA against luciferase (siLuc) had luciferase activity that was ~50% lower than cells that received CDP-Im nanoparticles with either the plasmid alone or the plasmid plus a control siRNA (siCON1).
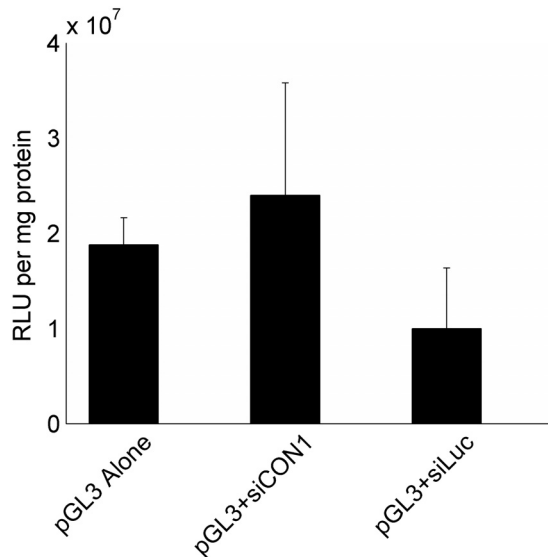
Figure 4.15. Luciferase expression 48 h after co-transfection of HeLa cells with nanoparticles containing pDNA and siRNA. Nanoparticles were formulated at a charge ratio of 3 (+/-) by combining CDP-Im with pGL3-CV (pGL3 Alone), pGL3-CV and a control siRNA (pGL3+siCON1), or pGL3-CV and an siRNA against luciferase (pGL3+siLuc).

4.4.11 Nanoparticles are multifunctional, integrated systems for nucleic acid delivery

The results presented here highlight the importance of creating a nanoparticle that consists of multiple components that function together as a system, and control over size, surface modification, payload protection, and targeting ligand to payload ratio are key parameters to consider when designing nucleic acid delivery vehicles for in vivo systemic use. These parameters also represent some of the major advantages of nanoparticle composites for delivery of nucleic acids instead of using carrier-free delivery methods. Nucleic acid delivery vehicles can help reduce renal clearance while adding features such as stabilization against nuclease degradation, cell-specific targeting, and large payload

delivery. These features make them well-suited for the systemic delivery of nucleic acids in general, and we have shown that the system investigated here can deliver pDNA, siRNA, and DNAzymes in vitro and in vivo (7,17,19,20).

The capability to fine-tune the delivery vehicle's properties combined with an understanding of how those properties affect its function in biological systems represent two key factors necessary for optimization of nucleic acid delivery vehicles. This study demonstrates the importance of a rational approach in delivery vehicle design and lays a foundation for further in vivo studies to understand the relationships between the properties of nanoparticle delivery systems and their biological function. The approach to designing nanoparticle delivery vehicles that is outlined here can be used for other synthetic materials and is thus not limited to the cyclodextrin polymer-based system illustrated.

4.5 Acknowledgments

4.6 References

1. Morrissey, D.V., Blanchard, K., Shaw, L., Jensen, K., Lockridge, J.A., Dickinson, B., McSwiggen, J.A., Vargeese, C., Bowman, K., Shaffer, C.S. et al. (2005) Activity of stabilized short interfering RNA in a mouse model of hepatitis B virus replication. *Hepatology*, **41,** 1349-1356.
2. Layzer, J.M., McCaffrey, A.P., Tanner, A.K., Huang, Z., Kay, M.A. and Sullenger, B.A. (2004) In vivo activity of nuclease-resistant siRNAs. *RNA*, **10,** 766-771.
3. Schatzlein, A.G. (2003) Targeting of synthetic gene delivery systems. *J Biomed Biotechnol*, **2,** 149-158.
4. Soutschek, J., Akinc, A., Bramiage, B., Charisse, K., Constien, R., Donoghue, M., Elbashir, S., Geick, A., Hadwiger, P., Harborth, J. et al. (2004) Therapeutic silencing of an endogenous gene by systemic administration of modified siRNAs. *Nature*, **432,** 173-178.
5. Dykxhoorn, D.M., Palliser, D. and Lieberman, J. (2006) The silent treatment: siRNAs as small molecule drugs. *Gene Ther*, **13,** 541-552.
6. Song, E., Zhu, P., Lee, S.-K., Chowdhury, D., Kussman, S., Dykxhoorn, D.M., Feng, Y., Palliser, D., Weiner, D.B., Shankar, P. et al. (2005) Antibody mediated in vivo delivery of small interfering RNAs via cell-surface receptors. *Nat Biotechnol*, **23,** 709-717.
7. Hu-Lieskovan, S., Heidel, J.D., Bartlett, D.W., Davis, M.E. and Triche, T.J. (2005) Sequence-specific knockdown of EWS-FLI1 by targeted, nonviral delivery of small interfering RNA inhibits tumor growth in a murine model of Ewing's sarcoma. *Cancer Res*, **65,** 8984-8992.
8. Ogris, M., Brunner, S., Schuller, S., Kircheis, R. and Wagner, E. (1999) PEGylated DNA/transferrin-PEI complexes: reduced interaction with blood components, extended circulation in blood and potential for systemic gene delivery. *Gene Ther*, **6,** 595-605.
9. Morrissey, D.V., Lockridge, J.A., Shaw, L., Blanchard, K., Jensen, K., Breen, W., Hartsough, K., Machemer, L., Radka, S., Jadhav, V. et al. (2005) Potent and persistent in vivo anti-HBV activity of chemically modified siRNAs. *Nat Biotechnol*, **23,** 1002-1007.
10. Zimmermann, T.S., Lee, A.C.H., Akinc, A., Bramlage, B., Bumcrot, D., Fedoruk, M.N., Harborth, J., Heyes, J.A., Jeffs, L.B., John, M. et al. (2006) RNAi-mediated gene silencing in non-human primates. *Nature*, **441,** 111-114.
11. Plank, C., Mechtler, K., Szoka, F.C.J. and Wagner, E. (1996) Activation of the complement system by synthetic DNA complexes: a potential barrier for intravenous gene delivery. *Hum Gene Ther*, **7,** 1437-1446.
12. Chonn, A., Cullis, P.R. and Devine, D.V. (1991) The role of surface charge in the activation of the classical and alternative pathways of complement by liposomes. *J Immunol*, **146,** 4234-4241.
13. Venturoli, D. and Rippe, B. (2005) Ficoll and dextran vs. globular proteins as probes for testing glomerular permselectivity: effects of molecular size, shape, charge, and deformability. *Am J Physiol Renal Physiol*, **288,** F605-613.

14. Dreher, M.R., Liu, W., Michelich, C.R., Dewhirst, M.W., Yuan, F. and Chilkoti, A. (2006) Tumor vascular permeability, accumulation, and penetration of macromolecular drug carriers. *J Natl Cancer I*, **98,** 335-344.

15. Rensen, P., Sliedregt, L., Ferns, M., Kieviet, E., van Rossenberg, S., van Leeuwen, S., van Berkel, T. and Biessen, E. (2001) Determination of the upper size limit for uptake and processing of ligands by the asialoglycoprotein receptor on hepatocytes in vitro and in vivo. *J Biol Chem*, **276,** 37577-37584.

16. Mishra, S., Webster, P. and Davis, M.E. (2004) PEGylation significantly affects cellular uptake and intracellular trafficking of non-viral gene delivery particles. *Eur J Cell Biol*, **83,** 97-111.

17. Davis, M.E., Pun, S.H., Bellocq, N.C., Reineke, T.M., Popielarski, S.R., Mishra, S. and Heidel, J.D. (2004) Self-assembling nucleic acid delivery vehicles via linear, water-soluble cyclodextrin-containing polymers. *Curr Med Chem*, **11,** 1241-1253.

18. Mishra, S., Heidel, J.D., Webster, P. and Davis, M.E. (2006) Imidazole groups on a linear, cyclodextrin-containing polycation produce enhanced gene delivery via multiple processes. *J Control Release*, **116,** 179-191.

19. Bellocq, N.C., Pun, S.H., Jensen, G.S. and Davis, M.E. (2003) Transferrin-containing polymer-based particles for tumor-targeted gene delivery. *Bioconjugate Chem*, **14,** 1122-1132.

20. Pun, S.H., Bellocq, N.C., Cheng, J., Grubbs, B.H., Jensen, G.S., Davis, M.E., Tack, F., Brewster, M., Janicot, M., Janssens, B. et al. (2004) Targeted delivery of RNA-cleaving DNA enzyme (DNAzyme) to tumor tissue by transferrin-modified, cyclodextrin-based particles. *Cancer Biol Ther*, **3,** 31-40.

21. Blandamer, M.J., Cullis, P.M. and Engberts, J.B.F.N. (1998) Titration microcalorimetry. *J Chem Soc Faraday T*, **94,** 2261-2267.

22. Perry, C.S., Charman, S.A., Prankerd, R.J., Chiu, F.C.K., Scanlon, M.J., Chalmers, D. and Charman, W.N. (2006) The binding interaction of synthetic ozonide antimalarials with natural and modified β-cyclodextrins. *J Pharm Sci*, **95,** 146-158.

23. Hansen, P.L., Cohen, J.A., Podgornik, R. and Parsegian, V.A. (2003) Osmotic properties of poly(ethylene glycols): quantitative features of brush and bulk scaling laws. *Biophys J*, **84,** 350-355.

24. Pun, S.H. and Davis, M.E. (2002) Development of a nonviral gene delivery vehicle for systemic application. *Bioconjugate Chem*, **13,** 630-639.

25. Adams, G.P., Tai, M.-S., McCartney, J.E., Marks, J.D., Stafford III, W.F., Houston, L.L., Huston, J.S. and Weiner, L.M. (2006) Avidity-mediated enhancement of in vivo tumor targeting by single-chain Fv dimers. *Clin Cancer Res*, **12,** 1599-1605.

26. Phillips, J., Rutledge, L. and Winters, W. (1986) Transferrin binding to two human colon carcinoma cell lines: characterization and effect of 60 Hz electromagnetic fields. *Cancer Res*, **46,** 239-244.

27. Shir, A., Ogris, M., Wagner, E. and Levitzki, A. (2006) EGF receptor-targeted synthetic double-stranded RNA eliminates glioblastoma, breast cancer, and adenocarcinoma tumors in mice. *PLoS Med*, **3,** e6.

5 Noninvasive in vivo imaging using PET and BLI to monitor the biodistribution and function of tumor-targeted siRNA nanoparticles after intravenous injection in mice[†]

5.1 Abstract

Noninvasive in vivo imaging technologies can provide quantitative information about the spatiotemporal distribution and function of molecules in living organisms. Here, we demonstrate an approach using positron emission tomography (PET) and bioluminescent imaging (BLI) to quantify the in vivo biodistribution and function of nanoparticles formed with cyclodextrin-containing polycations (CDP) and small interfering RNA (siRNA). Conjugation of the metal chelator, 1,4,7,10-tetraazacyclododecane-1,4,7,10-tetraacetic acid (DOTA), to the 5' end of the siRNA molecules allows labeling with ^{64}Cu for PET imaging. Since the siRNA molecules target luciferase, BLI of mice bearing luciferase-expressing Neuro2A subcutaneous tumors before and after PET imaging enabled correlation of functional efficacy with the biodistribution data. Both naked siRNA and siRNA packaged into nanoparticles showed rapid blood clearance with significant accumulation in the liver and kidneys. Despite the poor pharmacokinetics of the nanoparticle formulations, both non-targeted and transferrin (Tf)-targeted siRNA nanoparticles showed detectable tumor signal (~1% ID/cm^3) by PET 1 d post injection, and the Tf-targeted siRNA nanoparticles reduced luciferase activity by ~50% relative to non-targeted siRNA nanoparticles after 1 d. Therefore, the primary advantage of targeted nanoparticles may be associated with processes involved in cellular

---

uptake rather than overall tumor localization. Moreover, we propose a physiologically based mechanism that could result in nanoparticle disruption primarily within the kidney, helping to explain the rapid blood clearance of the nanoparticles after systemic administration. This dissociation mechanism could have broad implications for the design of nucleic acid nanoparticles formed through electrostatic interactions and will likely facilitate the design of long-circulating nanoparticles.

5.2 Introduction

RNA interference (RNAi) is a powerful trigger of sequence-specific gene silencing, and its potential therapeutic use for treating diseases such as cancer is being widely investigated. Synthetic small interfering RNA (siRNA) molecules 19-21 bp in length can act as the mediators of RNAi if applied exogenously, but they must reach the intracellular environment to exert their effect. Therefore, therapeutic application of siRNAs requires their effective delivery into the target cells of interest. To address the challenge of nucleic acid delivery, a variety of approaches have been developed with varying success, including covalent attachment of antibodies or cholesterol, liposome encapsulation, or nanoparticle formation with cationic lipids or polymers (1-4). Nanoparticle encapsulation of siRNAs can help reduce renal clearance while adding features such as stabilization against nuclease degradation, tunable cell-specific targeting, and large payload delivery. We previously have described a cyclodextrin-containing polycation (CDP) and its interaction with siRNA to form targeted siRNA nanoparticles with diameters <100 nm that carry a payload of ~2,000 siRNA molecules (5). These nanoparticles have been used to deliver functional siRNA to tumors in vivo, inhibiting tumor growth in a disseminated model of Ewing's sarcoma (6). Importantly, these

nanoparticles show no clinical signs of toxicity in mice or non-human primates at the doses used for in vivo efficacy (7).

Recently, Medarova et al. described the use of MRI and fluorescence imaging to monitor the tumor accumulation and functional activity of magnetic nanoparticles covalently linked to siRNAs (8). This study illustrated the power of multimodality imaging approaches to help correlate the biodistribution of therapeutic entities with their biological activity. We attempt to extend this methodology further by employing microPET/CT to monitor the real-time, whole-body biodistribution kinetics and tumor localization of injected siRNA nanoparticles while concurrently using BLI to measure the luciferase knockdown by the delivered siRNA molecules. By formulating the nanoparticles with or without Tf targeting ligands, the effect of cell-specific targeting on both biodistribution and function can be studied.

A recent report by de Wolf et al. examined the effect of polycationic carriers on the pharmacokinetics and tumor localization of siRNA (9). They noted that formulation of the siRNA into polycationic carriers had little effect on the biodistribution and tumor localization compared to naked siRNA. Both naked siRNA and siRNA packaged into the carriers exhibited rapid blood clearance with tissue distribution mainly to the kidneys and liver within the first 15 minutes after injection.

In an extension of the aforementioned studies, we employ microPET/CT and BLI to determine the kinetics of the biodistribution and tumor localization of intravenously administered CDP-based siRNA nanoparticles while simultaneously quantifying the functional efficacy of the delivered siRNA molecules through luciferase reporter protein knockdown. This methodology represents a generalized procedure for studying any

siRNA-based carrier system in vivo, and we believe these results provide important insights into the design and optimization of nanoparticle carriers for systemic siRNA delivery.

5.3   Materials and methods

5.3.1   siRNA sequence

To create the DOTA-modified siRNA, RNA oligonucleotides were ordered from Integrated DNA Technologies. The antisense strand (5'-UAUCGAAGGACUCUGGCACdTdT-3') was ordered unmodified. The sense strand (5'-GUGCCAGAGUCCUUCGAUAdTdT-3') was ordered unmodified or with a 5' Amino Modifier C6 modification to place an amine at the 5' end of this sense strand. The annealed siRNA duplex is designed to target luciferase mRNA.

5.3.2   Synthesis of DOTA-siRNA

1,4,7,10-tetraazacyclododecane-1,4,7,10-tetraacetic acid mono(*N*-hydroxysuccinimide ester) (DOTA-NHS-ester) was ordered from Macrocyclics. The DOTA-NHS-ester reacts with the terminal amine on the amine-modified RNA sense strand to form a stable amide bond. To a microcentrifuge tube were added the RNA sense strand with a 100-fold molar excess of DOTA-NHS-ester in Chelex-100-treated carbonate buffer (pH 9). The contents were allowed to react with stirring for ~4 h at room temperature. The DOTA-RNAsense conjugate was ethanol precipitated with 0.1 volumes of 3M sodium chloride and 2.5 volumes of ethanol followed by incubation overnight at -20°C. The precipitation mixture was then centrifuged, washed with 70% ethanol, centrifuged again, and resuspended in water at a concentration of 1 mM. Finally, the purified DOTA-RNAsense was annealed to the unmodified antisense strand to yield

DOTA-siRNA. All liquids were pre-treated with Chelex-100 (Bio-Rad) to remove trace metal contaminants.

5.3.3   *Verification of DOTA-siRNA conjugation*

To verify successful conjugation of DOTA to siRNA, a procedure was designed to compare the ability of DOTA-siRNA to coordinate gadolinium (Gd^{3+}) relative to free DOTA. To a microcentrifuge tube were added equimolar amounts of gadolinium chloride ($GdCl_3$) and either DOTA or DOTA-siRNA in 0.1 M ammonium acetate buffer (pH 6). The microcentrifuge tubes were incubated for 15 min at 75°C for the labeling reaction. Subsequently, half of the labeling reaction was combined with an equal volume of 1 mM arsenazo III. The presence of any free gadolinium ions results in a hypochromic shift from 548 nm to 660 nm. Therefore, the absorbance at 660 nm was measured for each sample using a Tecan Safire plate reader. Comparison to a standard curve allowed estimation of the amount of free gadolinium remaining in each sample.

5.3.4   *In vitro transfection*

Neuro2A-Luc cells with constitutive luciferase expression were seeded at $2x10^4$ cells per well in 24-well plates 2 days prior to transfection and grown in DMEM supplemented with 10% FBS and antibiotics (penicillin/streptomycin). siRNA was complexed with Oligofectamine (Invitrogen) according to manufacturer's instructions and applied to each well in a total volume of 200 μL Opti-MEM I (Invitrogen). Transfection media was removed and replaced with complete media after 5 h. The kinetics of the luciferase knockdown by unmodified and DOTA-conjugated siRNA were determined using the Xenogen IVIS 100 as described previously (10).

5.3.5 ^{64}Cu labeling of DOTA-siRNA

^{64}Cu chloride was produced at Washington University (St. Louis, MO). Upon arrival, the ^{64}Cu chloride was mixed with 0.25 M ammonium acetate (pH 7) and transferred to a new microcentrifuge tube. Citrate buffer (pH 5) was added to this microcentrifuge tube to achieve a final concentration of 0.1 M citrate buffer. DOTA-siRNA in water was added to achieve a final DOTA-siRNA:^{64}Cu ratio of 250:1 for labeling. The contents of the tube were mixed and then allowed to sit for 1 h at 60°C. The labeling reaction was purified by gel filtration or ethanol precipitation. Gel filtration was performed using MicroSpin G-25 columns (Amersham Biosciences) according to manufacturer's instructions. Ethanol precipitation was accomplished by adding 0.1 volumes of 3M sodium acetate and 2.5 volumes of pre-chilled ethanol followed by incubation for ~2 h at -80°C. The precipitation reaction was then centrifuged to pellet the DOTA-siRNA, washed with 70% ethanol, centrifuged again, and resuspended in water to yield ^{64}Cu-DOTA-siRNA.

5.3.6 Nanoparticle formation

Before addition to the nucleic acid, the CDP was mixed with AD-PEG at a 1:1 AD-PEG:β-CD (mol:mol) ratio in water. Targeted nanoparticles contained AD-PEG-transferrin (AD-PEG-Tf) as a percentage of the total AD-PEG in the mixture. For example, 1 mol% AD-PEG-Tf nanoparticles contained 0.01 moles AD-PEG-Tf for every 0.99 moles AD-PEG, and 0.1 wt% AD-PEG-Tf nanoparticles contained 0.001 g of AD-PEG-Tf for every 1 g of AD-PEG. The mixture of CDP, AD-PEG, and AD-PEG-Tf in water was then added to an equal volume of siRNA (or a mixture of unmodified siRNA and DOTA-siRNA) in water such that the ratio of positive charges from CDP to negative

charges from the nucleic acid was equal to the desired charge ratio of 3 (+/-). An equal volume of 10% (w/v) glucose in water was added to the resulting nanoparticles to give a final concentration of 5% (w/v) glucose suitable for injection.

5.3.7 Dynamic light scattering (DLS)

Nanoparticle formulations were diluted to a volume of ~1.5 mL, placed in a cuvette, and inserted into a ZetaPALS (Brookhaven Instruments Corporation) instrument to measure both the size and zeta potential. Reported effective hydrodynamic diameters represent the average values from a total of 5-10 runs of 30 seconds each, while zeta potentials represent the average of 10 runs each.

5.3.8 Serum stability of siRNA nanoparticles

Nanoparticles were formed in water at a charge ratio of 3 (+/-) with an siRNA concentration of 0.5 g/L, and subsequently incubated in 50% mouse serum (Sigma) for 4 h at 37°C and 5% CO_2. Aliquots of the nanoparticles were removed at the specified time points (1 h, 4 h, 17 h, 43 h) and run on an agarose gel to determine the amount of intact siRNA remaining. Nanoparticles that were incubated in water instead of mouse serum were loaded as controls for each gel. Displacement of the nucleic acid from the nanoparticles was achieved by adding 1% sodium dodecyl sulfate (SDS) to the sample immediately prior to gel loading. Gel electrophoresis was performed by applying 100 V for 30 min, and the siRNA bands were visualized by ethidium bromide staining. Quantification of the band intensities was accomplished using ImageJ software.

5.3.9 Salt stability of siRNA and pDNA nanoparticles

Nanoparticles were formulated as described above with a 1:1 AD-PEG:β-CD (mol:mol) ratio and a charge ratio of 3 (+/-). Nanoparticles were formed at an siRNA or

pDNA concentration of 0.5 g/L. A portion of the nanoparticle formation (containing 1 µg siRNA) was added to a microcentrifuge tube and mixed with either 1% SDS or sodium chloride (NaCl) at a range of concentrations from 0 to 1.5 M NaCl. The samples were allowed to incubate for 3-5 min at room temperature before being loaded into a 1% agarose gel. Gel electrophoresis was performed by applying 100 V for 30 min (siRNA nanoparticles) or 80 V for 60 min (pDNA nanoparticles), and the bands were visualized by ethidium bromide staining. Quantification of the amount of siRNA or pDNA present in intact nanoparticles (remaining in the well at the top of the gel) was performed using ImageJ image analysis software.

5.3.10 Animals and tumor formation

Severe combined immunodeficient (NOD/scid) mice were purchased from Jackson Laboratories. All animal manipulations were performed with sterile technique following the guidelines of the UCLA Animal Research Committee. Neuro2A-Luc cells were cultured in DMEM supplemented with 10% FBS, 2 mg/mL glucose, 100 units/mL of penicillin, and 100 units/mL of streptomycin. Exponentially growing Neuro2A-Luc cells were removed from the plate with trypsin, resuspended in PBS and Matrigel (BD Biosciences), and injected subcutaneously into the right flank of NOD/scid mice at 1-$2x10^6$ cells per mouse. Animals underwent microPET/CT scanning after tumors had grown to an approximate size of 6-7 mm in diameter.

5.3.11 MicroPET/CT imaging

MicroPET/CT imaging was performed with a microPET FOCUS 220 PET scanner (11) (Siemens Preclinical Solutions) and MicroCAT II CT scanner (Siemens Preclinical Solutions). Mice were placed on a heating pad (30°C) and anesthetized using

1.5-2% isoflurane starting 15 min prior to injection. 3.7-11.1 MBq (100-300 μCi) of ^{64}Cu was injected via tail vein while the animals were positioned on the scanner bed before a dynamic PET study was acquired for one hour. Mice were then placed in an imaging chamber that minimizes positioning errors between PET and CT to less than 1 mm (11). PET images were reconstructed by filtered back projection, using a ramp filter to yield an image resolution of 1.7 mm. Immediately after the PET scan, mice underwent a 7-minute microCT scan, using routine image acquisition parameters (11). The microCT scan was used for anatomical localization of the tissue concentrations of the ^{64}Cu over time in the microPET study. Static PET scans were acquired the following day (~18-24 h after the initial injection) with another CT scan for anatomical co-registration.

To determine temporal changes of tracer concentration in various organs, elliptical regions of interest (ROI) were placed in the area of the organ that exhibited the highest ^{64}Cu activity as determined by visual inspection. To ensure accurate anatomical positioning of the ROIs in the various organs, ROIs were placed on fused microPET/CT images generated by the AMIDE software (12). Activity concentrations are expressed as percent of the decay-corrected injected activity per cm^3 of tissue (can be approximated as %ID/g) using the AMIDE software. The activity in each ROI over time is reported as the percent of the decay-corrected injected activity per cm^3 (%ID/cm^3), and these values were normalized to an elliptical cylinder ROI drawn over the entire mouse to correct for the actual injected activity.

5.3.12 Bioluminescent imaging (BLI)

Bioluminescent imaging was performed using a Xenogen IVIS 100 imaging system. Mice were anesthetized with 2.5% isoflurane and injected i.p. with 0.2 mL of a

15 g/L D-luciferin solution in PBS. Light emission was measured 10 minutes after injection of the D-luciferin solution, and bioluminescent signals were quantified using Living Image software (Xenogen,).

5.4 Results

5.4.1 *Synthesis and characterization of DOTA-siRNA*

To verify conjugation of DOTA to the siRNA, a non-radioactive assay was designed to quantify the relative ability of DOTA-siRNA and free DOTA to coordinate gadolinium.   Incubation with DOTA-siRNA typically yielded gadolinium binding efficiencies that were about 50% of that observed for free DOTA.

Since the DOTA-siRNA is also designed to target the luciferase mRNA, its ability to silence luciferase expression in luciferase-expressing cell lines was compared to that of unmodified siRNA against luciferase (Figure 5.1). While the unmodified siRNA is able to achieve a maximum luciferase knockdown of >75%, the DOTA-siRNA achieves about 50% maximum luciferase knockdown, indicating a slight loss in activity after DOTA conjugation. Furthermore, the duration of the knockdown is consistent with an RNAi-based mechanism (10).
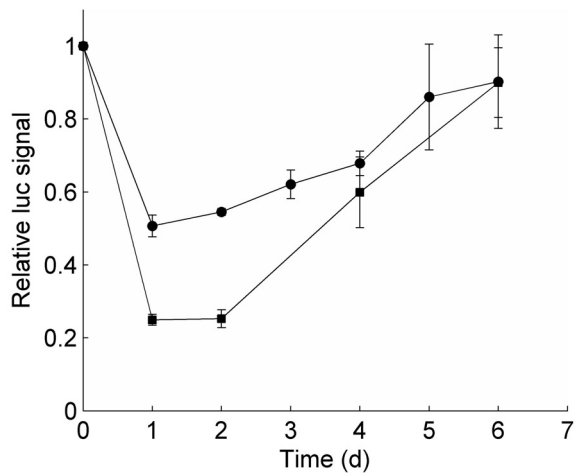
Figure 5.1. Luciferase knockdown by unmodified and DOTA-conjugated siRNA in luciferase-expressing Neuro2A-Luc cells. Luciferase knockdown is reported relative to the luciferase activity from cells transfected with equal doses of the siCON control sequence. Circles = DOTA-siRNA, squares = unmodified siRNA. Error bars = *SD*.

5.4.2   *Formation of nanoparticles containing DOTA-siRNA*

Since conjugation of DOTA to the siRNA molecules may interfere with nanoparticle assembly, dynamic light scattering and gel electrophoresis were used to analyze the nanoparticles formed with DOTA-siRNA. The fraction of the total siRNA that is modified with DOTA has a negligible effect on nanoparticle zeta potential and only a minor effect on nanoparticle size, leading to a slightly larger hydrodynamic diameter as the fraction of DOTA-siRNA is increased (Figure 5.2). Gel electrophoresis shows that nanoparticles formed with or without DOTA-siRNA have similar migration patterns, and the majority of the siRNA (unmodified or DOTA-conjugated) remains bound within the nanoparticles after formation.
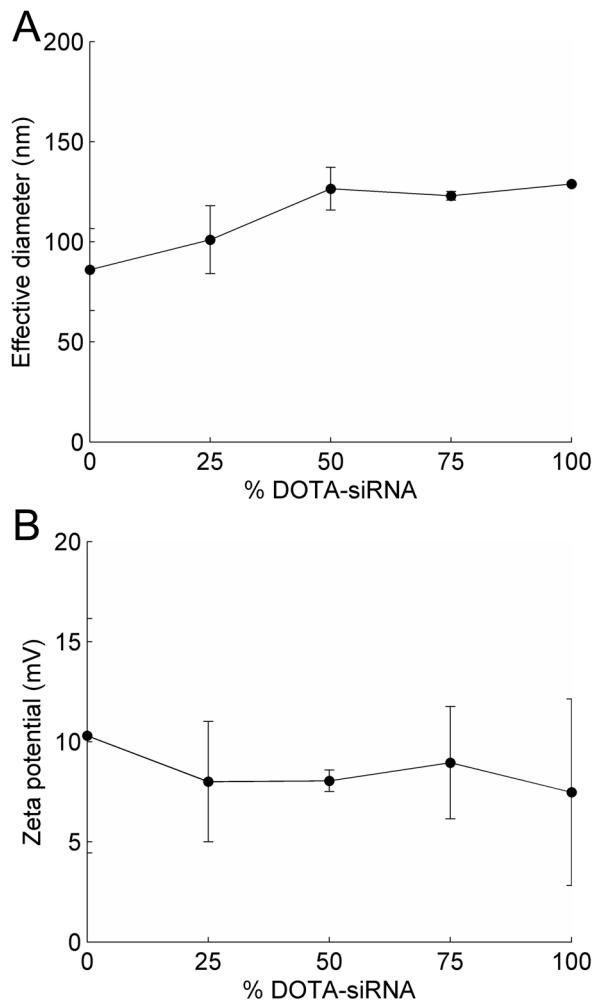
Figure 5.2. Effective hydrodynamic diameter (A) and zeta potential (B) of nanoparticles formed with 0 to 100% DOTA-siRNA. Error bars = *SD*.

5.4.3 ^{64}Cu-labeling of DOTA-siRNA

After labeling the DOTA-siRNA with ^{64}Cu, purification was accomplished using one of two methods: gel filtration or ethanol precipitation. Aliquots of ^{64}Cu-DOTA-siRNA purified by the two methods were separated by gel electrophoresis and the amount of radioactivity in the bands was quantified by a gamma counter. Relative to the total amount loaded per well, 95% and 90% of the radioactivity was associated with the siRNA band for the ^{64}Cu-DOTA-siRNA purified by gel filtration and ethanol precipitation, respectively. Estimation of the overall yield of the recovery was made

using ImageJ analysis of the band intensities, indicating the total amount of siRNA recovered instead of the fraction of the radioactivity in the purification reaction associated with the DOTA-siRNA. According to the relative band intensities, close to 90% of the initial siRNA in the labeling reaction was recovered after ethanol precipitation, whereas only about 30% of the siRNA was recovered after gel filtration.

5.4.4   *Serum stability of DOTA-siRNA nanoparticles*

Nanoparticles were formed with unmodified siRNA or with DOTA-siRNA representing either 20% or 50% of the total siRNA in the nanoparticles. These nanoparticles were then incubated in 50% mouse serum for 1 to 43 hours and analyzed by gel electrophoresis. The total amount of siRNA (unmodified or DOTA-conjugated) remaining at each time point was quantified by ImageJ analysis of the relative band intensities. All three types of nanoparticles demonstrated essentially equivalent stability against nuclease degradation of the encapsulated siRNA, with an estimated half-life of ~11 h (Figure 5.3). This indicates that the nanoparticle formulations do provide stabilization against siRNA nuclease degradation, since the naked siRNA duplexes degrade in mouse serum with a half-life of approximately 1 h (13).
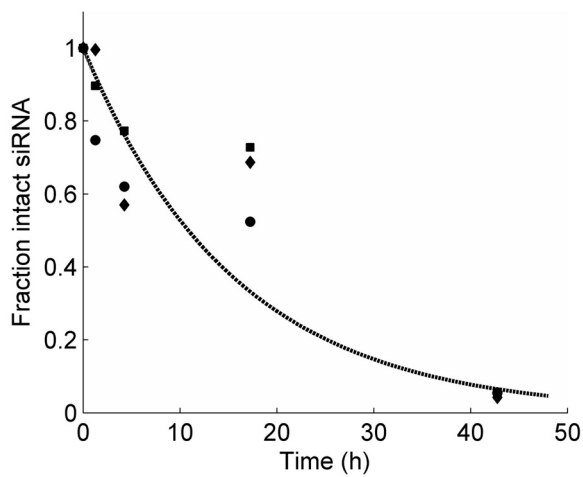
Figure 5.3. Nuclease stability of nanoparticle-encapsulated siRNA after incubation at 37°C and 5% CO_2 in 50% mouse serum. After gel electrophoresis, band intensities were quantified with ImageJ software and plotted versus time to estimate the degradation half-life of the encapsulated siRNA. Circles = nanoparticles formed with unmodified siRNA, diamonds = nanoparticles formed with 20% DOTA-siRNA, squares = nanoparticles formed with 50% DOTA-siRNA.

5.4.5   Biodistribution of naked siRNA and siRNA nanoparticles after intravenous administration

MicroPET/CT was used to examine the kinetics of the biodistribution and tumor localization of ^{64}Cu-labeled molecules after intravenous injection in mice. Reconstructed microPET/CT images of mice at 1, 10, and 60 min after injection are shown in Figure 5.4. The images were quantified using AMIDE software and the %ID/cm^3 was calculated for each ROI over all time frames. The resulting time-activity curves shown in Figure 5.5 represent the averages from 2 (^{64}Cu, ^{64}Cu-DOTA) or 3 (^{64}Cu-DOTA-siRNA ,Tf-targeted nanoparticles) independent experiments.
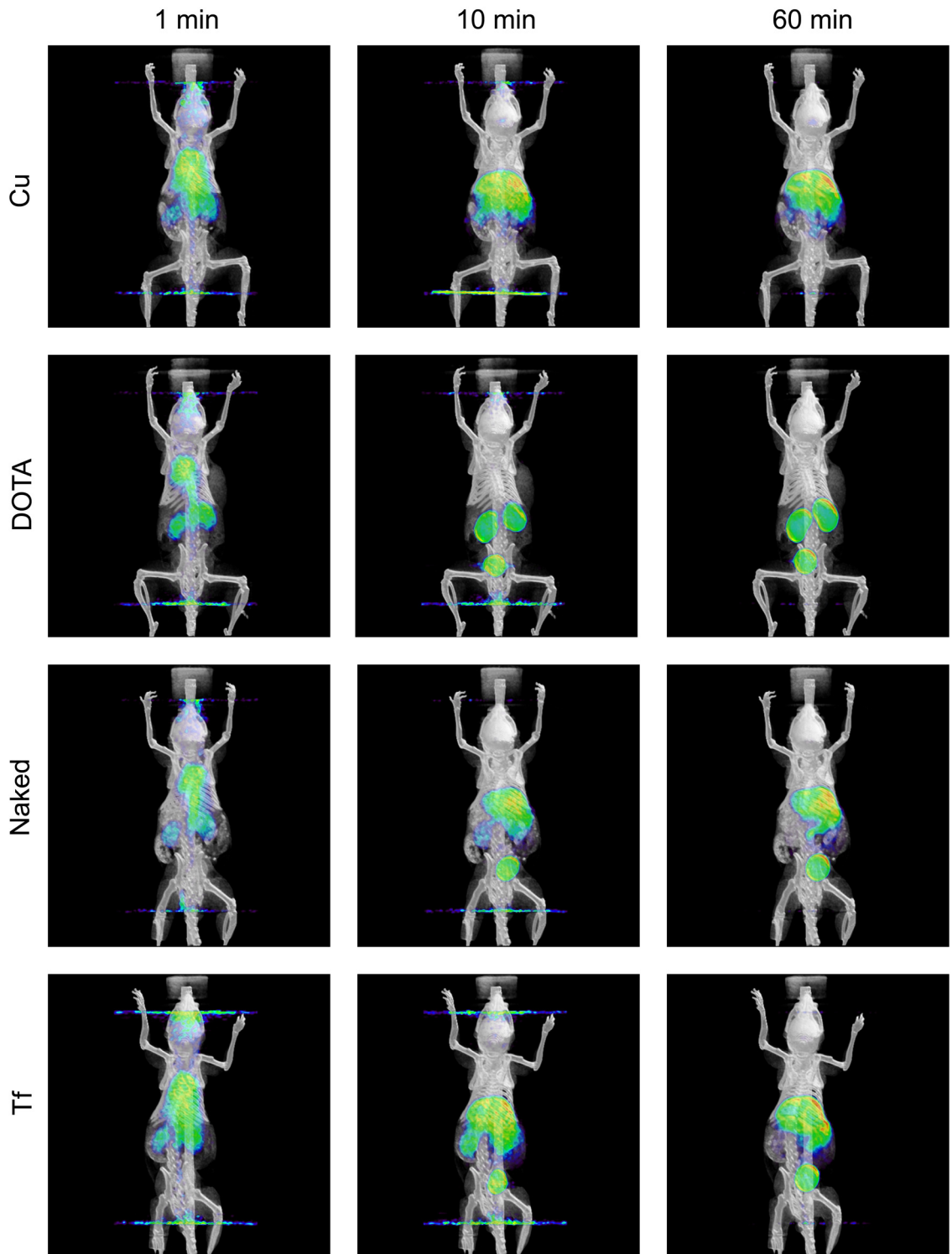
Figure 5.4. Fused microPET/CT images of mice at 1, 10, and 60 min after intravenous injection of free ^{64}Cu (Cu), ^{64}Cu-labeled DOTA (DOTA), ^{64}Cu-labeled DOTA-siRNA (Naked), and Tf-targeted nanoparticles (Tf) containing ~50% ^{64}Cu-labeled DOTA-siRNA. All images are displayed on the same scale (min threshold = 1 %ID/cm^3, max threshold = 5 %ID/cm^3).
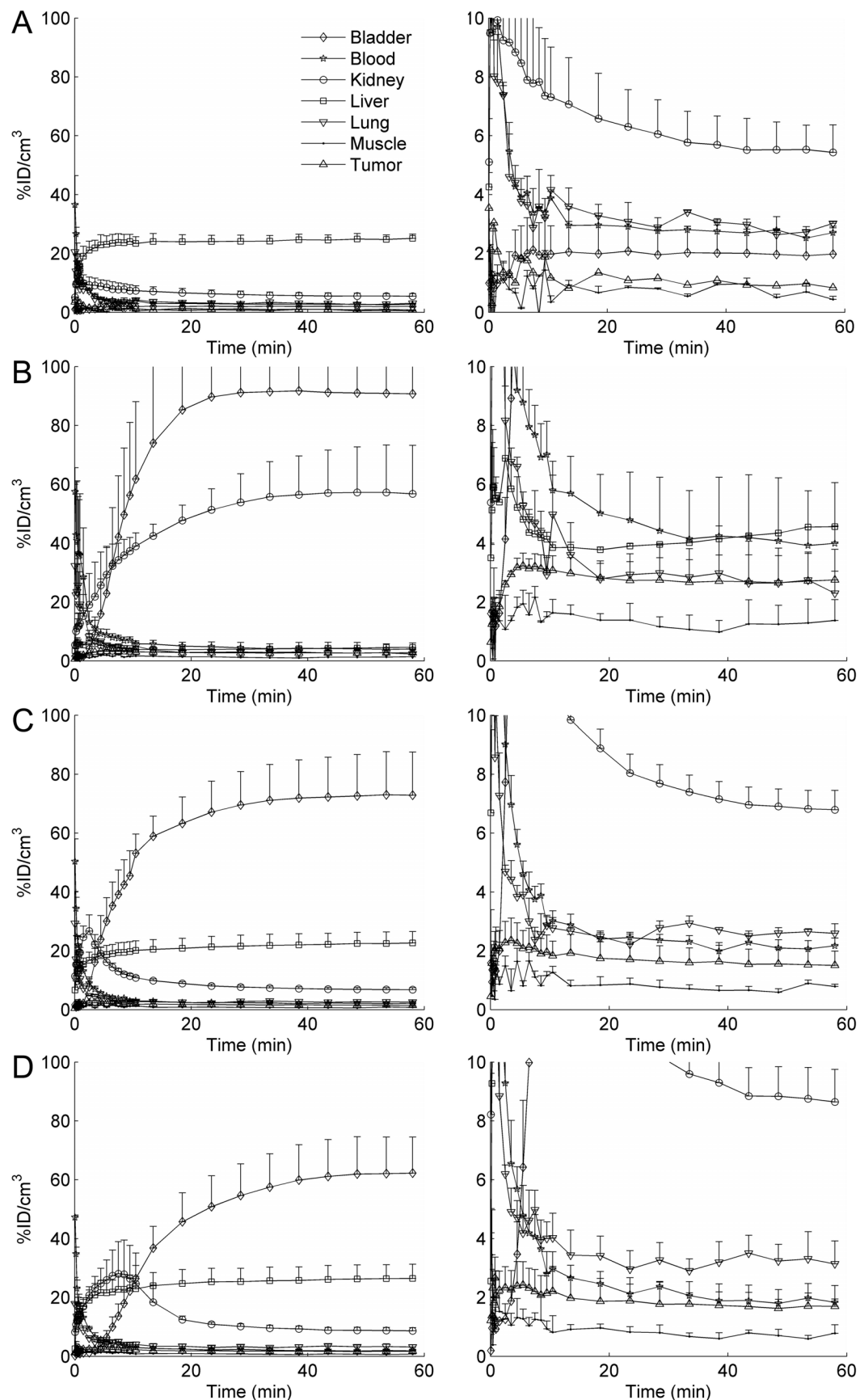
Figure 5.5. Average time-activity curves for the first 60 min after intravenous injection of (A) ^{64}Cu, (B) ^{64}Cu-labeled DOTA, (C) ^{64}Cu-labeled DOTA-siRNA, and (D) Tf-targeted nanoparticles containing ~50% ^{64}Cu-labeled DOTA-siRNA. Regions of interest (ROI) were drawn within each tissue or organ and the %ID/cm^3 for each ROI was calculated over all time frames using AMIDE software. Error bars = *SE*.

^{64}Cu alone accumulates rapidly in the liver, likely a result of binding to serum proteins such as albumin or ceruloplasmin (14). However, when the ^{64}Cu is chelated by DOTA and injected systemically in mice, the majority of the injected dose rapidly enters the kidney, with some clearing to the bladder. This importantly shows that the ^{64}Cu is not released by the DOTA in the serum, since any free ^{64}Cu would rapidly accumulate in the liver. These results are also consistent with the kidney clearance of other metal chelators, such as DTPA (15). When the DOTA is conjugated to an siRNA molecule and labeled with ^{64}Cu (^{64}Cu-DOTA-siRNA), the tissue distribution is different from either the ^{64}Cu alone or the ^{64}Cu-DOTA, with biodistribution kinetics characterized by rapid blood clearance resulting from both liver accumulation and kidney filtration into the urine. The total siRNA administered per mouse was equal to 2.5 mg/kg, and this ^{64}Cu-DOTA-siRNA was purified by ethanol precipitation. Since the labeling efficiency for the DOTA-siRNA was approximately 30-50%, the fraction of DOTA-siRNA [DOTA-siRNA/(DOTA-siRNA+normal siRNA)] was around 50%. The plasma concentration of the ^{64}Cu-DOTA-siRNA was fit using a biexponential decay with an initial elimination half-life of 1.8 min and a terminal elimination half-life of 61.9 min. The rapid initial elimination half-life is expected for the siRNA molecules whose small size (~13 kDa) allows first-pass renal clearance. Previously, Soutschek et al. reported an siRNA plasma half-life of ~6 min, consistent with the short half-life observed here (1). Additionally, Braasch et al. observed that intravenously injected siRNA accumulated in the kidney and

liver, with a peak in the kidney concentration 5 min after injection (16). Again, these observations are consistent with the values obtained here using microPET.

microPET/CT was also used to examine the kinetics of the biodistribution and tumor localization of siRNA nanoparticles after intravenous injection in mice. Given that the total dose of siRNA within the nanoparticles was the same as that used for naked siRNA (2.5 mg/kg), the fraction of DOTA-siRNA [DOTA-siRNA/(DOTA-siRNA+normal siRNA)] was still approximately 50%. The biodistribution of the ^{64}Cu-DOTA-siRNA packaged into the Tf-targeted nanoparticles appears very similar to that observed for naked ^{64}Cu-DOTA-siRNA, except the nanoparticle formulation led to slightly higher liver accumulation and a delayed peak in kidney activity.

The significant portion of the activity for the Tf-targeted nanoparticles that cleared rapidly through the kidneys and was excreted in the urine indicates the possibility of the presence of free siRNA. To investigate whether the free siRNA was present before injection, the nanoparticle formulations were analyzed by gel electrophoresis immediately before injection (Figure 5.6). The nanoparticle formulations showed <10% free siRNA when analyzed on the gel (Lanes 3 and 5 of Figure 5.6), and this small amount of free siRNA could also be an artifact from the gel electrophoresis procedure. Moreover, the slight decrease in the amount of migrating free siRNA at higher formulation charge ratios did not change the patterns of the time-activity curves after microPET/CT imaging. This supports the notion that any residual free siRNA prior to injection is not the dominant factor contributing to the kidney and bladder activity for the nanoparticle formulations. The urine was collected from mice injected with the siRNA nanoparticles and analyzed by agarose gel electrophoresis to further investigate whether

the activity observed in the kidney and bladder was associated with intact siRNA molecules (Figure 5.7). Visual inspection of the gel reveals a distinct band at the position corresponding to the migration distance of free siRNA (Lane 5 of Figure 5.7); however, a faint band is also seen at this same position for urine from mice that were not injected with any siRNA (Lane 8 of Figure 5.7). Subsequently, each lane was cut into four pieces (top, upper mid, lower mid, bottom) and a gamma counter was used to quantify the radioactivity in each region. At 30 min post injection, ~20% of the total radioactivity loaded into the lane was associated with the region corresponding to the migration distance of intact siRNA. This indicates that intact ^{64}Cu-DOTA-siRNA may be responsible for at least a portion of the observed kidney and bladder activity.
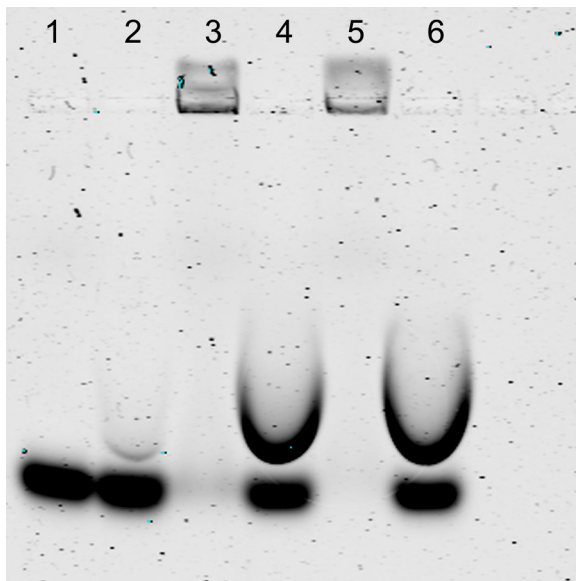
Figure 5.6. Gel electrophoresis analysis of ^{64}Cu-DOTA-siRNA nanoparticles prior to injection for microPET/CT imaging. Lane 1 = ^{64}Cu-DOTA-siRNA in water, Lane 2 = ^{64}Cu-DOTA-siRNA + 1% SDS in water, Lane 3 = ^{64}Cu-DOTA-siRNA packaged into Tf-targeted nanoparticles (charge ratio (+/-) = 3), Lane 4 = ^{64}Cu-DOTA-siRNA packaged into Tf-targeted nanoparticles (charge ratio (+/-) = 3) + 1% SDS, Lane 5 = ^{64}Cu-DOTA-siRNA packaged into Tf-targeted nanoparticles (charge ratio (+/-) = 6), Lane 6 = ^{64}Cu-DOTA-siRNA packaged into Tf-targeted nanoparticles (charge ratio (+/-) = 6) + 1% SDS.
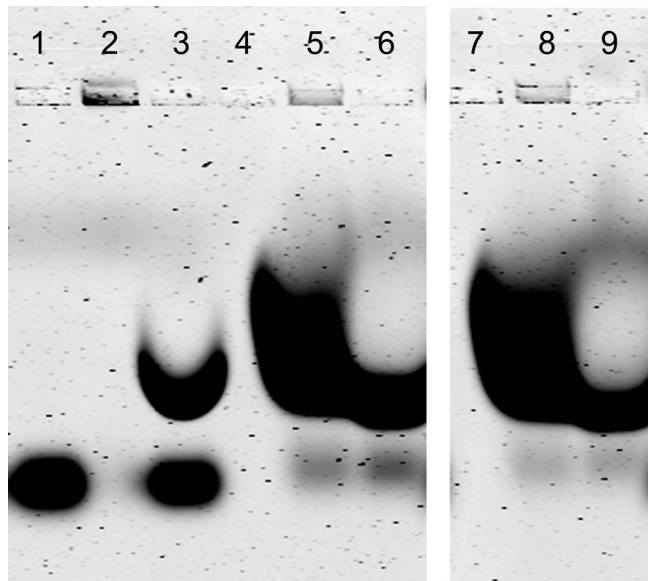
Figure 5.7. Gel electrophoresis analysis of urine samples from mice injected with ^{64}Cu-DOTA-siRNA nanoparticles. Lane 1 = Naked unmodified siRNA in water, Lane 2 = ^{64}Cu-DOTA-siRNA packaged into Tf-targeted nanoparticles (charge ratio (+/-) = 3), Lane 3 = ^{64}Cu-DOTA-siRNA packaged into Tf-targeted nanoparticles (charge ratio (+/-) = 3) + 1% SDS, Lane 4 = empty, Lane 5 = 20 μL urine from a mouse injected with ^{64}Cu-DOTA-siRNA packaged into Tf-targeted nanoparticles (charge ratio (+/-) = 3), Lane 6 = 20 μL urine from a mouse injected with ^{64}Cu-DOTA-siRNA packaged into Tf-targeted nanoparticles (charge ratio (+/-) = 3) + 1% SDS, Lane 7 = empty, Lane 8 = 20 μL urine from an untreated mouse, Lane 9 = 20 μL urine from an untreated mouse + 1% SDS.

In an attempt to elucidate a possible physiologically based mechanism for the nanoparticle dissociation and release of free siRNA after intravenous administration, gel electrophoresis was used to examine the stability of the nanoparticles against dissociation when incubated in physiological salt (NaCl) concentrations. As shown in Figure 5.8, incubation of the nanoparticles with increasing salt concentration from 0 to 1.5 M NaCl led to a decrease in the intensity of the band at the top of the gel (siRNA within nanoparticles) with a corresponding increase in the intensity of the bands corresponding to free siRNA (an apparent shift in mobility for free siRNA appears to occur at salt concentrations above ~1 M). Since the nanoparticles are formed by electrostatic interactions between the positively charged cationic polymer strands and the negatively charged siRNA molecules, high salt concentrations can weaken these interactions and

allow release of free siRNA. This salt-mediated disruption of the nanoparticles would be consistent with the slight delay in peak kidney activity observed for the nanoparticle formulations relative to naked siRNA. Such a delay would be indicative of the dissociation of the nanoparticles leading to release of the free siRNA that is then rapidly cleared by the kidneys. When the same experiment was conducted using pDNA instead of siRNA as the nucleic acid, the nanoparticles were not as easily disrupted by the presence of NaCl (Figure 5.8). These results indicate that the siRNA nanoparticles are more susceptible to salt-mediated disruption than pDNA nanoparticles, perhaps owing to the smaller polyanion size for the siRNA relative to plasmid DNA.
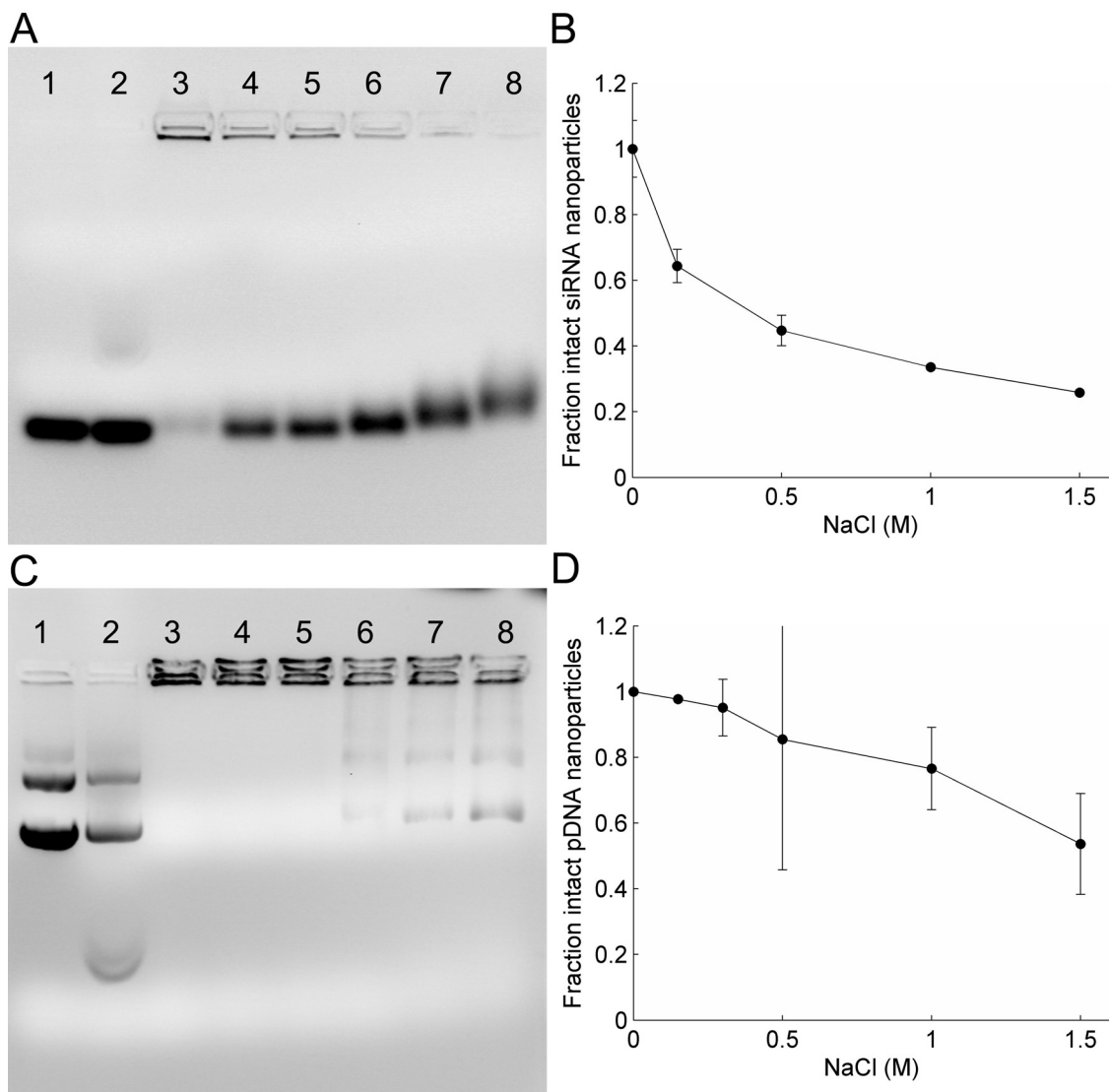
Figure 5.8. NaCl concentration-dependent disruption of Tf-targeted nanoparticles containing unmodified siRNA or pDNA. (A) Gel electrophoresis of siRNA nanoparticles: Lane 1 = naked siRNA, Lane 2 = nanoparticles + 1% SDS, Lane 3 = nanoparticles in water, Lane 4 = nanoparticles in 1X PBS, Lane 5 = nanoparticles in 0.15 M NaCl, Lane 6 = nanoparticles in 0.5 M NaCl, Lane 7 = nanoparticles in 1 M NaCl, Lane 8 = nanoparticles in 1.5 M NaCl. (B) Fraction of intact siRNA nanoparticles based on intensity in the wells (corresponding to siRNA within intact nanoparticles). The change in intensity with increasing NaCl concentration was normalized to the intensity for siRNA nanoparticles incubated in water alone (Lane 3). Error bars = *SD*. (C) Gel electrophoresis of pDNA nanoparticles: Lane 1 = naked pDNA, Lane 2 = nanoparticles + 1% SDS, Lane 3 = nanoparticles in water, Lane 4 = nanoparticles in 0.15 M NaCl, Lane 5 = nanoparticles in 0.3 M NaCl, Lane 6 = nanoparticles in 0.5 M NaCl, Lane 7 = nanoparticles in 1 M NaCl, Lane 8 = nanoparticles in 1.5 M NaCl. (D) Fraction of intact pDNA nanoparticles based on intensity in the wells (corresponding to pDNA within intact nanoparticles). The change in intensity with increasing NaCl concentration was normalized to the intensity for pDNA nanoparticles incubated in water alone (Lane 3).

5.4.6 Tumor localization and function of targeted vs. non-targeted siRNA nanoparticles

A multimodality imaging approach was taken to investigate the biodistribution and functional activity of siRNA delivered by Tf-targeted or non-targeted nanoparticles. MicroPET/CT was used to analyze the biodistribution and tumor localization of the siRNA nanoparticles, while BLI enabled quantification of the luciferase knockdown by the delivered siRNA against luciferase. The tissue distribution of the ^{64}Cu-DOTA-siRNA delivered by Tf-targeted and non-targeted nanoparticles was very similar for the first hour after injection, with similar blood clearance and tumor accumulation (Figure 5.9).
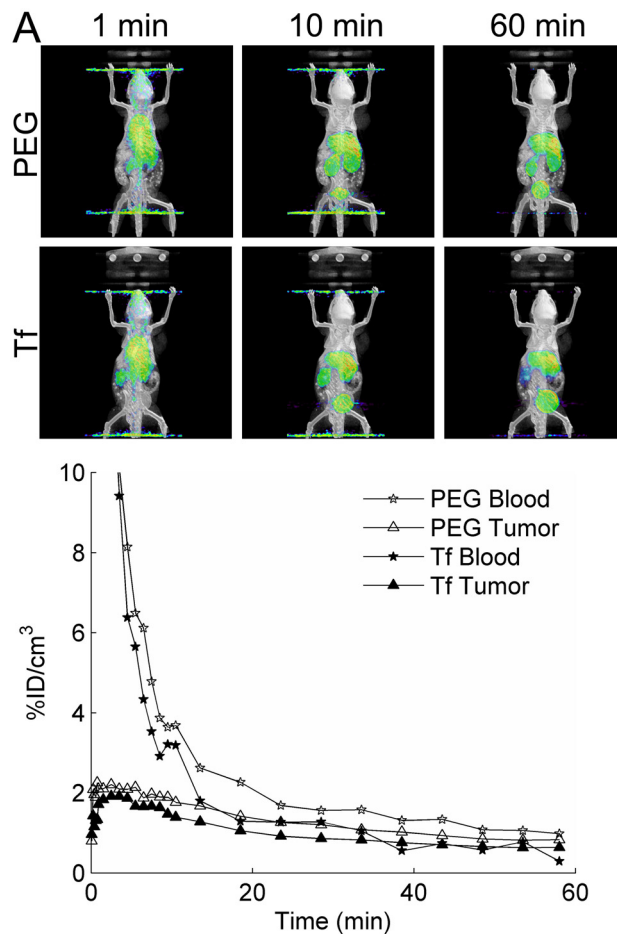
Figure 5.9. Tissue distribution of ^{64}Cu-DOTA-siRNA delivered intravenously by Tf-targeted and non-targeted nanoparticles for the first 60 min after injection. (A) Fused microPET/CT images of mice at 1, 10, and 60 min after injection. (B) Blood clearance and tumor localization of Tf-targeted and non-targeted siRNA nanoparticles for the first 60 min after injection.

Figure 5.10 shows the microPET/CT images (1 d post injection) and corresponding bioluminescent images (pre injection and 1 d post injection) of two representative mice. The average tumor activity at 1 d post injection measured by microPET was 1.1±0.3 %ID/cm^3 and 1.4±0.4 %ID/cm^3 for Tf-targeted and non-targeted nanoparticles, respectively. Taking advantage of the noninvasive nature of the microPET/CT imaging, the same mice were also examined for luciferase activity by BLI before injection and 1 d post injection. The relative luciferase knockdown by the delivered siRNA molecules was calculated based on the percent change in the tumor luciferase activity (Figure 5.10C). The relative increase of tumor luciferase activity in mice treated with Tf-targeted nanoparticles is 50% lower than that in mice treated with non-targeted nanoparticles. This provides strong evidence suggesting that the Tf-targeted nanoparticles are able to deliver more functional siRNA to the tumor cells than non-targeted nanoparticles. These data also corroborate our observations showing that tumor growth inhibition by a therapeutic siRNA was only observed when the siRNA was delivered by Tf-targeted nanoparticles and not by non-targeted nanoparticles (6).
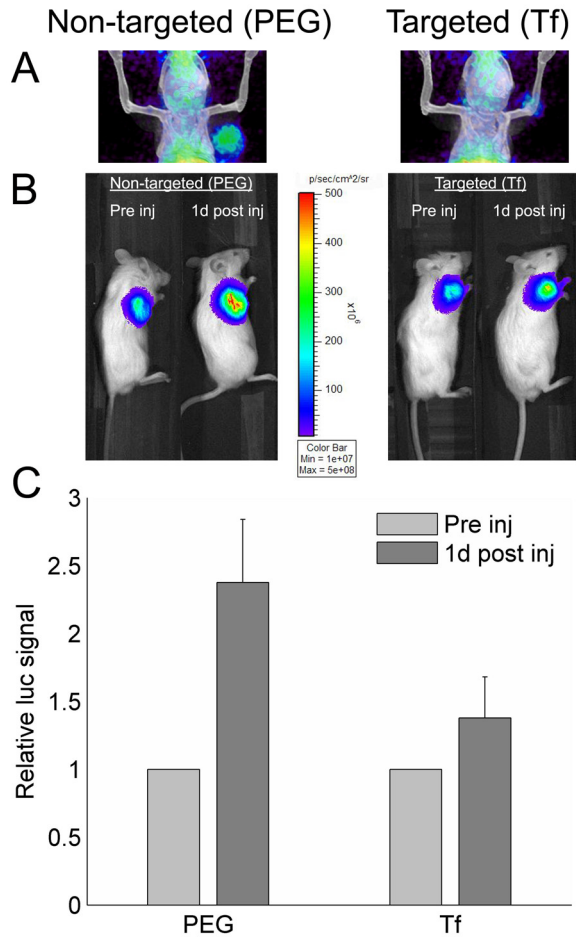
Figure 5.10. Multimodality in vivo imaging of siRNA nanoparticle delivery and function using microPET/CT and BLI. (A) Fused microPET/CT image showing tumor-associated activity 1 d post intravenous injection of Tf-targeted and non-targeted nanoparticles containing ^{64}Cu-DOTA-siRNA. Image scale: min threshold = 0.1 %ID/cm^3, max threshold = 1.5 %ID/cm^3). (B) BLI of the same mice shown in (A) before injection and 1 d post injection. (C) Relative change in luciferase expression 1 d after intravenous injection of Tf-targeted (n = 7) and non-targeted (n = 4) nanoparticles containing ^{64}Cu-DOTA-siRNA for simultaneous PET imaging. $p < 0.1$ based on a Student's t-Test with a two-tailed distribution.

5.5 Discussion

This study demonstrates the utility of noninvasive imaging technologies to

concurrently examine the biodistribution and in vivo efficacy of siRNA nanoparticles.

Synthesis of DOTA-conjugated siRNA molecules allowed labeling with ^{64}Cu, a positron

emitting radionuclide, and subsequent imaging by microPET. The spatiotemporal

distribution of the injected ^{64}Cu-labeled molecules was determined by co-registration of

the microPET images with anatomical information from microCT. The microPET

technology allows collection of high resolution, three-dimensional biodistribution of the

injected radiolabeled molecules over time. Therefore, the biodistribution of nanoparticles

containing ^{64}Cu-DOTA-siRNA could be followed after injection in living mice.

Furthermore, because microPET/CT is noninvasive, BLI was used to measure the tumor

luciferase activity in these same mice. By using an siRNA sequence that targets

luciferase, the relative change in luciferase activity before and after injection serves as an

indicator for siRNA function within the tumor cells.

The combination of microPET/CT and BLI represents a novel method to

concurrently examine the biodistribution and functional efficacy of siRNA nanoparticle

formulations in living subjects. Here, we used this methodology to investigate siRNA

nanoparticles formed using cyclodextrin-containing polycations (CDP), as CDP has

previously been shown to deliver functional siRNA to tumors in mice after systemic

administration (6). Additionally, the CDP-based siRNA nanoparticles can be formulated

with or without a Tf targeting ligand and can therefore be used to investigate the

differences in biodistribution and functional efficacy of targeted and non-targeted

nanoparticles.

DOTA-conjugated siRNA molecules targeting luciferase were synthesized by

reacting DOTA-NHS with an siRNA containing a 5'-NH$_2$. The resulting DOTA-siRNA

retained the ability to achieve luciferase knockdown in vitro, although the activity was

reduced relative to the unmodified siRNA. Incorporation of DOTA-siRNA into the

nanoparticles had negligible effects on the size and zeta potential of the resulting

nanoparticles. Furthermore, nanoparticles containing 0%, 20%, and 50% DOTA-siRNA

all exhibited similar serum stability with an siRNA half-life of approximately 11 h in 50% mouse serum. Radiolabeling efficiencies of the DOTA-siRNA with ^{64}Cu were typically around 30-50%. These results all indicate that DOTA-modification of siRNA molecules has negligible impact on nanoparticle properties and is therefore a viable strategy for creating radiolabeled siRNA nanoparticles for imaging by microPET.

The results of the microPET studies indicated that attachment of the transferrin targeting ligand to the surface of the nanoparticles had negligible effect on the tissue distribution observed by PET. Both targeted and non-targeted nanoparticles demonstrated nearly identical tumor localization kinetics, and at 1 d post injection showed similar tumor accumulation representing ~1% ID/cm^3. This is likely due to the nonspecific tumor accumulation resulting from the enhanced permeability and retention (EPR) effect, which effectively traps large macromolecules in the tumor microenvironment regardless of cell-specific binding or internalization. However, BLI was used to examine function in tandem with the tissue distribution studies by microPET, and unlike the results with microPET showing that the tissue distribution was approximately equal for both targeted and non-targeted nanoparticles, BLI revealed that the targeted nanoparticles were more effective in reducing tumor luciferase expression 1 d post injection. Previous studies with other targeted delivery systems have also led to similar conclusions that the targeting moieties do not necessarily increase the total tumor accumulation but instead contribute to enhanced internalization by the tumor cells (17,18).

Even though the Tf-targeted nanoparticles were able to achieve luciferase knockdown after systemic administration, the biodistribution by microPET indicated that

a significant portion of the injected siRNA dose was rapidly cleared by kidney filtration. The possibility that the siRNA nanoparticles dissociate upon injection into the bloodstream led to investigation of a physiologically based mechanism to explain this observation. This effect may be most pronounced in the kidney since renal physiology provides a reasonable explanation for the observations made in this study and elsewhere concerning complexes formed by electrostatic interactions with nucleic acids. Even if the intact nanoparticles are not filtered through the glomerulus on account of their size, they still can travel through the nephron of the kidney via the vasa recta. Because of the countercurrent concentrating mechanism utilized by the kidney, NaCl concentrations in the vasa recta at the papillary tip of the renal medulla reach approximately 0.4 M (19). It is possible that the greatest dissociation of the nanoparticles takes place here, as the electrostatic interactions between the cationic polymer and the siRNA may be compromised in such high salt concentrations. The results in Figure 5.8 indicate ~50% dissociation of the siRNA nanoparticles at concentrations of 0.4 M. Additionally, once the free siRNA is released into the complex milieu of the blood, there is little chance for it to re-associate with the nanoparticles before being bound by other blood components or rapidly cleared by the kidney (through either glomerular filtration on the next pass or by active transport by transporters located on the renal proximal tubule cells).

Several previous studies have demonstrated that increasing amounts of NaCl can lead to concentration-dependent dissociation of complexes formed between nucleic acids and cationic polymers or lipids (20-22). Eldred et al. observed that complexes between lysine-based peptide oligomers and plasmid DNA showed a sharp rise in the amount of unpackaged DNA at ~550 mM NaCl (20). Additionally, Oupicky et al. examined NaCl-

mediated dissociation of DNA complexes formed with the cationic polymer, poly-L-lysine (21). They showed that when the polyplexes were crosslinked with DTBP (dimethyl-3,3'-dithiobispropionimidate), the polyplexes did not exhibit NaCl-dependent dissociation. Furthermore, while the non-crosslinked PEGylated polyplexes exhibited rapid clearance from the blood circulation, the crosslinked PEGylated polyplexes showed enhanced blood circulation times. These observations would be consistent with the hypothesized mechanism for disruption of the electrostatic nanoparticle interactions during blood circulation, particularly in the medulla of the kidney.

Further studies need to be conducted to confirm whether the conditions reached in the kidney medulla may be responsible for the disruption of the siRNA nanoparticles in this study. This disruption mechanism may have broad implications for the general design of nanoparticles assembled through electrostatic interactions. Although the siRNA nanoparticles used in this study were still able to deliver sufficient siRNA to achieve luciferase knockdown measured by BLI, the microPET experiments demonstrated that the majority of the injected dose was cleared rapidly from the blood circulation through kidney filtration. To achieve more efficient systemic delivery of siRNA through nanoparticle formulations, it will be imperative to address the short blood circulation times observed for the nanoparticle formulations. For nanoparticles formed through electrostatic interaction with nucleic acids, the increased salt concentration reached in the kidney (especially in juxtamedullary nephrons) may lead to significant nanoparticle dissociation and release of free nucleic acid. If the nanoparticles are stabilized against salt-induced dissociation, then they may begin to exhibit the desired property of extended circulation times, especially if the stabilized nanoparticles are

coated with a PEG layer to reduce interaction with cells in the reticuloendothelial system. Most likely an optimum stability will exist for the nanoparticle formulations that prevents excessive release of payload during circulation while still allowing adequate release upon cellular internalization.

5.6 Acknowledgments

5.7 References

1. Soutschek, J., Akinc, A., Bramiage, B., Charisse, K., Constien, R., Donoghue, M., Elbashir, S., Geick, A., Hadwiger, P., Harborth, J. et al. (2004) Therapeutic silencing of an endogenous gene by systemic administration of modified siRNAs. *Nature*, **432,** 173-178.

2. Song, E., Zhu, P., Lee, S.-K., Chowdhury, D., Kussman, S., Dykxhoorn, D.M., Feng, Y., Palliser, D., Weiner, D.B., Shankar, P. et al. (2005) Antibody mediated in vivo delivery of small interfering RNAs via cell-surface receptors. *Nat Biotechnol*, **23,** 709-717.

3. Behlke, M.A. (2006) Progress towards in vivo use of siRNAs. *Mol Ther*, **13,** 644-670.

4. Zimmermann, T.S., Lee, A.C.H., Akinc, A., Bramlage, B., Bumcrot, D., Fedoruk, M.N., Harborth, J., Heyes, J.A., Jeffs, L.B., John, M. et al. (2006) RNAi-mediated gene silencing in non-human primates. *Nature*, **441,** 111-114.

5. Bartlett, D.W. and Davis, M.E. (2007) Physicochemical and biological characterization of targeted, nucleic acid-containing nanoparticles. *Bioconjugate Chem*, **18,** 456-468.

6. Hu-Lieskovan, S., Heidel, J.D., Bartlett, D.W., Davis, M.E. and Triche, T.J. (2005) Sequence-specific knockdown of EWS-FLI1 by targeted, nonviral delivery of small interfering RNA inhibits tumor growth in a murine model of Ewing's sarcoma. *Cancer Res*, **65,** 8984-8992.

7. Heidel, J.D., Yu, Z., Liu, J.Y.-C., Rele, S.M., Liang, Y., Zeidan, R.K., Kornbrust, D.J. and Davis, M.E. (2007) Administration in non-human primates of escalating intravenous doses of targeted nanoparticles containing ribonucleotide reductase subunit M2 siRNA. *P Natl Acad Sci USA*, **104,** 5715-5721.

8. Medarova, Z., Pham, W., Farrar, C., Petkova, V. and Moore, A. (2007) In vivo imaging of siRNA delivery and silencing in tumors. *Nat Med*, **13,** 372-377.

9. de Wolf, H.K., Snel, C.J., Verbaan, F.J., Schiffelers, R.M., Hennink, W.E. and Storm, G. (2007) Effect of cationic carriers on the pharmacokinetics and tumor localization of nucleic acids after intravenous administration. *Int J Pharm*, **331,** 167-175.

10. Bartlett, D.W. and Davis, M.E. (2006) Insights into the kinetics of siRNA-mediated gene silencing from live-cell and live-animal bioluminescent imaging. *Nucleic Acids Res*, **34,** 322-333.

11. Chow, P.L., Stout, D.B., Komisopoulou, E. and Chatziioannou, A.F. (2006) A method of image registration for small animal, multi-modality imaging. *Phys Med Biol*, **51,** 379-390.

12. Loening, A.M. and Gambhir, S.S. (2003) AMIDE: a free software tool for multimodality medical image analysis. *Mol Imaging*, **2,** 131-137.

13. Bartlett, D.W. and Davis, M.E. (2007) Effect of siRNA nuclease stability on the in vitro and in vivo kinetics of siRNA-mediated gene silencing. *Biotechnol Bioeng*, in press.

14. Owen, J., Charles A. and Orvis, A.L. (1970) Release of copper by rat liver. *Am J Physiol*, **218,** 88-91.

15. van de Water, F.M., Boerman, O.C., Wouterse, A.C., Peters, J.G.P., Russel, F.G.M. and Masereeuw, R. (2006) Intravenously administered short interfering RNA accumulates in the kidney and selectively suppresses gene function in renal proximal tubules. *Drug Metab Dispos*, **34,** 1393-1397.

16. Braasch, D.A., Paroo, Z., Constantinescu, A., Ren, G., Oz, O.K., Mason, R.P. and Corey, D.R. (2004) Biodistribution of phosphodiester and phosphorothioate siRNA. *Bioorgan Med Chem*, **14,** 1139-1143.

17. Maeda, N., Miyazawa, S., Shimizu, K., Asai, T., Yonezawa, S., Kitazawa, S., Namba, Y., Tsukada, H. and Oku, N. (2006) Enhancement of anticancer activity in antineovascular therapy is based on the intratumoral distribution of the active targeting carrier for anticancer drugs. *Biol Pharm Bull*, **29,** 1936-1940.

18. Kirpotin, D.B., Drummond, D.C., Shao, Y., Shalaby, M.R., Hong, K., Nielsen, U.B., Marks, J.D., Benz, C.C. and Park, J.W. (2006) Antibody targeting of long-circulating lipidic nanoparticles does not increase tumor localization but does increase internalization in animal models. *Cancer Res*, **66,** 6732-6740.

19. Edwards, A., Delong, M.J. and Pallone, T.L. (2000) Interstitial water and solute recovery by inner medullary vasa recta. *Am J Physiol Renal Physiol*, **278,** F257-F269.

20. Eldred, S.E., Pancost, M.R., Otte, K.M., Rozema, D., Stahl, S.S. and Gellman, S.H. (2005) Effects of side chain configuration and backbone spacing on the gene delivery properties of lysine-derived cationic polymers. *Bioconjugate Chem*, **16,** 694-699.

21. Oupicky, D., Carlisle, R. and Seymour, L. (2001) Triggered intracellular activation of disulfide crosslinked polyelectrolyte gene delivery complexes with extended systemic circulation in vivo. *Gene Ther*, **8,** 713-724.

22. Pozharski, E. and MacDonald, R.C. (2003) Lipoplex thermodynamics: determination of DNA-cationic lipid interaction energies. *Biophys J*, **85,** 3969-3978.

6 Sequence-specific knockdown of EWS-FLI1 by targeted, non-viral delivery of siRNA inhibits tumor growth in a murine model of metastatic Ewing's sarcoma[†]

6.1 Abstract

Systemic delivery of nucleic acid molecules is one of the major hurdles limiting the application of siRNA-based therapeutics for cancer treatment. Multifunctional nanoparticles are being investigated as systemic, nonviral nucleic acid delivery systems, and here we describe the use of cyclodextrin-containing polycations (CDP) to interact with small interfering RNA (siRNA) molecules to form nanoparticles that can be modified with transferrin (Tf) for targeting to transferrin receptor (TfR)-overexpressing tumor cells. Twice-weekly intravenous injections of Tf-targeted nanoparticles formed with an siRNA targeting the EWS-FLI1 oncogenic fusion protein are able to achieve sequence-specific knockdown of the EWS-FLI1 gene in vivo, leading to tumor growth inhibition in a disseminated model of Ewing's sarcoma. Removal of the targeting ligand or the use of a control siRNA sequence eliminates the anti-tumor effects. Additionally, no abnormalities in interleukin-12 and interferon-alpha, liver and kidney function tests, complete blood counts, or pathology of major organs are observed after injection of the nanoparticles. These data provide strong evidence for the safety and efficacy of this targeted, non-viral siRNA delivery system.

6.2   Introduction

Ewing's family of tumors (EFT) is a poorly differentiated mesenchymal malignancy that arises in bone or soft tissue. It is the second most common primary osseous malignancy in childhood and adolescence (1). Historical data show that virtually all patients die from metastases (e.g., <5% survival after localized therapy (2)). Systemic chemotherapy has improved survival of patients with localized disease, but patients with metastatic disease rarely benefit from continued therapy (3). A major factor contributing to this outcome is the development of multi-drug resistance by the time patients are treated for metastasis. The translocation t(11;22) is commonly detected in EFT and produces the chimeric EWS-FLI1 fusion gene found in 85% of EFT patients (3). The EWS domain replaces the normal transcriptional activator domain in the 5' region of the FLI1 DNA-binding protein, leading to altered transcriptional activation that contributes to the tumorigenic phenotype (1). Reduction of the EWS-FLI1 protein in EFT cells in vitro or in subcutaneous xenograft tumors by antisense oligonucleotides complementary to EWS-FLI1 mRNA results in decreased proliferation (4-6), suggesting a potential therapeutic intervention directed at this tumor-specific chimeric gene. Small interfering RNAs (siRNAs) have recently been shown to silence the EWS-FLI1 gene and suppress proliferation of an EFT cell line in vitro (7-9). To build upon these previous studies, the current study explores the use of systemically delivered siRNA against EWS-FLI1 to inhibit growth and dissemination of EFT cells in a xenograft model of Ewing's sarcoma.

As discussed in Chapter 4, nanoparticle carriers offer several features that make them attractive for systemic siRNA delivery. Cyclodextrin-containing polycations (CDP) can interact with small interfering RNA (siRNA) molecules to form nanoparticles that are

approximately 60-80 nm in diameter. The modular design of these nanoparticles enables modification with PEG molecules for steric stabilization and Tf targeting ligands for uptake by TfR-overexpressing tumor cells. The nanoparticles protect the nucleic acid payload from nuclease degradation, do not aggregate at physiological salt concentrations, and cause minimal erythrocyte aggregation and complement fixation. Here, we investigate their ability to deliver a therapeutic siRNA to tumor cells in vivo after intravenous administration.

The EFT cell line, TC71, is used to create a disseminated model of Ewing's sarcoma in NOD/scid mice. The TC71 cells engineered to express the luciferase gene (TC71-Luc) are injected by low-pressure tail-vein injection to mimic the metastatic process. The most common engraftment sites are lung, vertebral column, pelvis, femur, and soft tissue, corresponding to the most frequently observed sites for metastases in EFT patients (10). Live-animal bioluminescent imaging (BLI) is used to noninvasively track the growth of metastases in mice. We test the ability of targeted, non-viral delivery of siRNA against EWS-FLI1 to safely limit bulk metastatic tumor growth and prevent establishment of bulk metastatic disease from microscopic metastatic disease. We prove here the hypothesis that the targeted, non-viral delivery of siRNA can safely abrogate EWS-FLI1 expression and inhibit metastatic Ewing's tumor growth in vivo.

6.3   Materials and methods

6.3.1   *siRNA sequences*

siRNA targeting luciferase (siGL3), the breakpoint of EWS-FLI1 (siEFBP2), a

mutated negative control for siEFBP2 (siEFBP2mut), and a non-targeting control

sequence (siCON1) were obtained from Dharmacon Research, Inc..

siGL3:
        5'-----CUUACGCUGAGUACUUCGAdTdT
         dTdTGAAUGCGACUCAUGAAGCU-----5'

siEFBP2(7):
        5'---GCAGAACCCUUCUUAUGACUU
         UUCGUCUUGGGAAGAAUACUG---5'

siEFBP2mut(7):
        5'---GCAGAACCAGUCUUAUGACUU
         UUCGUCUUGGUCAGAAUACUG---5'

siCON1:
        5'---UAGCGACUAAACACAUCAAUU
         UUAUCGCUGAUUUGUGUAGUU---5'

6.3.2   *In vitro down-regulation of EWS-FLI1 in an EFT cell line*

TC71 cells were grown on 6-well plates in RPMI 1640 with 10% FBS (no

antibiotics) until they reached 30% confluency. siRNA was complexed with

Oligofectamine (Invitrogen) according to the manufacturer's instructions. The resulting

formulations were applied to each well at a final concentration of 100 nM. All transfected

cells were harvested at 48 h and gene expression was assessed by Western blot analysis.

Primary monoclonal antibodies against the C-terminal region of FLI1 were obtained from

BD Biosciences. Polyclonal antibodies against β-Actin were obtained from Santa Cruz

Biotechnology.

6.3.3 Injection of mice with TC71-Luc cells

TC71-Luc cells were grown in RPMI 1640 supplemented with 10% FBS and antibiotics (penicillin/streptomycin) and subsequently trypsinized and resuspended in serum-free RPMI 1640 for injection. Each mouse was injected with $5x10^6$ TC71-Luc cells by tail vein injection of 0.2 mL of the cell suspension. Mice were treated according to the NIH Guidelines for Animal Care and as approved by the Caltech Institutional Animal Care and Use Committee. All mice were 6-8 weeks of age at the time of injection.

6.3.4 Bioluminescent imaging of the mice

Longitudinal imaging of the mice was performed using the Xenogen IVIS 100 imaging system. D-luciferin (Xenogen) was dissolved in PBS at 15 g L^{-1}, and 0.2 mL of the 15 g L^{-1} luciferin solution was injected i.p. 10 minutes before measuring the light emission. Mice were anesthetized with an initial dose of 5% isoflurane followed by a maintenance dose of 2.5% isoflurane. Bioluminescent signals were quantified using Living Image software (Xenogen).

6.3.5 Formulation of non-viral, siRNA-containing nanoparticles for in vivo administration

Before addition to the nucleic acid, the CDP was mixed with AD-PEG at a 1:1 AD-PEG:β-CD (mol:mol) ratio in water. Targeted nanoparticles also contained transferrin-modified AD-PEG (AD-PEG-Tf) at a 1:1000 AD-PEG-Tf:AD-PEG (w:w) ratio. The mixture of CDP, AD-PEG, and AD-PEG-Tf in water was then added to an equal volume of siRNA in water such that the ratio of positive charges from CDP to negative charges from the nucleic acid was equal to the desired charge ratio of 3 (+/-).

An equal volume of 10% (w/v) glucose in water was added to the resulting nanoparticles to give a final concentration of 5% (w/v) glucose suitable for injection.

6.3.6 Consecutive-day delivery of siRNA to tumors in vivo

Mice with successful tumor cell engraftment received injection of formulations containing siRNA against luciferase (siGL3), EWS-FLI1 (siEFBP2) or a control sequence (siCON1) on two or three consecutive days as indicated. Each mouse (~20 g) received 0.2 mL of the appropriate formulation, containing 50 μg of siRNA corresponding to a 2.5 mg/kg dose, by low-pressure tail-vein injection using a 1-mL syringe and a 27-gauge needle.

6.3.7 Real Time Quantitative RT-PCR (Q-RT-PCR)

Total cellular RNA was isolated using RNA STAT-60 (Tel-Test) from homogenized tumors. cDNA was synthesized from 2 μg of DNase I (Invitrogen)-treated total RNA in a 42μl reaction volume using oligo–dT and Superscript II (Invitrogen) for 60 min at 42°C following suppliers' instructions. PCR primers were designed with MacVector 7.0 (Accelrys). The sequences are:

EWS-FLI1, forward, 5'-CGACTAGTTATGATCAGAGCAGT-3',

reverse, 5'-CCGTTGCTCTGTATTCTTACTGA-3';

β-Actin, forward, 5'-GCACCCCGTGCT GCTGAC-3',

reverse, 5'-CAGTGGTACGGCCAGAGG-3'.

PCR was performed as described previously (11). PCR conditions were 95°C for 900 s; 40 cycles of 95°C for 15 s, 60°C for 30 s, 72°C for 30 s; and a final denaturing stage from 60°C to 95°C. All PCR products were analyzed on a 1% agarose gel and a single band was observed except for negative controls. The reproducibility was evaluated by at least

three PCR measurements. The expression level of the target gene was normalized to internal β-actin and the mean and standard deviation of the target/β-actin ratios were calculated for sample-to-sample comparison.

6.3.8   Long-term delivery of siRNA to tumors in vivo

Fifty female NOD/scid mice were injected with $5x10^6$ TC71-Luc cells as described above. Immediately after cell injection, each mouse received an additional injection of 0.2 mL of one of the following formulations (n = 10 mice per group): 5% glucose (group A); naked siEFBP2 (group B); targeted nanoparticles containing siCON1 (group C); targeted nanoparticles containing siEFBP2 (group D); or non-targeted nanoparticles containing siEFBP2 (group E). Formulations were administered twice-weekly for four weeks. Images were taken immediately after the first injections for quality control of the injections and twice-weekly immediately before the injection of the formulations. We continued to monitor the tumor signal in the mice receiving targeted (group D) and non-targeted (group E) siEFBP2 formulations for an additional three weeks or until tumor burden required euthanization of the mice.

6.3.9   Toxicity, immune response, and pathology studies

Female C57BL/6 mice (Jackson Laboratories) were 6-8 weeks of age at the time of injection. To measure plasma cytokine levels, blood was harvested from mice 2 h and 24 h post-injection by cardiac puncture and plasma was isolated using Microtainer tubes (Becton Dickinson). Whole blood was used for complete blood count (CBC) analyses, and plasma was used for all liver enzyme and cytokine analyses. IL-12 (p40) (BD Biosciences) and IFN-α levels (PBL Biomedical Laboratories) were measured by ELISA according to the manufacturer's instructions. Major organs of the NOD/scid mice after

long-term treatment studies were collected, formalin-fixed and processed for routine

hematoxylin and eosin staining using standard methods. Images were collected using a

Nikon epifluorescent microscope with a DP11 digital camera.

6.4   Results

6.4.1   siRNA mediates down-regulation of EWS-FLI1 in cultured TC71 cells

Using a previously reported siRNA sequence targeting the EWS-FLI1 breakpoint

(siEFBP2)(7), we observed comparable and significant (greater than 50%) reduction in

EWS-FLI1 protein levels after Oligofectamine-mediated transfection (Figure 6.1).

Delivery of a mutant siRNA sequence (siEFBP2mut) failed to elicit such down-

regulation.
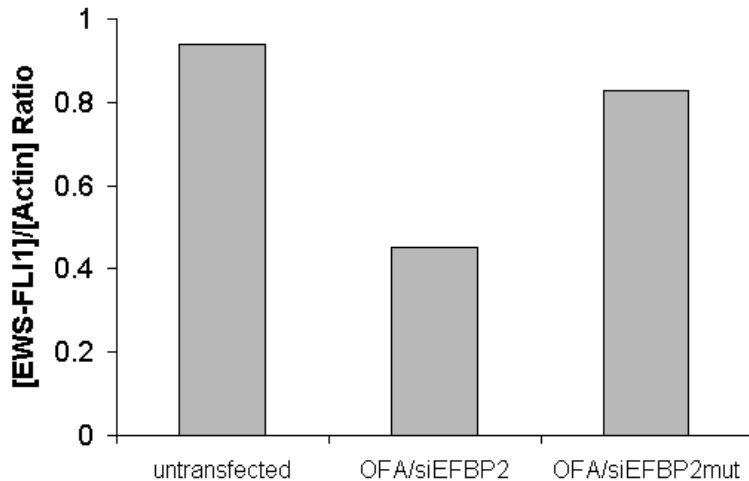
Figure 6.1. In vitro knockdown of EWS-FLI1 in cultured TC71 cells. At 48 h post-transfection, cells were lysed and total cell protein was denatured, electrophoresed, and transferred to a PVDF membrane that was probed with antibodies to EWS-FLI1 or actin (siEFBP2mut: mutant negative control). Average band intensities were determined by densitometry and the ratio of EWS-FLI1 to actin intensities was calculated.

6.4.2   Formulated siRNA against EWS-FLI1 inhibits tumor growth in vivo

Mice with successful engraftment of TC71-Luc cells were randomly selected for

treatment with targeted nanoparticles containing siEFBP2 on two consecutive days.

Assessment of the EWS-FLI1 expression in the tumors treated with two consecutive

siEFBP2 formulations showed a 60% down-regulation of EWS-FLI1 RNA level

compared to siCON1-treated tumors (p=0.046). (Figure 6.2). Therefore, the delivery of

targeted nanoparticles containing siEFBP2 is able to reduce EWS-FLI1 expression in the

established tumors.
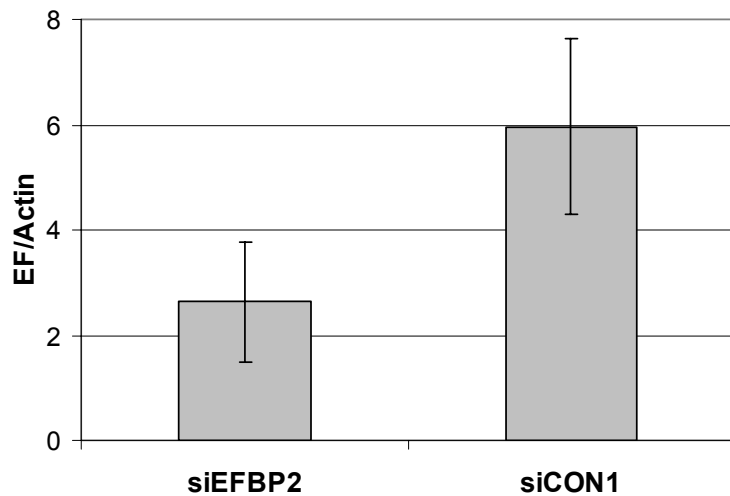
Figure 6.2. In vivo knockdown of EWS-FLI1 RNA levels in metastasized TC71-Luc tumors in mice. Tf-targeted nanoparticles containing 2.5 mg/kg of siEFBP2 or siCON1 were administered intravenously on days 19 and 20 after injection of TC71-Luc cells. Tumors were harvested on the third day. RNA was extracted and EWS-FLI1 level was determined by Q-RT-PCR.

6.4.3 Long-term, twice-weekly administration of targeted, formulated siEFBP2 inhibits tumor cell engraftment

To investigate the potential for tumor growth inhibition as a result of EWS-FLI1

knockdown, we employed a long-term treatment regimen in which formulations were

administered twice weekly beginning the same day as injection of TC71-Luc cells. These

studies allowed for the more careful investigation of the effects of variations in the

formulation conditions. Targeted nanoparticles containing siEFBP2 (group D)

dramatically inhibited the engraftment of TC71-Luc cells, with only 20% of the mice

showing any tumor growth compared to 90-100% in other treatment groups (Figure 6.3).

Neither the mice receiving naked siEFBP2 (group B) nor those receiving targeted

delivery of siCON1 (group C) showed any difference in tumor engraftment compared to

the control group that received only the 5% glucose carrier solution (group A).

Interestingly, tumors in mice treated with non-targeted nanoparticles containing siEFBP2

showed a delayed progression of tumor engraftment compared to the control groups.

Once significant tumors were established, however, the tumors seemed to grow at a rate

unaffected by continued treatment with the non-targeted nanoparticles containing

siEFBP2 (Figure 6.4). The tumor signal was monitored in the mice receiving targeted

(group D) and non-targeted (group E) nanoparticles containing siEFBP2 for an additional

three weeks until the tumor burden required euthanization of the mice. Whereas most of

the mice receiving non-targeted nanoparticles developed very large tumors, the majority

of the mice receiving targeted nanoparticles showed little or no tumor signal (Figure 6.3).

We conclude that treatment with the targeted nanoparticles containing siEFBP2 prevented

the tumor cell engraftment in these mice and slowed the growth of any tumors that did

develop.
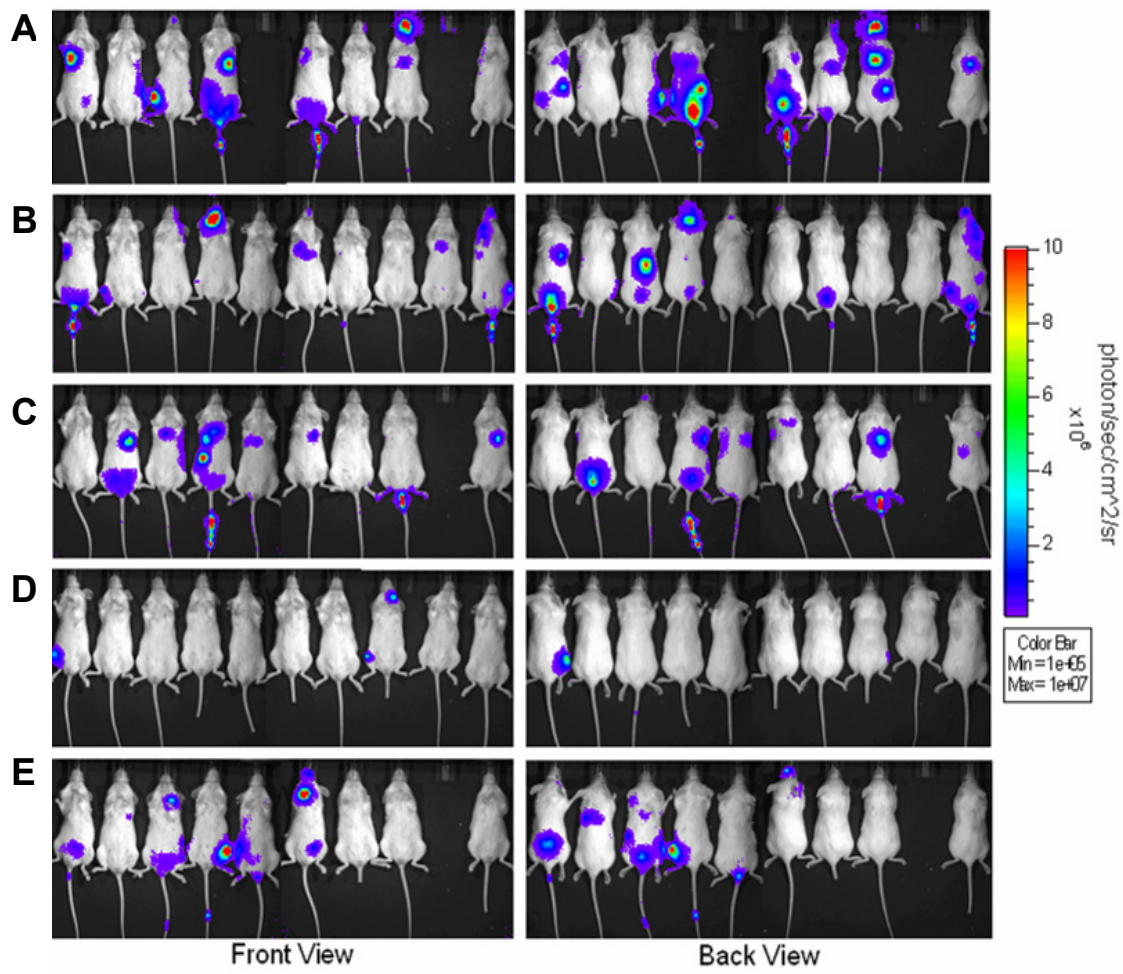
Figure 6.3. Bioluminescent images of the remaining mice from all treatment groups in NOD/scid mice 3.5 weeks after injection of $5x10^6$ TC71-Luc cells. Treatment was started on day 0 followed by twice-weekly injections of the treatment formulations. (A) = 5% glucose, (B) = Naked siEFBP2, (C) = Tf-targeted nanoparticles containing siCON1, (D) = Tf-targeted nanoparticles containing siEFBP2, (E) = Non-targeted nanoparticles containing siEFBP2.
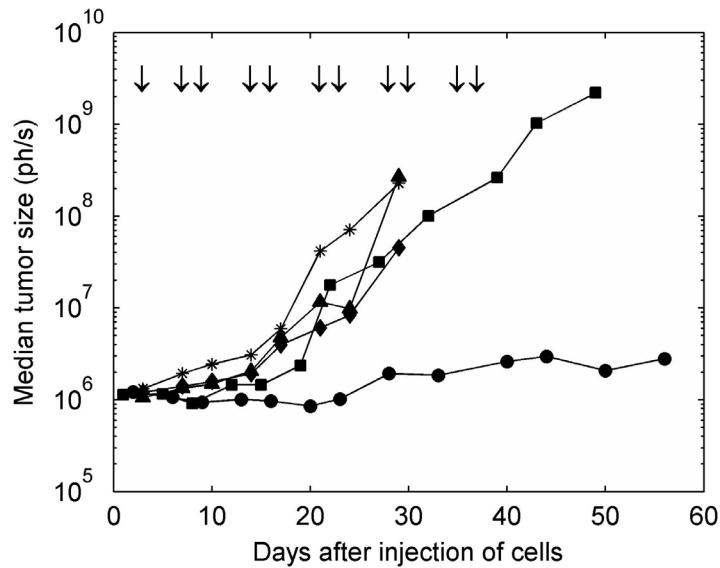
Figure 6.4. Median tumor size in NOD/scid mice after injection of 5×10^6 TC71-Luc cells on day 0 followed by twice-weekly injections (arrows) of the treatment formulations. Circles = Tf-targeted nanoparticles containing siEFBP2, squares = non-targeted nanoparticles containing siEFBP2, diamonds = Tf-targeted nanoparticles containing siCON1, triangles = naked siEFBP2, and asterisks = 5% glucose.

6.4.4   *No immune response or major organ damage was observed after treatment with targeted nanoparticles*

Since the ability of the NOD/scid mice to mount a possible immune response to these formulations is severely compromised, single tail-vein injections of formulations were repeated in immunocompetent mice (C57BL/6) and blood was collected at 2 h or 24 h after the injections. Complete blood counts (CBC) of whole blood showed insignificant changes in white blood cell (WBC) or platelet (PLT) counts (Figure 6.5). Levels of secreted liver enzymes (AST, ALT), blood urea nitrogen (BUN), and creatinine (CRE) were all unchanged, indicating a lack of damage to the liver or kidneys. No increases, resulting from formulations, in plasma interleukin-12 (IL-12) or interferon-alpha (IFN-α) at either 2 h or 24 h post-injection were observed (Figure 6.5).
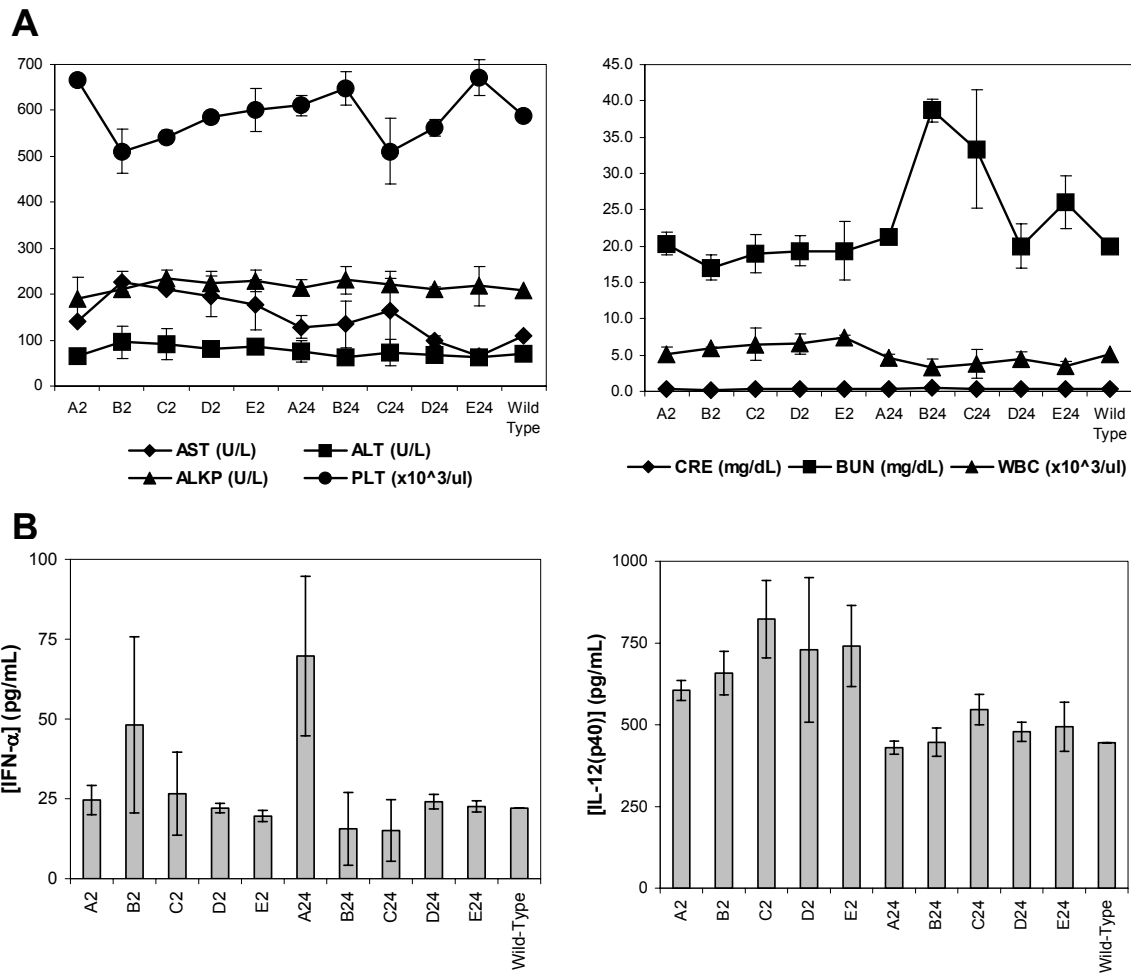
Figure 6.5. Evaluation of toxicity and immune response in mice after a single intravenous administration of formulated siRNA. (A) CBC and liver panel results for female C57BL/6 mice after a single intravenous dose of formulated siRNA. At 2 h or 24 h post-treatment, blood was drawn by cardiac puncture and plasma was isolated. Whole blood was used for determination of platelet (PLT) and white blood cell (WBC) counts. Plasma was used for measurement of aspartate aminotransferase (AST), alanine aminotransferase (ALT), alkaline phosphatase (ALKP), creatinine (CRE), and blood urea nitrogen (BUN). The averages of triplicate mice for each time point are plotted; error bars represent standard deviations. (B) Cytokine ELISA results for C57BL/6 mice after a single intravenous dose of formulated siRNA. The plasma levels of interleukin-12 (IL-12 (p40)) and interferon-alpha (IFN-α) in mice described above were measured by ELISA. Treatment groups: A = 5% glucose, B = naked siEFBP2, C = Tf-targeted nanoparticles containing siCON1, D = Tf-targeted nanoparticles containing siEFBP2, E = non-targeted nanoparticles containing siEFBP2, Wild-type = untreated. 2 = blood drawn 2 h after injection, 24 = blood drawn 24 h after injection.

We also performed pathological examination of the major organs (liver, kidney, brain, heart, lung, and pancreas) from the NOD/scid mice that received long-term treatments by hematoxylin and eosin (H&E) staining (Figure 6.6). No organ damage was observed with the nanoparticle formulations when compared to the 5% glucose and naked siEFBP2 treatment groups. Taken together, these results demonstrate the safety and low immunogenicity of these CDP-based nanoparticles.
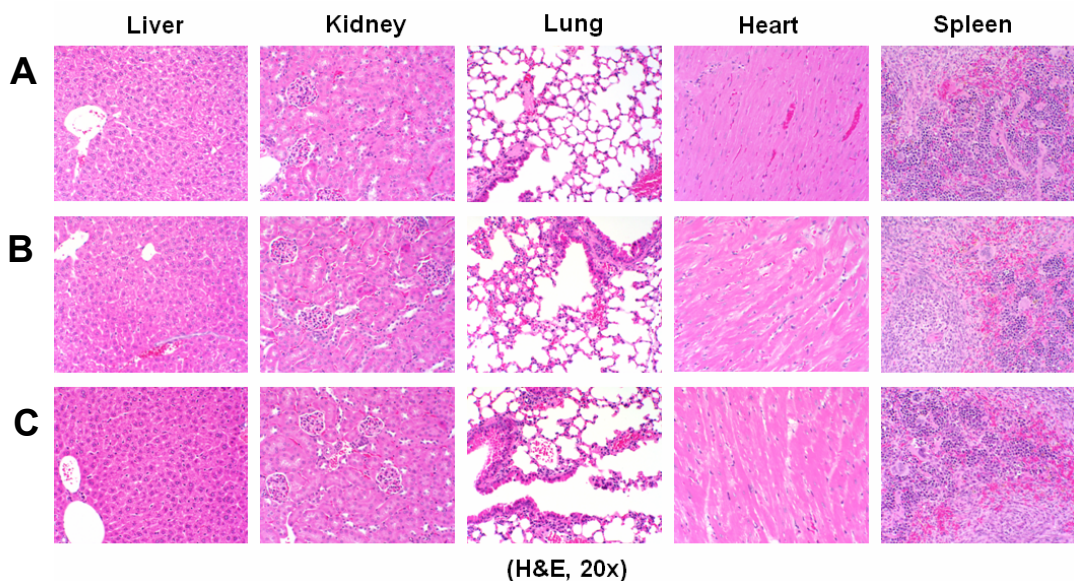
Figure 6.6. H&E staining of tissues from mice receiving long-term treatment with (A) 5% glucose, (B) naked siEFBP2, and (C) Tf-targeted nanoparticles containing siCON1.

6.5   Discussion

In this study, we describe the establishment of a highly reproducible and clinically relevant metastatic murine model for the Ewing's family of tumors in NOD/scid mice. Additionally, transduction of the EFT cells with the firefly luciferase gene enabled noninvasive, in vivo imaging of the mice to follow the fate of the injected tumor cells.

The tumor engraftment sites observed (lung, vertebral column, pelvis, femur and soft tissue) were comparable to the most common locations of metastases in EFT patients.

Small interfering RNA (siRNA) duplexes targeting the EWS-FLI1 fusion gene (siEFBP2) were formulated with CDP as described in Chapter 4. Targeted nanoparticles contained the transferrin targeting ligand to interact with the high levels of surface transferrin receptors expressed on the TC71 cells. This delivery system self-assembles with siRNA to form nanoparticles that are 60-80 nm in diameter.

Clinically, many tumors relapse after intensive treatment because of systemic dissemination of micrometastases. Nearly all EFT patients already have micrometastases at diagnosis, resulting in a >95% relapse rate when treated locally (2), and a 40% relapse rate after systemic chemotherapy (3). Therefore, effective treatment for elimination of circulating or dormant metastasized tumor cells after traditional therapy is needed. We explored the possibility of using targeted siRNA nanoparticles for this purpose by administration of the nanoparticles twice-weekly beginning the same day as injection of TC71-Luc cells. Of the different formulations tests, only the targeted nanoparticles containing siEFBP2 were able to achieve long-term tumor growth inhibition (Figure 6.4). Neither naked siEFBP2 nor targeted nanoparticles containing a control siRNA sequence showed any effect on tumor growth inhibition relative to the control group receiving only the 5% glucose carrier fluid. These results demonstrate the necessity of the delivery vehicle for systemic application and the sequence-specificity of the observed inhibition. We hypothesize that treatment with the targeted formulation of siEFBP2 assists in the prevention of the initial establishment of tumors in these mice from the injected cells and

slows the growth of any tumors that develop by downregulating the expression of the oncogenic fusion protein EWS-FLI1.

Notably, mice treated with non-targeted nanoparticles containing siEFBP2 showed an initial delay in tumor growth. However, the growth rate of tumors that eventually developed were unaffected by continuation of this treatment. The enhanced permeability and retention effect (EPR) leads to the accumulation of macromolecules in solid tumors, and both targeted and non-targeted nanoparticles may be able to accumulate in the tumors by this mechanism (12). This tumor accumulation of non-targeted nanoparticles was also observed by PET imaging, as discussed in Chapter 5. While some small fraction of the non-targeted nanoparticles may have entered tumor cells after accumulation in the tumor microenvironment, the inclusion of the Tf targeting ligand likely increases the overall uptake of the nanoparticles through receptor-mediated endocytosis. This increased uptake is likely responsible for the enhanced efficacy of Tf-targeted nanoparticles relative to non-targeted nanoparticles.

Recent in vitro reports have shown that siRNA sequences and their method of delivery may trigger an interferon response (13,14). Additionally, in vivo delivery of siRNA by lipids has resulted in potent interferon responses (15-17). Here, single tail-vein injections of all of the formulations were performed in immunocompetent (C57BL/6) mice to enable measurement of numerous blood markers that are indicative of an immune response. In contrast to results obtained from the injection of poly (I:C), a known immunostimulator through interactions with Toll-like receptor 3 (TLR3) (18), none of the formulations showed any significant effects on the levels of IL-12, IFN-α, white blood cells, platelets, secreted liver enzymes (ALT and AST), BUN, or CRE (Figure 6.5). All

of these observations with formulated siRNA are consistent with previous work showing a lack of immune response to naked siRNA (18). The cyclodextrin-based delivery system does not produce an interferon response even when siRNA is used that contains a motif known to be immunostimulatory when delivered in vivo with lipids (16) (published sequence is within siCON1). These results show the safety and low immunogenicity of CDP-containing formulations and demonstrate the attractiveness of this methodology for systemic, targeted delivery of nucleic acids. The in vivo gene silencing effect of siRNA by our delivery system is transient, permitting fine-tuning of the intensity and interval of the treatment. For example, the frequency of administration can be tuned for use in combination with other agents, and the treatment can be terminated within a few days if necessary.

This study demonstrates that, in contrast to naked siRNA delivery, the targeted siRNA nanoparticles used here are efficacious at low siRNA doses and do not require chemical modification for efficacy in vivo. Furthermore, the modular design of this delivery system enables it to be modified for targeting other tumor types by switching the specific targeting ligand attached to the surface of the nanoparticles. Importantly, the siRNA nanoparticles do not elicit a detectable immune response and are well-tolerated at the doses required for efficacy. We believe this treatment has the potential to be developed into a useful method for inhibition of metastatic EFT growth and may also have broad applicability in cancer therapy.

6.6 Acknowledgments

6.7 References

1. Ginsberg, J.P., Woo, S.Y., Johnson, M.E., Hicks, M.J. and Horowitz, M.E. (2002) In Pizzo, P. A. and Poplack, D. G. (eds.), *Principles and Practice of Pediatric Oncology*. Lippincott Williams & Wilkins, Philadelphia, pp. 973-1016.
2. Dahlin, D.C., Coventry, M.B. and Scanlon, P.W. (1961) Ewing's sarcoma. A critical analysis of 165 cases. *Am J Orthop*, **43-A,** 185-192.
3. Rodriguez-Galindo, C., Spunt, S.L. and Pappo, A.S. (2003) Treatment of Ewing sarcoma family of tumors: current status and outlook for the future. *Med Pediatr Oncol*, **40,** 276-287.
4. Tanaka, K., Iwakuma, T., Harimaya, K., Sato, H. and Iwamoto, Y. (1997) EWS-Fli1 antisense oligodeoxynucleotide inhibits proliferation of human Ewing's sarcoma and primitive neuroectodermal tumor cells. *J Clin Invest*, **99,** 239-247.
5. Maksimenko, A., Malvy, C., Lambert, G., Bertrand, J.R., Fattal, E., Maccario, J. and Couvreur, P. (2003) Oligonucleotides targeted against a junction oncogene are made efficient by nanotechnologies. *Pharm Res*, **20,** 1565-1567.
6. Maksimenko, A., Lambert, G., Bertrand, J.R., Fattal, E., Couvreur, P. and Malvy, C. (2003) Therapeutic potentialities of EWS-Fli-1 mRNA-targeted vectorized antisense oligonucleotides. *Ann N Y Acad Sci*, **1002,** 72-77.
7. Dohjima, T., Lee, N.S., Li, H., Ohno, T. and Rossi, J.J. (2003) Small interfering RNAs expressed from a Pol III promoter suppress the EWS/Fli-1 transcript in an Ewing sarcoma cell line. *Mol Ther*, **7,** 811-816.
8. Kovar, H., Ban, J. and Pospisilova, S. (2003) Potentials for RNAi in sarcoma research and therapy: Ewing's sarcoma as a model. *Semin Cancer Biol*, **13,** 275-281.
9. Chansky, H.A., Barahmand-Pour, F., Mei, Q., Kahn-Farooqi, W., Zielinska-Kwiatkowska, A., Blackburn, M., Chansky, K., Conrad, E.U., 3rd, Bruckner, J.D., Greenlee, T.K. et al. (2004) Targeting of EWS/FLI-1 by RNA interference attenuates the tumor phenotype of Ewing's sarcoma cells in vitro. *J Orthop Res*, **22,** 910-917.
10. Vormoor, J., Baersch, G., Decker, S., Hotfilder, M., Schafer, K.L., Pelken, L., Rube, C., Van Valen, F., Jurgens, H. and Dockhorn-Dworniczak, B. (2001) Establishment of an in vivo model for pediatric Ewing tumors by transplantation into NOD/scid mice. *Pediatr Res*, **49,** 332-341.
11. Zhang, J., Hu, S., Schofield, D.E., Sorensen, P.H. and Triche, T.J. (2004) Selective usage of D-Type cyclins by Ewing's tumors and rhabdomyosarcomas. *Cancer Res*, **64,** 6026-6034.
12. Tanaka, T., Shiramoto, S., Miyashita, M., Fujishima, Y. and Kaneo, Y. (2004) Tumor targeting based on the effect of enhanced permeability and retention (EPR) and the mechanism of receptor-mediated endocytosis (RME). *Int J Pharm*, **277,** 39-61.
13. Bridge, A.J., Pebernard, S., Ducraux, A., Nicoulaz, A.L. and Iggo, R. (2003) Induction of an interferon response by RNAi vectors in mammalian cells. *Nat Genet*, **34,** 263-264.

14. Sledz, C.A., Holko, M., de Veer, M.J., Silverman, R.H. and Williams, B.R. (2003) Activation of the interferon system by short-interfering RNAs. *Nat Cell Biol*, **5,** 834-839.

15. Hornung, V., Guenthner-Biller, M., Bourquin, C., Ablasser, A., Schlee, M., Uematsu, S., Noronha, A., Manoharan, M., Akira, S., de Fougerolles, A. et al. (2005) Sequence-specific potent induction of IFN-alpha by short interfering RNA in plasmacytoid dendritic cells through TLR7. *Nat Med*, **11,** 263-270.

16. Judge, A.D., Sood, V., Shaw, J.R., Fang, D., McClintock, K. and Maclachlan, I. (2005) Sequence-dependent stimulation of the mammalian innate immune response by synthetic siRNA. *Nat Biotechnol*, **23,** 457-462.

17. Ma, Z., Li, J., He, F., Wilson, A., Pitt, B. and Li, S. (2005) Cationic lipids enhance siRNA-mediated interferon response in mice. *Biochem Biophys Res Commun*, **330,** 755-759.

18. Heidel, J.D., Hu, S., Liu, X.F., Triche, T.J. and Davis, M.E. (2004) Lack of interferon response in animals to naked siRNAs. *Nat Biotechnol*, **22,** 1579-1582.

19. Davis, M.E., Pun, S.H., Bellocq, N.C., Reineke, T.M., Popielarski, S.R., Mishra, S. and Heidel, J.D. (2004) Self-assembling nucleic acid delivery vehicles via linear, water-soluble, cyclodextrin-containing polymers. *Curr Med Chem*, **11,** 179-197.

7 Growth inhibition of established subcutaneous tumors in mice after intravenous administration of siRNA nanoparticles: Impact of tumor-specific targeting and dosing schedule

7.1 Abstract

As nanoparticle carriers for systemic in vivo delivery of small interfering RNA (siRNA) near clinical application, the design of suitable dosing schedules will become particularly important for their efficacy. This study addresses issues of practical relevance for siRNA nanoparticle delivery by measuring the impact of tumor-specific targeting and the effect of dose and dose frequency on the survival of mice bearing established subcutaneous tumors. We have previously shown that cyclodextrin-containing polycations (CDP) can form siRNA nanoparticles that exhibit desirable properties for in vivo application. Furthermore, we showed that these siRNA nanoparticles could inhibit tumor formation in mice when they were injected twice-weekly beginning immediately after the initial injection of tumor cells in a metastatic cancer model. A major challenge for tumor-targeted siRNA nanoparticle delivery is to inhibit tumor growth in established tumors, where issues such as tumor penetration and interactions in the tumor microenvironment can become critical factors governing efficacy. Here, we form syngeneic subcutaneous tumors using the Neuro2A neuroblastoma cell line. Three consecutive daily doses of Tf-targeted nanoparticles carrying 2.5 mg/kg of two different siRNA sequences targeting ribonucleotide reductase subunit M2 (RRM2) slow the growth of tumors that are ~100 mm^3 at the beginning of treatment; non-targeted nanoparticles are significantly less effective when given at the

same dose. Furthermore, administration of the three doses on consecutive days or every

three days does not lead to statistically significant differences in tumor growth delay.

Mathematical model calculations of siRNA-mediated target protein knockdown and

tumor growth inhibition are used to elucidate possible mechanisms to explain the

observed effects and provide guidelines for designing more effective siRNA-based

treatment regimens.

7.2   Introduction

Delivery of a therapeutic agent to a desired site in the body after intravenous

administration often remains the rate-limiting step in the development of novel

therapeutic entities. Success hinges upon the ability to finely tune the properties of the

therapeutic entity so that it can achieve efficacy at the target site at acceptable

administered doses without inducing unacceptable toxic side effects. Small interfering

RNA (siRNA) molecules are no exception, as safe and effective systemic delivery

remains a major challenge impeding their widespread translation into the clinic (1).

siRNAs, which are double-stranded nucleic acids approximately 19-21 bp in

length, are the effectors of RNA interference (RNAi), a naturally occurring mechanism

for post-transcriptional gene silencing (2,3). These siRNAs find their cognate mRNAs

through Watson-Crick base pairing and subsequently trigger the degradation of these

target mRNAs. The effect of the mRNA degradation is a reduction in protein expression,

and this mechanism can be exploited therapeutically to inhibit the expression of disease-

associated targets such as ribonucleotide reductase (RNR). RNR is an attractive target

for cancer therapies since it catalyzes the reduction of ribonucleotides into

deoxyribonucleotides necessary for DNA replication and repair. Several potent siRNA

inhibitors of the M2 subunit of RNR (RRM2) have been identified, and these siRNAs have demonstrated the ability to inhibit the growth of tumor cell lines after transfection in vitro and transplantation into mice (4). A recent study by Avolio et al. demonstrated the in vitro and in vivo efficacy of an siRNA targeting ribonucleotide reductase (5). However, the dearth of suitable methods for in vivo siRNA delivery to tumors has yet limited translation of siRNAs for cancer therapy into the clinic.

Several promising strategies are currently being developed to specifically address systemic siRNA delivery. Covalent attachment of antibodies or cholesterol to the siRNAs can improve their pharmacokinetics and tissue distribution, addressing the problem of rapid renal clearance of naked siRNAs (6,7). Nanoparticle-based delivery vehicles also can improve the pharmacokinetics and tissue distribution of the delivered siRNAs, while providing additional properties such as large payload capacity and tunable surface modification. Stable nucleic acid lipid particles (SNALP) have been shown to deliver functional siRNA to the livers of mice and non-human primates leading to downregulation of *APOB* with good tolerability and minimal toxicity (8). These are non-targeted nanoparticles that passively accumulate in the liver and release their siRNA payload for uptake by the liver hepatocytes. Targeted nanoparticles attempt to enhance the uptake by certain cell populations through interactions with specific cell-surface receptors (9). For example, we have previously described a nanoparticle carrier based on cyclodextrin-containing polycations (CDP) that can be modified with transferrin-targeting ligands, and this system has shown efficacy in delivering functional siRNA to tumors in vivo (10-12).

In the study presented here, we examine the effects of using a CDP-based nanoparticle carrier to deliver therapeutic siRNAs at different dosing schedules to established subcutaneous tumors in mice. Tumor growth is followed by BLI and caliper measurements to measure changes in both cell viability and overall tumor burden. Mice are treated by low-pressure tail vein injection of the naked siRNAs or siRNA nanoparticles. Two different siRNAs targeting separate regions on RRM2 mRNA are shown to inhibit tumor cell growth in vitro and in vivo, while both an irrelevant control and a mismatched variant of one of the potent siRNAs do not show growth inhibition. Comparison of Tf-targeted and non-targeted nanoparticles as well as different dosing regimens is used to address practical considerations concerning optimal treatment design. Mathematical model calculations are used to provide possible explanations for the observed effects and to raise important issues for consideration when designing treatment regimens especially for cancer therapies that act through a cytostatic mechanism.

7.3   Materials and methods

7.3.1   *siRNA duplexes*

The sequences for the siRNA duplexes targeting the RRM2 gene (siR2A+5, siR2B+5, siR2B+6) have been previously described (4). siLuc is designed to target the firefly luciferase gene. These siRNAs were purchased as unmodified RNA duplexes from Integrated DNA Technologies. siCON is an unmodified siRNA bioinformatically designed to minimize the potential for targeting any human or mouse genes, and it was purchased as an RNA duplex from Dharmacon.

siR2A+5:
```
    sense:        5'- CGAGUACCAUGAUAUCUGGCA -3'
    antisense:    5'- CCAGAUAUCAUGGUACUCGAU -3'
```

siR2B+5:
```
    sense:        5'- GAUUUAGCCAAGAAGUUCAGA -3'
    antisense:    5'- UGAACUUCUUGGCUAAAUCGC -3'
```

siR2B+6:
```
    sense:        5'- AUUUAGCCAAGAAGUUCAGAU -3'
    antisense:    5'- CUGAACUUCUUGGCUAAAUCG -3'
```

siLuc:
```
    sense:        5'- GUGCCAGAGUCCUUCGAUAdTdT -3'
    antisense:    5'- UAUCGAAGGACUCUGGCACdTdT -3'
```

siCON:
```
    sense:        5'- UAGCGACUAAACACAUCAAUU -3'
    antisense:    5'- UUGAUGUGUUUAGUCGCUAUU -3'
```

7.3.2 *In vitro transfection*

Neuro2A-Luc cells with constitutive luciferase expression were seeded at $2x10^4$

cells per well in 24-well plates 2 days prior to transfection and grown in DMEM

supplemented with 10% FBS and antibiotics (penicillin/streptomycin). siRNA was

complexed with Oligofectamine (Invitrogen) according to manufacturer's instructions

and 20 pmol siRNA was applied to each well in a total volume of 200 μL Opti-MEM I

(Invitrogen). Transfection media was removed and replaced with complete media after 4

h. The kinetics of the luciferase knockdown were determined using the Xenogen IVIS

100 (Xenogen, Alameda, CA) as described previously (12). After the final time point,

phase contrast images of the cells were taken using a Sony CCD-IRIS/RGB video camera

attached to a Nikon Eclipse TE-300 inverted microscope.

7.3.3   Nanoparticle formation

Before addition to the nucleic acid, the CDP was mixed with adamantane (AD)-polyethylene glycol (PEG) at a 1:1 AD-PEG:β-CD (mol:mol) ratio in water. Targeted nanoparticles contained AD-PEG-transferrin (AD-PEG-Tf) as a percentage of the total AD-PEG in the mixture. For example, 1 mol% AD-PEG-Tf nanoparticles contained 0.01 moles AD-PEG-Tf for every 0.99 moles AD-PEG, and 0.1 wt% AD-PEG-Tf nanoparticles contained 0.001 g of AD-PEG-Tf for every 1 g of AD-PEG. The mixture of CDP, AD-PEG, and AD-PEG-Tf in water was then added to an equal volume of siRNA in water such that the ratio of positive charges from CDP to negative charges from the nucleic acid was equal to the desired charge ratio of 3 (+/-). An equal volume of 10% (w/v) glucose in water was added to the resulting nanoparticles to give a final concentration of 5% (w/v) glucose suitable for injection.

7.3.4   Dynamic light scattering (DLS)

Nanoparticle formulations were diluted to a volume of ~1.5 mL, placed in a cuvette, and inserted into a ZetaPALS (Brookhaven Instruments Corporation) instrument to measure both the size and zeta potential. Reported effective hydrodynamic diameters and zeta potentials represent the average values from a total of 10 runs each.

7.3.5   Animals and tumor formation

Female A/J mice were ordered from Jackson Laboratories. All tumor growth studies were performed when mice were 7-9 weeks old. Neuro2A-Luc cells were grown in DMEM supplemented with 10% FBS and antibiotics (penicillin/streptomycin) and subsequently trypsinized and resuspended in serum-free DMEM for injection. Each mouse was injected with 1×10^6 Neuro2A-Luc cells in the right flank to form a

subcutaneous tumor. Tumor growth was monitored by caliper measurements of tumor volume ($0.5 \times l \times w^2$) and bioluminescent imaging of total emitted ph/s from the tumor region of interest. Treatments were commenced when the tumors had reached approximately 100 mm^3.

7.3.6   Intravenous administration of siRNA formulations

Naked siRNA or siRNA nanoparticles were mixed with an equal volume of 10% (w/v) glucose in water to yield a 5% (w/v) glucose (D5W) carrier solution suitable for injection. Each mouse was injected via lateral tail vein with 0.2 mL of the formulation in a 5% glucose solution.

7.3.7   Bioluminescent imaging (BLI)

Cell culture plates or mice were imaged using the Xenogen IVIS 100 imaging system (Xenogen). D-luciferin (Xenogen) was dissolved in PBS at 15 g L^{-1}. For in vitro assays in 24-well plates, 50 μL of the 15 g L^{-1} luciferin solution was added to each well containing 1 mL of media. Light emission was measured 2-3 minutes after addition of the luciferin. For in vivo experiments, 0.2 mL of the 15 g L^{-1} luciferin solution was injected i.p. 10 minutes before measuring the light emission. Mice were anesthetized with an initial dose of 5% isoflurane followed by a maintenance dose of 2.5% isoflurane. Bioluminescent signals were quantified using Living Image software (Xenogen).

7.3.8   Histology and confocal immunofluorescence microscopy

A/J mice bearing subcutaneous Neuro2A-Luc tumors were injected via tail vein with Tf-targeted nanoparticles carrying 2.5 mg/kg Cy3-siLuc. 18 h after injection, the mice were euthanized and the tumors were harvested, immediately placed in OCT

(TissueTek), and frozen on dry ice. Samples were stored at -80°C until sectioning. 5-μm

thick cryosections were stained with hematoxylin and eosin (H&E) for histological

analysis. To prepare for immunofluorescence staining, 5-μm thick cryosections were

thawed and then fixed with acetone at -20°C for 15 min. Fixed cryosections were

blocked with normal donkey serum (Jackson ImmunoResearch) for 1 h at room

temperature, washed with PBS, and then placed in a humidity chamber for incubation

with the primary antibodies in PBS + 1% BSA for 2 h at room temperature. A rat anti-

mouse CD31 primary mAb (Pharmingen) was used at a dilution of 1:25, and a goat anti-

luciferase primary pAb (Promega) was used at a dilution of 1:50. After washing with

PBS, the cryosections were placed in a humidity chamber for incubation with the

secondary antibodies in PBS for 1 h at room temperature. An AF488-conjugated donkey

anti-rat secondary antibody (Invitrogen) was used at a dilution of 1:200, and a Cy5-

conjugated donkey anti-goat secondary antibody (Jackson ImmunoResearch) was used at

a dilution of 1:200. After washing with PBS, the slides were mounted using Biomeda

Gel/Mount. Confocal microscopy was performed using a Zeiss LSM 510 Meta laser-

scanning confocal microscope.

7.3.9   *Determination of treatment efficacy*

Quantification of the relative efficacy of various treatments was accomplished by

calculating the time for the tumor to reach a luciferase signal of 1×10^{10} ph/s or a volume

of 1000 mm^3. To facilitate comparison between treatment groups, the growth curves for

each group were time-shifted using linear regression of the log-transformed initial growth

curves so that the value at day 7 (pre-injection) for each group was 100 mm^3 (or 1×10^9

ph/s). The time to endpoint (TTE) was then calculated by linear regression of a log-

transformed growth curve created from the final time point and the three previous time points. Mice whose tumors never reached the end point size were assigned a TTE value equal to the final day of the study. Statistical significance of the difference in TTEs between treatment groups was assessed using log-rank tests with two-tailed p values. TTEs based on the luciferase signal endpoint of 1×10^{10} ph/s are designated "TTE luc."

7.3.10 Tolerability

Mouse body weight was determined every 2-3 days during the course of treatment. Acceptable toxicity for each treatment group was defined as a mean body weight loss of no less than 20% at any point during or after treatment.

7.3.11 Mathematical modeling

We added a cell death parameter to the mathematical model of siRNA-mediated gene silencing described previously to enable simulation of treatment with a therapeutic siRNA (12). The differential equation governing cell growth was modified so that the cell growth rate would be reduced by a factor of P/Po where P is defined as the target protein concentration and Po is defined as the initial steady-state protein concentration in the cell. The equation was also modified such that the growth rate would be reduced to 0 when P/Po is reduced below an arbitrary threshold of 0.5. No parameters were included to account for possible cell death in addition to reduction in growth rate; however, such modifications could be easily incorporated if knockdown of a certain target protein is known to directly induce cell death. Furthermore, no modifications were added to account for the length of time the target protein is reduced below the threshold of 0.5, although it could be imagined that this might be physiologically relevant. The protein degradation rate, *kdegprot*, was adjusted to reflect the RRM2 protein half-life of 6.3 h

(13). The extracellular elimination rate constant, *kelimec*, was adjusted to 0.06 h^{-1} since the observed stability of the siRNA particles when incubated in serum is approximately 11 h, as shown in Chapter 5. The *partition* parameter governing the amount of the injected dose that reaches the tumor was adjusted to 1.5×10^{-2}. Finally, tumor growth was modeled with a logistic growth equation where the maximum number of cells was limited to 1000× the initial number of injected cells. The remaining parameters were left unchanged from those described previously (12).

7.4   Results

7.4.1   In vitro growth inhibition by siRNAs targeting RRM2

Demonstration of the efficacy and sequence-specificity of the siRNA duplexes was first performed in cultured Neuro2A-Luc cells. The luciferase expression of the Neuro2A-Luc cells was monitored longitudinally using the Xenogen live-cell imaging system. Our previous work has shown that the luciferase knockdown in the Neuro2A-Luc cells lasts approximately 1 week with the greatest knockdown occurring 1-2 days after transfection (12). However, a different situation is observed when siRNAs that inhibit cell growth are applied. Instead of being used to follow the changes in luciferase expression, BLI is used to noninvasively measure the relative growth rates of the luciferase-expressing cells. The results in Figure 7.1 show the relative growth rates of cells transfected with siR2A+5, siR2B+5, siR2B+6, and siCON, and a phase contrast image of the cells in each treatment group after the final time point is shown to confirm the growth inhibition. The sequences for siR2A+5 and siR2B+5 were chosen based on their ability to reduce RRM2 protein levels in vitro and their complete sequence homology to mouse and human RRM2 (4). Furthermore, they target two separate sites

on the RRM2 mRNA. The sequence for siR2B+6 displayed reduced potency for RRM2

protein reduction relative to siR2A+5 and siR2B+5, even though it shares nearly

complete homology to the siR2B+5 sequence, indicating the highly specific nature of the

RNAi mechanism (4). Finally, siCON served as an irrelevant control sequence.

Consistent with the expected reductions in RRM2 protein levels, both siR2A+5 and

siR2B+5 inhibit cell growth relative to siR2B+6 and siCON. At the final time point, a

two-tailed Student's t-Test was used to assess the significance of the cell growth

inhibition by each treatment group. The growth inhibition by siR2B+5 relative to all

other treatment groups was highly significant ($p<0.005$), inhibition by siR2A+5 was

highly significant ($p<0.005$) relative to siCON and not quite significant relative to

siR2B+6 ($p=0.05$), and inhibition by siR2B+6 was not significant ($p>0.1$) relative to

siCON.
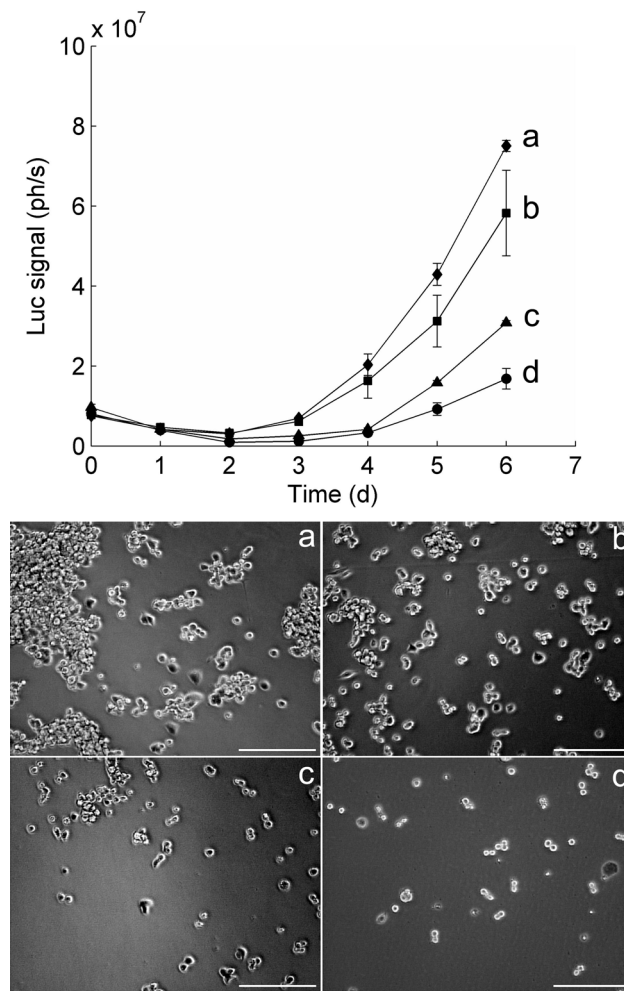
Figure 7.1. In vitro growth inhibition of Neuro2A-Luc cells after treatment with siCON (a), siR2B+6 (b), siR2A+5 (c), and siR2B+5 (d). Growth curves were measured for 6 consecutive days after treatment using live-cell bioluminescent imaging, and phase contrast images of cells from each of the four treatment groups were acquired after the final time point. The growth curves represent the mean luciferase signal from one (siR2A+5) or two (siR2B+5, siR2B+6, siCON) experiments with triplicate wells each. Error bars = *SE*.

7.4.2 *Schedule dependence of tumor growth inhibition in vivo by siRNA nanoparticles*

Based on the in vitro growth inhibition studies, siR2A+5 and siR2B+5 possess the

capability to inhibit cell growth once they are internalized into the Neuro2A-Luc cells.

When the siRNAs are administered intravenously in mice using the CDP-based

nanoparticle carriers, however, only a small percent of the injected siRNA dose even

reaches the tumor location, let alone is internalized by the target cells (as shown in

Chapter 5). Therefore, a systematic exploration of dose, dose frequency, and targeting ligand density was performed to determine what conditions may lead to sufficient delivery of the siRNAs into the Neuro2A-Luc tumor cells in mice to affect tumor growth rates.

Our previous work has shown that delivery of 2.5 mg/kg siRNA by the CDP-based nanoparticles was sufficient to achieve knockdown of a target gene in mouse tumors (11). Therefore, this dose was chosen as the initial dose for the investigations described here. The first set of experiments was conducted to determine the impact of dosing schedule. The rapid growth of the Neuro2A-Luc subcutaneous tumors provides the opportunity to conduct these experiments on a reasonable time scale, but it also limits the available dosing window since the length of time between the appearance of palpable tumors and their reaching the IACUC size limit is approximately 2 weeks. Figure 7.2 shows the effect of dosing schedules of qd×1, qd×3, or q3d×3 for doses of 2.5 mg/kg siRNA (siR2B+5 [n = 5], siR2B+6 [n = 5], and siCON [n = 4-5]) formulated into Tf-targeted (1 mol% Tf) nanoparticles. The data are represented as median luciferase signal (ph/s) measured by BLI. At all dosing schedules, siR2B+5 showed greater tumor growth inhibition than either siR2B+6 ($p<0.1$ for qd×1, $p<0.05$ for qd×3, and $p<0.1$ for q3d×3) or siCON ($p<0.1$ for qd×1, $p<0.15$ for qd×3, and $p<0.1$ for q3d×3). Although there was no statistically significant difference between the three dosing schedules of siR2B+5, the schedule of qd×3 (median TTE luc = 26.9 d) led to a greater delay in tumor growth relative to schedules of qd×1 (median TTE luc = 16.9 d) or q3d×3 (median TTE luc = 15.4 d). A single dose (qd×1) or three doses given every three days (q3d×3) yielded similar changes in the median tumor growth. The tumors may have grown to such a large

size by the time the last two doses of the q3d×3 schedule were given that the injected dose was unable to reach enough cells with an efficacious dose to impact tumor growth; therefore, this schedule had similar efficacy to a single dose. Three consecutive daily doses, however, may lead to sufficient siRNA accumulation at the tumor site and within the cells to have the desired impact on growth inhibition.

None of the treatments led to any overt signs of toxicity, and the mean body weight loss after treatment was ≤5% for all dosing schedules with siR2B+5, siR2B+6, and siCON. The body weight loss was transient with a maximum loss usually occurring within the 1-2 days immediately after treatment and a recovery to pre-treatment body weights thereafter.
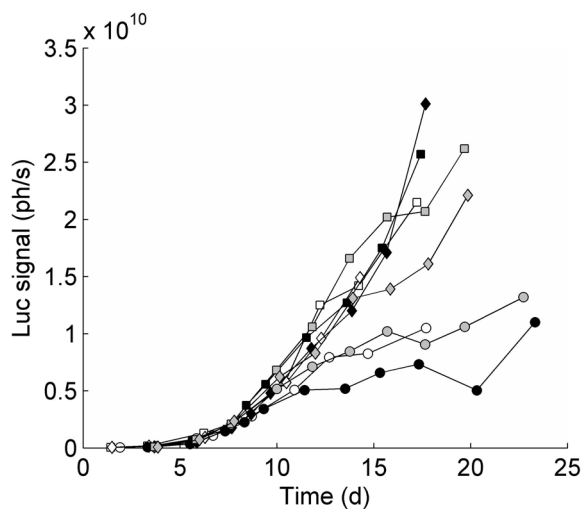
Figure 7.2. Effect of siRNA nanoparticle dosing schedule on the in vivo growth inhibition of established subcutaneous Neuro2A-Luc tumors in A/J mice. Tf-targeted nanoparticles containing 2.5 mg/kg of siR2B+5 (circles, n = 5), siR2B+6 (squares, n = 5), or siCON (diamonds, n = 4-5) were injected intravenously once (qd×1, white markers), on three consecutive days (qd×3, black markers), or once every three days (q3d×3, gray markers). Tumor growth was monitored by BLI, and the median luciferase signal is shown for each treatment group over the entire study period beginning with the initial injection of the cells. The first treatment was started around day 7 when the tumors achieved a luciferase signal of approximately 1×10^9 ph/s (~100 mm^3).

7.4.3 *Correlation between tumor bioluminescence (BLI) and tumor volume (caliper measurement)*

One advantage of using a subcutaneous tumor model for these studies is that the tumor growth can be quantified by either BLI or caliper measurement of tumor volume. Since the goal of these studies was to examine the tumor growth inhibition by the delivered siRNAs, it was necessary to verify that the changes in luciferase expression correlated with changes in physical tumor volume. Tumor luciferase signal (ph/s) as a function of tumor volume (mm^3) is shown in Figure 7.3. These data represent the compilation of the luciferase signal and size measurements for several hundred tumors, since each data point represents the mean value for one of the treatment groups (typically n = 5) of mice at a given time after injection. The best fit ($r^2 = 0.89$) was obtained using a power law regression with an exponent of 0.9. This shows that BLI ph/s and caliper tumor volume are highly correlated, and there is nearly a linear correlation over 4 orders of magnitude. The accuracy of the correlation is highest for tumors with volumes >100 mm^3, an observation also made by Paroo et. al using a luciferase-expressing HeLa cell line (14). Furthermore, the correlation holds for mice treated with the therapeutic siRNAs, showing that treatment does not hinder the capability of BLI to follow changes in tumor volume in this tumor model. Consistent with our ex vivo analysis of the tumors in this study, Smrekar et al. observed very little necrosis in Neuro2A tumors. As necrotic regions could affect the correlation between luciferase signal and tumor volume, their minimal presence in the Neuro2A tumors may contribute to the good correlation observed in Figure 7.3.
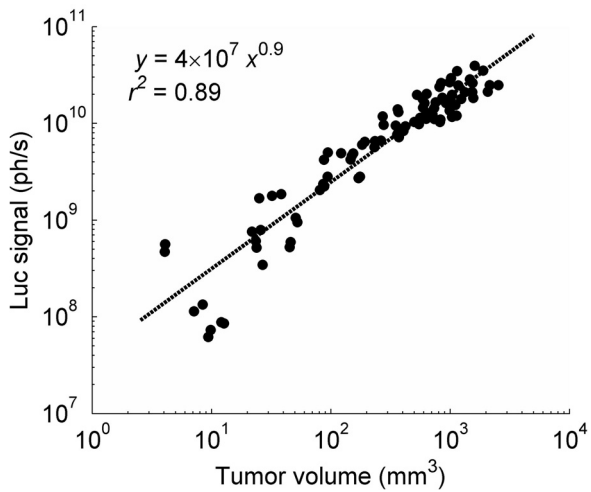
Figure 7.3. Correlation between tumor bioluminescence and tumor volume. Tumor luciferase signal (ph/s) as a function of tumor volume (mm³) is shown for data from several hundred independent measurements (each data point represents the mean value for one of the treatment groups [n = 3-5] of mice at a given time after injection). The dashed line represents the power law regression line (r^2 = 0.89) that provided the best fit to the data.

However, a higher variability in bioluminescent imaging was observed compared to caliper measurements, especially when tracking the growth curves over time. Tumors (especially at early time points) which were placed deeper under the skin showed lower luciferase signal even though the physical size was identical to tumors located closer to the surface. BLI was therefore affected by variability in tissue penetration of light as well as differences between animals in luciferin injection and tumor uptake. Although both BLI and caliper measurements were still used to follow tumor growth in all of the experiments described here, the remaining results are reported as mean tumor volume (mm³) owing to the reduced variability for caliper measurement of tumor volume. Notwithstanding, BLI can prove invaluable for tracking tumor growth in regions inaccessible to caliper measurement, such as sites of tumor metastasis, but such advantages are not apparent in a subcutaneous tumor model.

7.4.4   In vivo efficacy of naked siRNA vs. siRNA nanoparticles

The next set of experiments attempted to determine the effect of varying the

siRNA formulation conditions while maintaining the qd×3 dosing schedule. The results

in Figure 7.4A demonstrate the impact of variations in siRNA formulation conditions on

the mean tumor volume, while the survival curves (time to 1000 mm^3) for each treatment

group are shown in Figure 7.4B.
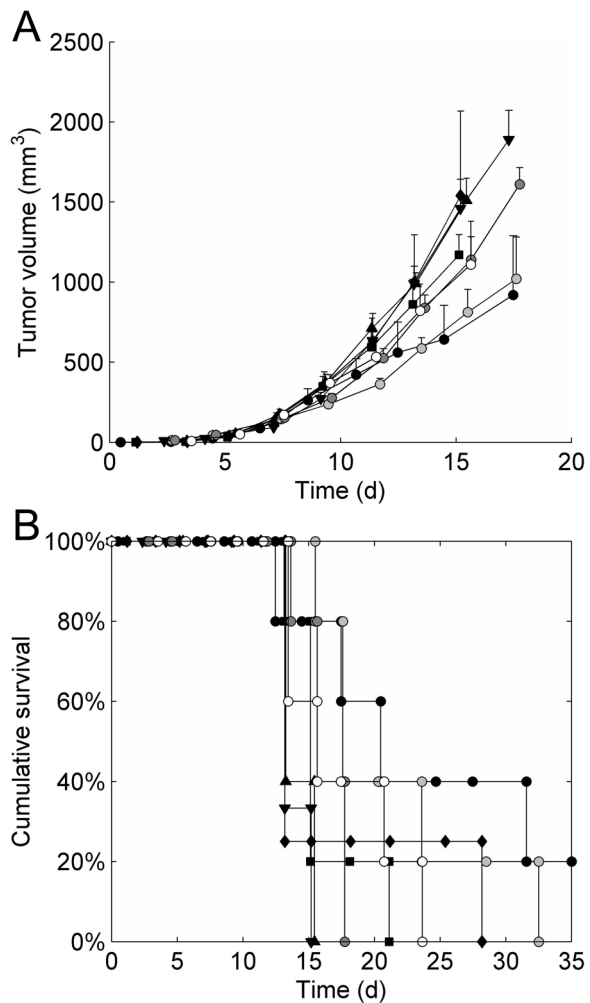
Figure 7.4. Effect of siRNA nanoparticle formulation on the in vivo growth inhibition of established subcutaneous Neuro2A-Luc tumors in A/J mice after intravenous injection of naked siRNA or siRNA nanoparticles for three consecutive days (qd×3). (A) Mean tumor volume. Error bars = *SE*. (B) Survival curves based on the endpoint of 1000 mm^3. Tf-targeted nanoparticles carrying 2.5 mg/kg of siR2B+5 were formulated without Tf targeting ligand (white circles, n = 5), with 0.1 wt% Tf (dark gray circles, n = 5), or with 1 mol% Tf (black circles, n = 5). Comparison is also made to Tf-targeted (1 mol%) nanoparticles carrying 5 mg/kg of siR2B+5 (light gray circles, n = 5), Tf-targeted (1 mol%) nanoparticles carrying 2.5 mg/kg of siR2B+6 (black squares, n = 5), Tf-targeted (1 mol%) nanoparticles carrying 2.5 mg/kg of siCON

(black diamonds, n = 4), 2.5 mg/kg of naked siR2B+5 (black triangles, n = 5), or no treatment (inverted black triangles, n = 3). The first treatment was started around day 7 when the tumors were ~100 mm^3.

Duxbury et al. reported that twice-weekly systemic administration of naked siRNA inhibited subcutaneous tumor growth in mice, and Avolio et al. showed subcutaneous tumor growth inhibition after thrice-weekly injection of naked siRNA (5,15). To test whether the same tumor growth inhibition was observed with naked siRNA as with the nanoparticle formulations in the Neuro2A subcutaneous tumor model studied here, 2.5 mg/kg of naked siR2B+5 (n = 5) was administered at the dosing schedule of qd×3 and the growth of tumors was followed over time. As with the nanoparticle formulations, the mice treated with naked siRNA showed a transient reduction in body weight ≤5%. The results in Figure 7.4 show that tumor growth in mice treated with naked siR2B+5 (median TTE = 12.9 d) was similar to that in untreated mice (n = 3, median TTE = 12.9 d). On the other hand, all treatments with the Tf-targeted nanoparticle formulations led to significant ($p<0.05$) changes in TTE relative to untreated mice or naked siR2B+5.

7.4.5   In vivo efficacy of targeted vs. non-targeted siRNA nanoparticles

Since the nanoparticle formulations appeared to be important for the efficacy of the delivered siRNA in the subcutaneous Neuro2A tumors, mice were treated with siR2B+5 at 2.5 mg/kg qd×3 formulated into nanoparticles containing 1 mol% Tf (n = 5), 0.1 wt% Tf (n = 5), or no Tf (non-targeted, n = 5) to assess the impact of Tf targeting ligand density. No adverse health events were observed after treatment with these formulations, and the transient body weight loss immediately after treatment was ≤5%. The data in Figure 7.4 indicate that nanoparticles with 1 mol% Tf were the most effective

for inhibiting tumor growth (median TTE = 17.6 d), while both non-targeted

nanoparticles (median TTE = 15.7 d) and those with only 0.1 wt% Tf (median TTE =

15.0 d) showed less inhibition of tumor growth relative to untreated mice (median TTE =

12.9 d). However, both the 1 mol% Tf and 0.1 wt% Tf formulations showed a

statistically significant ($p<0.05$) change in TTE relative to untreated mice, while the non-

targeted formulation did not ($p>0.3$). The targeting ligand likely helps to enhance the

intracellular uptake of the injected siRNA nanoparticles. In a metastatic xenograft model,

we previously showed efficacy using Tf-targeted (0.1 wt%) siRNA nanoparticles (11).

The greater efficacy observed here using the higher targeting ligand density (1 mol%)

may reflect the reduced, but not negligible, affinity between the human Tf and the mouse

TfR on mouse Neuro2A cells, or the use here of a subcutaneous instead of a metastatic

tumor model. Further studies will be needed to optimize nanoparticle targeting ligand

density, and the optimal density may depend on factors such as the cell line, tumor

location, and tumor size.

Finally, mice were treated with the Tf-targeted (1 mol%) nanoparticles qd×3 with

an siRNA dose of 5 mg/kg (n = 5). Treatment at the 5 mg/kg dose led to a transient

decrease in mean body weight of ~11%, approximately twice that observed for

formulations at 2.5 mg/kg; however, no other adverse health effects were observed.

Relative to untreated mice, there was a highly significant change in TTE ($p<0.005$).

However, as shown in Figure 7.4, there was no advantage for tumor growth inhibition

with a dose of 5 mg/kg (median TTE = 15.9 d) relative to a dose of 2.5 mg/kg (median

TTE = 17.6 d). This may indicate that the 2.5 mg/kg dose is sufficient to reduce the

RRM2 protein levels below the value necessary to inhibit cell growth; therefore, if the

higher dose does not reach a higher percentage of the tumor cells, no phenotypic difference would be observed. It is possible that the nanoparticles may have restricted access to different cell populations within the tumor that inherently limit the efficacy of the delivered siRNA, although these important effects of intratumoral nanoparticle and siRNA distribution have yet to be extensively tested for this system.

7.4.6 *Tumor growth inhibition in vivo correlates with in vitro cell growth inhibition*

Although the siR2A+5, siR2B+5, siR2B+6, and siCON sequences had different effects on Neuro2A-Luc cell growth in vitro, it remained to be shown whether these same trends would be observed after nanoparticle-mediated delivery to subcutaneous Neuro2A-Luc tumors in vivo. The results in Figure 7.5 show the mean tumor volume (mm^3) for mice treated qd×3 with Tf-targeted (1 mol%) nanoparticles containing 2.5 mg/kg of siR2A+5 (n = 5), siR2B+5 (n = 5), siR2B+6 (n = 5), or siCON (n = 4). Corroborating the correlation between BLI and physical tumor volume presented in Figure 7.3, the trends for mean tumor volume are the same as for median tumor light output (ph/s) shown in Figure 7.2; however, Figure 7.5 also contains the data for mice treated with Tf-targeted nanoparticles containing siR2A+5. Like siR2B+5, the siR2A+5 sequence leads to significant tumor growth delay relative to untreated mice ($p<0.005$). In vivo tumor growth inhibition by the delivered siRNAs parallels their in vitro efficacy, with the potency of in vivo growth inhibition following the trend of siR2B+5 (median TTE = 17.6 d) > siR2A+5 (median TTE = 17.0 d) > siR2B+6 (median TTE = 14.3 d) > siCON (median TTE = 13.1).
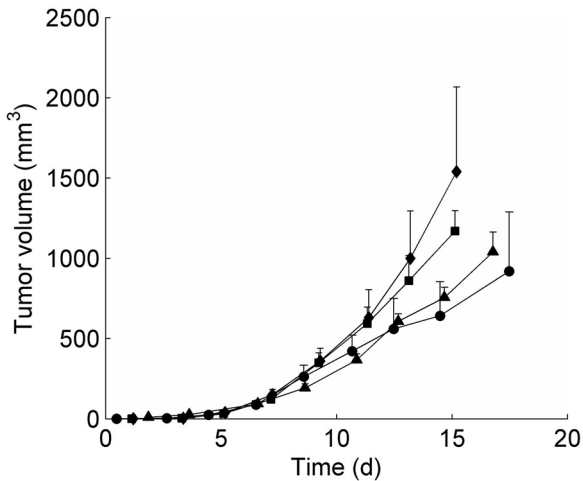
Figure 7.5. In vivo growth inhibition of established subcutaneous Neuro2A-Luc tumors in A/J mice after treatment with three independent sequences targeting RRM2 mRNA and an irrelevant control sequence. Tf-targeted (1 mol%) nanoparticles containing 2.5 mg/kg of siR2B+5 (circles), siR2B+6 (squares), siCON (diamonds), or siR2A+5 (triangles) were injected intravenously on three consecutive days (qd×3) once the tumors had reached a size of ~100 mm^3.

7.4.7   *Histology and confocal immunofluorescence microscopy*

To investigate the intratumoral distribution of siRNA after systemic delivery, H&E-staining and confocal immunofluorescence (IF) microscopy were used to examine cryosections of subcutaneous Neuro2A-Luc tumors excised from mice 18 h after tail-vein injection with Tf-targeted nanoparticles carrying 2.5 mg/kg Cy3-labeled siLuc (Figure 7.6). The H&E staining revealed the aggressive form of the Neuro2A-Luc tumors, characterized by densely packed tumor cells. However, IF staining for blood vessels using an anti-CD31 antibody showed that the tumors are also well-vascularized. This characteristic is particularly important to therapeutics that are applied intravenously and therefore require transport to the tumor through the blood vessels. Because of the extensive tumor vascularization, even intact nanoparticles that may have poor tissue penetration owing to their size (~70 nm) can potentially access a significant portion of the tumor cells. Cy3-labeled siLuc can be seen within the tumor cryosections in Figure 7.6,

although the intratumoral distribution of the siRNA molecules is highly heterogeneous.

Moreover, IF-staining for luciferase expression within the tumor cryosections indicated a

visible reduction in luciferase staining in the vicinity of the Cy3-labeled siLuc. This

would be consistent with functional activity of the delivered Cy3-siLuc that is designed

to inhibit luciferase expression. These results indicate that although the Tf-targeted

nanoparticles can deliver functional siRNA to the subcutaneous Neuro2A-Luc tumors,

their heterogeneous intratumoral distribution may limit the fraction of the tumor cells that

can be treated (Figure 7.6B).
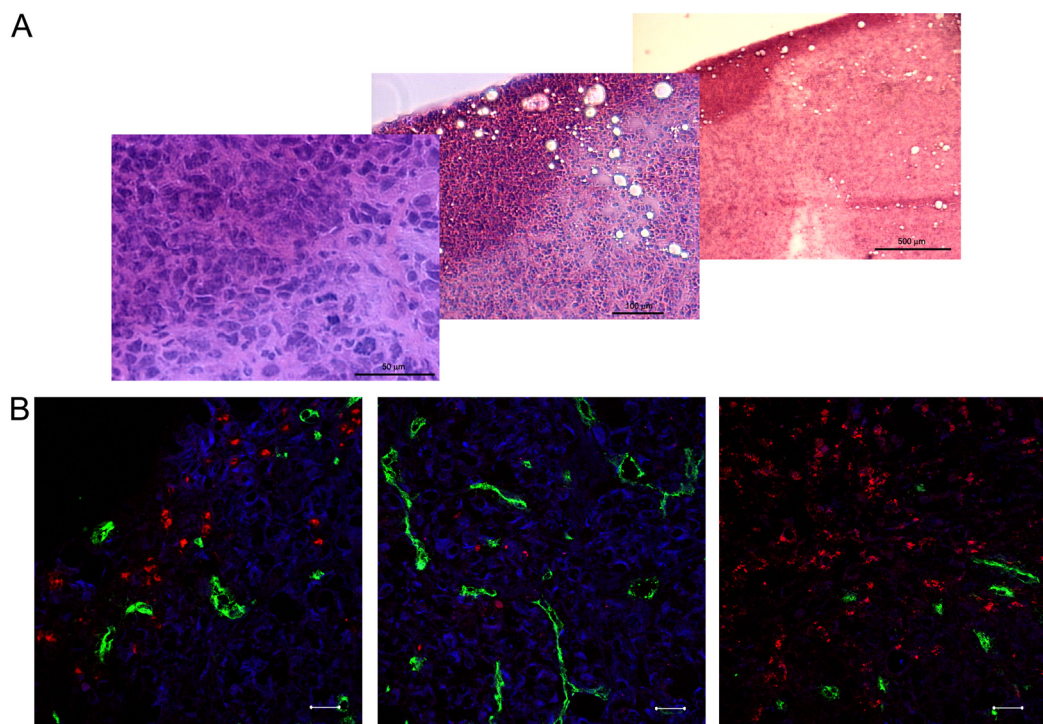
Figure 7.6. H&E staining (A) and confocal immunofluorescence microscopy (B) of Neuro2A-Luc tumor cryosections. Tumors were harvested 18 h after tail-vein injection of Tf-targeted nanoparticles containing Cy3-labeled siLuc (2.5 mg/kg). (A) H&E staining; images of the same tumor region are shown at 4X, 10X, and 40X magnification. (B) Confocal immunofluorescence microscopy of three different regions within the same tumor; green = anti-CD31, blue = anti-luciferase, red = Cy3-siLuc, and scale bar = 20 μm.

7.4.8 *Mathematical model simulations and insights for siRNA-based treatment design*

Based on our observations that a higher dose or a q3d×3 dosing schedule did not improve tumor growth inhibition, it may be that within the time frame of these experimental dosing schedules the nanoparticles essentially access the same region of tumor cells after each dose. Under such circumstances, there is no advantage to delivering more siRNA to the same region of cells once sufficient siRNA has been delivered to inhibit the growth of a given tumor cell. This is particularly important for therapeutic siRNAs which act to arrest cell growth or elicit cell death, since a threshold may exist beyond which further knockdown no longer achieves any advantage (i.e., the cell is already growth-arrested or dying). In these situations, multiple doses may not be needed for any given cell. On the other hand, multiple doses might be important if new cells are reached that either have not internalized any siRNA or have not internalized sufficient siRNA to pass beyond the threshold required for the phenotypic effect such as cell death. These concepts are illustrated in Figures 7.7 and 7.8 using a mathematical model to account for siRNA knockdown of a therapeutic target followed by cessation of cell growth if a threshold knockdown is achieved.

The duration of target knockdown after siRNA treatment is an important factor to consider when designing treatments. Figure 7.7 shows the expected duration of RRM2 protein knockdown after treatment (beginning on day 7) with 2.5 mg/kg qd×1 (I), 2.5 mg/kg q3d×3 (II), 2.5 mg/kg qd×3 (III), or 5 mg/kg qd×3 (IV). The only difference between Figures 7.8A and 7.8B is the rate of cell division of the tumor cells. In Figure 7.7A, the tumor cell doubling time is fixed at 1.5 d, so neither the maximum number of cells (logistic growth) nor target protein knockdown (even if the threshold knockdown is

surpassed) slow this growth. As expected, the knockdown lasts slightly longer than one

week (12). In Figure 7.7B, however, the tumor cell growth rate is reduced as a result of

target protein knockdown (proportional to relative protein level, P/Po), and growth is

halted if P/Po < 0.5. Although the logistic growth equation is also applied in Figure

7.7B, it has a minimal impact on the expected protein knockdown in these simulations

since removal of the maximum carrying capacity term does not significantly change the

observed target knockdown curves. Therefore, these simulations demonstrate that the

reduction in cell growth rate can lead to significantly longer target knockdown because of

the reduced dilution from cell division. In the absence of cell division, target knockdown

after siRNA delivery can last at least several weeks and even more than one month

(8,12,16). This effect may represent a particularly important consideration in light of the

increased use of cytostatic agents in oncology. If the treatment does not immediately

induce cell death but rather slows or inhibits cell growth, then the siRNA-mediated target

knockdown can persist for a substantial period after a single efficacious dose without the

need for further dosing of the cells.
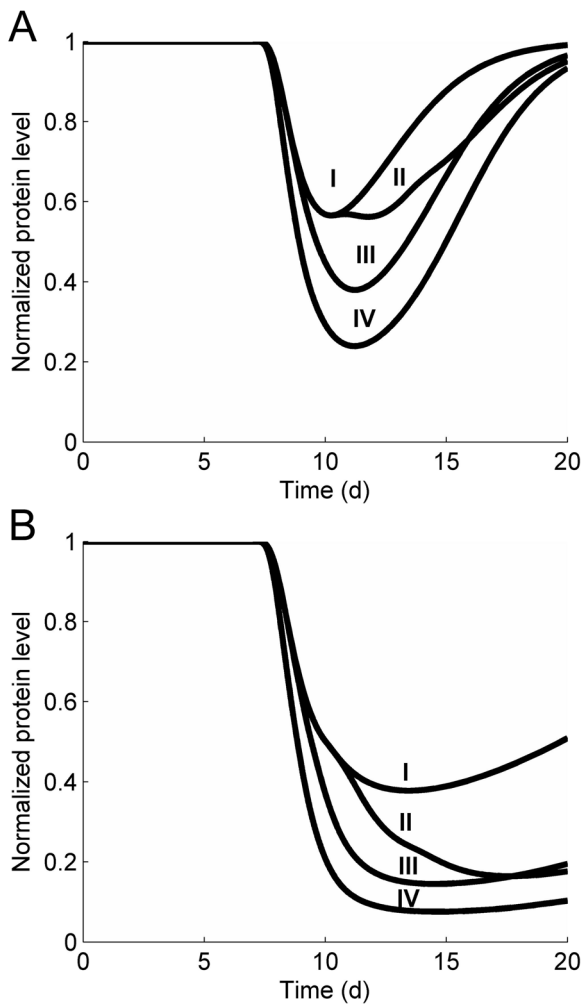
Figure 7.7. Model simulations showing the effect of tumor growth rate on the protein knockdown after siRNA nanoparticle treatment with dosing schedules of 2.5 mg/kg qd×1 (I), 2.5 mg/kg q3d×3 (II), 2.5 mg/kg qd×3 (III), or 5 mg/kg qd×3 (IV). (A) Protein knockdown in tumor cells with a constant doubling time of 1.5 d. (B) Protein knockdown in tumor cells with a growth rate that is slowed in proportion to protein knockdown and stopped once the protein knockdown passes the threshold of 50% protein knockdown.

The simulations in Figure 7.8 present an important caveat to the conclusions

drawn from Figure 7.7. Although the target knockdown in any given cell may persist for

a prolonged period if the tumor cell growth rate is reduced, it is highly unlikely that any

treatment reaches all of the cells in the tumor, as illustrated by the heterogeneous

intratumoral distribution of Cy3-siRNA shown in Figure 7.6. Particularly for relatively

large therapeutic entities such as the siRNA nanoparticles, access to certain regions

within the tumor can be limited. Even if multiple doses are given, this does not ensure that new cells are reached within the tumor. In fact, Figure 7.8A shows what would happen if no new cells are reached even with subsequent doses. Treatment (beginning on day 7) with 2.5 mg/kg qd×1 (I), 2.5 mg/kg q3d×3 (II), 2.5 mg/kg qd×3 (III), or 5 mg/kg qd×3 (IV) all lead to essentially identical tumor growth inhibition. This is because the additional doses do not provide any therapeutic benefit since the target protein is already reduced below the threshold required for cessation of growth (Figure 7.7B). In such a situation where no new cells are reached with each treatment, multiple doses (or higher doses) will only be advantageous if additional reduction in target protein levels leads to further therapeutic benefit (i.e., a greater reduction in cell growth rate or induction of apoptosis at sufficiently low target protein levels).

For comparison, the simulations in Figure 7.8B assume that each additional dose reaches 50% new cells. After three doses, this predicts that there will be populations of cells that have been reached with a single dose, two doses, or all three doses. This ability to reach new cells leads to a greater total fraction of the tumor cells that receive therapeutic doses of the siRNA, and the benefit is clearly seen in Figure 7.8B. Under these conditions, the dosing schedules of 2.5 mg/kg qd×3 (III) or 5 mg/kg qd×3 (IV) are the most effective, owing to the faster reduction in target protein levels leading to cell growth inhibition. Because the tumor is growing rapidly, the number of cells to be reached increases with time. Therefore, if more cells need to be reached, then an equivalent total dose of siRNA may not be as effective in a large tumor as it is in a small tumor (if 50% of the total tumor cells are reached in each case). Alternatively, to achieve the same intracellular levels of siRNA in the larger tumor, a lower fraction of the total

tumor cells must be reached. Either scenario will lead to lower overall efficacy. The

q3d×3 dosing schedule (II) in Figure 7.8B illustrates this point since the target protein

levels in a portion of the cells that are reached at later time points are not reduced below

the 50% threshold to stop cell growth.
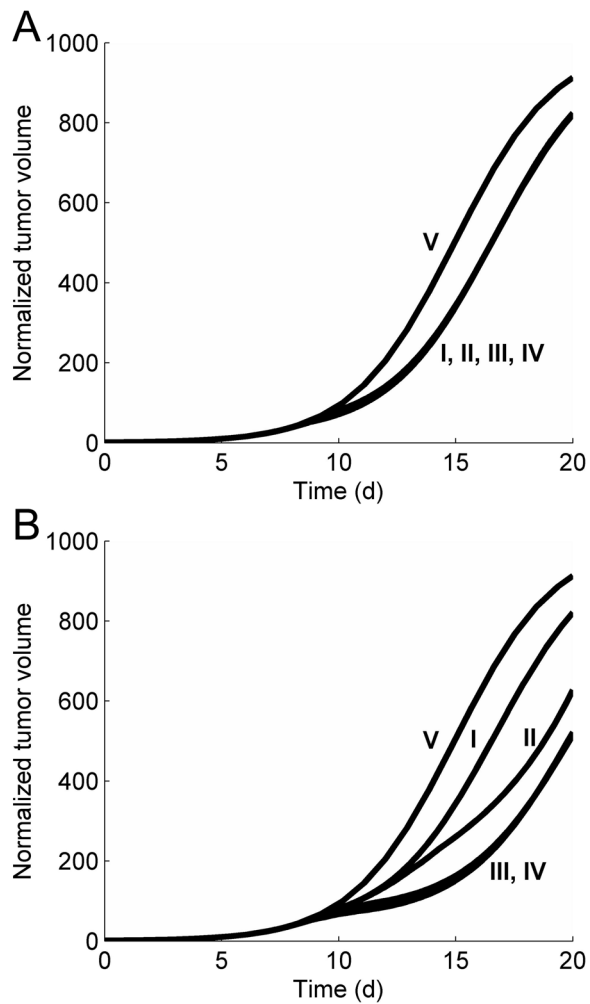
Figure 7.8. Model simulations comparing tumor growth inhibition after siRNA nanoparticle treatment in situations where (A) no new cells are reached or (B) 50% new cells are reached with each additional dose. Comparison is made between simulated siRNA nanoparticle treatment with dosing schedules of 2.5 mg/kg qd×1 (I), 2.5 mg/kg q3d×3 (II), 2.5 mg/kg qd×3 (III), or 5 mg/kg qd×3 (IV).

7.5 Discussion

In the present study, we demonstrated the ability of Tf-targeted siRNA

nanoparticles to inhibit the growth of established subcutaneous Neuro2A tumors in a

syngeneic mouse model. The siRNAs were designed to target the M2 subunit of ribonucleotide reductase (RRM2), a crucial enzyme involved in preparing nucleotides for DNA replication (17). Three separate siRNAs targeting different regions on the RRM2 transcript were tested for their ability to inhibit the growth of Neuro2A-Luc (luciferase expressing) cells in vitro relative to cells transfected with an irrelevant control sequence (siCON). Consistent with previously reported RRM2 protein knockdown by these sequences, the order of potency for cell growth inhibition was siR2B+5 > siR2A+5 > siR2B+6 (4). While siR2A+5 and siR2B+5 target completely distinct regions in the RRM2 mRNA transcript, siR2B+5 and siR2B+6 are shifted by only 1 base pair. Moreover, siR2A+5 and siR2B+5 show complete homology to mouse RRM2 mRNA, but siR2B+6 contains a single mismatch at the last nucleotide of the target region in mouse RRM2 mRNA. These examples support the exquisite sensitivity of RNAi while also providing support that the observed effects are due to specific RRM2 protein knockdown.

These same trends in potency are observed in vivo after intravenous administration of Tf-targeted nanoparticles carrying the siRNAs. siRNA nanoparticle dosing schedules of 2.5 mg/kg qd×1, 2.5 mg/kg qd×3, and 2.5 mg/kg q3d×3 were compared, and the 2.5 mg/kg qd×3 led to the most pronounced growth inhibition. Increasing the siRNA dose to 5 mg/kg did not yield greater tumor growth inhibition. Importantly, non-targeted nanoparticles given at a dose of 2.5 mg/kg qd×3 were less effective at achieving tumor growth inhibition. Several groups have reported similar trends showing that inclusion of a targeting ligand is necessary for achieving therapeutic efficacy, most likely by enhancing the intracellular delivery of the nanoparticle payload (18,19).

A particular concern with siRNA-based therapies is the possibility of nonspecific effects, such as immune stimulation, that could mask the sequence-specific effects of the siRNA (20). Toxicity studies in cynomolgus monkeys have been conducted after intravenous administration of Tf-targeted nanoparticles formed using the CDP delivery vehicle and the siR2B+5 sequence at siRNA doses up to 27 mg/kg (21). At siRNA doses up to 9 mg/kg, the Tf-targeted nanoparticles were well-tolerated with no overt signs of toxicity; importantly, there was a lack of significant complement activation or immune response at these doses. This indicates that the efficacy observed here is not related to non-specific effects from immune stimulation.

These results provide several important insights into systemic siRNA delivery using nanoparticle formulations. According to the in vitro data shown in Figure 7.2, a single dose of siRNA can be sufficient to achieve the phenotypic effect of cell growth arrest, presumably because a single dose can inhibit the RRM2 target long enough so that the rapidly dividing cells will attempt to divide during the window of inhibition, triggering the growth arrest or even cell death. With targets that disrupt cell division, for example, prolonged inhibition in any cell may not be needed, so the criteria used to choose the dosing intervals should not be designed to necessarily prolong inhibition in a given cell. Instead, multiple doses should be designed to maximize the fraction of cells reached with a sufficient siRNA dose for efficacy. The surprising observation that a higher siRNA dose did not lead to greater tumor growth inhibition can possibly be explained by the threshold hypothesis illustrated by the simulations in Figures 7.7 and 7.8. Essentially, if the target is already knocked down sufficiently in a cell, and the higher dose does not reach any greater fraction of the total tumor cells, then giving a

higher dose will provide no therapeutic advantage. This effect is magnified by the prolonged duration of target knockdown expected if cell growth is inhibited after treatment. These criteria would not be expected to apply for other therapeutic applications, such as infectious diseases or metabolic disorders, where the target may have to be continuously repressed to achieve the therapeutic effect. In such applications, multiple dosing schedules must be designed to maintain the silencing within a given cell. As we showed previously, this dosing schedule will be largely governed by the doubling time of the target cell (12).

In conclusion, these studies address issues of practical relevance for siRNA nanoparticle delivery including the impact of tumor-specific targeting and the effect of dose and dose frequency. The results emphasize the importance of rationally designing dosing schedules based on the characteristics of the therapeutic target, since the duration of gene inhibition in a given cell required for therapeutic efficacy will vary. Compared to systemically delivered naked siRNA molecules, tumor-targeted siRNA nanoparticle formulations were shown to be significantly more effective in slowing the growth of subcutaneous tumors. This increased efficacy may be attributed at least partly to the capability of nanoparticles to deliver thousands of individual siRNA molecules per cellular uptake event, increasing the chance for therapeutic efficacy within a cell. Furthermore, targeted nanoparticles are shown to be more effective than non-targeted nanoparticles, indicating that inclusion of a targeting ligand may be critical for uptake by the desired cell population after localization to the tumor microenvironment. These results emphasize the need to incorporate both tumor-specific (e.g., accessibility, number of target cells, and growth rate) and treatment-specific (e.g., threshold knockdown

required, cytostatic vs. cytotoxic, and duration of therapeutic effect after a given dose) parameters into the design of siRNA-based treatments for cancer therapy.

7.6   Acknowledgments

7.7 References

1. Behlke, M.A. (2006) Progress towards in vivo use of siRNAs. *Mol Ther*, **13,** 644-670.
2. Dykxhoorn, D.M., Palliser, D. and Lieberman, J. (2006) The silent treatment: siRNAs as small molecule drugs. *Gene Ther*, **13,** 541-552.
3. Elbashir, S.M., Harborth, J., Lendeckel, W., Yalcin, A., Weber, K. and Tuschl, T. (2001) Duplexes of 21-nucleotide RNAs mediate RNA interference in cultured mammalian cells. *Nature*, **411,** 494-498.
4. Heidel, J.D., Liu, J.Y.-C., Yen, Y., Zhou, B., Heale, B.S.E., Rossi, J.J., Bartlett, D.W. and Davis, M.E. (2007) Potent siRNA inhibitors of ribonucleotide reductase subunit RRM2 reduce cell proliferation in vitro and in vivo. *Clin Cancer Res*, **13,** 2207-2215.
5. Avolio, T.M., Yoon, L., Feng, N., Xiong, K., Jin, H., Wang, M., Vassilakos, A., Wright, J. and Young, A. (2007) RNA interference targeting the R2 subunit of ribonucleotide reductase inhibits growth of tumor cells in vitro and in vivo. *Anti-Cancer Drugs*, **18,** 377-388.
6. Song, E., Zhu, P., Lee, S.-K., Chowdhury, D., Kussman, S., Dykxhoorn, D.M., Feng, Y., Palliser, D., Weiner, D.B., Shankar, P. et al. (2005) Antibody mediated in vivo delivery of small interfering RNAs via cell-surface receptors. *Nat Biotechnol*, **23,** 709-717.
7. Soutschek, J., Akinc, A., Bramiage, B., Charisse, K., Constien, R., Donoghue, M., Elbashir, S., Geick, A., Hadwiger, P., Harborth, J. et al. (2004) Therapeutic silencing of an endogenous gene by systemic administration of modified siRNAs. *Nature*, **432,** 173-178.
8. Zimmermann, T.S., Lee, A.C.H., Akinc, A., Bramlage, B., Bumcrot, D., Fedoruk, M.N., Harborth, J., Heyes, J.A., Jeffs, L.B., John, M. et al. (2006) RNAi-mediated gene silencing in non-human primates. *Nature*, **441,** 111-114.
9. Schatzlein, A.G. (2003) Targeting of synthetic gene delivery systems. *J Biomed Biotechnol*, **2,** 149-158.
10. Bartlett, D.W. and Davis, M.E. (2007) Physicochemical and biological characterization of targeted, nucleic acid-containing nanoparticles. *Bioconjugate Chem*, **18,** 456-468.
11. Hu-Lieskovan, S., Heidel, J.D., Bartlett, D.W., Davis, M.E. and Triche, T.J. (2005) Sequence-specific knockdown of EWS-FLI1 by targeted, nonviral delivery of small interfering RNA inhibits tumor growth in a murine model of Ewing's sarcoma. *Cancer Res*, **65,** 8984-8992.
12. Bartlett, D.W. and Davis, M.E. (2006) Insights into the kinetics of siRNA-mediated gene silencing from live-cell and live-animal bioluminescent imaging. *Nucleic Acids Res*, **34,** 322-333.
13. Choy, B.K., McClarty, G.A., Chan, A.K., Thelander, L. and Wright, J.A. (1988) Molecular mechanisms of drug resistance involving ribonucleotide reductase: Hydroxyurea resistance in a series of clonally related mouse cell lines selected in the presence of increasing drug concentrations. *Cancer Res*, **48,** 2029-2035.

14. Paroo, Z., Bollinger, R., Braasch, D., Richer, E., Corey, D., Antich, P. and Mason, R. (2004) Validating bioluminescence imaging as a high-throughput, quantitative modality for assessing tumor burden. *Mol Imaging*, **3,** 117-124.
15. Duxbury, M.S., Matros, E., Ito, H., Zinner, M.J., Ashley, S.W. and Whang, E.E. (2004) Systemic siRNA-mediated gene silencing: a new approach to targeted therapy of cancer. *Ann Surg*, **240,** 667-676.
16. Bartlett, D.W. and Davis, M.E. (2007) Effect of siRNA nuclease stability on the in vitro and in vivo kinetics of siRNA-mediated gene silencing. *Biotechnol Bioeng***,** in press.
17. Cerqueira, N.M.F.S.A., Pereira, S., Fernandes, P.A. and Ramos, M.J. (2005) Overview of ribonucleotide reductase inhibitors: an appealing target in anti-tumour therapy. *Curr Med Chem*, **12,** 1283-1294.
18. Kirpotin, D.B., Drummond, D.C., Shao, Y., Shalaby, M.R., Hong, K., Nielsen, U.B., Marks, J.D., Benz, C.C. and Park, J.W. (2006) Antibody targeting of long-circulating lipidic nanoparticles does not increase tumor localization but does increase internalization in animal models. *Cancer Res*, **66,** 6732-6740.
19. Maeda, N., Miyazawa, S., Shimizu, K., Asai, T., Yonezawa, S., Kitazawa, S., Namba, Y., Tsukada, H. and Oku, N. (2006) Enhancement of anticancer activity in antineovascular therapy is based on the intratumoral distribution of the active targeting carrier for anticancer drugs. *Biol Pharm Bull*, **29,** 1936-1940.
20. Judge, A.D., Bola, G., Lee, A.C.H. and MacLachlan, I. (2006) Design of noninflammatory synthetic siRNA mediating potent gene silencing in vivo. *Mol Ther*, **13,** 494-505.
21. Heidel, J.D., Yu, Z., Liu, J.Y.-C., Rele, S.M., Liang, Y., Zeidan, R.K., Kornbrust, D.J. and Davis, M.E. (2007) Administration in non-human primates of escalating intravenous doses of targeted nanoparticles containing ribonucleotide reductase subunit M2 siRNA. *P Natl Acad Sci USA*, **104,** 5715-5721.

8 Future directions

The aim of this thesis is to help develop a rational approach for the application of siRNA therapeutics for cancer treatment. Through a methodical and quantitative analysis of siRNAs and their formulation into nanoparticles for systemic delivery, several observations were made that can help direct future research in the field.

A consistent theme throughout the thesis work was the emphasis on studying the dynamics of biological processes instead of merely looking at individual snapshots in time. It is apparent that the information obtained from time-course studies, as exemplified by the live-cell and live-animal imaging studies, provides unique insights into the behavior of the biological systems. Additionally, the tumor growth inhibition studies highlighted how these insights can be applied to design more effective siRNA-based cancer treatments. Future studies examining the kinetics of the knockdown of therapeutic targets, and not just the luciferase reporter gene, will be critical for optimizing the dosing schedules of siRNA therapeutics. Moreover, these studies must correlate the target knockdown with the observed phenotypic changes. For example, determination of a threshold knockdown or duration of knockdown required to achieve efficacy, as mentioned in Chapter 7, would provide more rigorous criteria for achieving successful therapeutic response with siRNAs.

Additional studies are also needed to further probe the mechanism and in vivo behavior of nanoparticle carriers for nucleic acids such as siRNA. In Chapter 5, the use of PET and BLI to study the in vivo biodistribution and function of siRNA nanoparticles raised several intriguing questions concerning their biological activity. Even though a significant portion of the injected siRNA appears to dissociate rapidly from the

nanoparticles after systemic administration, nanoparticle formulation still appears to facilitate the delivery of functional siRNA to the target cells. This is confirmed by the observations in Chapters 6 and 7 where targeted siRNA nanoparticles were shown to be more effective at achieving tumor growth inhibition than non-targeted siRNA nanoparticles or naked siRNAs alone. Elucidating the mechanism for these differences will be essential for designing treatments based on the targeted siRNA nanoparticles.

In Chapter 5, a mechanism was proposed whereby nanoparticles formed by electrostatic interactions with nucleic acids can be dissociated in the high salt environment within the bloodstream, particularly in the kidney. Studies will need to examine the factors responsible for making some nanoparticles more susceptible to dissociation in the presence of competing electrolytes. The electrostatic interactions may be more stable for polycations with higher molecular weight, but these polycations also may exhibit greater toxicity through mechanisms such as complement activation (as shown in Chapter 3). The short length of siRNAs may also contribute to the reduced strength of the electrostatic interactions within the nanoparticles. Future work must be done to explore how these interactions can be stabilized to keep the nanoparticles intact until reaching the desired target cell population after intravenous administration. Methods such as reversible crosslinking, as mentioned previously, may be required to achieve long circulation times while still allowing intracellular release of the nucleic acid payload.

A more thorough examination of the intratumoral distribution of the nanoparticles after intravenous administration will be important to the field of nanoparticle delivery. A fundamental issue to address is whether or not intact nanoparticles are responsible for the

observed therapeutic effects, or whether the siRNA payload is first released within the extracellular environment of the targeted cells. The results from Chapter 3 comparing the activity of unmodified and nuclease-stabilized siRNAs may be utilized to explore this question. It was shown that nuclease-stabilized siRNAs show significantly greater efficacy than unmodified siRNAs only if the siRNAs must first be exposed to a nuclease-rich extracellular environment; once the siRNAs are internalized into the cells, there is no observable difference in the persistence or magnitude of gene inhibition. Therefore, comparison of gene inhibition after delivery with unmodified and nuclease-stabilized siRNAs can indicate whether or not the siRNA is released prior to cellular internalization. If the siRNAs are only released after cellular internalization, then their efficacies would be expected to be very similar. However, extracellular release of the siRNAs may lead to an enhanced potency observed for the nuclease-stabilized siRNAs owing to their reduced degradation upon exposure to the nuclease-rich extracellular environment. Incomplete nuclease protection of the siRNA payload despite nanoparticle encapsulation can confound the conclusions from these studies, but the magnitude of this complication will be unknown until such studies are performed.

If intact nanoparticles are observed to accumulate at the target site, then another question to be explored is the impact of surface decoration with different targeting ligands. In the field of antibody therapeutics, the binding-site barrier effect limits the penetration of high-affinity antibodies. This same barrier may be particularly relevant to targeted nanoparticles, especially in light of the avidity effects conferred by the multivalency of multiple targeting ligands decorating the nanoparticle surface. If such a barrier does exist, then modifications of the targeting ligand density or the affinity of the

attached targeting ligands may be used to modulate the tumor penetration of the injected

nanoparticles. However, the size of nanoparticles may mask these binding-site barrier

effects if diffusion limitations dominate. These questions remain to be answered for

nanoparticle formulations.

Although not presented in this thesis work, initial studies were performed to develop

a high-affinity targeting ligand based on a single-chain antibody fragment against the

transferrin receptor. The antibody fragment was cloned from a parent plasmid containing

the anti-TfR scFv donated by Dr. David FitzGerald at the National Cancer Institute. It

was modified to contain a C-terminal cysteine residue to allow conjugation with PEG

conjugates for attachment to the nanoparticle surface. Conjugation of a fluorophore to

this C-terminal cysteine residue enabled the use of flow cytometry to examine the

binding properties of the anti-TfR scFv. It was shown to strongly bind to human TfR on

the HeLa human cancer cell line, but it exhibited no cross-reactivity to the mouse TfR on

the Neuro2A mouse cell line. Furthermore, competitive uptake experiments showed that

the binding of the anti-TfR scFv was not affected by the presence of Tf. As such, the

nanoparticles targeted with anti-TfR scFv, unlike those targeted by Tf, will not be

competed by endogenous Tf that is naturally present in the bloodstream. The parental

5e9 mAb from which the anti-TfR scFv is derived has a K_d of ~$2x10^{-9}$ M, whereas Tf has

a K_d of ~$3x10^{-8}$ M. Therefore, the anti-TfR scFv also possesses a much higher affinity

for the TfR than Tf. These scFv-targeted nanoparticles should exhibit extremely high

binding affinities for cells expressing the TfR owing to the higher affinity of the anti-TfR

scFv for the TfR, the absence of competition from free Tf, and the multivalency effects of

multiple surface targeting ligands.

Altogether, these proposed studies will provide important information concerning the design of nanoparticle carriers for systemic siRNA delivery. The work presented in this thesis provides a foundation upon which these other studies can be built. The practical nature of the topics explored and their direct relevance to clinical application will hopefully expedite the development of more effective cancer therapies using siRNA.